PARAMETRICALLY EXCITED TRANSVERSE PLANE INSTABILITIES ON HIGH SPEED PLANING HULLS

by

Oscar Darío Tascón Muñoz

A dissertation submitted in partial fulfillment
of the requirements for the degree of
Doctor of Philosophy
(Naval Architecture and Marine Engineering)
in The University of Michigan
2016

Doctoral Committee:

Professor Armin W. Troesch, Co-Chair
Assistant Professor Kevin J. Maki, Co-chair
Professor Bogdan I. Epureanu
Associate Professor Carolyn Q. Judge, United States Naval Academy
Brant R. Savander, P.E., Maritime Research Associates, LLC.

To my parents, Oscar Armando and Esperanza, my wife, Angela Liliana, and my sons, Andres Felipe and Santiago.

ACKNOWLEDGEMENTS

This dissertation is the culmination of many visits to Ann Arbor spanning several years. It would be nearly impossible to thank all the people who have made this endeavor possible. However, there are certain individuals and institutions to which I am deeply indebted and to whom I would like to express my profound gratitude.

First and foremost, Professor Armin Troesch has been a fully supportive mentor over these many years. My interest in ship dynamics was born in his *NA 540 - Marine Dynamics III* course and has only grown over the years studying by his side. I have found a lot of inspiration in the research that he has done over the course of his career on the dynamics and hydrodynamics of planing hulls. His enthusiasm, encouragement, and valid, well-reasoned opinions in the pursuit of excellence have made this the best dissertation possible.

Second, Professor Kevin Maki has provided a lot of insight into the solution of the 2-D impact problem by the Volume of Fluid method and the application of the 2D+t theory. I was lucky enough to attend his *NA 599 - Introduction to Numerical Hydrodynamics* and *NA 620 - Numerical Marine Hydrodynamics* courses. I agree with him in that *NA 599* has the potential to be one of the best courses offered at the University of Michigan.

I am very grateful to both Professor Troesch and Professor Maki for their trust in me, admitting me back into the program after several years' absence from the University of Michigan, and for providing all the support required to make this dissertation achievable.

Brant Savander awakened my interest for the hydrodynamics of planing hulls and the 2D+t theory during his *NA 401 - Small Craft Design* in 2002. His insights into the extension of the asymmetric 2-D impact theory to the asymmetric steady planing problem during the time I developed my Professional Degree thesis was invaluable.

Professor Bogdan Epureanu piqued my interest in the solution of non-linear dynamics problems by analytical methods. His *ME 648 - Nonlinear Oscillations and Stability of Mechanical Systems* provided the foundation for the work carried out in the approximate solution to the non-linear Hill's equation. The fruitful discussions with him and Professor Troesch on internal resonances and parametric excitations helped tremendously in my understanding of the problem.

Professor Carolyn Judge at the United States Naval Academy has shared with me the same interest for the problem addressed in this dissertation. Her experimental work on the hydrodynamics of planing hulls in asymmetric conditions has kept my interest alive over the years. Her generosity in sharing her experimental results on planing hulls, together with her insights into the problem, is greatly appreciated.

I would also like to express my gratitude to all the people at the Science and Technology Corporation for the Development of the Maritime Industry in Colombia - COTECMAR, who supported this effort from various areas within the organization.

I had the distinction to be the first recipient of the COTECMAR's scholarship for graduate studies in 2002. With this support, I completed two Master's degrees and a Professional Degree in Naval Architecture from 2002 to 2004. In 2005, I was offered the possibility to continue that effort into the Ph.D. program and since then I have received full support from the Colombian Navy and COTECMAR to complete my doctoral studies.

I am indebted to RADM Jorge E. Carreno, current president of COTECMAR, for his continuous encouragement and setting the standard by finishing his own Ph.D. program at the Universidad Politecnica de Madrid. Without his unconditional support it would not have been possible to carry out this work over so many years.

I would also like to express my deepest gratitude to the Colombian Navy for all their support over the years in helping me accomplish this important goal in my career. None of this would have been possible without the will and the trust of the Naval Staff, providing not only encouragement but also the permits and leave of absences required to complete the program.

Finally, I must thank my wife, Angela, and my sons, Andres Felipe and Santiago. I could not have finished this without their love, patience, sacrifice and continuous support.

TABLE OF CONTENTS

LIST OF FIGURES

Figure

LIST OF TABLES

Table

LIST OF APPENDICES

Appendix

ABSTRACT

PARAMETRICALLY EXCITED TRANSVERSE PLANE INSTABILITIES ON HIGH SPEED PLANING HULLS

by

Oscar Darío Tascón Muñoz

Co-Chair: Armin W. Troesch

Co-Chair: Kevin J. Maki

Planing hulls sometimes exhibit dynamic instabilities, endangering the safety of passengers and crew. Most of the efforts in understanding these phenomena have concentrated in the vertical plane (e.g., porpoising). Little has been done in the horizontal plane, where the emphasis has been placed in the understanding of progressive heeling. The physics and conditions under which planing hulls will develop oscillatory roll instabilities (e.g., chine walking) are still not well understood and therefore there are not accepted guidelines to prevent them. Consistent with this need of understanding, in this research a method for investigating the conditions under which high-speed planing hulls can exhibit large oscillatory roll motions parametrically excited by small heave and pitch motions is proposed.

A one-way coupling between heave-pitch and roll is assumed, and the roll equation of motion is written as a Hill's equation with third order non-linearities. The stability boundaries in the Ince-Strutt diagram are obtained, the influence of the different terms in the roll equation of motion on these boundaries is discussed, and conditions to be satisfied in order to avoid large amplitude periodic roll motions in the vicinity of the principal parametric resonance are derived. In order to reduce the coefficients for the roll equation of motion, the generalized forces and moments acting on a planing hull in asymmetric conditions are obtained by the 2D+t approach. The 2D+t solution cannot capture some 3-D effects such as the flow separation from the transom; therefore, an empirical correction is suggested to take this effect into consideration. Non-linear models are proposed for roll added mass and roll damping, based on Fourier analysis of the roll moment time series. It is shown that the presence of a third order harmonic of different sign than the first order harmonic in the out-of-phase component reduces the linear roll damping, increasing the probability of parametric roll.

Lastly, two of the conditions tested by Professor Judge at the United States Naval Academy (USNA) are used as case studies. The results show that high-speed planing hulls running at low mean wetted length and low trim are more prone to develop parametric roll than planing hulls running at high mean wetted length and high trim. This is consistent with what is observed in the field where lightly loaded high-speed planing hulls sometimes exhibit "chine-walking".

CHAPTER 1

Introduction

1.1 Background

Planing hulls due to their characteristics have been built for varied applications including recreation, racing, defense, police, search and rescue, among others. Unfortunately, sometimes they exhibit dynamic instabilities, endangering the safety of passengers and crew. Those instabilities have been reported (Cohen and Blount, 1986) in both the vertical and the horizontal plane and they include: rapid loss of running trim, progressive heeling (or non-oscillatory roll), porpoising, chine walking, broaching, and sudden combined roll-yaw motion. Most of the efforts in understanding these phenomena have concentrated in the vertical plane (e.g., porpoising) where Martin (1978), Troesch and Falzarano (1993), and Katayama (2002), among others, have shown that the onset of the heave and pitch instability can be predicted by linear theory, (i.e., by knowing the linear hydrodynamic added mass, damping and stiffness coefficients). However, little has been done in the horizontal plane, where most of the efforts have concentrated in the understanding of progressive heeling since it is found in a larger class of vessels (Blount and Codega, 1992). Blount and Codega (1992) proposed a series of tests in order to identify vessels prone to develop progressive heeling and provided design guidelines to avoid this type of instability.

These tests have been adopted in the International Code of Safety for High Speed Craft (IMO 2000 HSC Code) (IMO, 2008). However, in the same paper Blount and Codega (1992), referring to the dynamic instabilities that can be found in planing hulls, stated *"The problem is not well understood and accepted guidelines do not exist which will ensure adequate dynamic stability"*. Regarding the roll oscillatory instability (chine walking), this is still the case (Judge, 2014a). Therefore, there is a need to better understand the physics and conditions under which planing hulls will develop oscillatory roll instabilities.

1.2 Literature Review

The research carried out with the objective of understanding the dynamics of planing hulls can be traced down to universities and research centers. Therefore, this literature review has been organized by institutions. This review concentrates on the investigations carried out with the purpose of understanding dynamic instabilities in the horizontal plane.

1.2.1 University of Michigan

Fundamental studies have been conducted in the Department of Naval Architecture and Marine Engineering at the University of Michigan, Ann Arbor, on high speed planing technology. One of the objectives of those efforts was the development of a methodology for the prediction of hydrodynamic loads acting on planing hulls. The development of symmetric and asymmetric impact theories between 1992 and 2000 is clearly aligned with this objective due to the similar features between the impact flow and the cross sectional behavior of high speed planing. The symmetric impact theory of Vorus (1996) was extended by Savander et al. (2002) to the solution of

the problem of a general hull form in steady-planing, via a slender-body (or 2D+t) transformation. The asymmetric impact theories of Xu et al. (1998) and Judge et al. (1999) provided the foundation for the development of an asymmetric steady planning theory, via slender body theory (SBT). Piro and Maki (2011, 2012, 2013) provided the tools for the evaluation of planing hulls of general shape running with negative pitch angles, or large amplitude heave/pitch motions, since in the SBT transformation they will appear as 2D sections exiting the water. On the experimental side, two apparatuses were designed and constructed in order to carry out single degree of freedom decrement tests in roll, yaw or sway (Connors, 2001). Arguin Jr. and Troesch (2001); Arguin Jr. et al. (2001) proposed a methodology for the reduction of the hydrodynamic coefficients from those tests. A fully prismatic 20 degrees deadrise model was tested at one trim angle, one load coefficient, and four speeds. All these studies aimed at the simulation of the maneuvering characteristics of planing hulls, and the study of their transverse dynamic stability.

1.2.2 United States Naval Academy (USNA)

Extensive experimental work has been recently conducted in the Department of Naval Architecture and Ocean Engineering at the United States Naval Academy (USNA), Annapolis, on high-speed boats. The ultimate objective of this effort is a better understanding of the dynamics and hydrodynamics of the instabilities exhibited by planing boats. Therefore, the work has concentrated in obtaining information of the generalized forces acting on scaled planing boats as a function of loading coefficient, speed coefficient, roll amplitude and frequency when in steady state condition and when being forced in pure oscillatory motion. The results of these tests in steady condition have been reported in Judge (2012, 2013). Those corresponding to pure roll have been reported in Judge (2010, 2012); Judge and Judge (2013) and those

corresponding to pure oscillatory motion in heave (but with static roll) have been reported in Judge (2014a). The dependency of the linear added mass and linear damping coefficients on amplitude, frequency and speed was discussed in Judge and Judge (2013). Judge (2014a) showed the dependency of the linear heave added mass on roll displacement for large values of heel. Based on this information, Judge (2014b) derived empirical expressions for the computation of the lift and the roll moment on a heeled planing hull.

1.2.3 Osaka Prefecture University

Probably the most extensive experimental investigation into the instabilities of planing hulls has been conducted at Osaka Prefecture University. This effort started in 1994 with the construction of a high speed towing mechanism for the model basin. The experiments carried out addressed comprehensively the performance of high speed vessels including resistance, propulsion, seakeeping, maneuverability and dynamic instabilities in both the vertical and the horizontal plane. Katayama et al. (2010) presented a summary of the two-decades effort and highlighted the methods developed to estimate the onset of dynamic instabilities typical of planing hulls. Only those relevant to the study of transverse stability are summarized here. Tests were carried out on fully captive models towed at constant speed and different sinkage and orientation in order to obtain generalized forces and moments acting on planing hulls in steady asymmetric condition (Ikeda et al., 2000). Katayama and Ikeda (1996) carried out numerical simulations using a data base of hydrodynamic forces and moments in three degrees of freedom (heave-roll-pitch) and suggested that unstable roll could be induced by pitch, when its frequency is twice the roll natural frequency (a parametric excitation). It is important to mention that for these simulations the linear roll damping was obtained by Ikeda's method in its original form (a summary of Ikeda's

method for roll damping prediction is presented in Himeno (1981)). Forced roll oscillations tests showed that Ikeda's method under-predicted the linear roll damping and therefore a new "vertical lift component" was added to the original formulation. The rationale and derivation of this component was presented in Ikeda et al. (1998); Ikeda and Katayama (2000). Forced pure sway and pure yaw oscillatory motions showed that high amplitude roll motions can be excited by these modes when their frequency is close to the roll natural frequency. They also showed that high amplitude roll oscillatory motions can induce heave and pitch motions of twice the roll frequency (Katayama and Okumura, 2000). The effect of the wetted surface in the roll restoring moment was investigated in Katayama and Ikeda (2007) and an explanation was provided for progressive heeling. Katayama (2002) presented a summary of the methods developed to assess progressive heeling, bow diving, porpoising and transverse porpoising (chine-walking). In this paper, experimental and numerical time series are presented for a boat with a drift angle of 30 degrees oscillating in heave, roll and pitch (where the equilibrium roll angle is approximately 30 degrees and the roll amplitude is approximately 5 degrees).

1.2.4 Stevens Institute of Technology

An experimental investigation on captive models of idealized patrol boats was carried out in the Davidson Laboratory at Stevens Institute of Technology. The objective of this research was to obtain basic hydrodynamic information to be used in the investigation of maneuverability and dynamic stability of planing hulls. The results of the tests of three models in steady asymmetric conditions run at three different speeds were reported in Brown and Klosinski (1994a,b). The results of roll decrement tests on the same three models were reported in Brown and Klosinski (1995b,a). From these, empirical expressions for the linear added mass and damping of planing

hulls were derived. This information was used to develop a four degrees of freedom (surge-sway-roll-yaw) mathematical model based on hydrodynamics derivatives for the prediction of the maneuverability of planing hulls (Lewandowski, 1994) and to evaluate the transverse dynamic stability of planing hulls via linear stability analysis (Lewandowski, 1997). Also, Lewandowski (1996) derived semi-empirical expressions, based on the early work of Brown (1971), for the linear roll stiffness coefficient in order to evaluate the dynamic roll stability of planing hulls via linear stability analysis.

1.2.5 Delft University of Technology

An extensive experimental investigation was conducted at the Ship Hydromechanics Laboratory at TU Delft between 1995 and 1998. The objective of this effort was the development of a six degrees of freedom planing hull maneuvering simulator based on experimentally-obtained hydrodynamic derivatives. The models were initially tested in asymmetric steady planing conditions and the generalized forces and moments were measured in all six degrees of freedom (Toxopeus, 1996). Toxopeus et al. (1997) formulated a mathematical model that was used to investigate the dynamic stability of planing hulls and highlighted the importance of the pitch and roll damping. Plante (1998) carried out forced oscillations in sway and yaw and presented a refinement of Toxopeus model in Plante et al. (1998).

1.2.6 Amirkabir University of Technology

The efforts in the Department of Marine Engineering at Amirkabir University of Technology have been concentrated in the development of a six degrees of freedom simulator based on slender body theory, that can be understood as an extension of Zarnick (1978) model. Approximate solutions to the water impact of 2-D wedges in

three degrees of freedom, based on high frequency added mass, have been used as a basis for obtaining the generalized forces and moments acting on a planing hull. Results in both asymmetric steady planing (heel and sway) and asymmetric unsteady planing (pure roll and heave-roll-pitch) have been presented. Ghadimi et al. (2016b) simulated a boat in asymmetric planing conditions (heel and drift). Tavakoli et al. (2015) simulated a boat running with heel and being forced in roll, and computed time independent and time dependent linear roll coefficients as a function of some design parameters. Ghadimi et al. (2015, 2016a) simulated the motions in three degrees of freedom (heave-roll-pitch) of a planing hull at constant speed in waves, and preliminarily concluded that larger heave/pitch motions are obtained when the vessel is free to roll.

1.2.7 University of Naples "Federico II"

A theoretical and experimental study on the transverse stability of planing hulls was carried out in the Department of Naval Engineering at the University of Naples Federico II (Milanesi, 2002). Both steady state and oscillatory instabilities were treated in the study; however, the explanation to the oscillatory ones is given in terms of the change in pressure distribution when the boat is in asymmetric steady planing condition, as in Müller-Graf (1997). The experimental part of the study consisted of a series of tests on two fully prismatic models with deadrise angles of 10 and 30 degrees. The partly captive models (restrained in sway and yaw) were run down the tank at different speeds and forced in pure roll via the application of a harmonic moment. The results were fitted to a single degree of freedom linear roll equation of motion and conclusions were made with regards to the dependence of the coefficients (Linear added mass, damping and stiffness) on frequency and speed Balsamo et al. (2001, 2002).

1.2.8 University of Genoa

Studies in the Department of Naval Engineering at the University of Genoa have been conducted in particular connection with the application of the ISO Standard (ISO, 2015) on the stability assessment on small crafts (Ferrando et al., 2009; Ruscelli et al., 2012). Ruscelli et al. (2012) developed a methodology based on Lewandowski's formulation (Lewandowski, 1996, 1997, 2004) to assess the transverse dynamic stability of hard-chine planing hulls at the preliminary design stage. Ruscelli et al. (2012) validated the results with the experiments of Wellicome and Campbell (1984) and compared them with the criteria proposed by ISO (2015), obtaining in both cases satisfactory results. However, Ruscelli et al. (2012) admitted to the limitations of a methodology based on empirical formulations and linear theory. Ruscelli et al. (2012) highlighted the need for model and full scale experiments with the aim to develop more advanced methodologies and provide designers with reliable tools to assess the transverse dynamic stability of planing hulls. In fact, Ruscelli et al. (2012) suggested that *"a possible way of overcoming the limitations of the present methodologies can be found in a non-linear analysis of dynamic stability"*.

1.3 Research Objectives and Overview

The main objective of this research is to develop a method to investigate the conditions under which planing hulls can exhibit large oscillatory roll motions excited by small heave and pitch motions using non-linear stability analysis. To this end, this thesis is organized as follows:

In Chapter 2, the nonlinear coupled equations of motion for heave, roll and pitch are derived assuming that the hydrodynamic forces and moments can be written as

analytical functions of position, velocity and acceleration. By assuming an ordering in the coefficients, a single-degree-of-freedom reduced order model capable of describing the dynamics of the heave-roll-pitch system is derived, allowing the roll equation of motion to be written as a non-linear Hill's equation.

In Chapter 3, the time dependent and time independent forces and moments required to obtain the hydrodynamic coefficients in the equations of motion are computed by the 2D+t approach. The 2-D problems are solved with the commercial RANSE code Star-CCM+® and the results are compared with results obtained by other numerical methods available in the open literature. The numerical solutions obtained for the 2-D water entry problem are transformed, via the 2D+t approach, to obtain the forces and moments acting on constant deadrise planing hulls in steady state condition and in oscillatory roll motion. The results are validated by comparing them with experimental results available in the open literature.

In Chapter 4, the time dependent and time independent coefficients for the roll equation of motion are obtained via regression analysis of the time series of the forces and moments obtained experimentally and by the 2D+t approach.

In Chapter 5, the solution to the non-linear Hill's equation, representing the one-way coupling between heave-pitch and roll, is approximated by the Method of Multiple Scales in order to investigate the existence of periodic motions (limit cycles) and their stability.

In Chapter 6, the first order approximation to the non-linear Hill's equation is used to investigate conditions that could lead to unstable roll motions parametrically excited by harmonic pitch and heave motions using a 20 degrees constant deadrise planing hull as case study. The investigation is carried out in two stages; first, a region of interest in the design parameter space is identified by using stiffness coefficients obtained

by the 2D+t approach, together with linear added mass and damping coefficients derived from semi-empirical formulae available in the open literature; and second, a particular configuration inside the region of interest, for which experimental results are available, is investigated using linear and nonlinear added mass and damping coefficients obtained experimentally and by the 2D+t approach.

In Chapter 7 the work carried out is summarized, the main contributions are highlighted and recommendations for future work are suggested.

CHAPTER 2

Equations of Motion

2.1 Chapter Overview

The fully non-linear equations of motion of a floating rigid body have already been derived in several references; in this work, the notation in Fossen (1994) is used. Starting with the six-degrees-of-freedom equations of motion and introducing several assumptions, a single-degree-of-freedom reduced order model capable of describing the dynamics of the heave-roll-pitch system in the vicinity of a 2:1 parametric resonance is obtained.

2.2 Kinematics

Four reference frames are used to describe the geometry and the motions of the vessel in six-degrees-of-freedom. The geometry of the vessel and in particular the position of the center of gravity are described in a *Geometric Frame* fixed to the hull and oriented forward-starboard-up; the origin of this reference frame coincides with the intersection of the keel and the transom. The *Body-fixed Frame* is oriented such that the x-axis is parallel to the keel and points towards the bow, the y-axis points

towards port and the z-axis points up; its origin is located at the center of gravity. The *Hydrodynamic Frame* is not fixed to the hull but moves at the constant forward speed of the vessel; its origin coincides with the center of gravity. The position and orientation of the vessel are described with respect to an *Earth-fixed Frame* with origin on the undisturbed free water surface. This frame is assumed to be inertial since even for high-speed marine vehicles the accelerations of a point on the Earth surface can be neglected.

The equations of motion are written in the body-fixed frame described above, and correspond to variational equations, i.e., the motions in the coordinates correspond to perturbations from the steady state equilibrium. Also, the vessel is assumed to have port-starboard symmetry, and the axes of the body-fixed frame are assumed to be principal axes of inertia. With these assumptions the general six-degrees-of-freedom rigid-body equations of motion take the following form:

$$\begin{aligned} m\left(u_t - vr + wq\right) &= X \\ m\left(v_t - wp + ur\right) &= Y \\ m\left(w_t - uq + vp\right) &= Z \\ I_x p_t + \left(I_z - I_y\right) qr &= K \\ I_y q_t + \left(I_x - I_z\right) rp &= M \\ I_z r_t + \left(I_y - I_x\right) pq &= N \end{aligned} \tag{2.1}$$

where m is the mass of the vessel, (I_x, I_y, I_z) are the moments of inertia in the body-fixed frame. The components (u, v, w, p, q, r) correspond to the surge, sway, heave, roll, pitch and yaw velocities in the body-fixed frame (i.e., the velocities of the body-fixed frame relative to the Earth-fixed frame but written in the body-fixed frame), and the t subscript denotes differentiation with respect to time. The compo-

nents (X, Y, Z) correspond to the surge, sway and heave forces; and the components (K, M, N) correspond to roll, pitch and yaw moments, all of them defined in the body-fixed frame.

The right hand side of the equations of motion corresponds to the external forces including the generalized hydrodynamic forces, the forces generated by the propulsion system and the control surfaces, all of them described in the body-fixed reference frame. In this work, following Troesch and Falzarano (1993), only the radiation forces are taken into consideration. They are incorporated in the form of frequency independent added mass and damping under the assumption of high Froude number; i.e., gravity effects are dominated by inertial effects and therefore memory effects are of high order.

The interest lies in the heave-roll-pitch system; therefore, the vessel is assumed to be constrained in the lateral direction (sway) with no rotation around the vertical axis (yaw), so v and r are set equal to zero ($v = 0$, $r = 0$). Furthermore, it is assumed that the boat moves with constant forward velocity and the perturbations in the surge direction are negligible (i.e., $u = 0$). With these assumptions the six-degrees-of-freedom equations of motion reduce to:

$$\begin{aligned} m w_t &= Z \\ I_x p_t &= K \\ I_y q_t &= M \end{aligned} \tag{2.2}$$

Coordinates are transformed to quasi-coordinates by using the relationship between the vector of rates of change of the Euler angles $[\,\phi_t, \theta_t, \psi_t\,]$ and the vector of angular

velocities in the body-fixed coordinate system $[\,p, q, r\,]$:

$$
\begin{aligned}
p &= \phi_t - \psi_t \sin\theta \\
q &= \theta_t \cos\phi + \psi_t \cos\theta \sin\phi \\
r &= -\theta_t \sin\phi + \psi_t \cos\theta \cos\phi
\end{aligned}
\tag{2.3}
$$

where the components (ϕ, θ, ψ) correspond to the roll, pitch and yaw angles respectively.

Setting $r = 0$ in Eq. (2.3) yields the following relationships and approximations for small angles up to third order:

$$
\begin{aligned}
\psi_t &= \frac{\tan\phi}{\cos\theta}\theta_t \approx \phi\,\theta_t \\
p &= \phi_t - \tan\theta\tan\phi\,\theta_t \approx \phi_t - \phi\theta\theta_t \\
q &= \frac{1}{\cos\phi}\theta_t \approx \left(1 + \frac{\phi^2}{2}\right)\theta_t
\end{aligned}
\tag{2.4}
$$

2.3 Non-dimensionalization

The heave displacement is non-dimensionalized with the beam of the boat (B), the heave force with $\rho g B^3$ and the pitch moment with $\rho g B^4$:

$$
\bar{z} = \frac{z}{B} \qquad \bar{\phi} = \phi \qquad \bar{\theta} = \theta \tag{2.5}
$$

$$
\bar{Z} = \frac{Z}{\rho g B^3} \qquad \bar{K} = \frac{K}{\rho g B^4} \qquad \bar{M} = \frac{M}{\rho g B^4} \tag{2.6}
$$

and the time is scaled with $\sqrt{(g/B)}$

$$
\bar{t} = \sqrt{\frac{g}{B}}\,t \qquad (.)_{\bar{t}} = \sqrt{\frac{B}{g}}\,(.)_t \qquad (.)_{\bar{t}\bar{t}} = \frac{B}{g}\,(.)_{tt} \tag{2.7}
$$

so the time derivatives of the quasi-coordinates (z, ϕ, θ) scale as follows:

$$\bar{z}_{\bar{t}} = \sqrt{\frac{B}{g}}\,\frac{z_t}{B} = \frac{z_t}{\sqrt{Bg}} \qquad \bar{z}_{\bar{t}\bar{t}} = \frac{B}{g}\,\frac{z_{tt}}{B} = \frac{z_{tt}}{g} \tag{2.8}$$

$$\bar{\phi}_{\bar{t}} = \phi_{\bar{t}} = \sqrt{\frac{B}{g}}\,\phi_t \qquad \bar{\phi}_{\bar{t}\bar{t}} = \phi_{\bar{t}\bar{t}} = \frac{B}{g}\,\phi_{tt} \tag{2.9}$$

$$\bar{\theta}_{\bar{t}} = \theta_{\bar{t}} = \sqrt{\frac{B}{g}}\,\theta_t \qquad \bar{\theta}_{\bar{t}\bar{t}} = \theta_{\bar{t}\bar{t}} = \frac{B}{g}\,\theta_{tt} \tag{2.10}$$

The heave-roll-pitch non-dimensional system is written in quasi-coordinates as follows:

$$\begin{aligned} C_\Delta \bar{z}_{\bar{t}\bar{t}} &= \bar{Z} \\ \bar{I}_x \phi_{\bar{t}\bar{t}} &= \bar{K} \\ \bar{I}_y \theta_{\bar{t}\bar{t}} &= \bar{M} \end{aligned} \tag{2.11}$$

where the load coefficient C_Δ and the non-dimensional moments of inertia $\left(\bar{I}_x, \bar{I}_y\right)$ are given by:

$$C_\Delta = \frac{m}{\rho B^3} \qquad \bar{I}_x = \frac{I_x}{\rho B^5} \qquad \bar{I}_y = \frac{I_y}{\rho B^5} \tag{2.12}$$

The non-dimensional moments of inertia can be written in terms of the load coefficient using the radius of gyration (κ_x, κ_y):

$$\bar{I}_x = \left(\frac{\kappa_x}{B}\right)^2 C_\Delta \qquad \bar{I}_y = \left(\frac{\kappa_y}{B}\right)^2 C_\Delta \tag{2.13}$$

Typical values used in the design of surface ships, which have successfully been used

in the simulation of motions in planing hulls (Toxopeus, 1996), are given by:

$$0.36 \leq \left(\frac{\kappa_x}{B}\right) \leq 0.42 \qquad 0.22 \leq \left(\frac{\kappa_y}{B}\right) \leq 0.25 \tag{2.14}$$

2.4 Generalized External Forces and Moments

The generalized external forces and moments (Z, K, M) are assumed to be functions of position, velocity and acceleration. Following Abkowitz (1969), they can be written in terms of a Taylor Series Expansion about the steady state equilibrium, neglecting higher order acceleration terms and products of accelerations and velocities. According to Abkowitz (1969) the rationale behind neglecting these terms is threefold: (1) there are no terms of this type in the left hand side of the equations of motion (body inertial forces), so there will not be be terms of the same nature to add to the higher order fluid inertial terms, (2) experience has shown that adequate values for the fluid inertial terms can be obtained from potential theory showing the interaction between inertial and viscous forces to be small, and (3) in the case of submerged bodies, non-linear potential theory equations produce forces which are linear in the accelerations. The result has been compared with a general form of the non-linear heave-roll-pitch equations of motion derived from energy considerations following the work in Nayfeh et al. (1974) and Suleiman (2000). It has been claimed in Suleiman (2000) that in following this approach one will obtain equations of motion free from terms that will produce unphysical oscillatory motions in the absence of excitation. However, as shown in Nayfeh et al. (1974) this is only true when a specific form of the kinetic energy is used, which was obtained by comparison between results obtained from a perturbation method (the method of multiple scales) and the results of the energy approach. If a general form for the kinetic energy is used then there is no guarantee that those terms will not appear in the equations of motion. Also, the

analysis in Nayfeh et al. (1974) is restricted to vessels at rest, which is not the case in this work. With these considerations, the equations of motion derived from a Taylor Series approach give terms of the same nature as those that would have been obtained from the energy approach when a general form for the kinetic energy is used. The results of the energy approach are used to distinguish the different terms in the Taylor expansion according with their nature. Terms that can be obtained from a general form of the kinetic energy of the fluid are referred to as "Inertial" or "Added Mass", those that can be obtained from a general form of the potential energy of the fluid are referred to as "Restoring" or "Stiffness" terms and those that can be obtained from a general form of the dissipation function are referred to as "Dissipative" or "Damping" terms.

With this notation, and based on a limited set of experimental results, the Taylor series expansion is carried out up to third order in inertial and dissipative terms and up to fifth order in restoring terms. The products of accelerations, velocities and displacements, with the considerations stated above, assuming starboard-port symmetry and un-biased equilibrium in roll, can be conveniently written in the form of polynomials as follows:

Heave (Pitch) Equation of Motion

Inertial:

$$
\begin{array}{llll}
(z+\theta)^0 (z_{tt}+\theta_{tt}) & & & \\
(z+\theta)^1 (z_{tt}+\theta_{tt}) & (z+\theta)^0 (z_t+\theta_t)^2 & (z+\theta)^0 \left(\phi\,\phi_{tt}+\phi_t^2\right) & \\
(z+\theta)^2 (z_{tt}+\theta_{tt}) & (z+\theta)^1 (z_t+\theta_t)^2 & (z+\theta)^1 \left(\phi\,\phi_{tt}+\phi_t^2\right) & \phi^2 (z_{tt}+\theta_{tt}) \\
 & & & \phi\,\phi_t (z_t+\theta_t)
\end{array}
$$

Dissipative:

$$(z+\theta)^0 (z_t+\theta_t)$$

$$(z+\theta)^1 (z_t+\theta_t) \qquad (z+\theta)^0 \phi \phi_t$$

$$(z+\theta)^2 (z_t+\theta_t) \qquad (z+\theta)^1 \phi \phi_t \qquad \phi^2 (z_t+\theta_t) \qquad (z_t+\theta_t)^3$$

Restoring:

$$(z+\theta)^1 \phi^0$$

$$(z+\theta)^2 \phi^0 \qquad (z+\theta)^0 \phi^2$$

$$(z+\theta)^3 \phi^0 \qquad (z+\theta)^1 \phi^2$$

$$(z+\theta)^4 \phi^0 \qquad (z+\theta)^2 \phi^2 \qquad (z+\theta)^0 \phi^4$$

$$(z+\theta)^5 \phi^0 \qquad (z+\theta)^3 \phi^2 \qquad (z+\theta)^1 \phi^4$$

Roll Equation of Motion

Inertial:

$$(z+\theta)^0 \phi_{tt}$$

$$(z+\theta)^1 \phi_{tt} \qquad (z+\theta)^0 (z_t+\theta_t)^1 \phi_t \qquad (z+\theta)^0 (z_{tt}+\theta_{tt}) \phi$$

$$(z+\theta)^2 \phi_{tt} \qquad (z+\theta)^1 (z_t+\theta_t)^1 \phi_t \qquad (z+\theta)^1 (z_{tt}+\theta_{tt}) \phi \qquad (z_t+\theta_t)^2 \phi$$

Dissipative:

$$(z+\theta)^0\,\phi_t$$

$$(z+\theta)^1\,\phi_t \qquad (z+\theta)^0\,(z_t+\theta_t)^1\,\phi$$

$$(z+\theta)^2\,\phi_t \qquad (z+\theta)^1\,(z_t+\theta_t)^1\,\phi \qquad (z_t+\theta_t)^2\,\phi_t \qquad \phi^2\phi_t \qquad \phi_t^3$$

Restoring:

$$(z+\theta)^0\,\phi^1$$

$$(z+\theta)^1\,\phi^1$$

$$(z+\theta)^2\,\phi^1 \qquad (z+\theta)^0\,\phi^3$$

$$(z+\theta)^3\,\phi^1 \qquad (z+\theta)^1\,\phi^3$$

$$(z+\theta)^4\,\phi^1 \qquad (z+\theta)^2\,\phi^3 \qquad (z+\theta)^0\,\phi^5$$

where the elements of the expansion of the polynomials can be directly interpreted as the subscripts of the coefficients in the traditional maneuvering notation. The powers in zero and one in the polynomials have been kept in order to show explicitly the progression in the expansions. As an example, the hydrodynamic heave force represented up to second order would be obtained from the expansion of the following polynomials:

$$(z+\theta)^0\,(z_{tt}+\theta_{tt}) + (z+\theta)^1\,(z_{tt}+\theta_{tt}) + (z+\theta)^0\,(z_t+\theta_t)^2 + (z+\theta)^0\left(\phi\,\phi_{tt}+\phi_t^2\right) +$$

$$(z+\theta)^0\,(z_t+\theta_t) + (z+\theta)^1\,(z_t+\theta_t) + (z+\theta)^0\,\phi\,\phi_t +$$

$$(z+\theta)^1\,\phi^0 + (z+\theta)^2\,\phi^0 + (z+\theta)^0\,\phi^2 = z_{tt}+\theta_{tt}+zz_{tt}+z\theta_{tt}+\theta z_{tt}+\theta\theta_{tt}+$$

$$z_t^2+z_t\theta_t+\theta_t^2+\phi\phi_{tt}+\phi_t^2+z+\theta+z^2+z\theta+\theta^2+\phi^2$$

and therefore the hydrodynamic heave force (Z) would be expressed as follows:

$$Z \approx Z_{z_{tt}} z_{tt} + Z_{\theta_{tt}} \theta_{tt} + Z_{zz_{tt}} z z_{tt} + Z_{z\theta_{tt}} z \theta_{tt} + Z_{\theta z_{tt}} \theta z_{tt} + Z_{\theta\theta_{tt}} \theta\theta_{tt} + Z_{z_t z_t} z_t^2 + Z_{z_t\theta_t} z_t \theta_t +$$
$$Z_{\theta_t\theta_t} \theta_t^2 + Z_{\phi\phi_{tt}} \phi\phi_{tt} + Z_{\phi_t\phi_t} \phi_t^2 + Z_z z + Z_\theta \theta + Z_{zz} z^2 + Z_{z\theta} z\theta + Z_{\theta\theta} \theta^2 + Z_{\phi\phi} \phi^2$$

2.5 Reduced Order Model

The coefficients corresponding to polynomials in ϕ and ϕ_t in the heave and pitch equations of motion are assumed to be smaller than the coefficients corresponding to polynomials in pure heave/pitch. This ordering leads to a decoupling between the roll equation of motion and the coupled heave/pitch equations of motion giving rise to an effective one-way coupling between heave/pitch and roll. As a consequence of this, the solution to the heave/pitch system is assumed to be known and the roll equation of motion is given by Eq. (2.16).

Eq. (2.16) has been written in this form to show that the coefficients coupling heave and pitch with roll can be grouped as products of roll acceleration, roll velocity and roll stiffness. In addition to this, each line in the equation corresponds to inertial, damping or stiffness terms to a given order in the Taylor series expansion. The non-dimensionalization corresponding to each of the coefficients in the equation above is presented in Appendix A.

The coefficients in Eq. (2.16) are divided through by $\left(\bar{I}_x - \bar{K}_{\phi_{\bar{t}\bar{t}}}\right)$ and redefined using the following notation:

$$\hat{K} = \frac{\bar{K}}{\left(\bar{I}_x - \bar{K}_{\phi_{\bar{t}\bar{t}}}\right)} \tag{2.15}$$

$$
\begin{aligned}
\left(\bar{I}_x - \bar{K}_{\phi_{\bar{t}\bar{t}}}\right)\phi_{\bar{t}\bar{t}} = {} & \bar{K}_{\phi_{\bar{t}}}\phi_{\bar{t}} + \bar{K}_{\phi}\phi \\
& + \left(\bar{K}_{\bar{z}\phi_{\bar{t}\bar{t}}}\bar{z} + \bar{K}_{\theta\phi_{\bar{t}\bar{t}}}\theta\right)\phi_{\bar{t}\bar{t}} \\
& + \left(\bar{K}_{\bar{z}_{\bar{t}}\phi_{\bar{t}}}\bar{z}_{\bar{t}} + \bar{K}_{\theta_{\bar{t}}\phi_{\bar{t}}}\theta_{\bar{t}}\right)\phi_{\bar{t}} + \left(\bar{K}_{\phi\bar{z}_{\bar{t}\bar{t}}}\bar{z}_{\bar{t}\bar{t}} + \bar{K}_{\phi\theta_{\bar{t}\bar{t}}}\theta_{\bar{t}\bar{t}}\right)\phi \\
& + \left(\bar{K}_{\bar{z}\phi_{\bar{t}}}\bar{z} + \bar{K}_{\theta\phi_{\bar{t}}}\theta\right)\phi_{\bar{t}} + \left(\bar{K}_{\phi\bar{z}_{\bar{t}}}\bar{z}_{\bar{t}} + \bar{K}_{\phi\theta\bar{t}}\theta_{\bar{t}}\right)\phi \\
& + \left(\bar{K}_{\bar{z}\phi}\bar{z} + \bar{K}_{\phi\theta}\theta\right)\phi \\
& + \left(\bar{K}_{\bar{z}\bar{z}\phi_{\bar{t}\bar{t}}}\bar{z}^2 + \bar{K}_{\bar{z}\theta\phi_{\bar{t}\bar{t}}}\bar{z}\theta + \bar{K}_{\theta\theta\phi_{\bar{t}\bar{t}}}\theta^2\right)\phi_{\bar{t}\bar{t}} \\
& + \left(\bar{K}_{\phi\phi\phi_{\bar{t}\bar{t}}}\right)\phi^2\phi_{\bar{t}\bar{t}} \\
& + \left(\left(\bar{K}_{\bar{z}\bar{z}_{\bar{t}}\phi_{\bar{t}}}\bar{z} + \bar{K}_{\theta\bar{z}_{\bar{t}}\phi_{\bar{t}}}\theta\right)\bar{z}_{\bar{t}} + \left(\bar{K}_{\bar{z}\phi_{\bar{t}}\theta_{\bar{t}}}\bar{z} + \bar{K}_{\theta\phi_{\bar{t}}\theta_{\bar{t}}}\theta\right)\theta_{\bar{t}}\right)\phi_{\bar{t}} \\
& + \left(\left(\bar{K}_{\bar{z}\phi\bar{z}_{\bar{t}\bar{t}}}\bar{z} + \bar{K}_{\phi\theta\bar{z}_{\bar{t}\bar{t}}}\theta\right)\bar{z}_{\bar{t}\bar{t}} + \left(\bar{K}_{\bar{z}\phi\theta_{\bar{t}\bar{t}}}\bar{z} + \bar{K}_{\phi\theta\theta_{\bar{t}\bar{t}}}\theta\right)\theta_{\bar{t}\bar{t}}\right)\phi \\
& + \left(\bar{K}_{\phi\bar{z}_{\bar{t}}\bar{z}_{\bar{t}}}\bar{z}_{\bar{t}}^2 + \bar{K}_{\phi\bar{z}_{\bar{t}}\theta_{\bar{t}}}\bar{z}_{\bar{t}}\theta_{\bar{t}} + \bar{K}_{\phi\theta_{\bar{t}}\theta_{\bar{t}}}\theta_{\bar{t}}^2\right)\phi \\
& + \left(\bar{K}_{\phi\phi\phi_{\bar{t}}\phi_{\bar{t}}}\right)\phi\,\phi_{\bar{t}}^2 \\
& + \left(\bar{K}_{\bar{z}\bar{z}\phi_{\bar{t}}}\bar{z}^2 + \bar{K}_{\bar{z}\theta\phi_{\bar{t}}}\bar{z}\theta + \bar{K}_{\theta\theta\phi_{\bar{t}}}\theta^2\right)\phi_{\bar{t}} \\
& + \left(\bar{K}_{\bar{z}_{\bar{t}}\bar{z}_{\bar{t}}\phi_{\bar{t}}}\bar{z}_{\bar{t}}^2 + \bar{K}_{\bar{z}_{\bar{t}}\phi_{\bar{t}}\theta_{\bar{t}}}\bar{z}_{\bar{t}}\theta_{\bar{t}} + \bar{K}_{\phi_{\bar{t}}\theta_{\bar{t}}\theta_{\bar{t}}}\theta_{\bar{t}}^2\right)\phi_{\bar{t}} \\
& + \left(\bar{K}_{\phi\phi\phi_{\bar{t}}}\right)\phi^2\phi_{\bar{t}} \\
& + \left(\left(\bar{K}_{\bar{z}\phi\bar{z}_{\bar{t}}}\bar{z} + \bar{K}_{\phi\theta\bar{z}_{\bar{t}}}\theta\right)\bar{z}_{\bar{t}} + \left(\bar{K}_{\bar{z}\phi\theta_{\bar{t}}}\bar{z} + \bar{K}_{\phi\theta\theta_{\bar{t}}}\theta\right)\theta_{\bar{t}}\right)\phi \\
& + \left(\bar{K}_{\phi_{\bar{t}}\phi_{\bar{t}}\phi_{\bar{t}}}\right)\phi_{\bar{t}}^3 \\
& + \left(\bar{K}_{\bar{z}\bar{z}\phi}\bar{z}^2 + \bar{K}_{\bar{z}\phi\theta}\bar{z}\theta + \bar{K}_{\phi\theta\theta}\theta^2\right)\phi \\
& + \left(\bar{K}_{\phi\phi\phi}\right)\phi^3 \\
& + \left(\bar{K}_{\bar{z}\bar{z}\bar{z}\phi}\bar{z}^3 + \bar{K}_{\bar{z}\bar{z}\phi\theta}\bar{z}^2\theta + \bar{K}_{\bar{z}\phi\theta\theta}\bar{z}\theta^2 + \bar{K}_{\phi\theta\theta\theta}\theta^3\right)\phi \\
& + \left(\bar{K}_{\bar{z}\phi\phi\phi}\bar{z} + \bar{K}_{\phi\phi\phi\theta}\theta\right)\phi^3 \\
& + \left(\bar{K}_{\bar{z}\bar{z}\bar{z}\bar{z}\phi}\bar{z}^4 + \bar{K}_{\bar{z}\bar{z}\bar{z}\phi\theta}\bar{z}^3\theta + \bar{K}_{\bar{z}\bar{z}\phi\theta\theta}\bar{z}^2\theta^2 + \bar{K}_{\bar{z}\phi\theta\theta\theta}\bar{z}\theta^3 + \bar{K}_{\phi\theta\theta\theta\theta}\theta^4\right)\phi \\
& + \left(\bar{K}_{\bar{z}\bar{z}\phi\phi\phi}\bar{z}^2 + \bar{K}_{\bar{z}\phi\phi\phi\theta}\bar{z}\theta + \bar{K}_{\phi\phi\phi\theta\theta}\theta^2\right)\phi^3 \\
& + \left(\bar{K}_{\phi\phi\phi\phi\phi}\right)\phi^5
\end{aligned}
\tag{2.16}
$$

Using the new notation the roll equation of motion is given by Eq. (2.17):

$$
\begin{aligned}
\phi_{\overline{t}\overline{t}} = {} & \hat{K}_{\phi_{\bar{t}}}\phi_{\bar{t}} + \hat{K}_{\phi}\phi \\
& + \left(\hat{K}_{\bar{z}\phi_{\bar{t}\bar{t}}}\bar{z} + \hat{K}_{\theta\phi_{\bar{t}\bar{t}}}\theta\right)\phi_{\overline{t}\overline{t}} \\
& + \left(\hat{K}_{\bar{z}_{\bar{t}}\phi_{\bar{t}}}\bar{z}_{\bar{t}} + \hat{K}_{\theta_{\bar{t}}\phi_{\bar{t}}}\theta_{\bar{t}}\right)\phi_{\bar{t}} + \left(\hat{K}_{\phi\bar{z}_{\bar{t}\bar{t}}}\bar{z}_{\overline{t}\overline{t}} + \hat{K}_{\phi\theta_{\bar{t}\bar{t}}}\theta_{\overline{t}\overline{t}}\right)\phi \\
& + \left(\hat{K}_{\bar{z}\phi_{\bar{t}}}\bar{z} + \hat{K}_{\theta\phi_{\bar{t}}}\theta\right)\phi_{\bar{t}} + \left(\hat{K}_{\phi\bar{z}_{\bar{t}}}\bar{z}_{\bar{t}} + \hat{K}_{\phi\theta\bar{t}}\theta_{\bar{t}}\right)\phi \\
& + \left(\hat{K}_{\bar{z}\phi}\bar{z} + \hat{K}_{\phi\theta}\theta\right)\phi \\
& + \left(\hat{K}_{\bar{z}\bar{z}\phi_{\bar{t}\bar{t}}}\bar{z}^2 + \hat{K}_{\bar{z}\theta\phi_{\bar{t}\bar{t}}}\bar{z}\theta + \hat{K}_{\theta\theta\phi_{\bar{t}\bar{t}}}\theta^2\right)\phi_{\overline{t}\overline{t}} \\
& + \left(\hat{K}_{\phi\phi\phi_{\bar{t}\bar{t}}}\right)\phi^2\phi_{\overline{t}\overline{t}} \\
& + \left(\left(\hat{K}_{\bar{z}\bar{z}_{\bar{t}}\phi_{\bar{t}}}\bar{z} + \hat{K}_{\theta\bar{z}_{\bar{t}}\phi_{\bar{t}}}\theta\right)\bar{z}_{\bar{t}} + \left(\hat{K}_{\bar{z}\phi_{\bar{t}}\theta_{\bar{t}}}\bar{z} + \hat{K}_{\theta\phi_{\bar{t}}\theta_{\bar{t}}}\theta\right)\theta_{\bar{t}}\right)\phi_{\bar{t}} \\
& + \left(\left(\hat{K}_{\bar{z}\phi\bar{z}_{\bar{t}\bar{t}}}\bar{z} + \hat{K}_{\phi\theta\bar{z}_{\bar{t}\bar{t}}}\theta\right)\bar{z}_{\overline{t}\overline{t}} + \left(\hat{K}_{\bar{z}\phi\theta_{\bar{t}\bar{t}}}\bar{z} + \hat{K}_{\phi\theta\theta_{\bar{t}\bar{t}}}\theta\right)\theta_{\overline{t}\overline{t}}\right)\phi \\
& + \left(\hat{K}_{\phi\bar{z}_{\bar{t}}\bar{z}_{\bar{t}}}\bar{z}_{\bar{t}}^2 + \hat{K}_{\phi\bar{z}_{\bar{t}}\theta_{\bar{t}}}\bar{z}_{\bar{t}}\theta_{\bar{t}} + \hat{K}_{\phi\theta_{\bar{t}}\theta_{\bar{t}}}\theta_{\bar{t}}^2\right)\phi \\
& + \left(\hat{K}_{\phi\phi_{\bar{t}}\phi_{\bar{t}}}\right)\phi\,\phi_{\bar{t}}^2 \\
& + \left(\hat{K}_{\bar{z}\bar{z}\phi_{\bar{t}}}\bar{z}^2 + \hat{K}_{\bar{z}\theta\phi_{\bar{t}}}\bar{z}\theta + \hat{K}_{\theta\theta\phi_{\bar{t}}}\theta^2\right)\phi_{\bar{t}} \\
& + \left(\hat{K}_{\bar{z}_{\bar{t}}\bar{z}_{\bar{t}}\phi_{\bar{t}}}\bar{z}_{\bar{t}}^2 + \hat{K}_{\bar{z}_{\bar{t}}\phi_{\bar{t}}\theta_{\bar{t}}}\bar{z}_{\bar{t}}\theta_{\bar{t}} + \hat{K}_{\phi_{\bar{t}}\theta_{\bar{t}}\theta_{\bar{t}}}\theta_{\bar{t}}^2\right)\phi_{\bar{t}} \\
& + \left(\hat{K}_{\phi\phi\phi_{\bar{t}}}\right)\phi^2\phi_{\bar{t}} \\
& + \left(\left(\hat{K}_{\bar{z}\phi\bar{z}_{\bar{t}}}\bar{z} + \hat{K}_{\phi\theta\bar{z}_{\bar{t}}}\theta\right)\bar{z}_{\bar{t}} + \left(\hat{K}_{\bar{z}\phi\theta_{\bar{t}}}\bar{z} + \hat{K}_{\phi\theta\theta_{\bar{t}}}\theta\right)\theta_{\bar{t}}\right)\phi \\
& + \left(\hat{K}_{\phi_{\bar{t}}\phi_{\bar{t}}\phi_{\bar{t}}}\right)\phi_{\bar{t}}^3 \\
& + \left(\hat{K}_{\bar{z}\bar{z}\phi}\bar{z}^2 + \hat{K}_{\bar{z}\phi\theta}\bar{z}\theta + \hat{K}_{\phi\theta\theta}\theta^2\right)\phi \\
& + \left(\hat{K}_{\phi\phi\phi}\right)\phi^3 \\
& + \left(\hat{K}_{\bar{z}\bar{z}\bar{z}\phi}\bar{z}^3 + \hat{K}_{\bar{z}\bar{z}\phi\theta}\bar{z}^2\theta + \hat{K}_{\bar{z}\phi\theta\theta}\bar{z}\theta^2 + \hat{K}_{\phi\theta\theta\theta}\theta^3\right)\phi \\
& + \left(\hat{K}_{\bar{z}\phi\phi\phi}\bar{z} + \hat{K}_{\phi\phi\phi\theta}\theta\right)\phi^3 \\
& + \left(\hat{K}_{\bar{z}\bar{z}\bar{z}\bar{z}\phi}\bar{z}^4 + \hat{K}_{\bar{z}\bar{z}\bar{z}\phi\theta}\bar{z}^3\theta + \hat{K}_{\bar{z}\bar{z}\phi\theta\theta}\bar{z}^2\theta^2 + \hat{K}_{\bar{z}\phi\theta\theta\theta}\bar{z}\theta^3 + \hat{K}_{\phi\theta\theta\theta\theta}\theta^4\right)\phi \\
& + \left(\hat{K}_{\bar{z}\bar{z}\phi\phi\phi}\bar{z}^2 + \hat{K}_{\bar{z}\phi\phi\phi\theta}\bar{z}\theta + \hat{K}_{\phi\phi\phi\theta\theta}\theta^2\right)\phi^3 \\
& + \left(\hat{K}_{\phi\phi\phi\phi\phi}\right)\phi^5
\end{aligned}
\tag{2.17}
$$

In order to simplify the notation the coefficients are re-defined one more time and the over bars are dropped. In this new notation A stands for *Added-mass*, D stands for *Damping* and S stands for *Stiffness*.

$$
\begin{aligned}
&\phi_{tt} + \left(K_2^A z + K_3^A \theta\right) \phi_{tt} + \left(K_4^A z_t + K_5^A \theta_t\right) \phi_t + \left(K_6^A z_{tt} + K_7^A \theta_{tt}\right) \phi \\
&\quad + \left(K_8^A z^2 + K_9^A z\theta + K_{10}^A \theta^2\right) \phi_{tt} + \left(K_{11}^A\right) \phi^2 \phi_{tt} \\
&\quad + \left(\left(K_{12}^A z + K_{13}^A \theta\right) z_t + \left(K_{14}^A z + K_{15}^A \theta\right) \theta_t\right) \phi_t \\
&\quad + \left(\left(K_{16}^A z + K_{17}^A \theta\right) z_{tt} + \left(K_{18}^A z + K_{19}^A \theta\right) \theta_{tt}\right) \phi + \left(K_{20}^A z_t^2 + K_{21}^A z_t \theta_t + K_{22}^A \theta_t^2\right) \phi \\
&\quad + \left(K_{23}^A\right) \phi \, \phi_t^2 \\
&\quad + \left(K_1^D\right) \phi_t \\
&\quad + \left(K_2^D z + K_3^D \theta\right) \phi_t + \left(K_4^D z_t + K_5^D \theta_t\right) \phi \\
&\quad + \left(K_6^D z^2 + K_7^D z\theta + K_8^D \theta^2\right) \phi_t + \left(K_9^D z_t^2 + K_{10}^D z_t \theta_t + K_{11}^D \theta_t^2\right) \phi_t \\
&\quad + \left(K_{12}^D\right) \phi^2 \phi_t \\
&\quad + \left(\left(K_{13}^D z + K_{14}^D \theta\right) z_t + \left(K_{15}^D z + K_{16}^D \theta\right) \theta_t\right) \phi + \left(K_{17}^D\right) \phi_t^3 \\
&\quad + \left(K_1^S\right) \phi \\
&\quad + \left(K_2^S z + K_3^S \theta\right) \phi \\
&\quad + \left(K_4^S z^2 + K_5^S z\theta + K_6^S \theta^2\right) \phi + \left(K_7^S\right) \phi^3 \\
&\quad + \left(K_8^S z^3 + K_9^S z^2\theta + K_{10}^S z\theta^2 + K_{11}^S \theta^3\right) \phi + \left(K_{12}^S z + K_{13}^S \theta\right) \phi^3 \\
&\quad + \left(K_{14}^S z^4 + K_{15}^S z^3\theta + K_{16}^S z^2\theta^2 + K_{17}^S z\theta^3 + K_{18}^S \theta^4\right) \phi \\
&\quad + \left(K_{19}^S z^2 + K_{20}^S z\theta + K_{21}^S \theta^2\right) \phi^3 + \left(K_{22}^S\right) \phi^5 = 0
\end{aligned}
\tag{2.18}
$$

Where the correspondence between notations in Eq. (2.16) and Eq. (2.17) is:

First order

$$K_1^D = -\hat{K}_{\phi_{\bar{t}}} \qquad K_1^S = -\hat{K}_{\phi}$$

Second order

$$K_2^A = -\hat{K}_{\bar{z}\phi_{\bar{t}\bar{t}}} \qquad K_3^A = -\hat{K}_{\theta\phi_{\bar{t}\bar{t}}}$$

$$K_4^A = -\hat{K}_{\bar{z}_{\bar{t}}\phi_{\bar{t}}} \qquad K_5^A = -\hat{K}_{\theta_{\bar{t}}\phi_{\bar{t}}} \qquad K_6^A = -\hat{K}_{\phi\bar{z}_{\bar{t}\bar{t}}} \qquad K_7^A = -\hat{K}_{\phi\theta_{\bar{t}\bar{t}}}$$

$$K_2^D = -\hat{K}_{\bar{z}\phi_{\bar{t}}} \qquad K_3^D = -\hat{K}_{\theta\phi_{\bar{t}}} \qquad K_4^D = -\hat{K}_{\phi\bar{z}_{\bar{t}}} \qquad K_5^D = -\hat{K}_{\phi\theta\bar{t}}$$

$$K_2^S = -\hat{K}_{\bar{z}\phi} \qquad K_3^S = -\hat{K}_{\phi\theta}$$

Third order

$$K_8^A = -\hat{K}_{\bar{z}\bar{z}\phi_{\bar{t}\bar{t}}} \qquad K_9^A = -\hat{K}_{\bar{z}\theta\phi_{\bar{t}\bar{t}}} \qquad K_{10}^A = -\hat{K}_{\theta\theta\phi_{\bar{t}\bar{t}}} \qquad K_{11}^A = -\hat{K}_{\phi\phi\phi_{\bar{t}\bar{t}}}$$

$$K_{12}^A = -\hat{K}_{\bar{z}\bar{z}_{\bar{t}}\phi_{\bar{t}}} \qquad K_{13}^A = -\hat{K}_{\theta\bar{z}_{\bar{t}}\phi_{\bar{t}}} \qquad K_{14}^A = -\hat{K}_{\bar{z}\phi_{\bar{t}}\theta_{\bar{t}}} \qquad K_{15}^A = -\hat{K}_{\theta\phi_{\bar{t}}\theta_{\bar{t}}}$$

$$K_{16}^A = -\hat{K}_{\bar{z}\phi\bar{z}_{\bar{t}\bar{t}}} \qquad K_{17}^A = -\hat{K}_{\phi\theta\bar{z}_{\bar{t}\bar{t}}} \qquad K_{18}^A = -\hat{K}_{\bar{z}\phi\theta_{\bar{t}\bar{t}}} \qquad K_{19}^A = -\hat{K}_{\phi\theta\theta_{\bar{t}\bar{t}}}$$

$$K_{20}^A = -\hat{K}_{\phi\bar{z}_{\bar{t}}\bar{z}_{\bar{t}}} \qquad K_{21}^A = -\hat{K}_{\phi\bar{z}_{\bar{t}}\theta_{\bar{t}}} \qquad K_{22}^A = -\hat{K}_{\phi\theta_{\bar{t}}\theta_{\bar{t}}} \qquad K_{23}^A = -\hat{K}_{\phi\phi_{\bar{t}}\phi_{\bar{t}}}$$

$$K_6^D = -\hat{K}_{\bar{z}\bar{z}\phi_{\bar{t}}} \qquad K_7^D = -\hat{K}_{\bar{z}\theta\phi_{\bar{t}}} \qquad K_8^D = -\hat{K}_{\theta\theta\phi_{\bar{t}}} \qquad K_9^D = -\hat{K}_{\bar{z}_{\bar{t}}\bar{z}_{\bar{t}}\phi_{\bar{t}}}$$

$$K_{10}^D = -\hat{K}_{\bar{z}_{\bar{t}}\phi_{\bar{t}}\theta_{\bar{t}}} \qquad K_{11}^D = -\hat{K}_{\phi_{\bar{t}}\theta_{\bar{t}}\theta_{\bar{t}}} \qquad K_{12}^D = -\hat{K}_{\phi\phi\phi_{\bar{t}}} \qquad K_{13}^D = -\hat{K}_{\bar{z}\phi\bar{z}_{\bar{t}}}$$

$$K_{14}^D = -\hat{K}_{\phi\theta\bar{z}_{\bar{t}}} \qquad K_{15}^D = -\hat{K}_{\bar{z}\phi\theta_{\bar{t}}} \qquad K_{16}^D = -\hat{K}_{\phi\theta\theta_{\bar{t}}} \qquad K_{17}^D = -\hat{K}_{\phi_{\bar{t}}\phi_{\bar{t}}\phi_{\bar{t}}}$$

$$K_4^S = -\hat{K}_{\bar{z}\bar{z}\phi} \qquad K_5^S = -\hat{K}_{\bar{z}\phi\theta} \qquad K_6^S = -\hat{K}_{\phi\theta\theta} \qquad K_7^S = -\hat{K}_{\phi\phi\phi}$$

Fourth order

$$K_8^S = -\hat{K}_{\bar{z}\bar{z}\bar{z}\phi} \qquad K_9^S = -\hat{K}_{\bar{z}\bar{z}\phi\theta} \qquad K_{10}^S = -\hat{K}_{\bar{z}\phi\theta\theta} \qquad K_{11}^S = -\hat{K}_{\phi\theta\theta\theta}$$
$$K_{12}^S = -\hat{K}_{\bar{z}\phi\phi\phi} \qquad K_{13}^S = -\hat{K}_{\phi\phi\phi\theta}$$

Fifth order

$$K_{14}^S = -\hat{K}_{\bar{z}\bar{z}\bar{z}\bar{z}\phi} \qquad K_{15}^S = -\hat{K}_{\bar{z}\bar{z}\bar{z}\phi\theta} \qquad K_{16}^S = -\hat{K}_{\bar{z}\bar{z}\phi\theta\theta} \qquad K_{17}^S = -\hat{K}_{\bar{z}\phi\theta\theta\theta}$$
$$K_{18}^S = -\hat{K}_{\phi\theta\theta\theta\theta} \qquad K_{19}^S = -\hat{K}_{\bar{z}\bar{z}\phi\phi\phi} \qquad K_{20}^S = -\hat{K}_{\bar{z}\phi\phi\phi\theta} \qquad K_{21}^S = -\hat{K}_{\phi\phi\phi\theta\theta}$$
$$K_{22}^S = -\hat{K}_{\phi\phi\phi\phi\phi}$$

Since the objective of this work is to study the effect of periodic steady state motions in heave and pitch in the roll degree of freedom, the solution of heave-pitch system is assumed to be of the form:

$$z = \zeta_3 \cos \omega t \qquad \theta = \zeta_5 \cos(\omega t + \alpha_5) \tag{2.19}$$

where ω is the non-dimensional frequency of oscillation and α_5 represents the phase difference between pitch and heave. Notice that Eq. (2.19) can represent the solution to the autonomous problem i.e., stable periodic oscillations in heave and pitch in calm water *(porpoising)* or to the non-autonomous problem i.e., the heave/pitch response in head seas.

Substitution of Eq. (2.19) into Eq. (2.18) yields an equation of the form:

$$\begin{aligned}
&\phi_{tt} + \left(f_0^{\phi_{tt}} + \sum_{k=1}^{2} \left(f_k^{\phi_{tt}} \cos\left(k\,\omega t - \psi_k^{\phi_{tt}} \right) \right) \right) \phi_{tt} \\
&\quad + \left(K_{11}^{A} \right) \phi^2 \phi_{tt} + \left(K_{23}^{A} \right) \phi\, \phi_t^2 \\
&\quad + \left(K_{1}^{D} \right) \phi_t + \left(f_0^{\phi_t} + \sum_{k=1}^{2} \left(f_k^{\phi_t} \cos\left(k\,\omega t - \psi_k^{\phi_t} \right) \right) \right) \phi_t \\
&\quad + \left(K_{12}^{D} \right) \phi^2 \phi_t + \left(K_{17}^{D} \right) \phi_t^3 \\
&\quad + \left(K_{1}^{S} \right) \phi + \left(f_0^{\phi} + \sum_{k=1}^{4} \left(f_k^{\phi} \cos\left(k\,\omega t - \psi_k^{\phi} \right) \right) \right) \phi \\
&\quad + \left(K_{7}^{S} \right) \phi^3 + \left(f_0^{\phi\phi\phi} + \sum_{k=1}^{2} \left(f_k^{\phi\phi\phi} \cos\left(k\,\omega t - \psi_k^{\phi\phi\phi} \right) \right) \right) \phi^3 \\
&\quad + \left(K_{22}^{S} \right) \phi^5 = 0
\end{aligned} \tag{2.20}$$

where the amplitudes and phases of the periodic coefficients are given by:

$$f_k^{(.)} = \sqrt{\left(f_{ks}^{(.)} \right)^2 + \left(f_{kc}^{(.)} \right)^2} \qquad \psi_k^{(.)} = \tan^{-1}\left(\frac{f_{ks}^{(.)}}{f_{kc}^{(.)}} \right) \qquad k = 1 \ldots 4 \tag{2.21}$$

and the expressions for each of them in terms of the coefficients in Eq. (2.18), after a fair amount of algebraic manipulation, are given in the Appendix B. An example of the first three terms follows:

$$f_0^{\phi_{tt}} = \frac{1}{2} \left(K_8^A \zeta_3^2 + K_9^A \zeta_3 \zeta_5 \cos\alpha_5 + K_{10}^A \zeta_5^2 \right) \tag{2.22}$$

$$\begin{aligned}
f_{1s}^{\phi_{tt}} &= -K_3^A \zeta_5 \sin\alpha_5 \\
f_{1c}^{\phi_{tt}} &= K_2^A \zeta_3 + K_3^A \zeta_5 \cos\alpha_5
\end{aligned} \tag{2.23}$$

Rescaling time in Eq. (2.20) with $\tau = \omega t$ yields:

$$
\begin{aligned}
&\phi_{\tau\tau} + \left(f_0^{\phi_{tt}} + \sum_{k=1}^{2} \left(f_k^{\phi_{tt}} \cos\left(k\,\tau - \psi_k^{\phi_{tt}} \right) \right) \right) \phi_{\tau\tau} \\
&\quad + \left(K_{11}^{A} \right) \phi^2 \phi_{\tau\tau} + \left(K_{23}^{A} \right) \phi\, \phi_{\tau}^2 \\
&\quad + \frac{1}{\omega} \left(K_{1}^{D} \right) \phi_{\tau} + \frac{1}{\omega} \left(f_0^{\phi_t} + \sum_{k=1}^{2} \left(f_k^{\phi_t} \cos\left(k\,\tau - \psi_k^{\phi_t} \right) \right) \right) \phi_{\tau} \\
&\quad + \frac{1}{\omega} \left(K_{12}^{D} \right) \phi^2 \phi_{\tau} + \omega \left(K_{17}^{D} \right) \phi_{\tau}^3 \\
&\quad + \frac{1}{\omega^2} \left(K_{1}^{S} \right) \phi + \frac{1}{\omega^2} \left(f_0^{\phi} + \sum_{k=1}^{4} \left(f_k^{\phi} \cos\left(k\,\tau - \psi_k^{\phi} \right) \right) \right) \phi \\
&\quad + \frac{1}{\omega^2} \left(K_{7}^{S} \right) \phi^3 + \frac{1}{\omega^2} \left(f_0^{\phi\phi\phi} + \sum_{k=1}^{2} \left(f_k^{\phi\phi\phi} \cos\left(k\,\tau - \psi_k^{\phi\phi\phi} \right) \right) \right) \phi^3 \\
&\quad + \frac{1}{\omega^2} \left(K_{22}^{S} \right) \phi^5 = 0
\end{aligned}
\tag{2.24}
$$

Based on experimental results and the fair comparison with a quasi-static approximation presented in Ikeda et al. (2000) the inertial terms are expected to be smaller than the damping and the stiffness terms. Also, the coefficients of products of velocities are expected to be smaller than coefficients of products of position and velocity and smaller than pure positional coefficients. With this rationale, the following ordering is assumed in the coefficients of Eq. (2.18):

$$
\begin{aligned}
\epsilon^{-2} &: K_{14\ldots18}^{S} \\
\epsilon^{-1} &: K_{6\ldots8}^{D} \quad K_{4\ldots6}^{S} \quad K_{8\ldots11}^{S} \\
\epsilon^{1} &: K_{2\ldots5}^{A} \quad K_{6,7}^{A} \quad K_{11}^{A} \quad K_{23}^{A} \\
&: K_{1}^{D} \quad K_{4,5}^{D} \quad K_{12}^{D} \quad K_{17}^{D} \\
&: K_{7}^{S} \quad K_{12,13}^{S} \\
\epsilon^{2} &: K_{22}^{S}
\end{aligned}
\tag{2.25}
$$

where the coefficients not listed in Eq. (2.25) are assumed to be $\mathcal{O}(1)$. Assuming ζ_3 and ζ_5 to be $\mathcal{O}(\epsilon)$, and discarding terms of $\mathcal{O}(\epsilon^2)$ and above in Eq. (2.18) yields:

$$\begin{aligned}
&\phi_{tt} + \left(K_{11}^A\right)\phi^2\phi_{tt} + \left(K_{23}^A\right)\phi\,\phi_t^2 + \\
&\quad + \left(K_1^D\right)\phi_t + \left(K_2^D z + K_3^D\theta\right)\phi_t + \left(K_6^D z^2 + K_7^D z\theta + K_8^D\theta^2\right)\phi_t + \\
&\quad + \left(K_{12}^D\right)\phi^2\phi_t + \left(K_{17}^D\right)\phi_t^3 + \\
&\quad + \left(K_1^S\right)\phi + \left(K_2^S z + K_3^S\theta\right)\phi + \\
&\quad + \left(K_4^S z^2 + K_5^S z\theta + K_6^S\theta^2\right)\phi + \left(K_7^S\right)\phi^3 = 0
\end{aligned} \tag{2.26}$$

which reduces Eq. (2.24) to:

$$\begin{aligned}
&\phi_{\tau\tau} + \left(K_{11}^A\right)\phi^2\phi_{\tau\tau} + \left(K_{23}^A\right)\phi\,\phi_\tau^2 \\
&\quad + \frac{1}{\omega}\left(K_1^D\right)\phi_\tau + \frac{1}{\omega}\left(f_0^{\phi_t} + \sum_{k=1}^{2}\left(f_k^{\phi_t}\cos\left(k\,\tau - \psi_k^{\phi_t}\right)\right)\right)\phi_\tau \\
&\quad + \frac{1}{\omega}\left(K_{12}^D\right)\phi^2\phi_\tau + \omega\left(K_{17}^D\right)\phi_\tau^3 \\
&\quad + \frac{1}{\omega^2}\left(K_1^S\right)\phi + \frac{1}{\omega^2}\left(f_0^{\phi} + \sum_{k=1}^{2}\left(f_k^{\phi}\cos\left(k\,\tau - \psi_k^{\phi}\right)\right)\right)\phi \\
&\quad + \frac{1}{\omega^2}\left(K_7^S\right)\phi^3 = 0
\end{aligned} \tag{2.27}$$

where the $f_{ks}^{(.)}$ and $f_{kc}^{(.)}$ to be used in Eq. (2.21) to obtain the $f_k^{(.)}$ and $\psi_k^{(.)}$ terms in Eq. (2.27) are given by the following expressions:

$$f_0^{\phi_t} = +\frac{1}{2}\left(K_6^D\zeta_3^2 + K_7^D\zeta_3\zeta_5\cos\alpha_5 + K_8^D\zeta_5^2\right) \tag{2.28}$$

$$\begin{aligned}
f_{1s}^{\phi_t} &= -\,K_3^D\zeta_5\sin\alpha_5 \\
f_{1c}^{\phi_t} &= +\left(K_2^D\zeta_3 + K_3^D\zeta_5\cos\alpha_5\right)
\end{aligned} \tag{2.29}$$

$$f_{2s}^{\phi_t} = -\frac{1}{2}\left(K_7^D \zeta_3 \zeta_5 \sin\alpha_5 + K_8^D \zeta_5^2 \sin 2\alpha_5\right) \tag{2.30}$$
$$f_{2c}^{\phi_t} = +\frac{1}{2}\left(K_6^D \zeta_3^2 + K_7^D \zeta_3 \zeta_5 \cos\alpha_5 + K_8^D \zeta_5^2 \cos 2\alpha_5\right)$$

$$f_0^{\phi} = +\frac{1}{2}\left(K_4^S \zeta_3^2 + K_5^S \zeta_3 \zeta_5 \cos\alpha_5 + K_6^S \zeta_5^2\right) \tag{2.31}$$

$$f_{1s}^{\phi} = -K_3^S \zeta_5 \sin\alpha_5 \tag{2.32}$$
$$f_{1c}^{\phi} = +\left(K_2^S \zeta_3 + K_3^S \zeta_5 \cos\alpha_5\right)$$

$$f_{2s}^{\phi} = -\frac{1}{2}\left(K_5^S \zeta_3 \zeta_5 \sin\alpha_5 + K_6^S \zeta_5^2 \sin 2\alpha_5\right) \tag{2.33}$$
$$f_{2c}^{\phi} = +\frac{1}{2}\left(K_4^S \zeta_3^2 + K_5^S \zeta_3 \zeta_5 \cos\alpha_5 + K_6^S \zeta_5^2 \cos 2\alpha_5\right)$$

Eq. (2.27) can be re-arranged to yield:

$$\begin{aligned}
&\phi_{\tau\tau} + \frac{1}{\omega}\left(K_1^D + f_0^{\phi_t}\right)\phi_\tau + \frac{1}{\omega}\left(f_1^{\phi_t}\cos\left(\tau - \psi_1^{\phi_t}\right)\right)\phi_\tau \\
&\quad + \frac{1}{\omega^2}\left(K_1^S + f_0^{\phi}\right)\phi + \frac{1}{\omega^2}\left(f_1^{\phi}\cos\left(\tau - \psi_1^{\phi}\right)\right)\phi \\
&\quad + \frac{1}{\omega}\left(f_2^{\phi_t}\cos\left(2\,\tau - \psi_2^{\phi_t}\right)\right)\phi_\tau + \frac{1}{\omega^2}\left(f_2^{\phi}\cos\left(2\,\tau - \psi_2^{\phi}\right)\right)\phi \\
&\quad + \left(K_{11}^A\right)\phi^2\phi_{\tau\tau} + \left(K_{23}^A\right)\phi\,\phi_\tau^2 \\
&\quad + \frac{1}{\omega}\left(K_{12}^D\right)\phi^2\phi_\tau + \omega\left(K_{17}^D\right)\phi_\tau^3 + \frac{1}{\omega^2}\left(K_7^S\right)\phi^3 = 0
\end{aligned} \tag{2.34}$$

Eq. (2.34) is a nonlinear homogenous ODE with time dependent linear stiffness and damping in addition to nonlinearities involving products of angular rotation and angular velocity.

The solution of Eq. (2.34) when the frequency of the heave/pitch response is nearly twice the roll natural frequency is the one of interest for this research. Notice that for this particular case the time dependent term with harmonics of order other than one only contribute to the approximate solution via the $f_0^{(.)}$ terms by changing the linear damping and linear stiffness terms (K_1^D, K_1^S).

With this in mind, in Chapter 5 an approximate solution is sought to an equation of the form:

$$\begin{aligned} x_{tt} + (\delta + \epsilon\cos(t-\psi_1))\, x + (B_1 + f_{\phi_t}\cos(t-\psi_2))\, x_t + \\ C_3 x^3 + A_3 x\, x_t^2 + B_2 x^2 x_t + B_3 x_t^3 = 0 \end{aligned} \tag{2.35}$$

in the vicinity of the principal parametric resonance when $\delta \approx 0.25$, where the correspondence between Eq. (2.34) and Eq. (2.35) is as follows:

$$\begin{aligned} &\delta = \frac{1}{\omega^2}\left(K_1^S + f_0^{\phi}\right) \qquad \epsilon = \frac{1}{\omega^2}\left(f_1^{\phi}\right) \qquad \psi_1 = \psi_1^{\phi} \\ &B_1 = \frac{1}{\omega}\left(K_1^D + f_0^{\phi_t}\right) \qquad f_{\phi_t} = f_1^{\phi_t} \qquad \psi_2 = \psi_1^{\phi_t} \\ &C_3 = \frac{1}{\omega^2}\left(K_7^S\right) \qquad A_3 = K_{23}^A \qquad B_2 = \frac{1}{\omega}\left(K_{12}^D\right) \qquad B_3 = \omega\left(K_{17}^D\right) \end{aligned} \tag{2.36}$$

In Eq. (2.35) the nonlinear added mass term $A_2 = K_{11}^A$ have been omitted because, as will be shown in Chapter 4, this term is aliased with $A_3 = K_{23}^A$ and therefore the two terms cannot be identified simultaneously by the least squares method unless a relation between them is known in advance (or assumed). Since A_2 is a nonlinear term in the highest derivative, and therefore it might cause problems to classical numerical schemes developed for the solution of ODEs, it was decided to only identify A_3.

CHAPTER 3

Slender Body Theory (2D+t)

3.1 Chapter Overview

In this chapter the time dependent and time independent forces and moments required to obtain the hydrodynamic coefficients in the equations of motion are computed. The time dependent forces and moments are restricted to the pure roll motion according to the ordering assumed in the previous chapter. The time independent forces and moments are computed in four degrees of freedom due to the relative importance of the stiffness terms in the equations of motion. The 2D+t method, also know as High Speed Strip Theory (HSST) or Slender Body Theory (SBT), is applied to the computation of the hydrodynamic forces acting on a planing hull in both unsteady and steady conditions. In both cases the 3-D problem is approximated by a series of unsteady 2-D problems. The 2-D problems are solved with the commercial RANSE code Star-CCM+® and the results are compared with those of Wu et al. (2004) and Xu et al. (2010). Having set-up the solution of the 2-D problem, the 3-D problem is approximated by the 2D+t approach and the conditions tested by Judge (2010, 2012); Judge and Judge (2013) for the unsteady case and with Brown and Klosinski (1994a,b) and Judge (2013, 2014a,b) for the steady cases are simulated. The computational results show very good agreement in the horizontal plane but overpredict the forces

and moments in the vertical plane. Based on these findings a semi-empirical correction is proposed in order to account for flow separation at the transom (referred to as a near-transom correction). In Chapter 4, the time series for the forces and moments will be used to compute the inertial and dissipative coefficients in the roll equation of motion. Also, the time independent forces and moments, obtained by systematically varying the attitude of the planing hull from equilibrium, will be used to compute the stiffness coefficients.

The information presented in this chapter is based on the preliminary results in Tascon et al. (2009) for the solution to the steady planing problem and in Tascon and Algarin (2013) for the solution of the unsteady planing problem. Additional comparisons with the experimental results of Judge (2013, 2014a,b) are presented, new findings are discussed and the conclusions are updated accordingly.

3.2 Introduction

The Slender Body Theory (SBT) or 2D+t has been applied by several researchers to solve the motions of high speed slender vessels in waves. The original idea is usually traced back to the work of Chapman (1976) in the investigation of the forces acting on a yawed flat plate. New developments, implementations and direct applications to ship hydrodynamics can be found in Yeung and Kim (1985), Maruo (1982), Zhao et al. (1997), Kashiwagi (1997), Fontaine and Tulin (2001), Savander et al. (2002), Battistin and Iafrati (2002), Kreuzer and Sichermann (2005), Kihara et al. (2005), Holloway and Davis (2006) and Sun and Faltinsen (2012), among others. In these works the SBT is also referred as 2.5D, High Speed Slender Body Theory (HSSBT), High Speed Ship Strip Theory (HSSST) or Time Domain Strip Theory. Most of these applications however have concentrated on the vertical plane with one of the

few exceptions being the work of Kreuzer and Sichermann (2005) in the investigation of parametric roll. A recent example of the application of the 2D+t theory to the specific case of a planing hull heaving and pitching in waves has been presented in Sun and Faltinsen (2010).

In this chapter, the interested is in obtaining the generalized forces and moments acting on a planing hull moving at constant speed either with prescribed harmonic motion or at fixed attitude, in order to compute the hydrodynamic coefficients in the roll equation of motion derived in Chapter 2. The 2D+t is applied to the particular case of a prismatic planing hull moving at constant forward speed while is being oscillated with pure harmonic roll motion; this case is referred to as *Asymmetric Unsteady Planing*. Next, the 2D+t is applied to the case of the same planing hull moving at constant speed and fixed attitude. In this case heel (ϕ), trim (θ) and drift (ψ) angles are allowed in order to generalize the results for what is referred to as *Asymmetric Steady Planing*; however, for the three degrees of freedom problem (heave-roll-pitch) the planing hull is assumed to be moving in a straight path and therefore the drift angle is set to zero ($\psi = 0$).

3.3 Slender Body Theory (2D+t)

In this study, the prismatic hull is assumed to be moving in equilibrium planing conditions with constant speed (x_{t_E}) as defined in the Earth-fixed coordinate system. At time zero, the origin of an Earth-fixed reference frame coincides with the intersection of the free surface and the keel line. This reference frame is for convenience oriented normal to the longitudinal component (u), in the body-fixed coordinate system, of the forward velocity (x_{t_E}), Fig. 3.1.

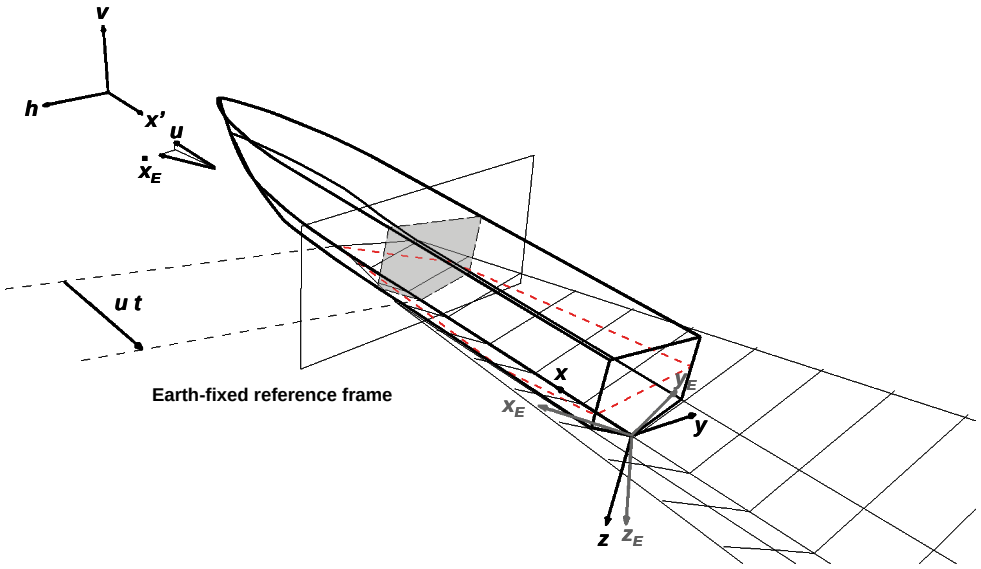

Figure 3.1: Coordinate Systems for the 2D+t Approach.

In the case of a slender body, the longitudinal derivatives are much smaller than the derivatives in the transverse plane. Accordingly, the solution to the three-dimensional problem can be approximated by the solution of a series of unsteady two-dimensional problems on Earth-fixed control planes. The body boundary conditions are satisfied with the velocity of the points on the hull surface mapped onto the 2-D control planes.

The 2-D solution is started on each control plane once the keel crosses the intersection between the control plane and the undisturbed wetted surface, and continues until the transom has crossed that same control plane. The solution obtained in this way is independent of downstream conditions only and therefore cannot account for separation of the flow at the stern, unless some sort of Kutta condition is introduced in order to fulfill atmospheric pressure at the transom (e.g., Savander et al. (2002)). Also, the solution in each control plane has no contribution from any control plane aft, so it is a fully 2-D solution equivalent to the inner solution presented in Yeung and Kim (1981). This is consistent with the high-frequency assumption in the 3-D

planing problem. In fact, Yeung and Kim (1985) matched their inner solution with an outer 3-D solution in order to capture low-frequency effects. Taking advantage of the fact that the vessel is moving at constant speed a new control plane, parallel to the Earth-fixed reference frame shown in Fig. 3.1, is introduced at the bow at each time step defined as $dt = dx'/u$ in order to avoid interpolation of the sectional forces and moments obtained on each control plane. The coordinate system for the solution of the impact problem in the 2-D control planes is presented in Fig. 3.2.

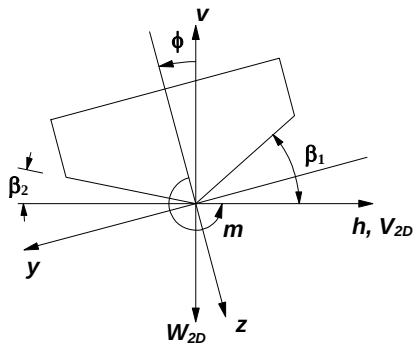

Figure 3.2: Asymmetric 2-D water impact.

The six degrees of freedom hydrodynamic generalized forces, defined in the body-fixed coordinate system, for the three dimensional problem, are obtained at each time step by integrating along the keel wetted length (SKWL) the two dimensional sectional forces computed by the Volume of Fluid (VOF) method in the active control planes (i.e., those which are within the wetted length of the planing hull). In the case of the asymmetric steady planing case the solution can be obtained in a single control plane (e.g., Savander et al. (2002)). The 2-D water impact problems are solved by the VOF method in order to allow for the possibility of flow separated from the keel and re-attachement. The way in which the 2-D problem is set up in order to solve the equivalent problems for the asymmetric steady and unsteady 3-D planing problems is presented in the following sections.

3.4 Solution of the 2-D Impact Problem by the Volume of Fluid (VOF) Method

Faltinsen et al. (2004) highlighted the challenges associated to the simulation of some specific hydrodynamic problems with Reynolds-Averaged Navier-Stokes Equations (RANSE) Computational Fluid Dynamics (CFD) due to the presence of the free surface and its unsteady nature. However, in recent years many examples of the application of commercial CFD programs based on the VOF method to the solution of two dimensional impact problems have shown promising results (e.g., Seif et al. (2005), Fairlie-Clarke and Tveitnes (2008), Godderidge et al. (2008)). In the aforementioned examples, the 2-D water impact has been modeled as a stationary object subject to a uniform flow stream, and only in one of these cases (Seif et al., 2005) asymmetry in the form of heel has been included.

Encouraged by these results, the commercial CFD program Star-CCM+ is used to solve the problem of a two-dimensional constant deadrise wedge impacting the water in asymmetric conditions. In Star-CCM+ the free surface is captured (position and shape) by using a volume-of-fluid homogeneous multiphase model, which assumes a common velocity, pressure and temperature field for all phases. The flow equations are solved for velocity and pressure in a segregated manner, with a predictor-corrector approach that uses a Rhie-and-Chow-type pressure-velocity coupling combined with a SIMPLE-type algorithm (CD-Adapco 2013).

For this particular application viscosity is neglected under the assumption of large Froude number (for the 3-D unsteady/steady planing problems); therefore, the problem is solved under the assumptions of flow of an inviscid and incompressible fluid. The peculiarities of the computational set up used to solve the asymmetric 2-D water impact are presented in the following two subsections.

3.4.1 Water impact of a 2-D heeled wedge with vertical and rotational velocities

In order to extend the results obtained in this section to 3-D solutions by the 2D+t approach and compare with Judge (2010, 2012); Judge and Judge (2013), the 2-D water entry of a wedge with constant deadrise angle of 20 degrees is simulated as a rotating body motion subject to a uniform flow stream. The 2D+t results will account for the hydrostatic contribution to the fluid force since gravity is included in the solution of the 2-D impact problem. In the case of forced roll oscillations, the body-boundary condition in the 2-D control planes corresponds exactly to that of a two dimensional heeled wedge impacting the water with vertical velocity $W_{2D} = \sin(\theta)x_{t_E}$ and angular velocity $\Phi_{t_{2D}} = p(t)$.

The simulation domain is a rectangular region that extends seven times the beam of the wedge towards the side, seven times towards the bottom and one and a half times towards the top. Polyhedral cells are used, with finer cells close to the body growing from the keel of the wedge towards the chines. The boundary conditions are specified by defining the sides of the wedge and the sides of the domain as walls, the bottom as a velocity inlet and the top of the domain as a pressure outlet (Fig. 3.3a). The computational domain is divided in two regions; the region containing the wedge rotates inside the fixed region. The motion of the wedge is prescribed in the Rotation Motion model by providing angular velocity in one degree-of-freedom (roll) to the rotating region and being this subject to a uniform flow stream of velocity W_{2D}. The problem is solved under the assumptions of flow of an inviscid and incompressible fluid.

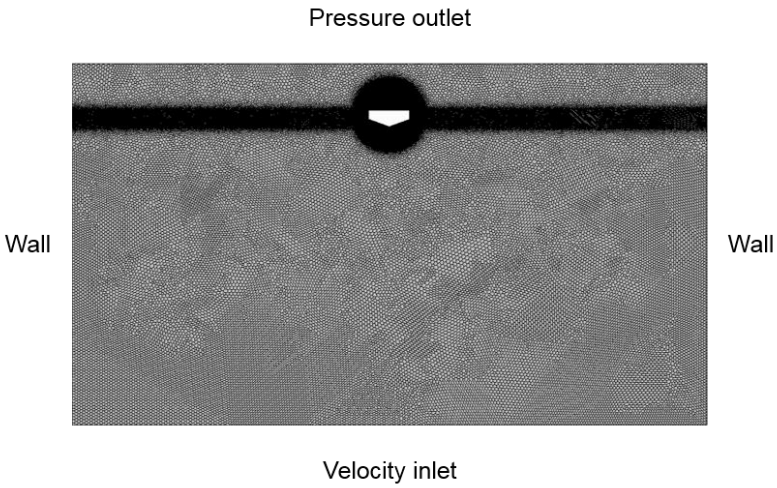

(a) Solution domain

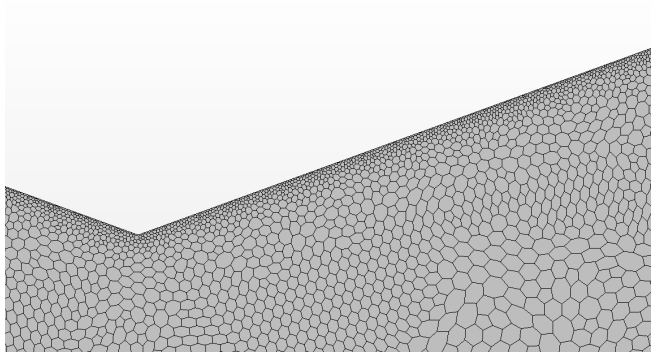

(b) Detail of the medium mesh close to the wedge

Figure 3.3: Solution domain for the water impact of a 2-D heeled wedge with vertical and rotational velocities

A numerical uncertainty study was conducted on both space and time following Eça and Hoekstra (2014). The spatial discretization (grid independence) study was conducted with three meshes of 65,000 (coarse), 140,000 (medium) and 230,000 (fine) cells. The time discretization study was conducted with four time steps, starting with $\Delta t = 0.0020$ s and halving it successively until reaching $\Delta t = 0.00025$ s. The best compromise between accuracy and computational time was found with the medium mesh (Fig. 3.3b) with time step $\Delta t = 0.0010$ s and 20 inner iterations; therefore, this configuration is used to compute the solutions presented in this chapter.

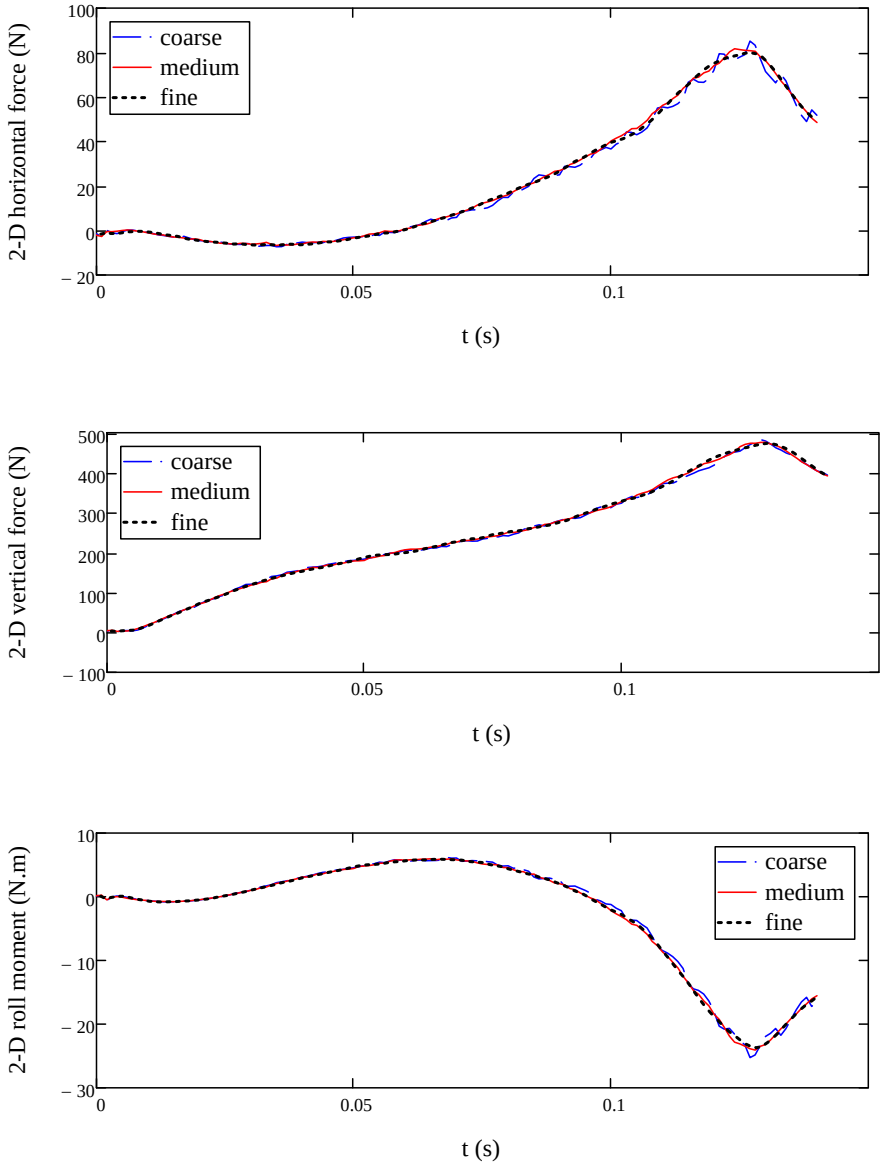

Figure 3.4: Mesh independence study for the water impact of a 2-D heeled wedge with vertical and rotational velocities, simulated with time step 0.0010 s. Water entry of a $\beta_G = 20°$ wedge at constant vertical velocity ($W_{2D} = 0.431$ m s^{-1}) and prescribed rotational motion ($\phi(t) = 10° \sin(9.425(t - 0.019))$), initially heeled at $\phi_0 = -9.656°$.

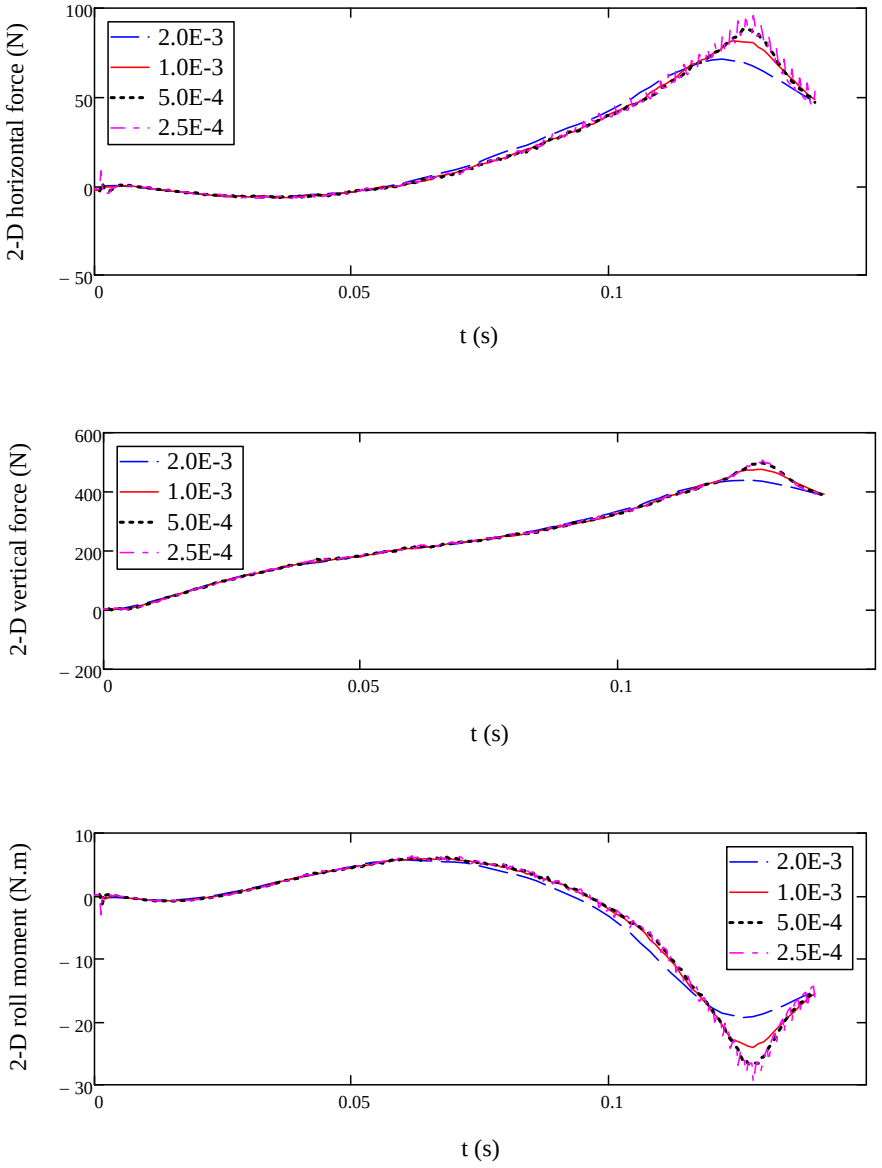

Figure 3.5: Time independence study for the water impact of a 2-D heeled wedge with vertical and rotational velocities, simulated on the medium mesh ($\sim$ 140,000 cells). Water entry of a $\beta_G = 20°$ wedge at constant vertical velocity ($W_{2D} = 0.431$ m s^{-1}) and prescribed rotational motion ($\phi(t) = 10° \sin(9.425(t - 0.019))$), initially heeled at $\phi_0 = -9.656°$.

The results for the horizontal and vertical forces and the roll moment for time step $\Delta t = 0.0010$ s computed in the medium mesh are shown in Fig. 3.4. The results for the horizontal and vertical forces and the roll moment for the four different time steps computed in the medium mesh are shown in Fig. 3.5. The solution is checked for convergence by monitoring the reduction in the order of magnitude of the residuals and the convergence of the total pressure force on the body after each set of inner iterations.

Xu et al. (2010) solved the water entry problem of a wedge in free fall in 3-DOF (horizontal, vertical and rotational velocities) by using velocity potential theory and the stretched coordinate system method. They compared their results with those of Wu et al. (2004) for the special case of vertical water entry of a symmetrical wedge to demonstrate the stability and accuracy of the results. Also, as a special case, the water entry of a wedge at constant vertical and rotational velocities was simulated. The pressure distributions presented in their work have been used to obtain force and moment coefficients, with forces non-dimensionalized by $\rho W_{2D}^2 (W_{2D}t)$ and moment by $\rho W_{2D}^2 (W_{2D}t)^2$, as a function of vertical distance $(W_{2D}t)$; these results are used for comparison with those produced by the current CFD simulation and presented in Fig. 3.6.

The agreement between the results increases as time progresses. The disagreement in the early stages of impact might be due to the use of the similarity solution based on the translational motion as initial solution for the boundary element method or due to the limited number of cells available for the computation of the pressure distribution in the VOF method. In general terms, the vertical force and the roll moment agree very well while the horizontal force is slightly lower than that obtained by the boundary element method.

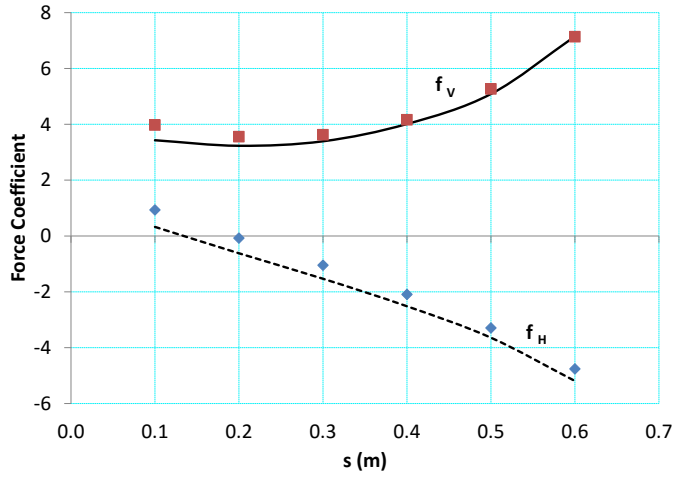

(a) Force Coefficients (f_H,f_V)

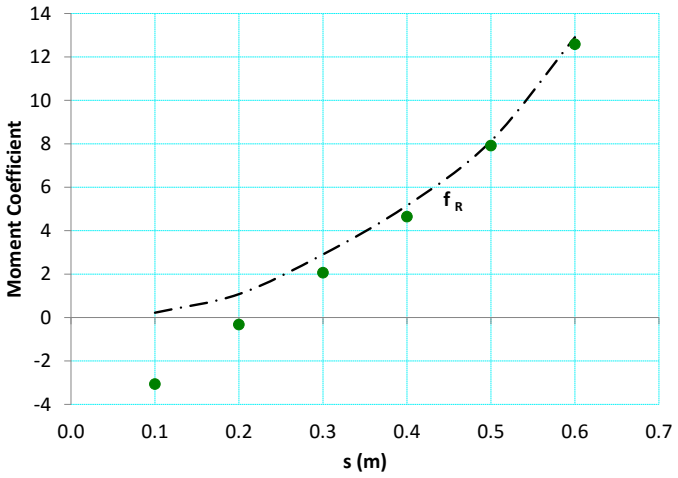

(b) Roll Moment Coefficient (f_R)

Figure 3.6: Comparison between Xu et al. (2010) numerical (symbols) and the CFD (lines) force and moment coefficients (f_H,f_V,f_R) as a function of wedge submergence (s) for the water entry of a $\beta_G = 45°$ wedge at constant vertical ($W_{2D} = 5$ m s^{-1}) and rotational velocity ($\omega = -2.5$ rad s^{-1}) initially heeled at $\phi_0 = 10°$ ($\beta_1 = 55°$, $\beta_2 = 35°$) during chines un-wetted.

3.4.2 Water impact of a 2-D heeled wedge with vertical and horizontal velocities

The final aim is to compare the results of the 2D+t approach to the asymmetric steady planing case with the experimental results of Brown and Klosinski (1994a,b) and Judge (2013, 2014a,b). Therefore, in order to be able to generalize the 2-D impact results and extend them to models with different beam, gravity is neglected and the problem is solved on wedges having a half beam (B/2) of one meter impacting the water with the velocities non-dimensionalized by W_{2D}. In the asymmetric steady planing case, the body-boundary condition in the 2-D control plane corresponds exactly to that of a two dimensional heeled wedge impacting the water with horizontal and vertical velocities (V_{2D}, W_{2D}). The 2-D impact problem, Fig. 3.2, is set up in the same fashion as in Judge et al. (1999), where the deadrise angles ($\beta_{1,2}$) are related to the body fixed heel angle (ϕ) by $\beta_{1,2} = \beta_G \pm \phi$, where β_G is the deadrise of the wedge.

A non-dimensional impact time (τ) is defined together with force and moment coefficients (Cf_h, Cf_v, Cf_m) to be used in the computation of the sectional forces (f_h, f_v) and sectional moment (f_m), Eq. (3.1) and Eq. (3.2) respectively. The coefficients (Cf_y, Cf_z, Cm_x) for the calculation of the forces and moments in the body fixed coordinate system are obtained via a simple transformation, Eq. (3.3).

$$\tau \equiv \frac{W_{2D}}{\frac{B}{2}} t \tag{3.1}$$

$$\begin{pmatrix} Cf_h \\ Cf_v \\ Cf_m \end{pmatrix} = \frac{1}{\rho W_{2D}^2 \frac{B}{2}} \begin{pmatrix} f_h \\ f_v \\ \frac{2}{B} f_m \end{pmatrix} \tag{3.2}$$

$$\begin{pmatrix} Cf_y \\ Cf_z \\ Cm_x \end{pmatrix} = \begin{bmatrix} -\cos(\phi) & -\sin(\phi) & 0 \\ \sin(\phi) & -\cos(\phi) & 0 \\ 0 & 0 & 1 \end{bmatrix} \begin{pmatrix} Cf_h \\ Cf_v \\ Cm_m \end{pmatrix} \tag{3.3}$$

The 2-D asymmetric water entry of wedges, with constant deadrise angle is simulated as a rigid body motion with constant velocity. Tables 3.1, 3.2, and 3.3 present the cases that have been simulated corresponding to hulls with 30, 20 and 10 degrees deadrise angles respectively; the numbers inside the tables correspond to the non-dimensional horizontal impact velocity (V_{2D}/W_{2D}). These values have been chosen in order to be able to compare the application of the SBT with some of the cases reported in Brown and Klosinski (1994a,b) and Judge (2013, 2014a,b).

The simulation domain is a rectangular region that extends four times the beam of the wedge towards the side, six times towards the bottom and three times towards the top. A total of approximately 102,000 polyhedral cells are used, with finer cells close to the body growing from the keel of the wedge towards the chines. A grid independence study, with meshes ranging from 90,000 cells to 189,000 cells, was conducted and a discretization error of 0.5% for the selected mesh was found by using a generalized Richardson extrapolation method (Roy, 2005). The solution is checked for convergence by monitoring the reduction in the residuals and the convergence of the total pressure force on the body after each set of inner iterations.

ψ	ϕ			
	-10°	0°	10°	20°
0°	0	0	0	0
5°	0.84	0.84	0.84	0.84
10°	1.69	1.69	1.69	1.69
15°	2.56	2.56	2.56	2.56

Table 3.1: Summary of 2-D Impact Cases Simulated for the $\beta_G = 30°$ hull as a function of heel (ϕ) and drift (ψ). The numbers inside the table correspond to the non-dimensional horizontal impact velocity (V_{2D}/W_{2D})

ψ	ϕ			
	-10°	0°	10°	20°
0°	0	0	0	
5°	0.84	0.84	0.84	
10°	1.69	1.69	1.69	
15°	2.56	2.56	2.56	

Table 3.2: Summary of 2-D Impact Cases Simulated for the $\beta_G = 20°$ hull as a function of heel (ϕ) and drift (ψ). The numbers inside the table correspond to the non-dimensional horizontal impact velocity (V_{2D}/W_{2D})

ψ	ϕ			
	-10°	0°	10°	20°
0°		0		
5°		0.84		
10°		1.69		
15°		2.56		

Table 3.3: Summary of 2-D Impact Cases Simulated for the $\beta_G = 10°$ hull as a function of heel (ϕ) and drift (ψ). The numbers inside the table correspond to the non-dimensional horizontal impact velocity (V_{2D}/W_{2D})

The boundary conditions are specified by defining the sides of the wedge as walls, the bottom and sides of the domain as velocity inlets and the top of the domain as a pressure outlet. A time step of 0.002 seconds with 20 inner iterations was used through all the simulations. The combination of time step (0.0001s to 0.005s) and number of inner iterations (10 to 150) was tested on several mesh sizes and selected using Courant number less than 0.15 (Fairlie-Clarke and Tveitnes, 2008) and minimum CPU time as criteria. The motion of the wedge is prescribed in the Rigid Body Motion model by providing linear velocities in two degrees of freedom, angular velocity is not considered in any of the cases presented in this subsection. The Rigid Body Motion model is used in Star-CCM+ for unsteady simulations in which rigid mesh motions are specified. The problem is solved under the assumptions of flow of an inviscid and incompressible fluid, with gravity neglected.

Judge et al. (2004) in their literature review concluded that most investigations of water entry have concentrated their efforts in solving the purely vertical impact problem. In the same reference, a summary of the work that has been completed for asymmetric (or oblique) water impact is presented. The majority of the results presented in these papers correspond to pressure distributions and/or separation-ventilation conditions at the keel, during the stages when self-similar flow is maintained, i.e., before the flow reaches one of the chines. Since the interest of this research is the determination of the generalized restoring forces, the distribution of the transient forces in the two-dimensional impact model is the one of interest; unfortunately, this information is not available from aforementioned papers.

More recently, Xu et al. (2008) have solved the similarity flow in the asymmetric impact problem of a two-dimensional wedge by using a boundary-element method linked to an analytical solution for the jet based on the shallow water approximation. They compared their results with those of Semenov and Iafrati (2006) for the special

case of vertical water entry finding overall agreement in the pressure distributions. The force and moment coefficients, with forces non-dimensionalized by $\rho W_{2D}^2 (W_{2D}t)$ and moments by $\rho W_{2D}^2 (W_{2D}t)^2$, as a function of non-dimensional horizontal impact velocity (V_{2D}/W_{2D}), as presented in their work are used for comparison with those produced by the current CFD simulation, Fig. 3.7.

Excellent agreement between the results is observed in the prediction of the horizontal force; the vertical force and the moment are slightly lower than those obtained by the boundary element method. The combinations of deadrise, heel angle and non-dimensional horizontal impact velocity were selected by Xu et al. (2008) such that no separation of the flow from the keel is present; on the other hand, the results from the CFD simulations include cases in which separation with and without re-attachment were observed.

These regions are identified in Fig. 3.7 as region 1 for attached flow (Fig. 3.8a), region 2 for flow separated from the keel with re-attachment (Fig. 3.8b), and region 3 for separated flow (Fig. 3.8c). The onset of separation from the keel coincides with that predicted by Judge et al. (2004). In regions 2 and 3, the vertical force and the moment coefficients deviate from the linear trend observed by Xu et al. (2008) as expected.

It is important to highlight that in the CFD simulations the fluid is not potential (irrotational) just assumed inviscid, even though, numerical damping exists since dissipative-like terms are created in the discretization of the fluid equations for the solution of the problem by the VOF method. Therefore, the presence of numerical damping acts, in a sense, like viscosity and therefore forces an implied Kutta condition at the sharp edged keel.

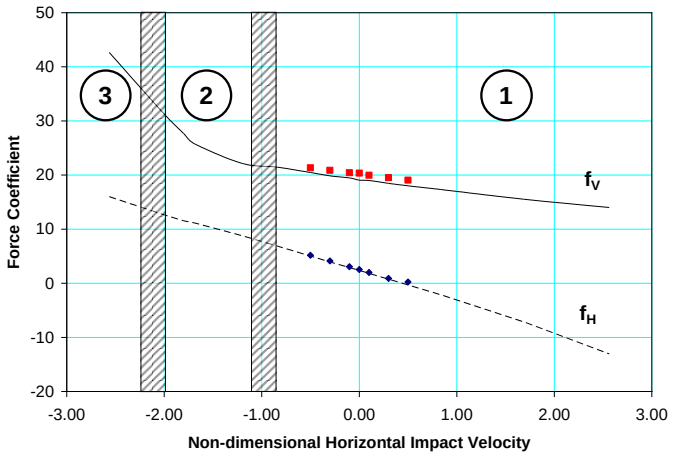

(a) Force Coefficients (f_H,f_V)

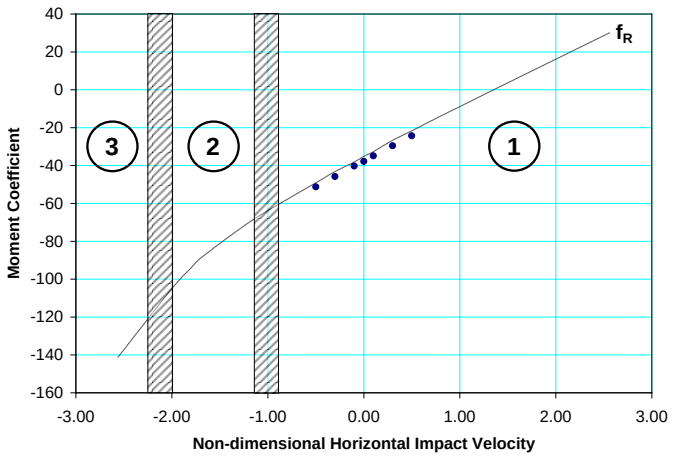

(b) Roll Moment Coefficient (f_R)

Figure 3.7: Comparison between Xu et al. (2008) numerical (symbols) and the CFD (lines) force and moment coefficients for the $\beta_G = 30°$ wedge, heeled $\phi = 10°$ ($\beta_1 = 40°$ $\beta_2 = 20°$) during chines un-wetted phase

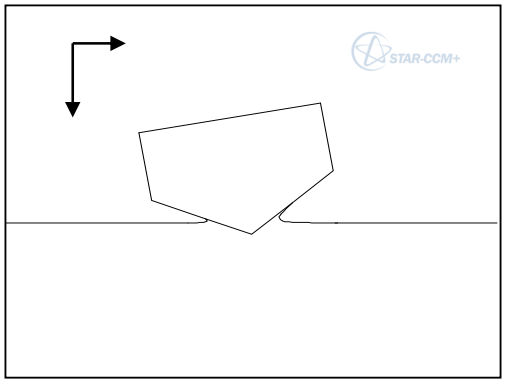

(a) Region 1: Attached Flow

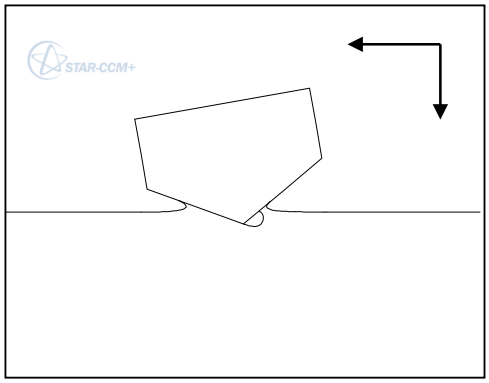

(b) Region 2: Separated flow with re-attachment

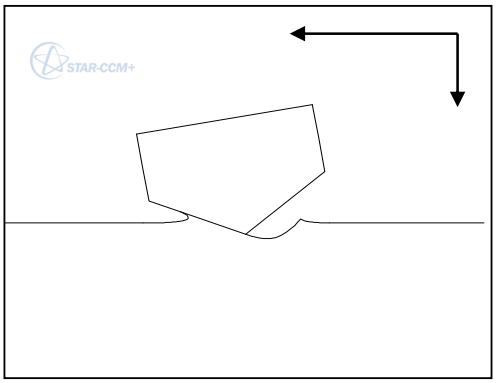

(c) Region 3: Separated flow

Figure 3.8: Flow separation from the keel during chines un-wetted phase. Example corresponds to a $\beta_G = 30°$ wedge, heeled $\phi = 10°$ ($\beta_1 = 40°$ $\beta_2 = 20°$)

3.5 Asymmetric Unsteady Planing

Judge (2010, 2012); Judge and Judge (2013) conducted an extensive series of captive model tests at the United States Naval Academy (USNA) in order to obtain fundamental hydrodynamic information about planing hulls. The objective of their efforts was to provide the scientific community with data required for the study of the dynamics of planing hulls, particularly transverse stability. The scale model has a pure prismatic cross section of constant 20 degrees dead-rise angle and vertical sides that run from amidships to the transom. The quantities measured in the test program included the generalized forces in 3-DOF (heave, sway and roll); heave and sway in the Earth-fixed coordinate system and roll in the body-fixed coordinate system. Additionally, underwater photographs of the hulls were taken in each condition tested, from which the wetted lengths were determined. Here the interest is to compare the numerical solutions obtained by the 2D+t approach with these experimental results.

To assess the validity of the 2D+t approach and to make initial observations about the dependency of the roll moment on load coefficient (C_Δ), beam Froude number (C_v), roll amplitude (ϕ_0) and frequency of oscillation (f), it was decided to run a 2^4 full factorial design of experiments (DOE). The lower and upper values used for these factors are presented in Table 3.4.

As in Sun and Faltinsen (2012), a total of 20 active control planes were used throughout all the computations presented in this section for the asymmetric unsteady planing case. However, an independence study showed that as few as 10 control planes could be used without compromising the accuracy of the solution. The wedges used in the solution of the problem have the same dimensions as the prismatic cross sections of the model tested by Judge (2010, 2012); Judge and Judge (2013).

Factors	Lower	Upper
C_Δ	0.15	0.29
C_v	2.9	4.3
ϕ_0	10°	20°
f	1.5 Hz	2.5 Hz

Table 3.4: DOE factors and levels.

In order to validate the approach, the numerical and experimental time histories of the heave force and the pitch moment in the Earth-fixed coordinate system and the roll moment in the body-fixed coordinate system are compared. Fig. 3.9 presents the case of the heavier configuration ($C_\Delta = 0.29$) run at the lowest speed coefficient ($C_v = 2.9$) and the smallest roll amplitude ($\phi_0 = 10°$) for the minimum ($f = 1.5$ Hz) and the maximum ($f = 2.5$ Hz) frequencies tested. For comparison, Fig. 3.10 presents the case of the lighter configuration ($C_\Delta = 0.15$) run at the highest speed coefficient ($C_v = 4.3$) and the largest roll amplitude ($\phi_0 = 20°$) for the minimum ($f = 1.5$ Hz) and the maximum ($f = 2.5$ Hz) frequencies tested. As expected, higher non-linearities are observed in the latter case. The "average" of the experimental results for each run was constructed by taking the Fourier transform of the time series and assuming harmonics larger than seven to be noise. The forward speed and the frequency of oscillation determined the number of cycles to be used for these calculations, since the forward speed for each test was kept constant during at least two seconds. A minimum of two cycles were used for the cases with high forward speed and low frequency, and as many as twenty cycles for the cases with low forward speed and high frequency. In the figures, the "averaged" signal together with the original signal (raw) is compared with the numerical (2D+t) time series for one period of oscillation. Expanded views of all figures used for these comparisons can be found in Appendix C.

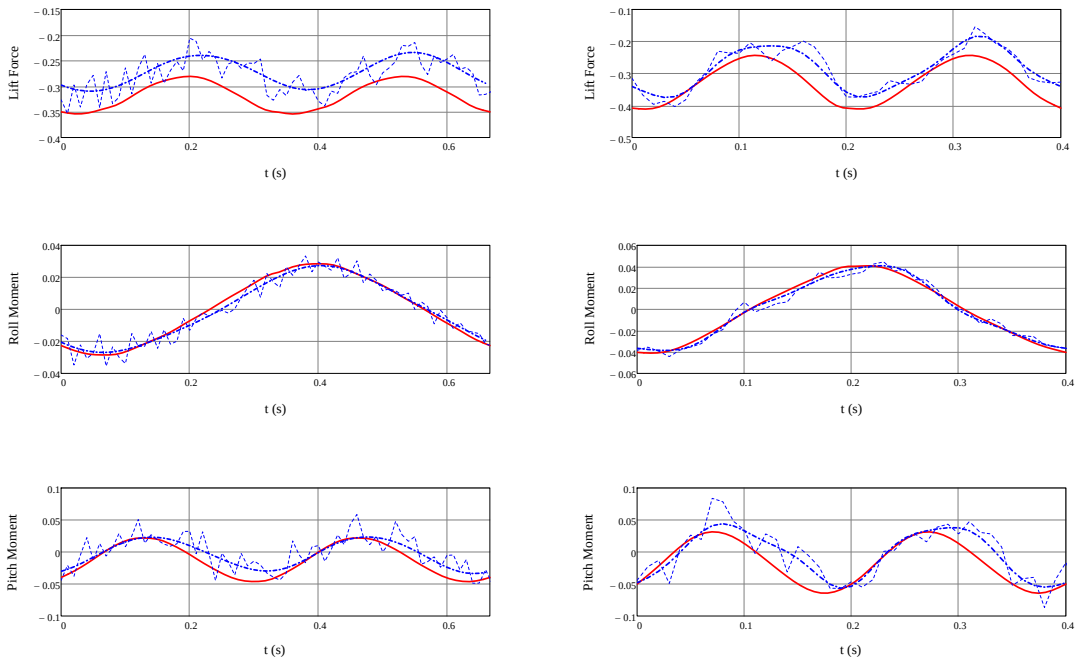

(a) $f = 1.5$ Hz (b) $f = 2.5$ Hz

Figure 3.9: Time series comparison of non-dimensional lift force and roll and pitch moments between 2D+t theory (solid line) and experiments (averaged: dash-dotted line; raw: dotted line) in forced roll. Experimental conditions: $C_\Delta = 0.29$, $C_v = 2.9$, $\phi_0 = 10^\circ$

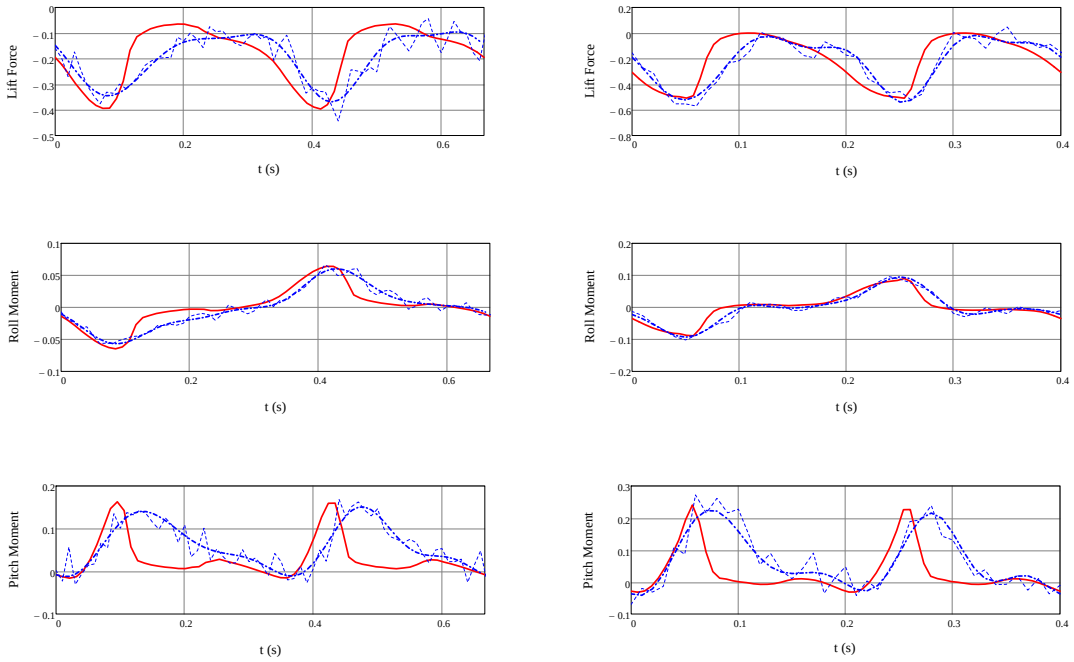

(a) $f = 1.5$ Hz (b) $f = 2.5$ Hz

Figure 3.10: Time series comparison of non-dimensional lift force and roll and pitch moments between 2D+t theory (solid line) and experiments (averaged: dash-dotted line; raw: dotted line) in forced roll. Experimental conditions: $C_\Delta = 0.15$, $C_v = 4.3$, $\phi_0 = 20^\circ$

In Tascon and Algarin (2013) the biggest discrepancy was found in the results corresponding to the maximum frequency of oscillation tested, where the experimental results showed peaks in both the sway force and the roll moment at the times where the roll amplitude is a maximum.

It was found after re-analysis of the experimental time series and personal communication with Professor Judge at the United States Naval Academy (USNA) that in some experimental runs the mass moment of inertia was much larger than the one reported in Judge and Judge (2013) (i.e., $I_x = 0.0298$ lbf.in.s^2).

Taking the above into consideration, a value of $I_x = 1.97$ lbf.in.s^2 has been used to obtain the experimental time series shown in this chapter for comparison with the numerical results. The latter value corresponds to a non-dimensional radius of gyration of $\kappa_x/B = 0.333$ very close to the lower limit of the values typically used in ship design as referenced in Chapter 2 (i.e., $0.36 \leq \kappa_x/B \leq 0.42$).

An example of the results using the two different values for the non-dimensional radius of gyration is presented in Fig. 3.11 for the heavier configuration ($C_\Delta = 0.29$) and in Fig. 3.12 for the lighter configuration ($C_\Delta = 0.15$). In all cases there is an improvement in the agreement between the experimental and the numerical results when the larger value of the non-dimensional radius of gyration is used.

Tascon and Algarin (2013) reported that the computational results showed fair to good agreement with the experimental results. In general, the sway force and the roll moment were well predicted while the heave force was over-predicted. 3-D effects, particularly those related to the separation of the fluid at the transom were believed to be the major cause of disagreement as pointed out in Lai (1994).

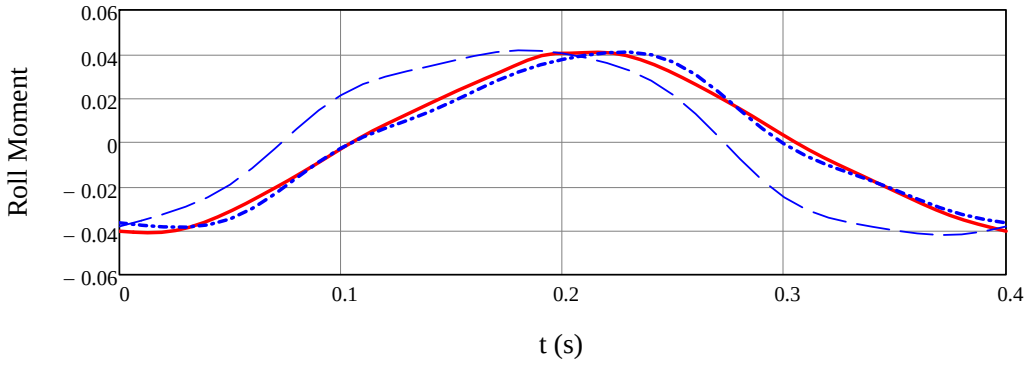

(a) $C_v = 2.9$, $\phi_0 = 10°$

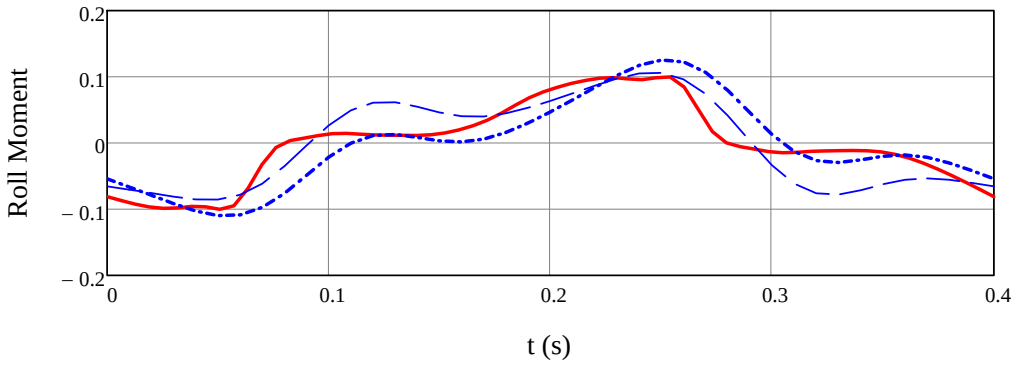

(b) $C_v = 4.3$, $\phi_0 = 20°$

Figure 3.11: Time series comparison of non-dimensional roll moments between 2D+t theory (solid line) and experiments (dashed and dash-dotted lines) for the heavier configuration ($C_\Delta = 0.29$) in forced roll oscillations at $f = 2.5$ Hz showing the effect of the model's roll moment of inertia. Non-dimensional radius of gyration: $\kappa_x/B = 0.041$ (dashed line), $\kappa_x/B = 0.333$ (dash-dotted line)

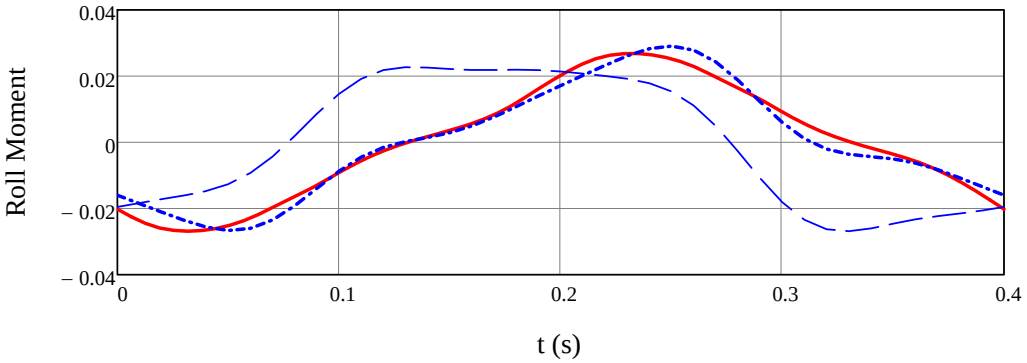

(a) $C_v = 2.9$, $\phi_0 = 10°$

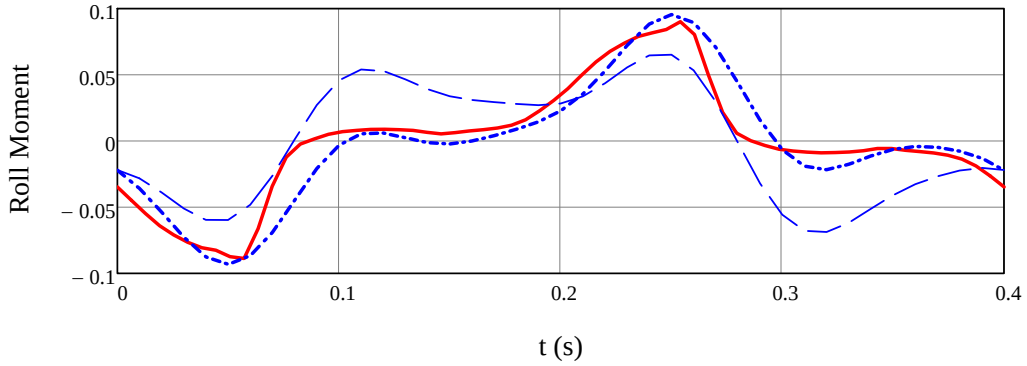

(b) $C_v = 4.3$, $\phi_0 = 20°$

Figure 3.12: Time series comparison of non-dimensional roll moments between 2D+t theory (solid line) and experiments (dashed and dash-dotted lines) for the lighter configuration ($C_\Delta = 0.15$) in forced roll oscillations at $f = 2.5$ Hz showing the effect of the model's roll moment of inertia. Non-dimensional radius of gyration: $\kappa_x/B = 0.041$ (dashed line), $\kappa_x/B = 0.333$ (dash-dotted line)

In Tascon and Algarin (2013) the transom correction suggested by Garme (2005) was applied to the 2-D force distribution, using a non-dimensional value of $a_{\mathrm{ND}} = 0.34$, and an improvement in the agreement between the numerical and the experimental results was found in the heave force. However, it was observed that the value of a_{ND} used worked very well for the lower beam Froude number ($C_v = 2.9$) but for the higher beam Froude number ($C_v = 4.3$) a lower value of a_{ND} would have worked better. This came as no surprise taking into consideration that Garme (2005) proposed a single value of a_{ND} for the correction as a compromise solution since he observed that a single a_{ND} did not work in every case.

The results of the application of the SBT approach to the asymmetric steady planing cases, to be presented in the next section, show similar trends in the sense that forces and moments in the horizontal plane appear to be well predicted but in the vertical plane they are clearly over-predicted. Taking this into consideration, a near-transom correction, to be described at the end of this chapter, is proposed.

The time series to be presented in this chapter correspond to the application of this near-transom correction (NTC) to the results obtained by the 2D+t approach. In general the agreement between the numerical and the experimental results improves when the near-transom correction is applied. In order to show the effect of the NTC, in Fig. 3.13 the non-dimensional lift force without NTC is presented for the two configurations in forced roll oscillations with $\phi_0 = 10^\circ$ and $f = 1.5$ Hz. In Fig. 3.14 the non-dimensional lift force with NTC is presented for the same configurations and testing conditions as before. A side by side comparison of the information presented in these two figures is shown in Fig. 3.15.

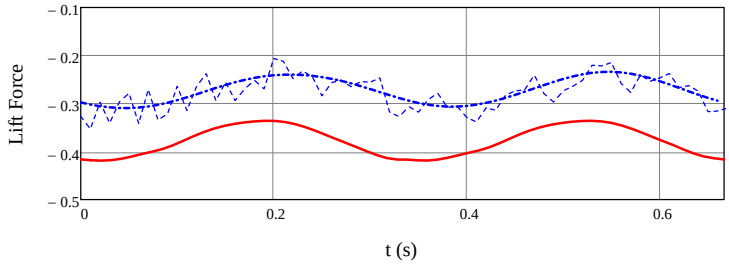

(a) $C_\Delta = 0.29$, $C_v = 2.9$, without NTC

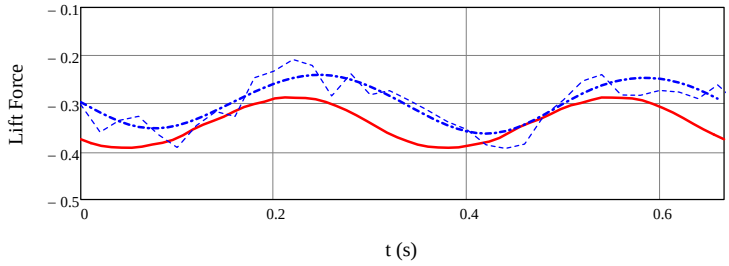

(b) $C_\Delta = 0.29$, $C_v = 4.3$, without NTC

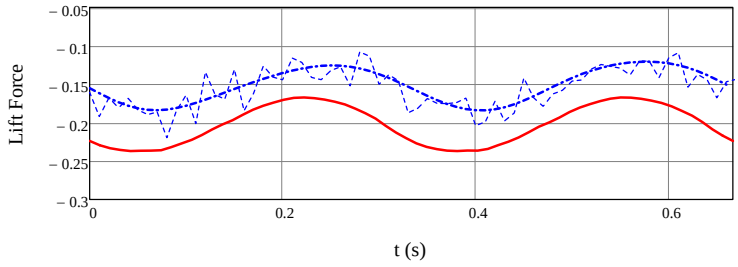

(c) $C_\Delta = 0.15$, $C_v = 2.9$, without NTC

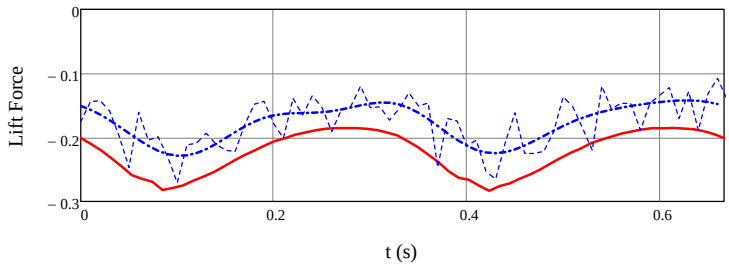

(d) $C_\Delta = 0.15$, $C_v = 4.3$, without NTC

Figure 3.13: Time series comparison of non-dimensional lift force between 2D+t theory without near-transom correction (NTC) (solid line) and experiments (dashed and dash-dotted lines) in forced roll oscillations with $\phi_0 = 10°$ and $f = 1.5$ Hz

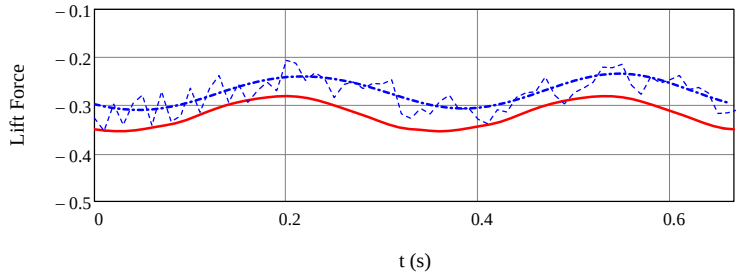

(a) $C_\Delta = 0.29$, $C_v = 2.9$, with NTC

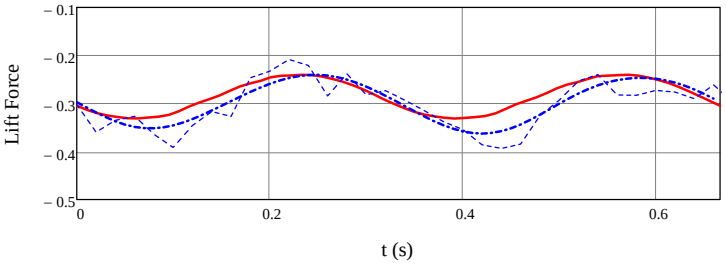

(b) $C_\Delta = 0.29$, $C_v = 4.3$ with NTC

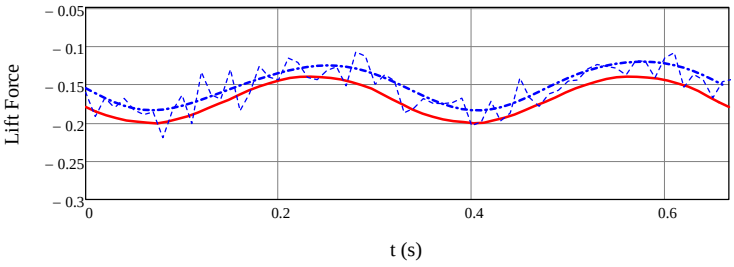

(c) $C_\Delta = 0.15$, $C_v = 2.9$, with NTC

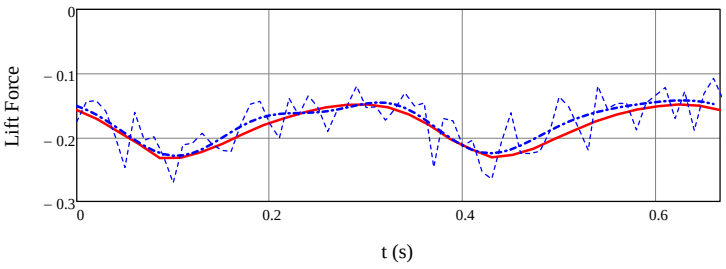

(d) $C_\Delta = 0.15$, $C_v = 4.3$ with NTC

Figure 3.14: Time series comparison of non-dimensional lift force between 2D+t theory with near-transom correction (NTC) (solid line) and experiments (dashed and dash-dotted lines) in forced roll oscillations with $\phi_0 = 10°$ and $f = 1.5$ Hz

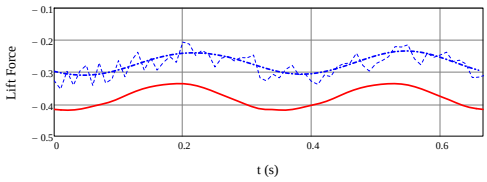

(a) $C_\Delta = 0.29$, $C_v = 2.9$, without NTC

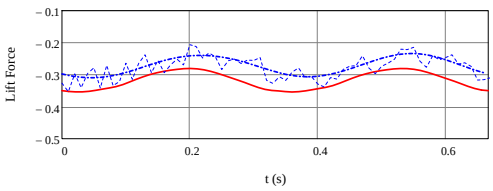

(b) $C_\Delta = 0.29$, $C_v = 2.9$, with NTC

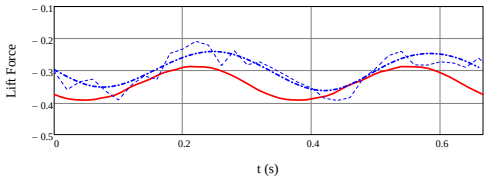

(c) $C_\Delta = 0.29$, $C_v = 4.3$, without NTC

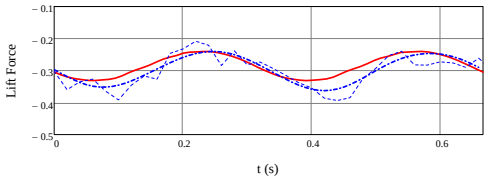

(d) $C_\Delta = 0.29$, $C_v = 4.3$ with NTC

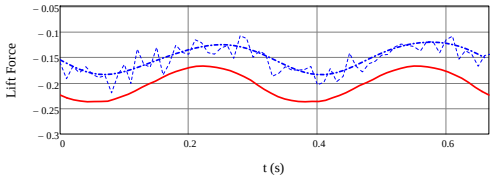

(e) $C_\Delta = 0.15$, $C_v = 2.9$, without NTC

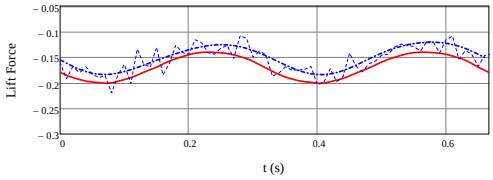

(f) $C_\Delta = 0.15$, $C_v = 2.9$, with NTC

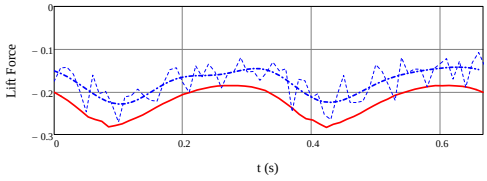

(g) $C_\Delta = 0.15$, $C_v = 4.3$, without NTC

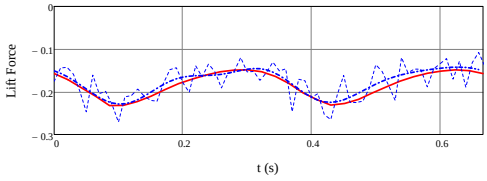

(h) $C_\Delta = 0.15$, $C_v = 4.3$ with NTC

Figure 3.15: Time series comparison of non-dimensional lift force between 2D+t theory (solid line) and experiments (dashed and dash-dotted lines) in forced roll oscillations with $\phi_0 = 10°$ and $f = 1.5$ Hz showing the effect of the near-transom correction (NTC)

For consistency with the work developed as part of this research effort, in Appendix C the time series for the heave force (Lift) and the roll and pitch moments are presented. In general the agreement between the numerical and the experimental results is fair to very good. The general differences between the numerical simulations and the experiments (and therefore expected causes for disagreement between the two) are:

1. The geometry simulated numerically correspond to that of a constant deadrise wedge while the geometry tested at the USNA is only fully prismatic in the aft region; therefore, better agreement is expected for the configurations with smaller keel wetted length (e.g., the lighter configuration run at high speed).

2. In the numerical simulations it was assumed that the roll axis coincided with the vertical center of gravity; however, it was found that this was not the case, in the experiments the roll axis was at 5.67 in (14.4 cm) and the center of gravity at 5.29 in (13.4 cm); therefore the motion prescribed in the numerical simulations does not coincide exactly with that prescribed in the experiments and this difference is specially notorious in the high amplitude runs.

3. The numerical simulations do not account for the water rise in front of the hull. This is likely to be the cause of the phase difference between the numerical and the experimental results, since the effect would be equivalent to the impact (in the 2-D control planes) to be initiated sooner.

4. The 2-D control planes are parallel to the transom and therefore there is a $(\sin\theta)$ error in the computation of the hydrostatic force. This error is expected to be smaller than simply accounting for the volume below the undisturbed water line as was done in Tascon et al. (2009) for the asymmetric steady planing case.

In summary, the best agreement between the numerical and the experimental results is found for the lighter configuration cases when the amplitude of the roll motion is small ($\phi_0 = 10°$). The comparison for the 16 cases corresponding to Table 3.4 is presented in Appendix C.

In order to measure the computational efficiency of the 2D+t solution in contrast with a fully 3-D numerical solution, the 2-D impact solution is compared with 3-D results for the planing problem obtained using the same solver as part of a different but related research effort (Algarin and Tascon, 2014a). The 3-D simulations correspond to the same geometry tested by Judge and Judge (2013). The simulation domain extends one length to the front, three lengths to the back, four beams to the side, three beams to the top and six beams to the bottom. A total of approximately 3.7×10^6 polyhedral cells were used with finer cells close to the body and at least 80 cells covering half of the bottom of the wedge. As in the 2-D simulations, the problem is solved under the assumptions of flow of an inviscid and incompressible fluid with gravity neglected.

The objective of the simulations was to produce time series for the roll moment, validate the numerical results with the experimental results of Judge and Judge (2013) and produce new results for lower amplitudes and frequencies than those tested in the experiments. The results showed in general a lack of resolution of the peaks in the roll moment time series in comparison with the experimental time series. This effect could be caused by the limited number of cells used to compute the pressure distribution in 2-D cross section of the bottom of the planing hull in comparison with the 2-D solutions used in the 2D+t approach.

Table 3.5 presents the comparison for the case with $C_\Delta = 0.29$, $C_v = 2.9$, $\phi_0 = 15°$, $f = 3.0$ Hz. The 2D+t solution obtained at each time step on 20 control planes requires a total of 36 water impact solutions (2-D) in order to compute half period of the forced roll motion being simulated.

The 3-D solution in contrast requires to be run for more than one period in order for the flow to stabilize and produce periodic time series (the same requirement for a model test in a towing tank). For this particular example, the 3-D simulation ran for two periods and repeatability of the last half portion of the period was observed.

Factors	3-D	2-D
Cells (#)	$\sim 3,700,000$	$\sim 140,000$
CPU time (hr)	~ 428	~ 2.5
Simulations (#)	1	36
Total CPU time (hr)	~ 428	~ 90

Table 3.5: Comparison of computational time between 2D+t (with 20 control planes) and 3-D solutions. $C_\Delta = 0.29$, $C_v = 2.9$, $\phi_0 = 15°$, $f = 3.0$ Hz

The difference in total CPU time is approximately five times in favour of the 2D+t solution. Also, the 2-D solutions can be re-used to obtain interpolated solutions for conditions run at the same amplitude and frequency for the same value of the vertical impact velocity (W_{2D}) in the equivalent 2-D problem. This is possible due to the fact that different combinations of trim angle and forward speed can yield the same vertical impact velocity, and since the reference planes are parallel to the transom there is no change in the geometry of the wedge.

3.6 Asymmetric Steady Planing

Brown and Klosinski (Brown and Klosinski, 1994a,b) conducted an extensive series of captive model tests at the Davidson Laboratory in order to obtain fundamental hydrodynamic information about planing hulls. The objective of their efforts was to provide the scientific community with data required for the study of the dynamics of planing hulls, particularly transverse stability, yaw/roll stability, course-keeping ability, maneuvering and control. The 1:26.66 scale models correspond to notional patrol boats having a LBP of 100 feet, a beam of 20 feet and a displacement of 100 long tons. These idealized patrol boats have a pure prismatic cross section of constant deadrise and vertical sides that run from amidships to the transom. This selection of hull-form is ideal for comparison with theories that predict generalized forces which act on a maneuvering planing hull. The quantities measured in the test program included the generalized forces in all six degrees-of-freedom, and the results tabulated in different coordinate systems. Additionally, underwater photographs of the hulls were taken in each condition tested, from which the wetted lengths and wetted areas were determined.

More recently, Judge (Judge, 2013, 2014a,b) conducted a series of captive model tests at the towing tank of the United States Naval Academy (USNA) as part of an experimental program designed to investigate the transverse stability of planing hulls. A wooden planing hull model with a constant deadrise of 20 degrees was tested at different displacements and speeds, with fixed attitudes in sinkage, trim and heel. For these tests the quantities measured included lift and sway forces, along with heel moment. As in the case of Brown and Klosinski (1994a,b), underwater photographs were taken in order to obtain wetted lengths. Here the interest is to compare the SBT (2D+t) solution with the experimental results reported in Brown and Klosinski (1994a,b) and Judge (2013, 2014a,b).

In the asymmetric steady planing case, the prismatic hull is assumed to be moving in steady planing condition with constant heel (ϕ), trim (θ) and drift (ψ) angles. At time zero, the origin of the first Earth-fixed reference frame (2-D control plane) coincides with the intersection of the free surface and the keel line. The body-boundary condition in this plane corresponds exactly to that of a two dimensional heeled wedge impacting the water with horizontal and vertical velocities (V_{2D}, W_{2D}):

$$\begin{pmatrix} u \\ V_{2D} \\ W_{2D} \end{pmatrix} = \begin{pmatrix} \cos(\theta)\cos(\psi) \\ \sin(\psi) \\ \sin(\theta)\cos(\psi) \end{pmatrix} x_{t_E} \tag{3.4}$$

It is interesting to note that the solution to the asymmetric steady planing case can be computed from any 2-D control plane that has been completely crossed by the planing hull (i.e., starting at the intersection of the keel line with the free surface and ending with the crossing of the transom), since the solution on each control plane crossed in this way will be identical. Therefore, the transformation $\partial/\partial t = u\ \partial/\partial x'$ is used to relate the solution of the unsteady 2-D impact problem to the 3-D steady planing problem and compute the solution in one control plane.

With this transformation the non-dimensional impact time is related to the longitudinal coordinate (x') by Eq. (3.5).

$$\tau = \frac{\tan(\theta)}{\frac{B}{2}} x' \tag{3.5}$$

The six degrees of freedom hydrodynamic generalized forces, defined in the body-fixed coordinate system, for the three dimensional problem, are obtained by integrating the two dimensional sectional forces along the keel wetted length (SKWL).

The force and moment coefficients as defined in Brown and Klosinski (1994a,b), are given by:

$$\begin{pmatrix} F' \\ M' \end{pmatrix} = \frac{1}{\frac{1}{2}\rho\, x_{t_E}^2 B^2} \begin{pmatrix} F \\ \frac{1}{B} M \end{pmatrix} \tag{3.6}$$

Using the same non-dimensionalization, the force and moment coefficients for comparison with the experimental results take the form of Eq. (3.7) and Eq. (3.8).

$$\begin{pmatrix} Y'_{HD} \\ Z'_{HD} \\ K'_{HD} \end{pmatrix} = \frac{1}{4} \sin 2\theta \cos^2 \psi \int_0^{\tau_{\max}} \begin{pmatrix} Cf_y \\ Cf_z \\ \frac{1}{2} Cm_x \end{pmatrix} d\tau \tag{3.7}$$

$$\begin{pmatrix} M'_{HD} \\ N'_{HD} \end{pmatrix} = \frac{1}{4} \cos^2 \theta \cos^2 \psi \int_0^{\tau_{\max}} \tau \begin{pmatrix} Cf_z \\ -Cf_y \end{pmatrix} d\tau + \frac{\tau_{\max}}{2 \tan \theta} \begin{pmatrix} -Z'_{HD} \\ Y'_{HD} \end{pmatrix} \tag{3.8}$$

The slenderness assumption ($\partial/\partial x' << \partial/\partial v, \partial/\partial h$) implies slowly varying transverse sections in the longitudinal direction (Maruo, 1967; Tuck, 1975; Savander, 1997). In Savander (1997) a "slenderness angle", γ, is defined as the apex half angle formed by the intersection of the free surface and the hull. Taking into consideration the effect of the heel angle, ϕ, the slenderness angle corresponding to heeled side, γ_2 is defined by:

$$\gamma_2 = \tan^{-1} \frac{\sin \theta}{\tan(\beta_G - \phi)} \tag{3.9}$$

and the requirement for slenderness is that γ_2 is $o(1)$.

For the case of the heeled planing hull with given deadrise angle, β_G, the 2D+t solution is expected to deteriorate as the heel angle increases since on the heeled side for a given trim angle, θ, the slenderness angle, γ_2, increases with the heel angle, ϕ. The longitudinal perturbation flow velocities on the heeled side reach the same order of magnitude as the transverse perturbation flow velocities on that side violating the slenderness assumption. In view of Eq. (3.9), the limits of applicability of the 2D+t in the asymmetric case would be governed by the heeled side flow, with small trim angles being required in order to satisfy a slenderness angle as the heel is increased. The effect of drift angle, ψ, is to increase the aspect ratio of the hull with respect to the flow velocity. Therefore, the asymmetric 2D+t is expected to be applicable for small values of heel (or small drift combined with positive heel) with maximum heel angles being a function of deadrise and trim angle in order to satisfy a specified slenderness angle, γ_2. Comparisons between fully 3-D RANSE solutions and 2D+t solutions would be required in order to assess the limits of applicability of the theory by looking at the relative orders of magnitude of the perturbation flow velocities in the longitudinal and transverse directions and by comparing pressure distributions and free surface profiles; these are recommended as future work. Here, the practical range of applicability of the asymmetric 2D+t is partially addressed by looking at experimental results.

Therefore, before comparing the experimental results with the simulations by the 2D+t approach, it was decided to plot the spray root lines for the different configurations tested by Brown and Klosinski (1994a,b) with a two-fold purpose: (1) to assess the quality of the tests particularly with what refers to symmetry, and (2) to assess the viability of the approach proposed by looking for parallelism in the spray root lines when plotting them as a function of speed coefficient for a given orientation in space (ϕ, θ, ψ).

The spray root lines have been obtained with the information provided for keel wetted length, starboard and port chines wetted lengths, and starboard and port wetted beam fraction at the transom (recorded in the cases in which the spray root line crossed the transom or the flow separated before reaching the chine). It is worth mentioning that the spray root lines are not necessarily straight lines as found by Xu et al. (1998), but here are represented as such for simplicity and given the information available from the reports.

In all figures, the non-dimensional length starts from the forward perpendicular and ends at the transom; the thick dashed line corresponds to the place where the prismatic section of the hull starts. The comparison of cases tested with the same positive and negative heel angle (and without drift angle) showed in the majority of the cases spray root lines anti-symmetry (e.g., Fig. 3.16) as expected for a hull with starboard-port symmetry. Parallelism between spray root lines, as in Fig. 3.17, was found for those configurations for which the keel wetted lengths laid within the prismatic region of the hull; since in the experiments the model was free to heave, and all of them were run at the same beam loading coefficient, the keel wetted length decreases with speed. Therefore, most of these cases used for comparison correspond to the runs at the higher speed coefficients ($C_v = 3, 4$). At the bottom of each of the two figures the transformation to the time domain for the unsteady 2-D impact problem is presented, showing the collapse of the spray root lines and indicating the feasibility of the slender body approach. The spray root lines obtained from the 2D+t simulation (+ symbols) are also plotted showing in most of the cases excellent agreement with the experimental results. In these figures, the non-dimensional time starts at the intersection between the undisturbed water surface and the keel, corresponding to the origin of the 2-D reference frame. The thick dashed line is located at the maximum non-dimensional time, equivalent to the length of the prismatic section of the hull (via the SBT transformation).

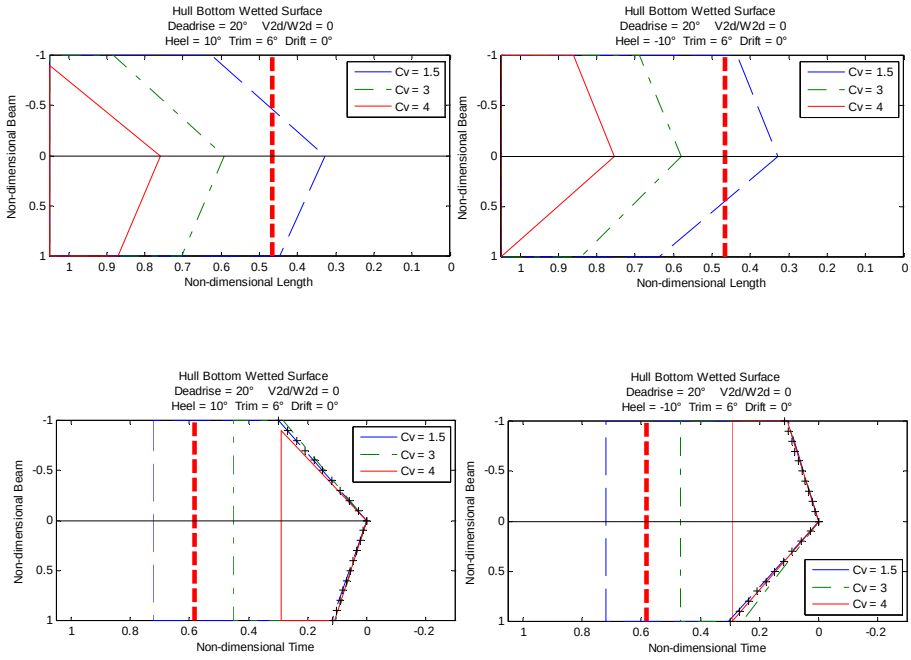

Figure 3.16: Comparison of spray root lines for anti-symmetric ($\pm\phi$) running attitudes. (+++) 2D+t. The vertical thick dashed line corresponds to the place where the prismatic section of the hull starts.

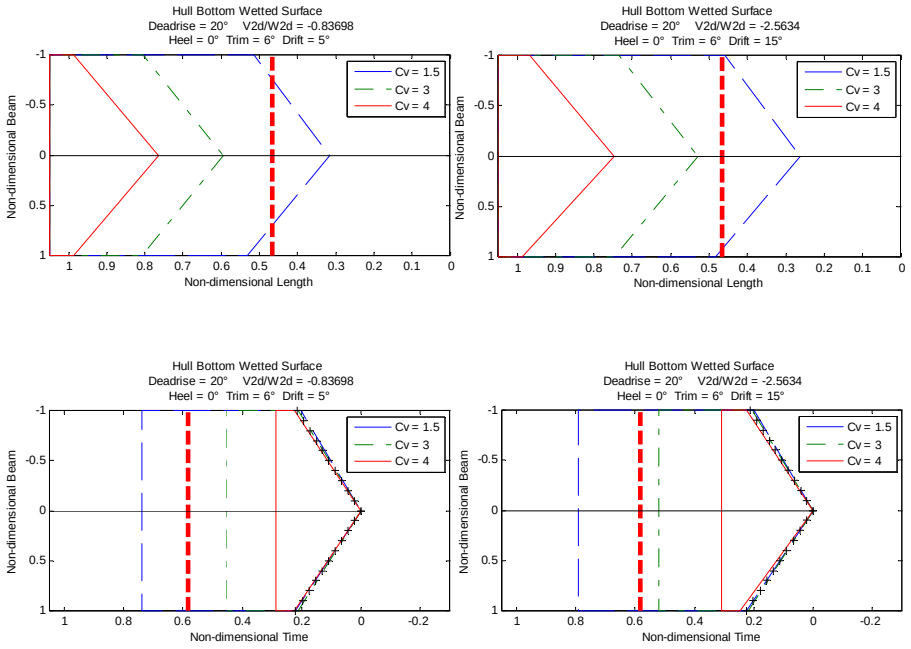

Figure 3.17: Comparison of spray root lines for different drift angles. (+++) 2D+t. The vertical thick dashed line corresponds to the place where the prismatic section of the hull starts.

Savitsky et al. (1958) commented on some of the interesting features of the spray root lines they found in their tests with a 20 degrees deadrise surface. Even though the majority of their observations agree with the results of the tests performed by Brown and Klosinski (1994a,b) on the equivalent hull ($\beta_G = 20°$), some of them do not. For instance, the wave rise at the leading edge of the tested configurations was independent of the drift angle only for the cases with no heel. Also, the spray-root angle at the leading edge of the rolled-down side was not equal to that of a wedge whose deadrise angle is equal to β_G less the roll angle, and the angle of the spray-root line relative to the keel for the rolled-up side was dependent on roll angle.

The present simulations were carried out for the cases in which at least 90% of the static keel wetted length (SKWL) was within the prismatic region in order to be able to make a fair comparison with the experimental results. These correspond to runs at high beam Froude number ($C_v = 3, 4$) and high trim angle ($\theta = 6$).

Comparisons between the experimental (symbols) and numerical (lines) results for some selected runs of the $\beta_G = 20°$ hull are presented in Fig. 3.18 for $C_v = 3$ and in Fig. 3.19 for $C_v = 4$. Sway force, roll moment and yaw moment coefficients, are plotted as a function of drift angle (ψ), using roll angle (ϕ) as a parameter. All the results are referred to a right-hand body-fixed coordinate system with origin at the intersection of the keel with the transom; the x-axis is aligned with the keel and the y-axis points toward the starboard side. The length used for the simulations correspond to the static keel wetted length reported by Brown and Klosinski (1994a,b).

The computational results show fair to good agreement with the experimental results, with the largest difference present in the cases with the largest degree of asymmetry (i.e., combinations of positive drift angle with negative heel angle). In general, the sway force and the roll moment coefficients are well predicted while the yaw moment coefficient is under-predicted.

The biggest discrepancy is found in the results corresponding to the lower beam Froude number ($C_v = 3$) where gravity is expected to be more important due to the fact that they correspond to the runs with the largest SKWL (and therefore largest transom draft).

In an attempt to account for the effect of gravity in the 2D+t results, but recognizing this as an engineering approximation, the volume below the undisturbed water surface is calculated for each configuration and used to compute the hydrostatic force. The generalized hydrostatic forces and moments were added to the 2D+t results to obtain total generalized forces and moments acting on the hull.

Comparisons between the experimental (symbols) and numerical (lines) results for the same conditions of the $\beta_G = 20°$ hull presented in Figs. 3.18 and 3.19 are presented in Fig. 3.20 for $C_v = 3$ and in Fig. 3.21 for $C_v = 4$ showing the effect of the addition of the static component.

Side by side comparisons between the experimental (symbols) and numerical (lines) results for the same runs of the $\beta_G = 20°$ hull are presented in Fig. 3.22 for $C_v = 3$ and in Fig. 3.23 for $C_v = 4$. The plots on the left, on each figure, correspond to the dynamic component, while those on the right correspond to the sum of the dynamic and static components. A better agreement is obtained with the experimental results at both beam Froude numbers.

Equivalent comparisons between the experimental (symbols) and numerical (lines) results for the $\beta_G = 30°$ hull run at $C_v = 4$ are presented in Fig. 3.24 to Fig. 3.26. The best agreement is found for the cases with combinations of small drift angle and small positive heel angles as expected from the limits of the slenderness assumption.

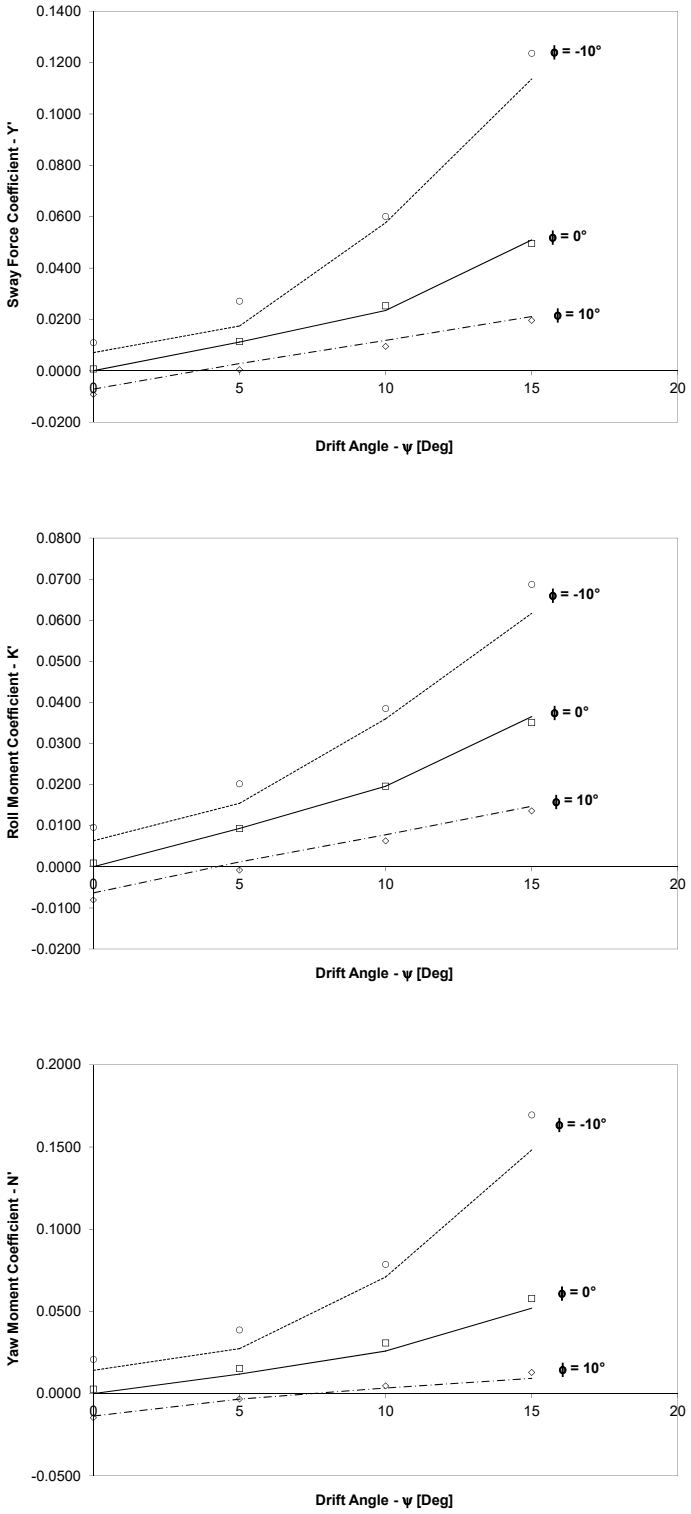

Figure 3.18: Comparisons of sway force, roll moment and yaw moment coefficients between Brown and Klosinski (1994b) experimental (symbols) and numerical (2D+t dynamic; lines) results for the $\beta_G = 20^\circ$ hull, at $\theta = 6^\circ$, $C_v = 3$.

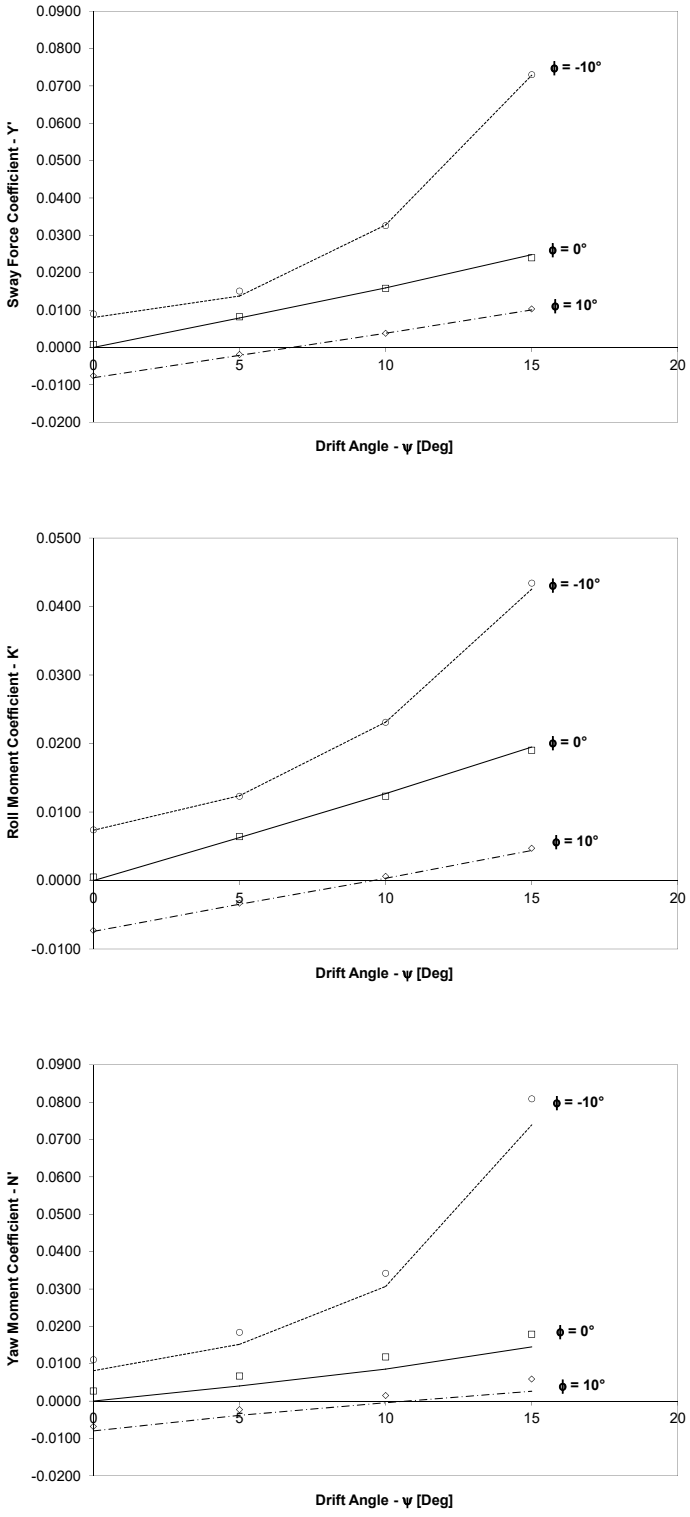

Figure 3.19: Comparisons of sway force, roll moment and yaw moment coefficients between Brown and Klosinski (1994b) experimental (symbols) and numerical (2D+t dynamic; lines) results for the $\beta_G = 20^\circ$ hull, at $\theta = 6^\circ$, $C_v = 4$.

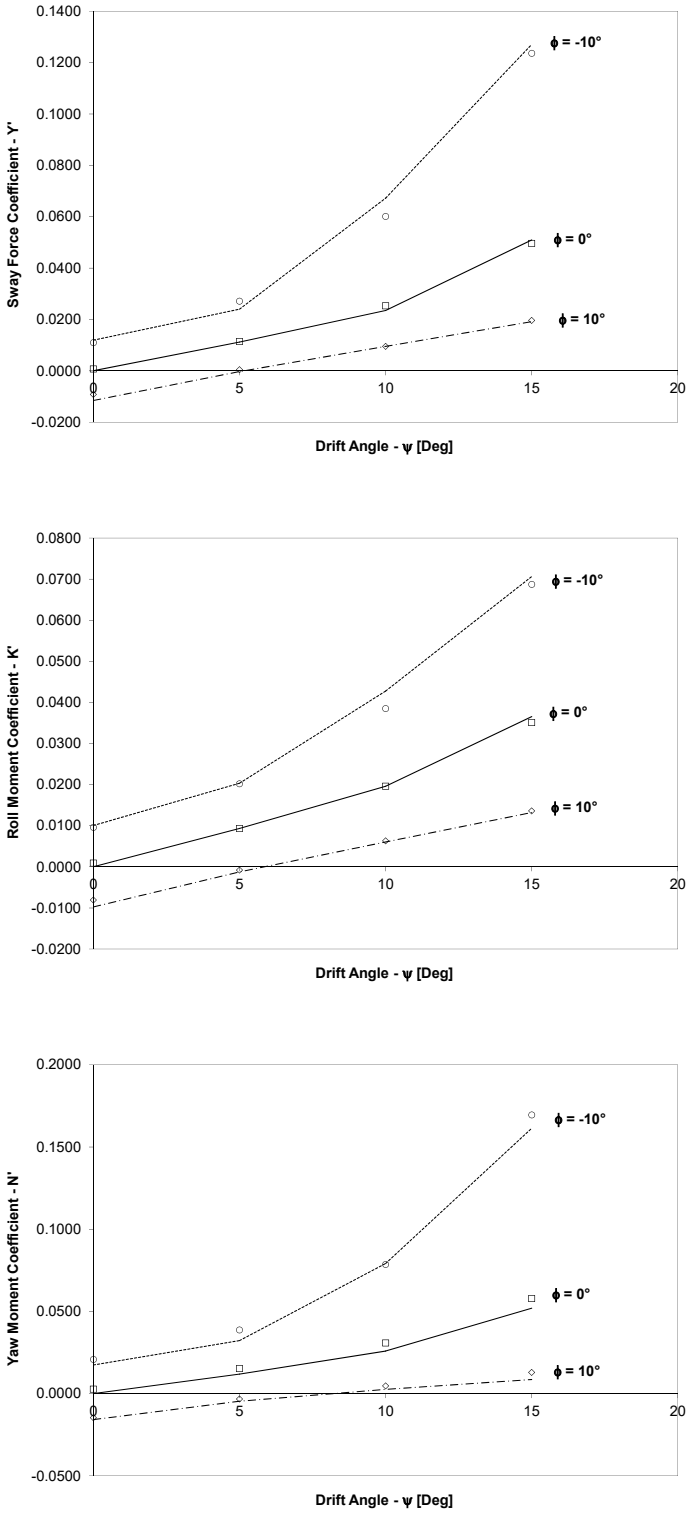

Figure 3.20: Comparisons of sway force, roll moment and yaw moment coefficients between Brown and Klosinski (1994b) experimental (symbols) and numerical (2D+t dynamic plus static; lines) results for the $\beta_G = 20^\circ$ hull, at $\theta = 6^\circ$, $C_v = 3$.

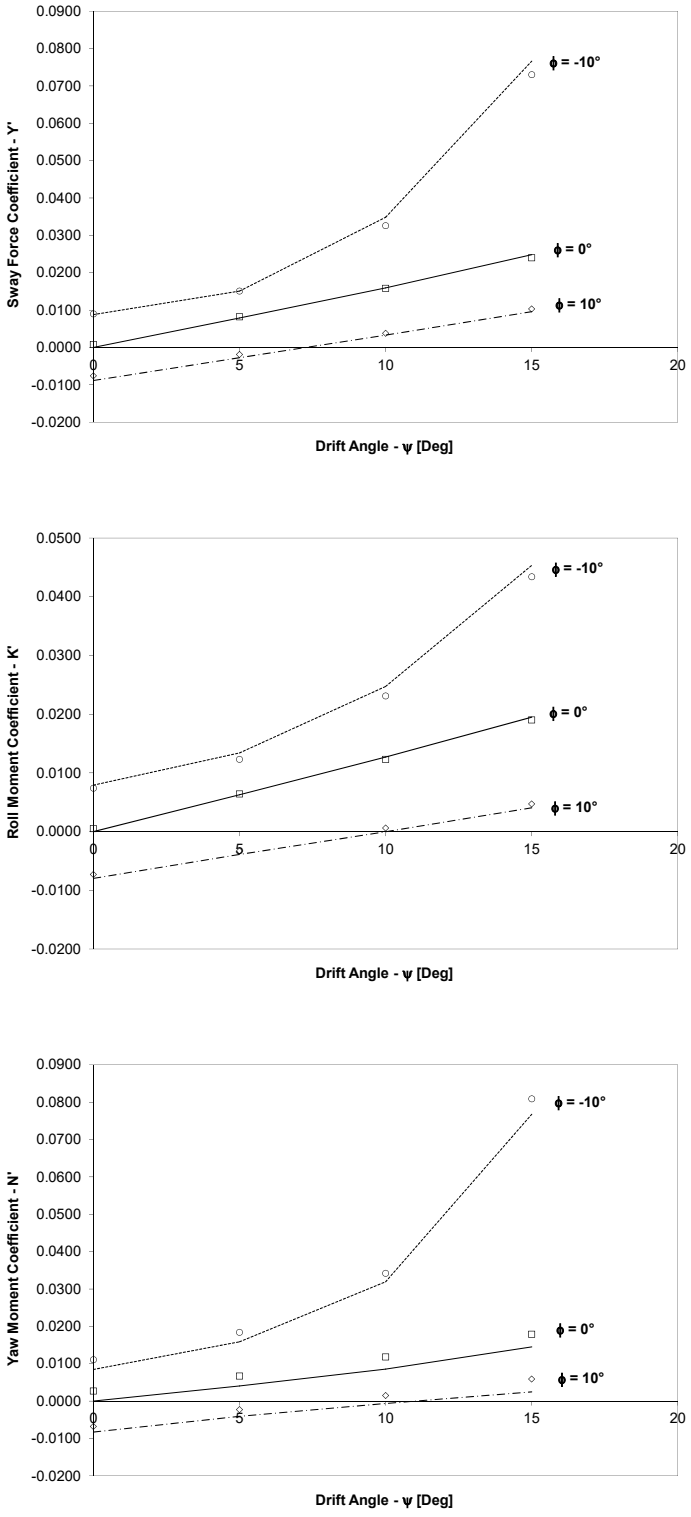

Figure 3.21: Comparisons of sway force, roll moment and yaw moment coefficients between Brown and Klosinski (1994b) experimental (symbols) and numerical (2D+t dynamic plus static; lines) results for the $\beta_G = 20^\circ$ hull, at $\theta = 6^\circ$, $C_v = 4$.

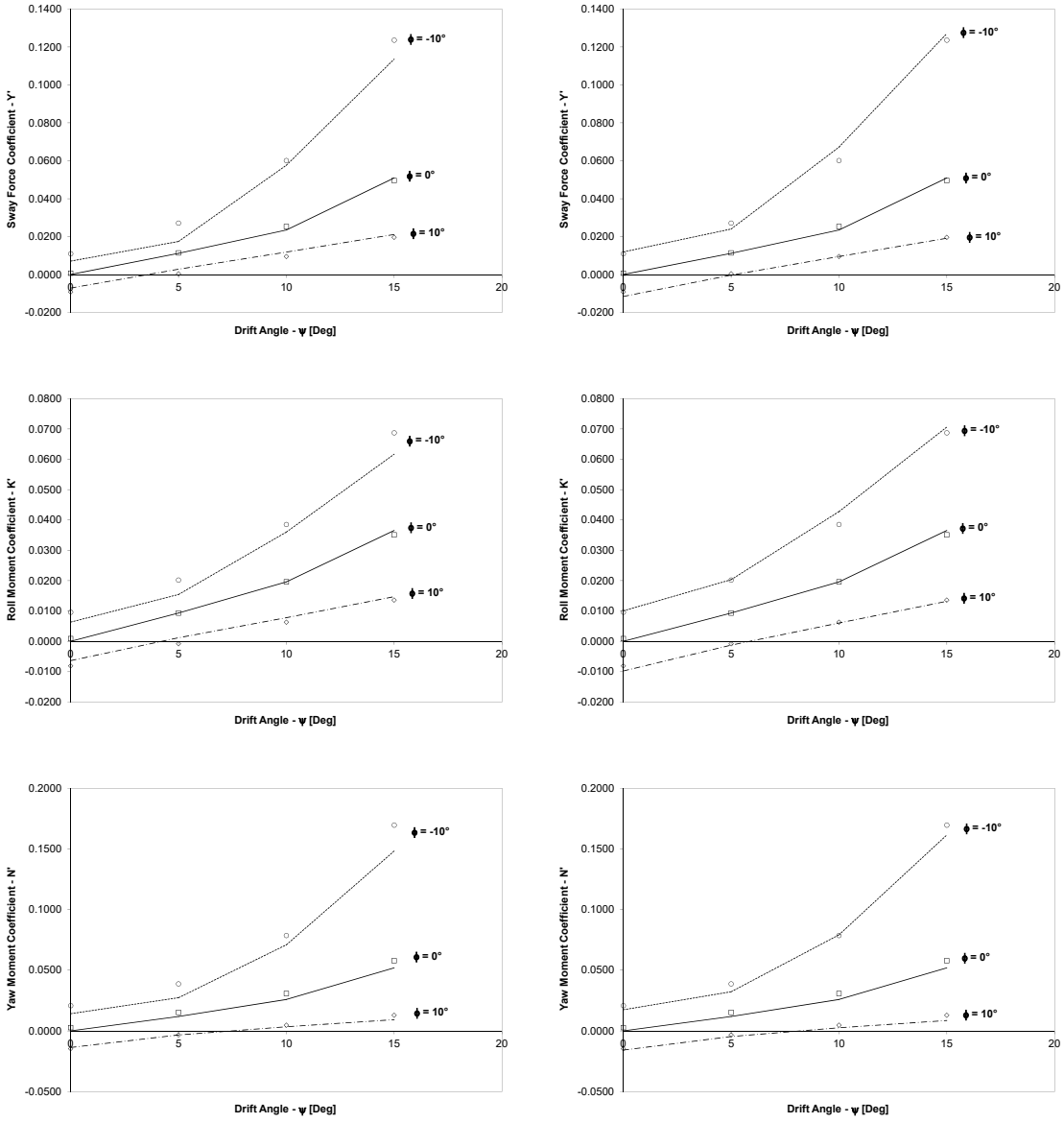

Figure 3.22: Comparisons of sway force, roll moment and yaw moment coefficients between Brown and Klosinski (1994b) experimental (symbols) and numerical (lines) results for the $\beta_G = 20°$ hull, at $\theta = 6°$, $C_v = 3$, without (left) and with (right) hydrostatic component.

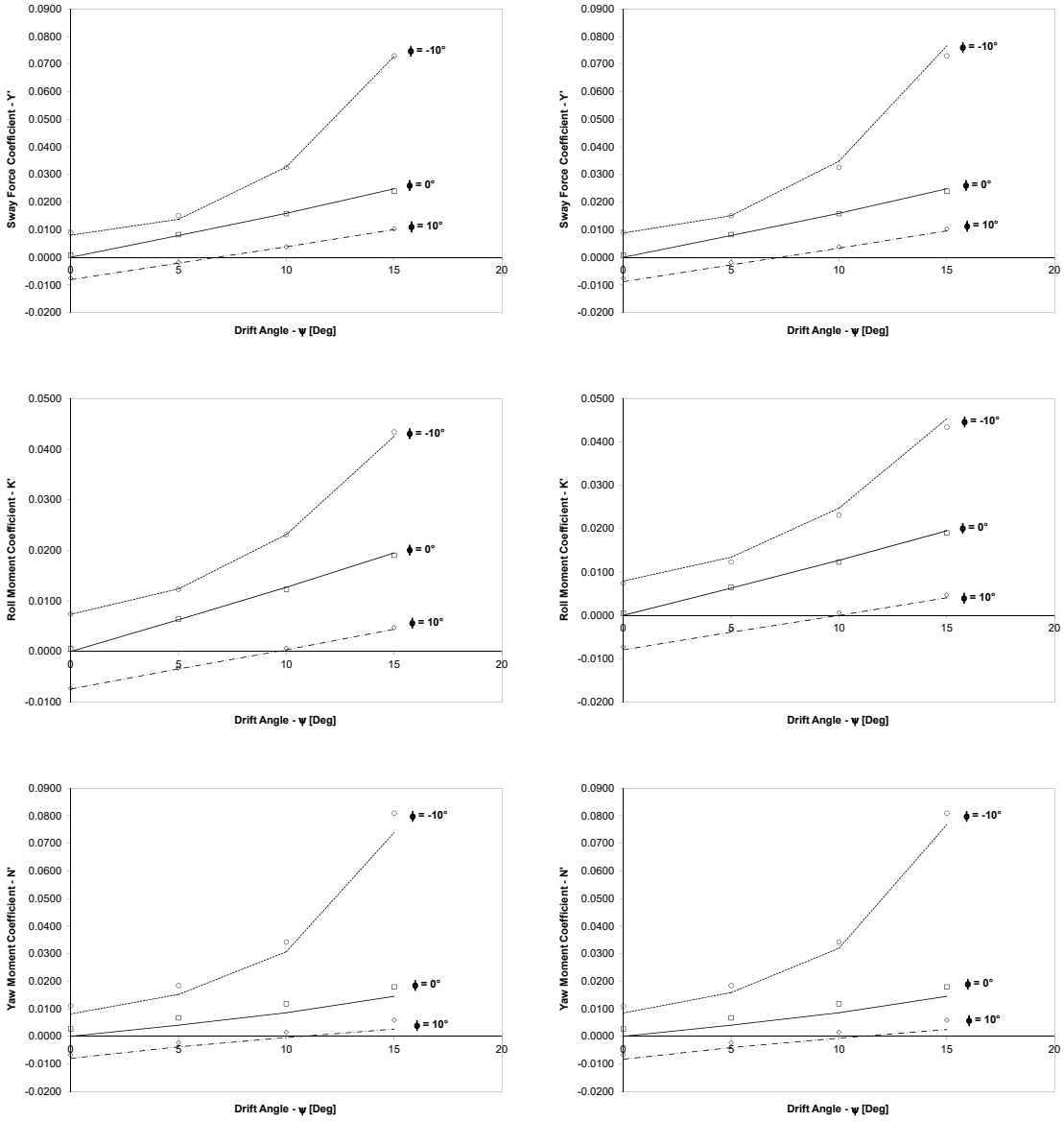

Figure 3.23: Comparisons of sway force, roll moment and yaw moment coefficients between Brown and Klosinski (1994b) experimental (symbols) and numerical (lines) results for the $\beta_G = 20°$ hull, at $\theta = 6°$, $C_v = 4$, without (left) and with (right) hydrostatic component.

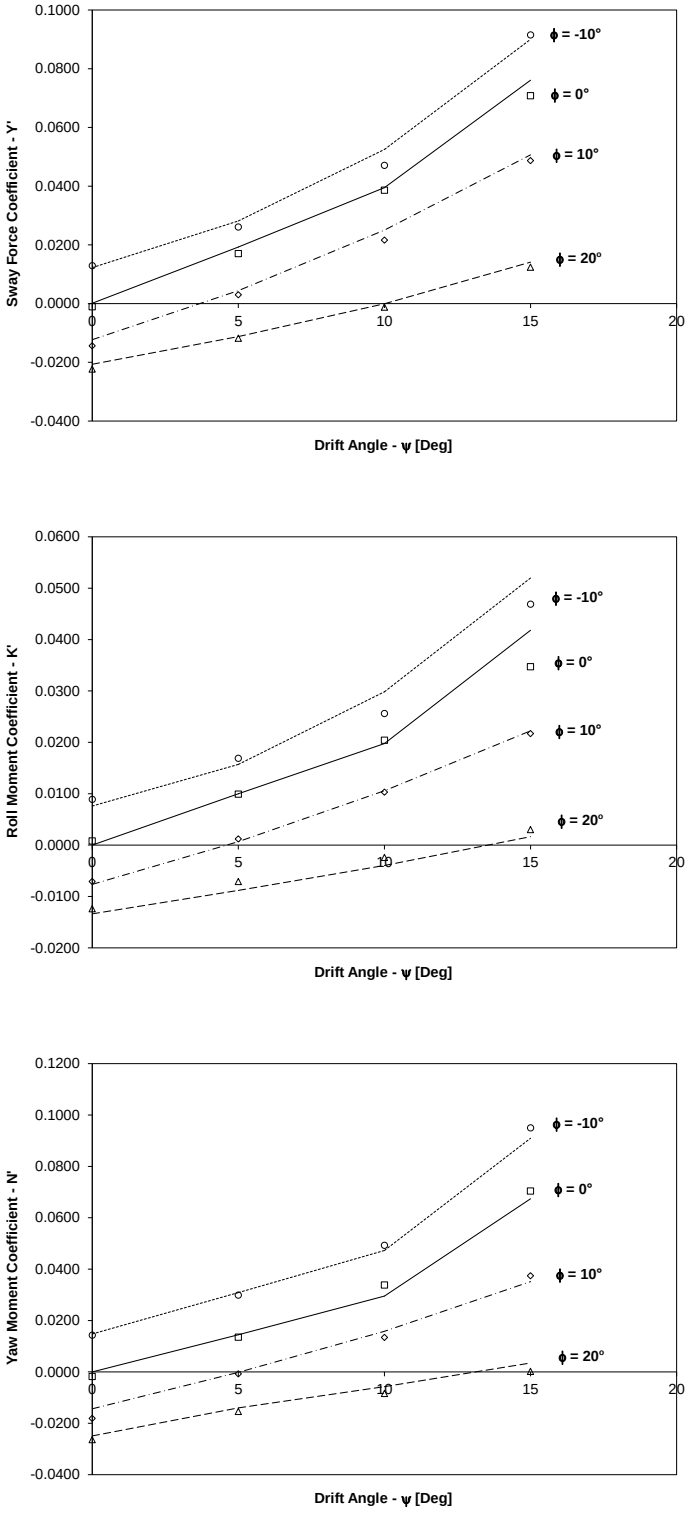

Figure 3.24: Comparisons of sway force, roll moment and yaw moment coefficients between Brown and Klosinski (1994a) experimental (symbols) and numerical (2D+t dynamic; lines) results for the $\beta_G = 30^\circ$ hull, at $\theta = 6^\circ$, $C_v = 4$.

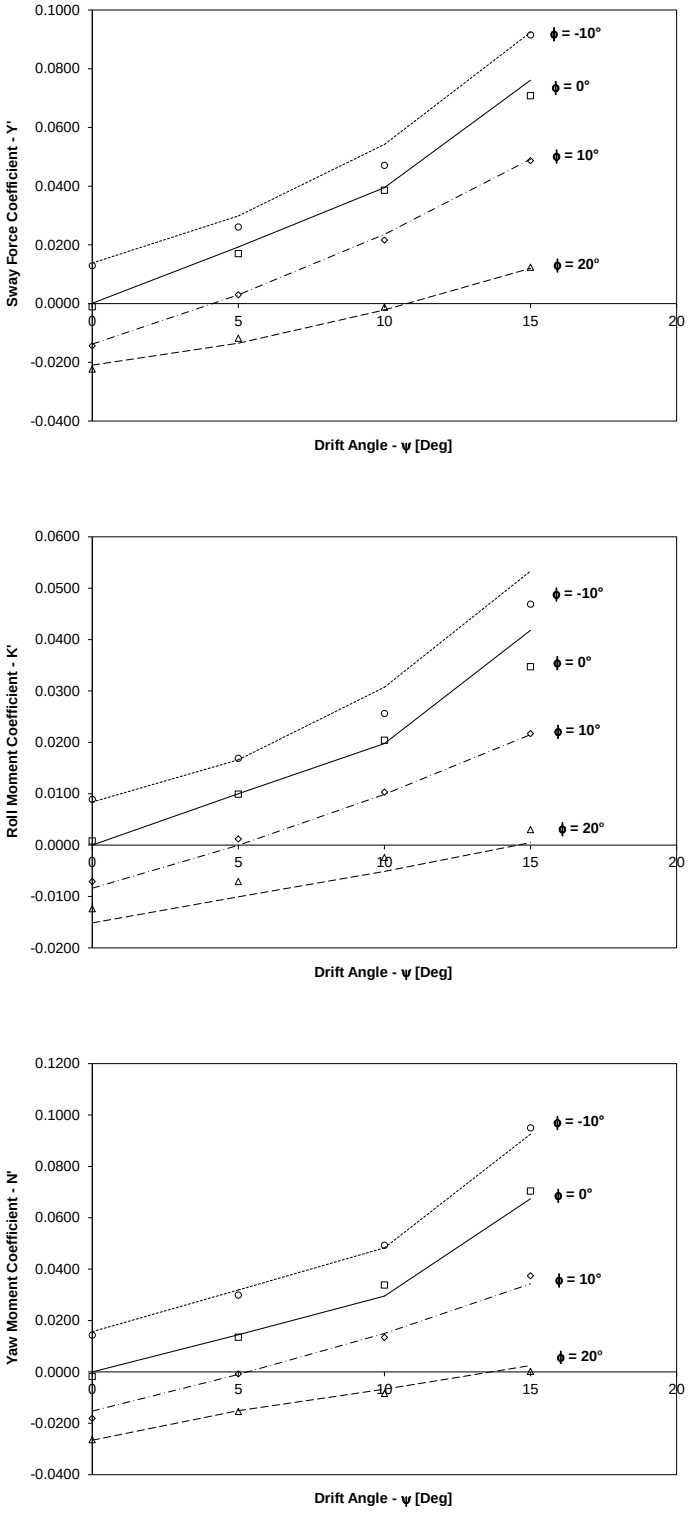

Figure 3.25: Comparisons of sway force, roll moment and yaw moment coefficients between Brown and Klosinski (1994a) experimental (symbols) and numerical (2D+t dynamic plus static; lines) results for the $\beta_G = 30^\circ$ hull, at $\theta = 6^\circ$, $C_v = 4$.

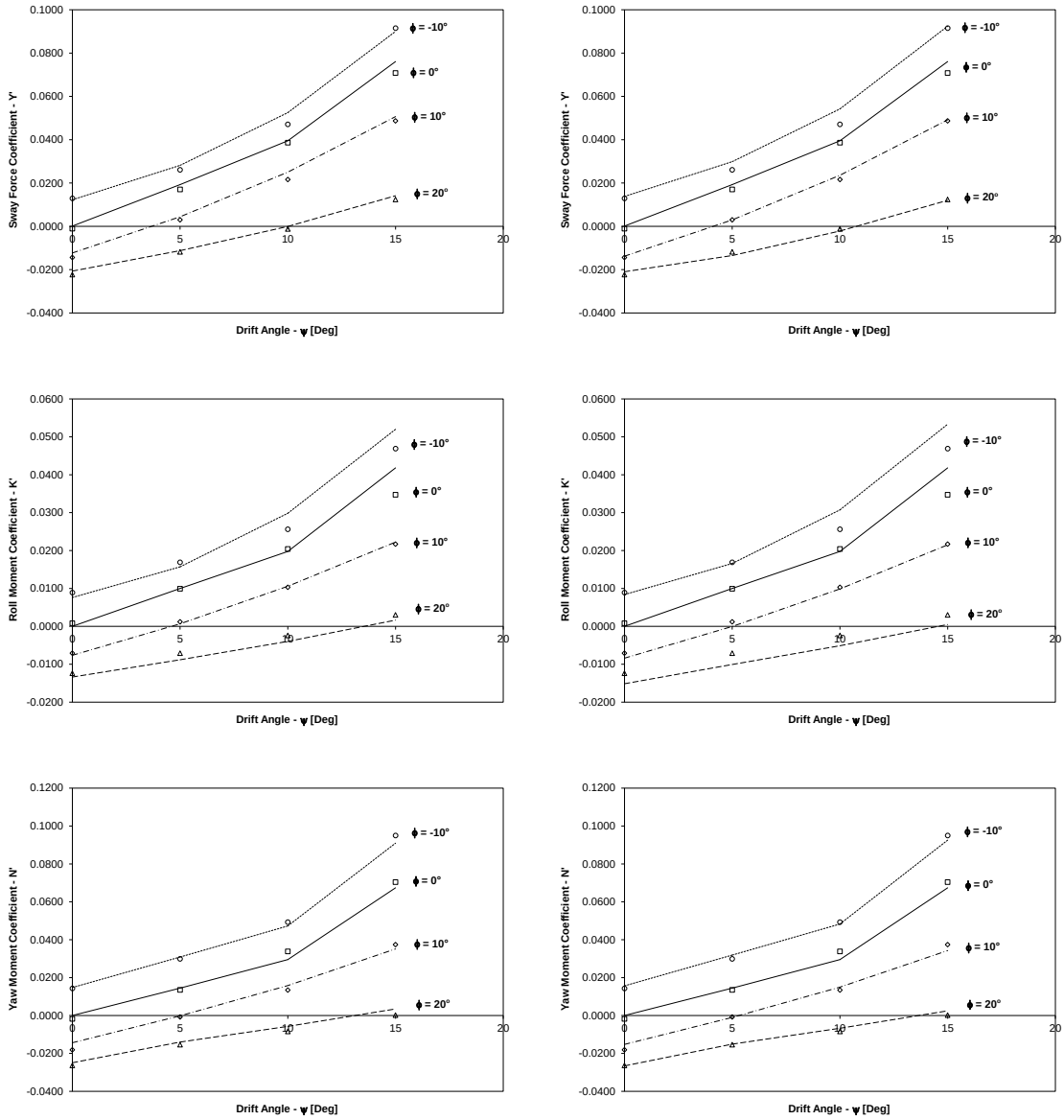

Figure 3.26: Comparisons of sway force, roll moment and yaw moment coefficients between Brown and Klosinski (1994a) experimental (symbols) and numerical (lines) results for the $\beta_G = 30°$ hull, at $\theta = 6°$, $C_v = 4$, without (left) and with (right) hydrostatic component.

Two particular cases are worth to be highlighted here and they correspond to the runs of the $\beta_G = 30^\circ$ hull being towed at $C_v = 4$, at $\psi = 15^\circ$, and $\phi = 0^\circ, -10^\circ$. In these two cases, given the combination of heel angle and horizontal to vertical velocity ratio in the 2-D impact problem, separation of the flow at the keel without re-attachment and side wetting are obtained, giving rise to an over-prediction in vertical force that translates into an over-prediction of the roll moment coefficient. Brown and Klosinski (1994a,b) reported that for the experiments, spray strips made of brass shim stock were fitted at the chines of the model (extending vertically downward from the model chine by 0.8 mm) in order to ensure clean separation of water from the chine; however, this feature was not modelled in the geometry used for the CFD simulations.

Brown and Klosinski (1994a,b) also stated that for some of the runs using the Rotary Arm, particularly those in which the model is yawed out of the turn, *"the flow over the port side separated all the way along the keel, and substantial air ingestion and aeration is present"*. It appears though that this behaviour was not observed in the towing tank straight line runs, as can be confirmed by the report of the keel and chine wetted lengths. Three dimensional effects, particularly important in the chine unwetted region, could delay the separation from the keel or could cause reattachment of the flow and explain the afore mentioned disagreement with the experimental results.

The numerical and experimental results are compared as matched pairs and their agreement is tested using a paired t-test. Values of the probability above 0.05 indicate that the null hypothesis (there is no difference between the means of the numerical and the experimental results at the 0.05 significance level) should be accepted. The statistics of the comparison confirm the agreement between the numerical and the experimental results for the sway force, and roll moment coefficients. In the average, the yaw moment coefficient is slightly under-predicted.

At the lower speed ($C_v = 3$), the heave force and the pitch moment coefficients are under-predicted while the opposite is true at the higher speed ($C_v = 4$). In Table 3.6 the statistics of the comparison between the numerical results, obtained from the application of the SBT approach (dynamic component), and the experimental results, are presented for the lower speed runs.

In Table 3.7 the statistics of the comparison between the numerical results, obtained from the application of the SBT approach (dynamic component), and the experimental results, are presented for the higher speed runs.

Statistics	Y'	Z'	K'	M'	N'
Mean difference	0.00089	0.00602	0.00145	-0.02600	-0.00180
Std. Error	0.00126	0.00295	0.00185	0.00239	0.00199
t-Ratio	0.70573	2.04332	0.78430	-10.9140	-0.88371
Prob. $> \|t\|$	0.48940	0.05320	0.44310	<0.0001	0.38850
Correlation	0.98784	0.85541	0.91084	0.81560	0.99169

Table 3.6: Statistics of paired comparisons between numerical (dynamic) and experimental results for Cv = 3.

Statistics	Y'	Z'	K'	M'	N'
Mean difference	0.00073	-0.01380	0.00016	-0.00170	-0.00140
Std. Error	0.00034	0.00263	0.00037	0.00277	0.00050
t-Ratio	2.15962	-5.24630	0.44910	-0.60795	-2.89284
Prob. $> \|t\|$	0.03950	<0.0001	0.65680	0.54770	0.00730
Correlation	0.99786	-0.00830	0.99526	0.72113	0.99681

Table 3.7: Statistics of paired comparisons between numerical (dynamic) and experimental results for Cv = 4.

When the hydrostatic force is artificially accounted for, the heave force coefficient is over-predicted; the pitch moment coefficient is under-predicted at the lower speed, but it corresponds to the observed value at the higher speed.

The statistics for the lower speed runs with the numerical results including the hydrostatic force component are presented in Table 3.8, and those corresponding to the higher speed runs are presented in Table 3.9.

Statistics	Y'	Z'	K'	M'	N'
Mean difference	-0.00080	-0.02220	0.00124	-0.00770	-0.00260
Std. Error	0.00082	0.00081	0.00140	0.00139	0.00086
t-Ratio	-0.95974	-27.2615	0.88648	-5.53626	-2.95744
Prob. $> \|t\|$	0.34990	<0.0001	0.38700	<0.0001	0.00840
Correlation	0.99764	0.86997	0.94856	0.97640	0.99732

Table 3.8: Statistics of paired comparisons between numerical (total) and experimental results for Cv = 3.

Statistics	Y'	Z'	K'	M'	N'
Mean difference	0.00074	-0.02040	0.00017	0.00170	-0.00110
Std. Error	0.00039	0.00265	0.00045	0.00294	0.00053
t-Ratio	1.91755	-7.69777	0.37013	0.57632	-2.10357
Prob. $> \|t\|$	0.06540	<0.0001	0.71410	0.56860	0.04450
Correlation	0.99826	-0.18070	0.99643	0.76390	0.99572

Table 3.9: Statistics of paired comparisons between numerical (total) and experimental results for Cv = 4.

Sun and Faltinsen (2007) and Iafrati and Broglia (2008) found similar discrepancies for the heave force and the pitch moment coefficient, for the symmetric steady planing case analyzed via 2D+t theory. As mentioned in the previous section, they are believed to be caused by three dimensional effects, particularly important in the chine un-wetted and in the transom stern regions, which cannot be modeled by the 2D+t theory. In the next section, a near-transom correction (NTC) is developed in order to account for the separation of the flow at the transom.

3.7 Near-transom Correction

The SBT approach is unable to predict the flow separation at the transom due to the independence of downstream conditions in the solution as already explained. Therefore, the solutions obtained by this method need to be corrected in some way in order to account for this phenomenon, which is believed to be the most important of those related with the flow three dimensionality as reported by Lai (1994). Several corrections have been proposed to the dynamic and the static component of the hydrodynamic force; some examples follow.

Martin (1978) references the work of Pabst (1931) and Shuford (1958) in the definition of a correction factor to account for the three dimensionality of the flow. The correction is based on the value of the mean wetted length (λ) and suggests that three dimensional effects are very important for small λ. Martin (1978) adopted Shuford's correction in his formulae and applied it to the hydrodynamic component of both the lift force and the trim moment. Lewandowski (1997) references the work of Brown (1971) where a static force reduction factor (i.e., a correction to the hydrostatic component) is used, but suggests that this expression underestimates the lift at lower speeds ($C_v < 2.5$). In order to account for this, Lewandowski (1997) developed a side-wetting-correction-factor. Falstinsen (2005) also concentrated on the hydrostatic component and suggested a reduction in the keel wetted length for the computation of the static lift. The reduction value of half beam is based on comparisons between his 2D+t solution and Savitsky's formulae for constant deadrise planing hullls. Garme (2005) proposed a correction over the sectional force distribution based on a reduction function that is zero at the transom and approaches one at some reduction length afore. He concludes that simulations based on 2-D high frequency added-mass coefficients together with near transom lift corrections perform well at $C_v > 2$. Garme (2005) also observed that the reduction length is dependent on the formulation used

for the 2-D high frequency added-mass. Even though he uses a single value of correction length through his computations he acknowledges that this is a compromise solution since no single value fits all the results when comparing numerical and experimental solutions. More recently, Morabito (2014) proposed a correction function to the longitudinal pressure distribution fitted to experimental data found in the open literature. Morabito (2014) noticed that the pressures start to drop significantly at approximately half beam forward of the transom (the same distance used in Faltinsen's correction to the hydrostatic component) and that forward of that distance the pressure distribution appears almost unaffected by the flow separation of the transom. Therefore, Morabito (2014) proposes a reduction function in the same spirit of that proposed by Garme (2005) but to be applied to the longitudinal pressure distribution. Even though the regression variables in Morabito's formula were obtained from high speed planing experiments almost free from gravity effects, he applies the same reduction function to both the static and the dynamic components of the hydrodynamic pressure distribution.

In order to develop a correction function for the 2D+t results presented here, the 2-D impact solution is compared with 3-D results for the planing problem obtained using the same solver as part of a different but related research effort (Algarin and Tascon, 2014b). The 3-D simulations correspond to the case of a fully prismatic hull with $\beta_G = 20°$. The simulation domain extends one length to the front, three lengths to the back, four beams to the side, three beams to the top and six beams to the bottom; a symmetry plane is used since there is port-starboard symmetry. A total of approximately 2×10^6 polyhedral cells were used with finer cells close to the body and at least 80 cells covering half of the bottom of the wedge. As in the 2-D simulations, the problem is solved under the assumptions of flow of an inviscid and incompressible fluid with gravity neglected.

The objective of the simulations was to observe the change in the longitudinal force distribution as the trim and the mean wetted length changes. All the cases were run at a beam Froude number of $C_v = 4$ and pressure probes running parallel to the transom were located along the keel wetted length. From these probes the sectional force was obtained by integration of the pressure distribution.

The 3-D steady planing problem is transformed into the 2-D impact problem using Eq. (3.5), the vertical impact velocity is computed with Eq. (3.4) and the vertical force coefficient Cf_v with Eq. (3.2). In Fig. 3.27 the comparison for the cases with trim angle $\theta = 3.5°$ and $\theta = 6.0°$ is presented for the four different approximate values of mean wetted length simulated (i.e., $\lambda \sim 1, 2, 3, 4$).

Here the agreement between the 3-D and the 2-D results is improved by correcting the 3-D results in such a way that the position where the water reaches the chine is the same in all cases. This corresponds with the observation of Iafrati and Broglia (2008) in the sense that interpreting the water rise up in front of the 3-D hull as an initial submergence in the 2-D impact problem improves the agreement between 2D+t and 3-D results.

It is also interesting to notice that the force distribution in the 3-D results corresponding to the smaller trim angle are closer to the peak in the 2-D solution. This is an indication that 3-D effects at the transition from chines-dry to chines-wet grow in importance as the trim angle increases. This result is expected since at high trim angles the slenderness assumption is violated.

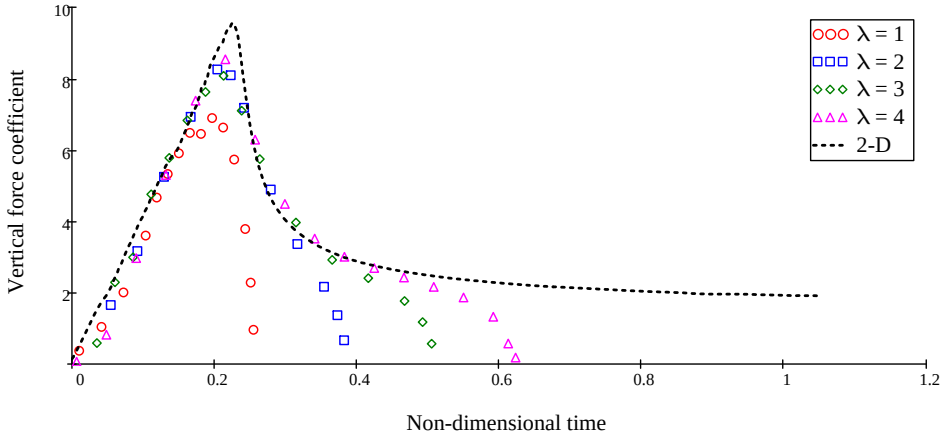

(a) $\theta = 3.5°$

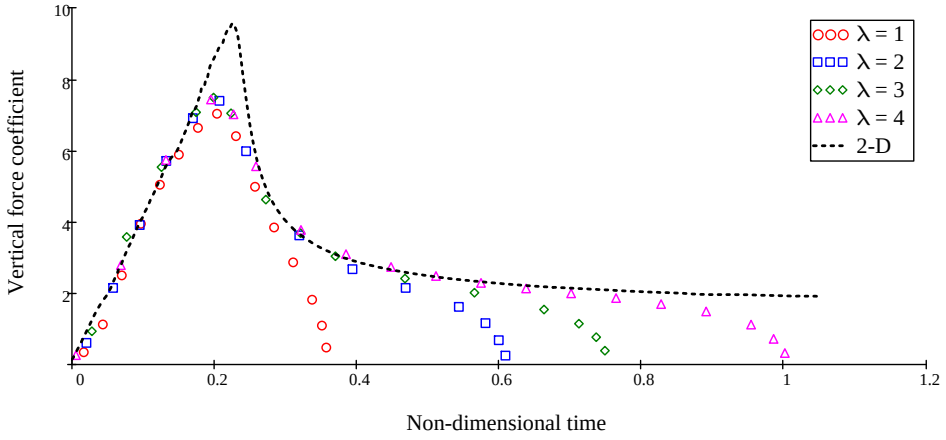

(b) $\theta = 6.0°$

Figure 3.27: Vertical force coefficient as a function of non-dimensional time for a prismatic hull with $\beta_G = 20°$. 2-D solution (dotted line), 3-D solution (symbols)

Looking at Fig. 3.27 it is observed that the error in computing the lift force from the 2D+t solution increases with a decrease in the maximum non-dimensional impact time and therefore with a decrease in mean wetted length, which coincides with the observations of Pabst (1931) and Shuford (1958) that 3-D effects are more important for lower values of λ. In order to account for this change in behavior an equation of the following form is proposed:

$$f_{\mathrm{red}}(\tau) = \sqrt{\frac{(\tau_{\max} - \tau)^{1.5}}{b(a,d) + (\tau_{\max} - \tau)^{1.5}}} \qquad \text{where} \qquad b(a,d) = a\sqrt{\frac{{\tau_{\mathrm{ave}}}^{d}}{1 + {\tau_{\mathrm{ave}}}^{d}}} \quad (3.10)$$

where τ_{ave} is a mean non-dimensional impact time defined in the same way as the mean wetted length λ in the 3-D planing problem; more precisely, for a fully prismatic hull $\tau_{\mathrm{ave}} = 2\,\lambda\tan(\theta)$ and $\tau_{\mathrm{ave}} = \tau_{\max} - 0.5\,\tau_{\mathrm{peak}}$ where τ_{peak} is the value of τ where the vertical force coefficient is maximum; for a wedge with $\beta = 20°$ and no heel this value is $\tau_{\mathrm{peak}} = 0.226$. In the chines-dry case the mean non-dimensional impact time reduces to $\tau_{\mathrm{ave}} = 0.5\,\tau_{\max}$.

In order to find the unknown regression coefficients (a, d) in Eq. (3.10) the process is started by finding the value of b that minimizes the squared error between the 2-D solution and the 3-D solution in the aft region for each of the eight cases tested. Then, the vector of b values obtained to the non-linear function $b(a, d)$ is fitted using an optimized version of the Levenberg-Marquardt method implemented in Mathcad®. Following this procedure the values for $a = 0.041$ and $d = 2.070$ are obtained with a correlation coefficient of $R^2 = 0.929$. A visual result of the fitting is presented in Fig. 3.28 and the result of the application of the correction to each of the cases simulated is presented in Fig. 3.29 and Fig. 3.30.

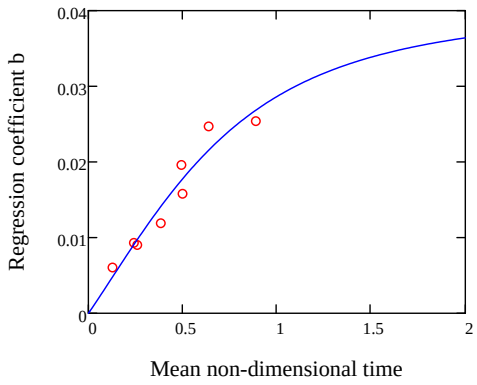

Figure 3.28: Fitting of regression coefficient b in Eq. (3.10)

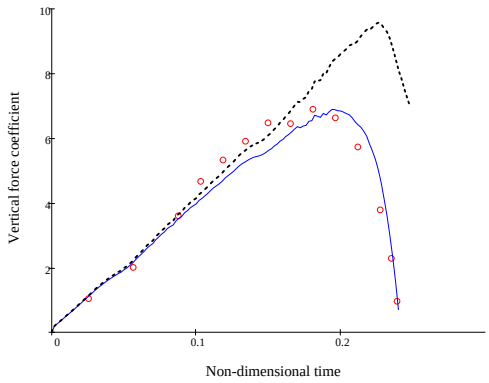

(a) $\theta = 3.5°$ $\lambda \sim 1$

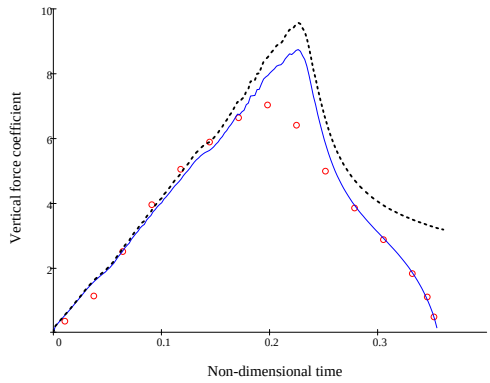

(b) $\theta = 6.0°$ $\lambda \sim 1$

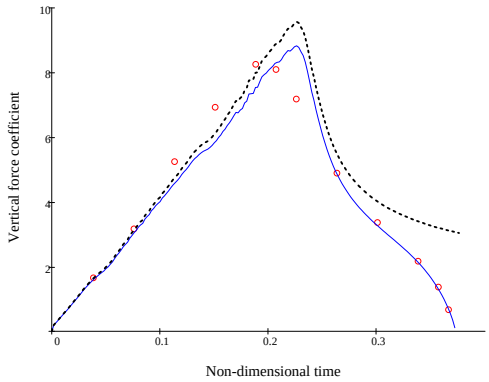

(c) $\theta = 3.5°$ $\lambda \sim 2$

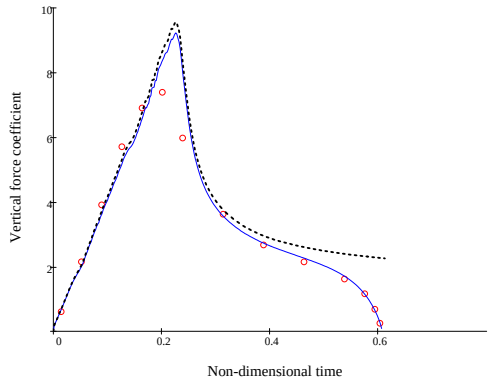

(d) $\theta = 6.0°$ $\lambda \sim 2$

Figure 3.29: Near-transom correction applied to the 2-D CFD solution compared with the transformation of the 3-D CFD solution for a prismatic hull with $\beta_G = 20°$, $\lambda \sim 1, 2$. 2-D solution (dotted line), 2-D solution with correction (solid line), 3-D solution (symbols)

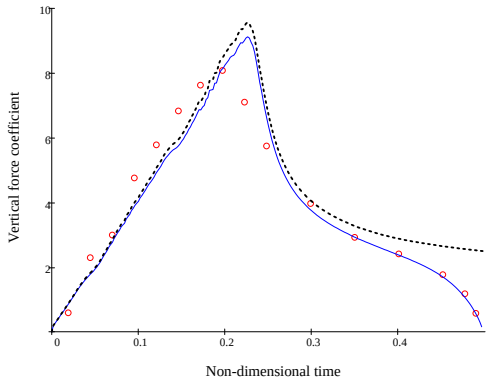

(a) $\theta = 3.5°$ $\lambda \sim 3$

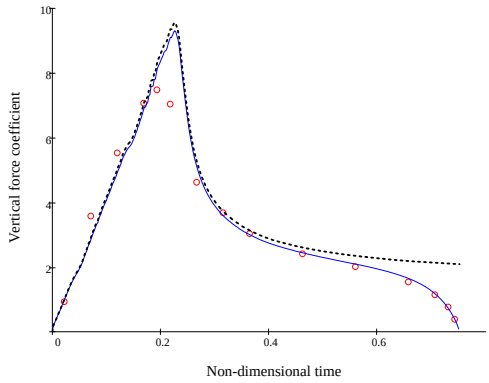

(b) $\theta = 6.0°$ $\lambda \sim 3$

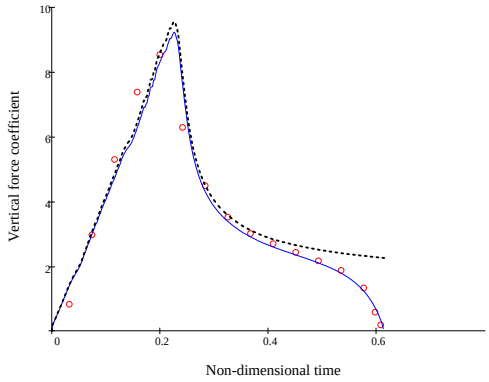

(c) $\theta = 3.5°$ $\lambda \sim 4$

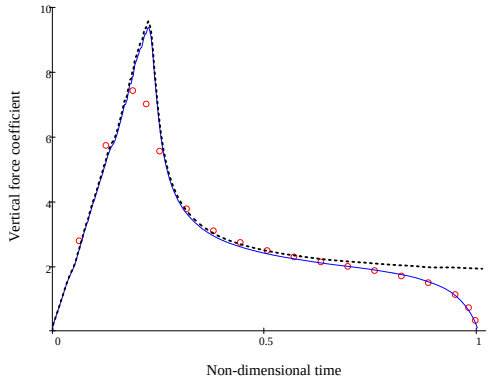

(d) $\theta = 6.0°$ $\lambda \sim 4$

Figure 3.30: Near-transom correction applied to the 2-D CFD solution compared with the transformation of the 3-D CFD solution for a prismatic hull with $\beta_G = 20°$, $\lambda \sim 3, 4$. 2-D solution (dotted line), 2-D solution with correction (solid line), 3-D solution (symbols)

The behavior of the near-transom correction for small values of the mean wetted length is tested by looking at experimental cases in chines-dry condition in Brown and Klosinski (1994b) and Judge (2014a). The value of b that minimizes the squared error between the experimental and the numerical lift results is computed from these experiments. These values are plotted in Fig. 3.31 together with the numerical values used to regress the coefficients in Eq. (3.10). The fit is still good, the results are distributed on both sides of the regression line, the correlation coefficient decreases to $R^2 = 0.856$ but the residuals do not show bias.

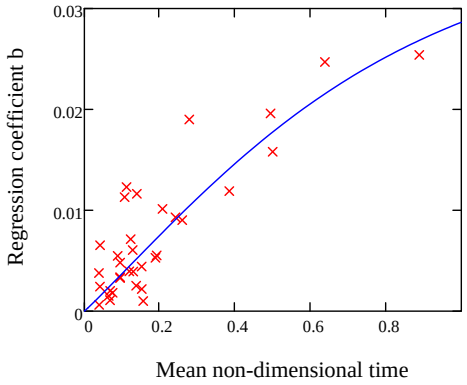

Figure 3.31: Fitting of regression coefficient b in Eq. (3.10) compared with numerical and experimental results in the small λ region

In the interest of understanding the dependence of the correction on the deadrise angle, results obtained on a fully prismatic hull with $\beta_G = 10°$, as reported in Algarin and Tascon (2014b) are used for comparison and the procedure applied to the hull with $\beta_G = 20°$ is repeated. The 3-D steady planing problem is transformed into the 2-D impact problem using Eq. (3.5), the vertical impact velocity is computed with Eq. (3.4) and the vertical force coefficient Cf_v with Eq. (3.2). In Fig. 3.32 the comparison for the cases with trim angle $\theta = 6.0°$ is presented for the four different approximate values of mean wetted length simulated (i.e., $\lambda \sim 1, 2, 3, 4$).

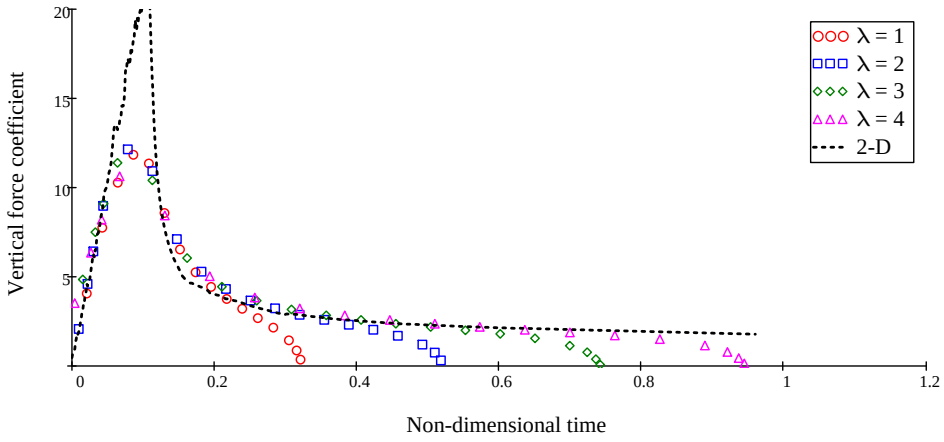

Figure 3.32: Vertical force coefficient as a function of non-dimensional time for a prismatic hull with $\beta_G = 10°$. 2-D solution (dotted line), 3-D solution (symbols)

A visual result of the application of the correction to each of the cases simulated is presented in Fig. 3.33. For these cases with $\beta_G = 10°$ the value of $\tau_{\text{peak}} = 0.105$. The agreement observed suggests that the correction is independent of deadrise angle. This coincides with the corrections proposed by Pabst (1931) and Shuford (1958) which depend only on mean wetted length (λ).

For additional validation, the 2D+t solution is compared with the experimental results of Judge (2014a). These experiments correspond to the lighter configuration ($C_\Delta = 0.15$) tested at two speeds ($C_v = 3.6, 4.3$), five roll angles ($\phi = 0°, 5°, 10°, 15°, 20°$) and five sinkage positions with a maximum perturbation equivalent to half the nominal draft ($\zeta_3 = \pm 0.5\, T_D$). The comparisons are presented for the lift force non-dimensionalized with the weight of the model and for the roll moment non-dimensionalized with the product of the weight and the beam of the model.

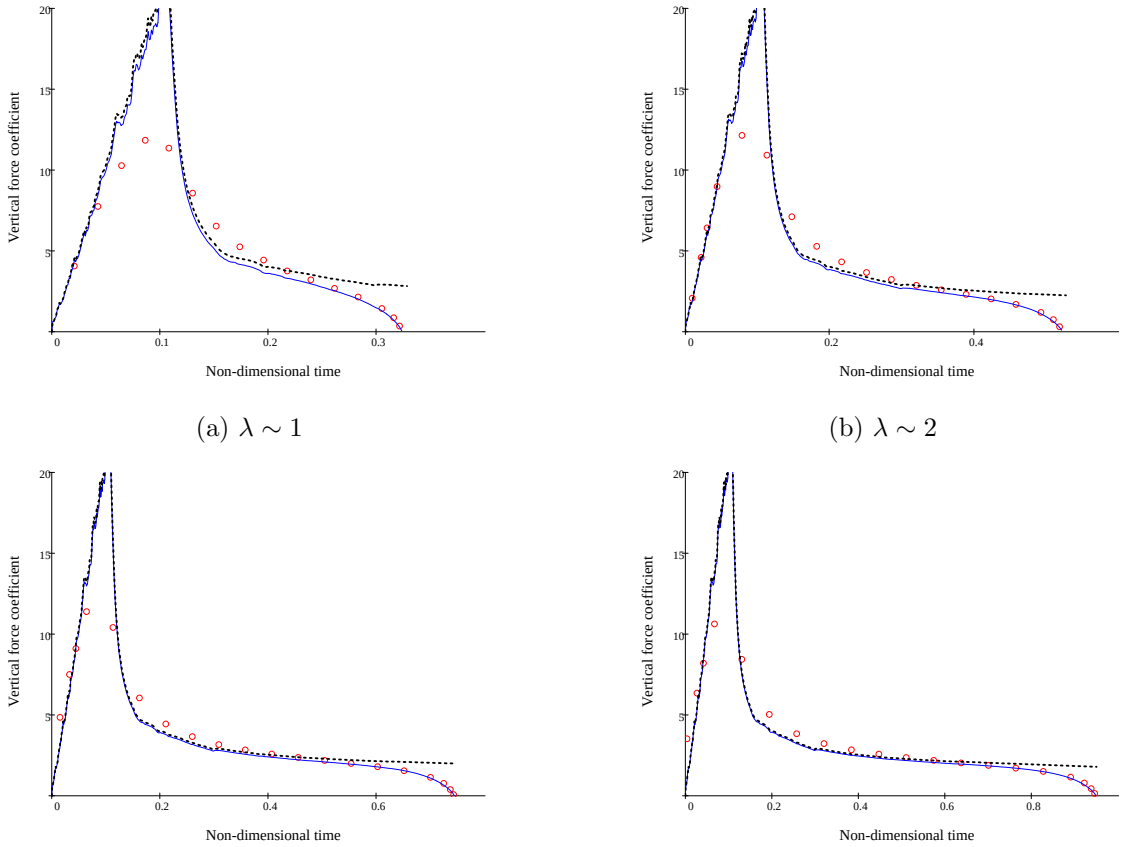

(a) $\lambda \sim 1$

(b) $\lambda \sim 2$

(c) $\lambda \sim 3$

(d) $\lambda \sim 4$

Figure 3.33: Near-transom correction applied to the 2-D CFD solution compared with the transformation of the 3-D CFD solution for a prismatic hull with $\beta_G = 10°$, $\theta = 6.0°$. 2-D solution (dotted line), 2-D solution with correction (solid line), 3-D solution (symbols)

The non-dimensional keel wetted length (λ_{k0}) reported for the nominal condition ($\phi = 0$, $\zeta_3 = 0$) is used as a reference for the numerical computation. The change in the non-dimensional keel wetted length (λ_k) is computed as in Troesch (1992) by assuming that the free-surface acts as a stationary plane:

$$\lambda_k = L_{cg} + \frac{V_{cg}\cos\phi}{\tan\theta_E} - \frac{Z_{wl} + \zeta_3}{\sin\theta_E} \tag{3.11}$$

where

$$Z_{wl} = (L_{cg} - \lambda_{k0})\sin\theta_E + V_{cg}\cos\theta_E \tag{3.12}$$

In Eq. (3.11) and Eq. (3.12), all the distances have been non-dimesionalized with the beam. Z_{wl} is the vertical distance from the undisturbed water line to the center of gravity, L_{cg} and V_{cg} describe the position of the center of gravity in the geometric coordinate system with origin at the intersection between the keel and the transom, ζ_3 is the sinkage (positive up) and ϕ is the roll angle in the body-fixed coordinate system.

In Figs. 3.34, 3.35 and 3.36 the results for $C_v = 3.6$ are presented and in Figs. 3.37, 3.38 and 3.39 those corresponding to $C_v = 4.3$. The agreement between the numerical and the experimental results for the lift force when the numerical results have been corrected with the NTC is remarkable. However, notice that the best agreement between the numerical and the experimental results for the roll moment is obtained when the numerical results have not been corrected with the NTC. This is an area that requires further investigation.

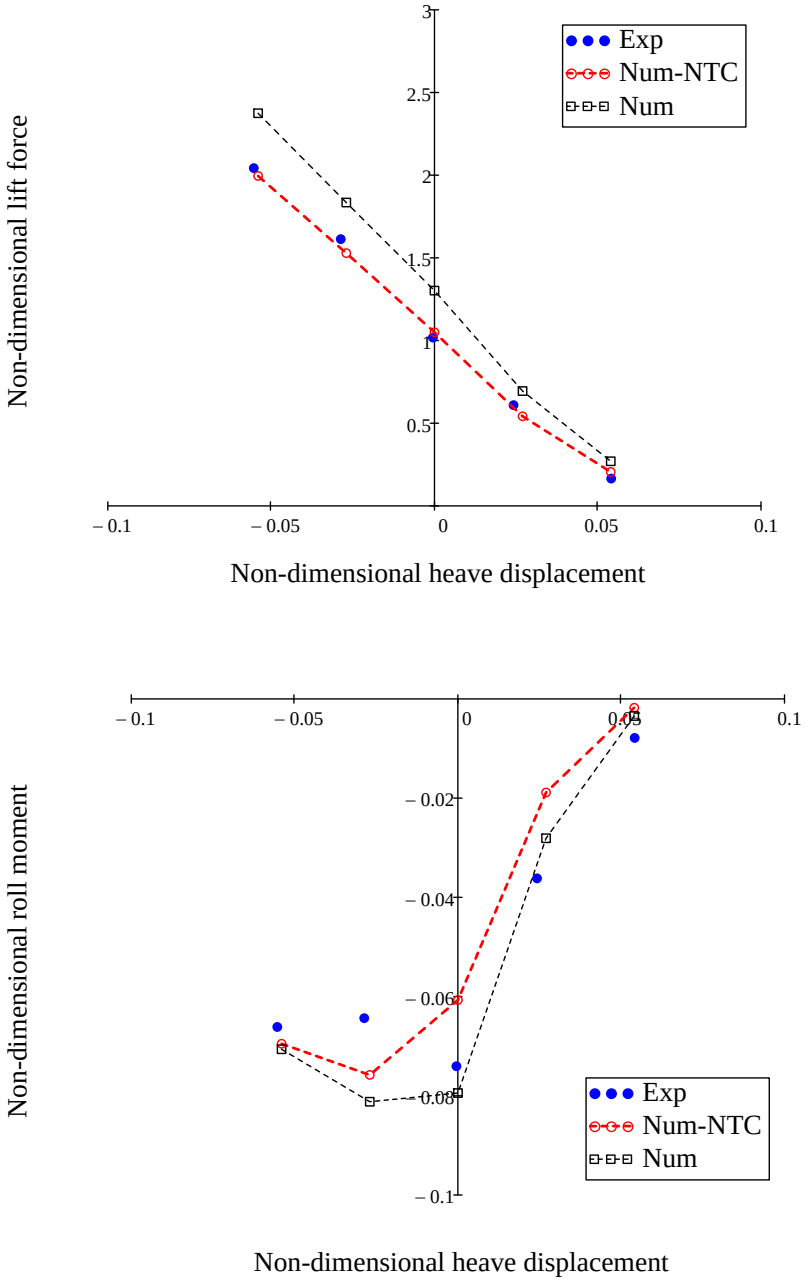

Figure 3.34: Comparison of non-dimensional lift force (top) and non-dimensional roll moment (bottom) as a function of non-dimensional heave displacement. Experimental condition: $C_\Delta = 0.15$, $C_v = 3.6$, $\phi = 5°$. Experimental results (Exp), 2D+t results with NTC (Num-NTC), 2D+t results without NTC (Num)

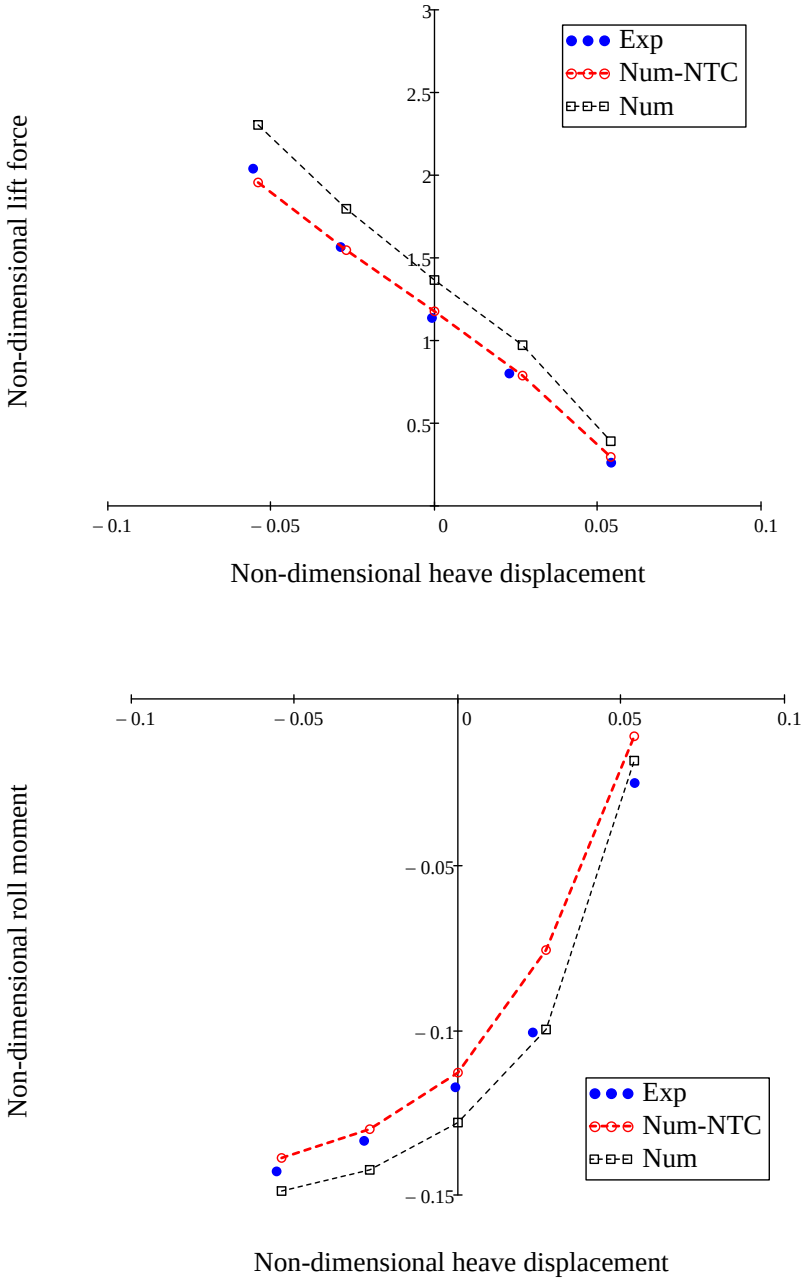

Figure 3.35: Comparison of non-dimensional lift force (top) and non-dimensional roll moment (bottom) as a function of non-dimensional heave displacement. Experimental condition: $C_\Delta = 0.15$, $C_v = 3.6$, $\phi = 10°$. Experimental results (Exp), 2D+t results with NTC (Num-NTC), 2D+t results without NTC (Num)

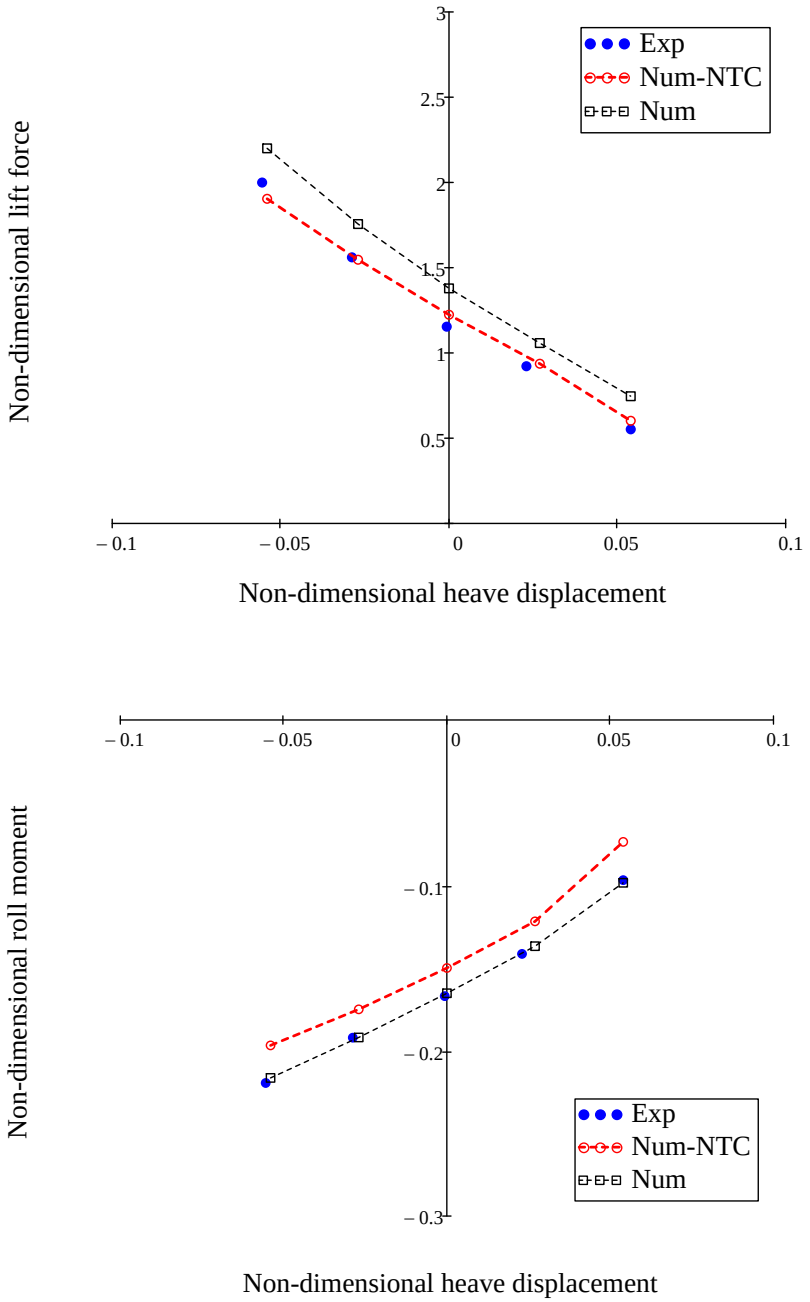

Figure 3.36: Comparison of non-dimensional lift force (top) and non-dimensional roll moment (bottom) as a function of non-dimensional heave displacement. Experimental condition: $C_\Delta = 0.15$, $C_v = 3.6$, $\phi = 15°$. Experimental results (Exp), 2D+t results with NTC (Num-NTC), 2D+t results without NTC (Num)

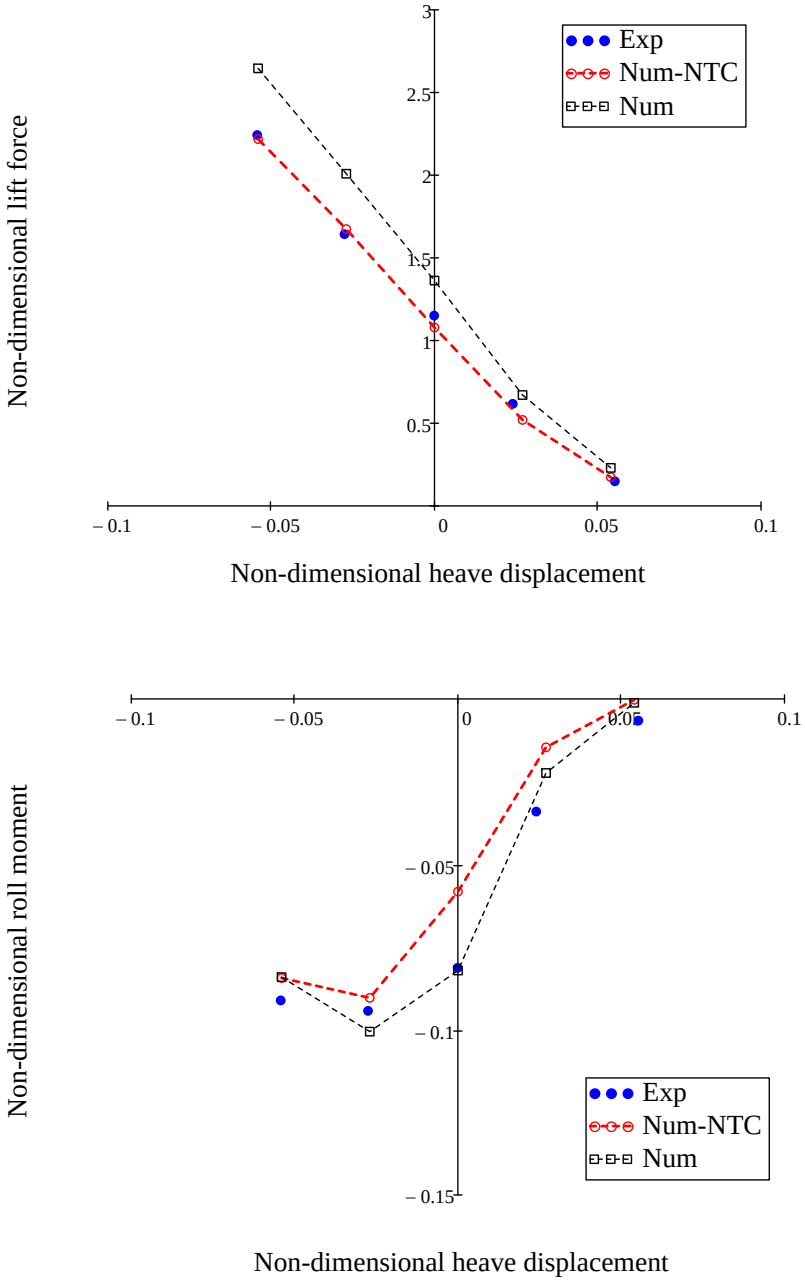

Figure 3.37: Comparison of non-dimensional lift force (top) and non-dimensional roll moment (bottom) as a function of non-dimensional heave displacement. Experimental condition: $C_\Delta = 0.15$, $C_v = 4.3$, $\phi = 5°$. Experimental results (Exp), 2D+t results with NTC (Num-NTC), 2D+t results without NTC (Num)

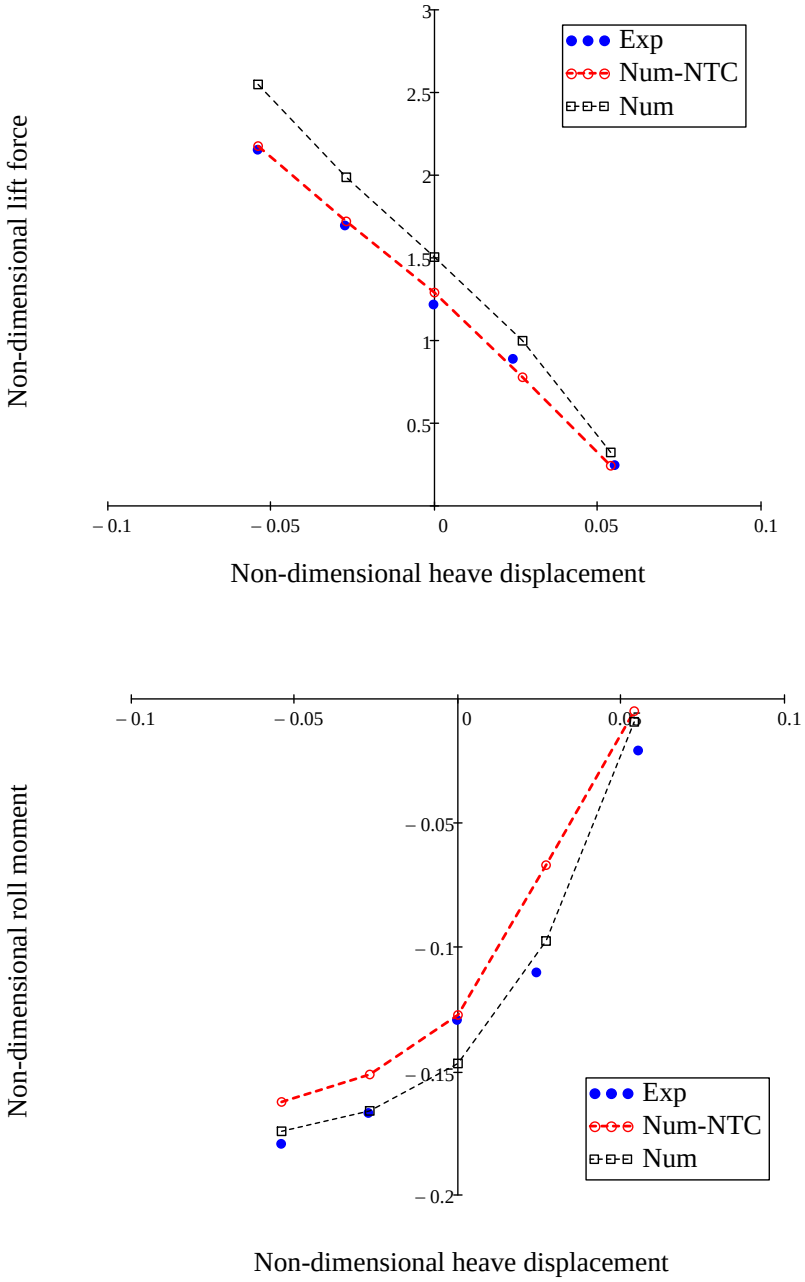

Figure 3.38: Comparison of non-dimensional lift force (top) and non-dimensional roll moment (bottom) as a function of non-dimensional heave displacement. Experimental condition: $C_\Delta = 0.15$, $C_v = 4.3$, $\phi = 10°$. Experimental results (Exp), 2D+t results with NTC (Num-NTC), 2D+t results without NTC (Num)

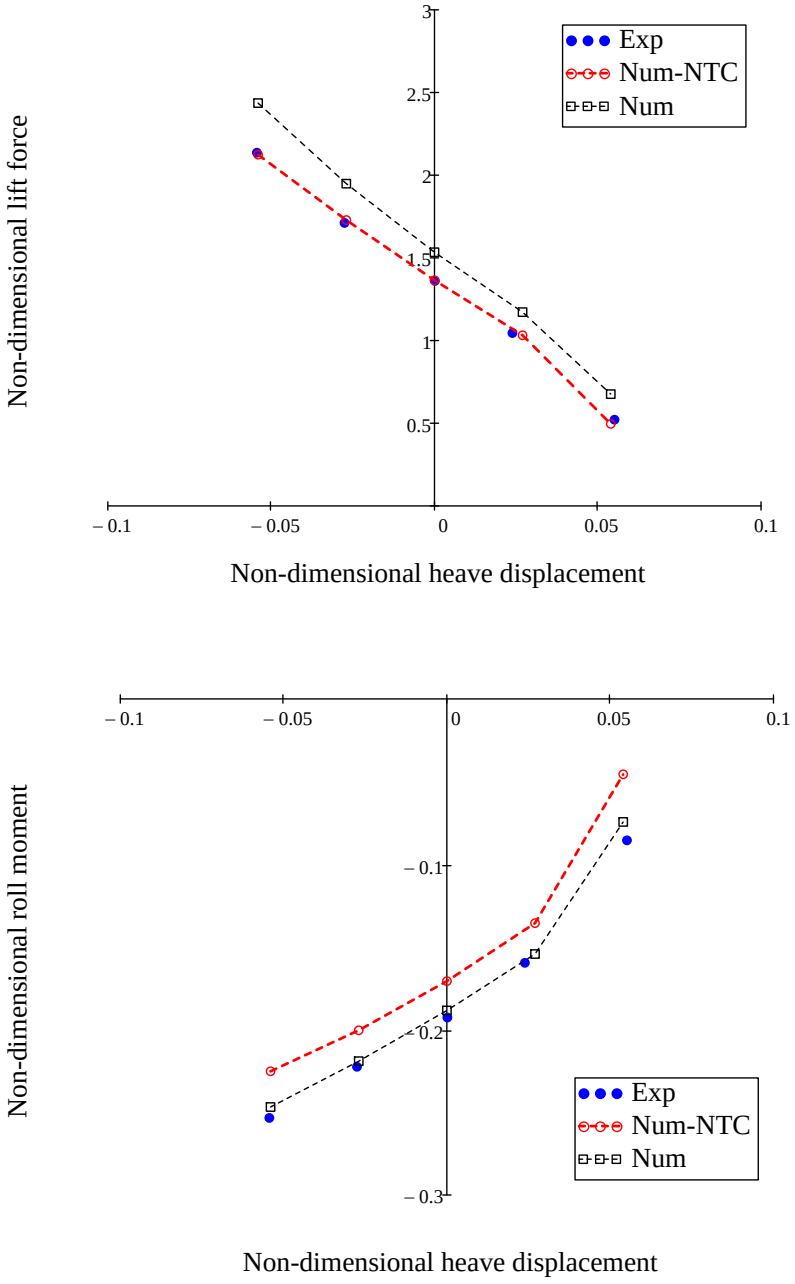

Figure 3.39: Comparison of non-dimensional lift force (top) and non-dimensional roll moment (bottom) as a function of non-dimensional heave displacement. Experimental condition: $C_\Delta = 0.15$, $C_v = 4.3$, $\phi = 15°$. Experimental results (Exp), 2D+t results with NTC (Num-NTC), 2D+t results without NTC (Num)

3.8 Conclusions

The SBT (2D+t) approach has been applied to compute the forces and moments acting on a planing hull being towed at different attitudes and speeds and forced in pure harmonic roll motion. The resulting 2-D unsteady problems of a constant deadrise wedge impacting the water have been solved using the commercial RANSE CFD program Star-CCM+.

In the unsteady planing problem the computational results of the forces and moments show fair to very good agreement with the experimental results. The best agreement is found for the cases with small roll amplitude as expected from the limits of applicability of the 2D+t. The disagreement presented in Tascon and Algarin (2013) for the cases with the largest frequency of oscillation, where the experimental time series showed peaks in the sway force and roll moment at $t = T/4$ and $t = 3T/4$, has been corrected by using a larger value for the roll moment of inertia than the one reported in Judge and Judge (2013). This has been done after re-examination of the experimental time series and personal communication with Professor Carolyn Judge at the USNA.

The forces and moments acting on a planing hull being towed at constant speed and different attitudes, including heel and drift, have also been computed. The numerical results of the forces and moments show fair to good agreement with the experimental results, with the largest difference present in the cases with the largest degree of asymmetry (i.e., combinations of positive drift angle with negative heel angle) where the slenderness assumption is most probably being violated Also, in these cases separation of the flow at the keel without re-attachment and side wetting are obtained in the 2-D impact problem and consequently the forces and moments are over-predicted.

The 2D+t solution cannot capture some 3-D effects such as the transition from chines-dry to chines-wet condition and flow separation from the transom, with the latter being the one with the greatest influence in the computation of forces and moments. The solutions obtained for forces and moments in the horizontal plane appear to be less affected by this due to a "cancellation" effect between the pressure distributions on the two opposite sides. However, when there is separation at the keel this cancellation effect breaks and the correction for flow separation at the transom plays an important role in preventing the forces and moments to be over-predicted. Taking this into consideration, an empirical correction for separation at the transom has been proposed. This correction, obtained from re-analysis of 3-D high fidelity inviscid RANSE simulations of prismatic geometries with 20 degrees constant deadrise angle and comparison with experimental results of models with 10, 20 and 30 degrees deadrise angles appears to be dependent mainly on aspect ratio as suggested by researchers at NACA on their early work on seaplanes back in the thirties and fifties (Pabst (1931), Shuford (1958)).

In the following chapter these results will be used to compute the coupled higher order inertial, dissipative and restoring coefficients in the roll equation of motion in order to investigate the development of parametric roll on planing hulls.

CHAPTER 4

Coefficients in the Roll Equation of Motion

4.1 Chapter Overview

In this chapter the time series for the forces and moments obtained in Chapter 3 are used to compute the inertial and dissipative coefficients in the roll equation of motion. The stiffness coefficients are computed from the time independent forces and moments obtained by varying the attitude of the planing hull from equilibrium. The numerical results for the linear added mass, damping and stiffness coefficients are compared with those reported in Judge and Judge (2013). Additionally, the numerical results for the stiffness coefficients coupling heave and roll are compared with the results reported in Judge (2014a). Tascon and Algarin (2013) showed that a linear added mass, linear damping and non-linear stiffness model is unable to predict large amplitude and large frequency motions, specially in the cases when the mean wetted length is small (e.g., a light boat at high speed). Therefore, in this chapter models are proposed for non-linear added mass and non-linear damping and values for the coefficients in these models are obtained under the assumption of weak dependence on amplitude and frequency of oscillation. The importance of the third order harmonic in the out of phase component of the roll moment and its impact in the evaluation of the roll damping is shown.

4.2 Introduction

The interest in this chapter is to compute the hydrodynamic coefficients in the roll equation of motion derived in Chapter 2, which is reproduced here for convenience:

$$\begin{aligned}
&\phi_{tt} + \left(K_{11}^{A}\right)\phi^2\phi_{tt} + \left(K_{23}^{A}\right)\phi\,\phi_t^2 + \\
&\quad + \left(K_{1}^{D}\right)\phi_t + \left(K_{2}^{D}z + K_{3}^{D}\theta\right)\phi_t + \left(K_{6}^{D}z^2 + K_{7}^{D}z\theta + K_{8}^{D}\theta^2\right)\phi_t + \\
&\quad + \left(K_{12}^{D}\right)\phi^2\phi_t + \left(K_{17}^{D}\right)\phi_t^3 + \\
&\quad + \left(K_{1}^{S}\right)\phi + \left(K_{2}^{S}z + K_{3}^{S}\theta\right)\phi + \\
&\quad + \left(K_{4}^{S}z^2 + K_{5}^{S}z\theta + K_{6}^{S}\theta^2\right)\phi + \left(K_{7}^{S}\right)\phi^3 = 0
\end{aligned} \tag{4.1}$$

Eq. (4.1) is expressed in classical maneuvering notation in order to show the linear added-mass coefficient ($K_{\phi_{tt}}$) explicitly:

$$\begin{aligned}
(I_x)\phi_{tt} = &(K_{\phi_{tt}})\phi_{tt} + (K_{\phi\phi\phi_{tt}})\,\phi^2\phi_{tt} + (K_{\phi\phi_t\phi_t})\,\phi\,\phi_t^2 + \\
&+ (K_{\phi_t})\,\phi_t + (K_{z\phi_t}z + K_{\theta\phi_t}\theta)\,\phi_t + \left(K_{zz\phi_t}z^2 + K_{z\theta\phi_t}z\theta + K_{\theta\theta\phi_t}\theta^2\right)\phi_t + \\
&+ (K_{\phi\phi\phi_t})\,\phi^2\phi_t + (K_{\phi_t\phi_t\phi_t})\,\phi_t^3 + \\
&+ (K_{\phi})\,\phi + (K_{z\phi}z + K_{\phi\theta}\theta)\,\phi + \\
&+ \left(K_{zz\phi}z^2 + K_{z\phi\theta}z\theta + K_{\phi\theta\theta}\theta^2\right)\phi + (K_{\phi\phi\phi})\,\phi^3
\end{aligned} \tag{4.2}$$

There are eighteen hydrodynamic coefficients that need to be identified on the right hand side of Eq. (4.2). From these eighteen coefficients, three of them are inertial (or added mass), eight of them are dissipative (or damping) and the remaining seven are restoring (or stiffness). All the inertial and dissipative coefficients can be obtained from dynamic tests in which the model is excited in pure roll.

The restoring coefficients can be found from forces and moments measured in static (or steady state) tests where the model is systematically perturbed in heave, roll and pitch from equilibrium.

With this in mind, Eq. (4.2) is re-written as the sum of three functions representing the nature of the coefficients:

$$(I_x)\phi_{tt} = K^A(\phi_{tt}, \phi_t, \phi) + K^D(\phi_t, z, \phi, \theta) + K^S(z, \phi, \theta) \tag{4.3}$$

where the functions $K^A(\phi_{tt}, \phi_t, \phi)$, $K^D(\phi_t, z, \phi, \theta)$ and $K^S(z, \phi, \theta)$ are given by the following expressions:

$$K^A(\phi_{tt}, \phi_t, \phi) = (K_{\phi_{tt}})\phi_{tt} + (K_{\phi\phi\phi_{tt}})\,\phi^2\phi_{tt} + (K_{\phi\phi_t\phi_t})\,\phi\,\phi_t^2 \tag{4.4}$$

$$\begin{aligned} K^D(\phi_t, z, \phi, \theta) = {} & (K_{\phi_t})\,\phi_t + (K_{z\phi_t}z + K_{\theta\phi_t}\theta)\,\phi_t + (K_{\phi\phi\phi_t})\,\phi^2\phi_t + \\ & + \left(K_{zz\phi_t}z^2 + K_{z\theta\phi_t}z\theta + K_{\theta\theta\phi_t}\theta^2\right)\phi_t + (K_{\phi_t\phi_t\phi_t})\,\phi_t^3 \end{aligned} \tag{4.5}$$

$$\begin{aligned} K^S(z, \phi, \theta) = {} & (K_{\phi})\,\phi + (K_{z\phi}z + K_{\phi\theta}\theta)\,\phi + \\ & + \left(K_{zz\phi}z^2 + K_{z\phi\theta}z\theta + K_{\phi\theta\theta}\theta^2\right)\phi + (K_{\phi\phi\phi})\,\phi^3 \end{aligned} \tag{4.6}$$

In the following sections the time independent (stiffness) and the time dependent (added mass and damping) coefficients are obtained via regression analysis of the experimental results obtained by Professor Judge at the USNA (Judge and Judge, 2013) and the numerical results obtained by the 2D+t approach in Chapter 3.

4.3 Time Independent Coefficients

The stiffness coefficients in Eq. (4.6) are obtained by perturbing the attitude of the planing hull from equilibrium in heave (z), roll (ϕ) and pitch (θ), and fitting a multivariate polynomial regression surface through it, where the coefficients of this polynomial correspond to the coefficients being identified.

4.3.1 Experiments and Simulations

The experimental set-up reported in Judge and Judge (2013) and Judge (2014a) is used to compute the stiffness coefficients in Eq. (4.1). This is done for two configurations seen as extremes in the possible behaviour to be observed; the heavier configuration ($C_\Delta = 0.29$) run at the lower speed ($C_v = 2.9$), and the lighter configuration ($C_\Delta = 0.15$) run at the higher speed ($C_v = 4.3$). Judge and Judge (2013) presented results for the pure roll stiffness coefficients in classical seakeeping notation for the two configurations tested ($C_\Delta = 0.15, 0.29$) at three different speeds ($C_v = 2.9, 3.6, 4.3$) and five different roll angles ($\phi = 0°, 5°, 10°, 15°, 20°$). Judge (2014a) presented experimental results for the lighter configuration ($C_\Delta = 0.15$) tested at two different speeds ($C_v = 3.6, 4.3$), five roll angles ($\phi = 0°, 5°, 10°, 15°, 20°$) and five heave positions with a maximum perturbation equivalent to half the nominal draft ($z = \pm 0.5\, T_D$). In Judge (2014a) the interest was to show the effect of the roll angle and the heave displacement in the lift force; therefore, no information was presented with regards to the roll moment. However, the roll moment was recorded and Professor Judge has made the information available in order to perform the comparison with the numerical results.

4.3.2 Stiffness Model

In Judge and Judge (2013) a third order odd model was assumed for the static roll; however, it was suggested that a fifth order model could be more appropriate to fit the results for the lighter configuration at large roll angles. Here, a general third order model in heave-roll-pitch is assumed in order to investigate the relative importance of the different coupling stiffness coefficients. Therefore, the roll stiffness force is assumed to be represented by the following model:

$$K^S(z,\phi,\theta) = (K_\phi)\,\phi + (K_{z\phi}z + K_{\phi\theta}\theta)\,\phi + \\ + \left(K_{zz\phi}z^2 + K_{z\phi\theta}z\theta + K_{\phi\theta\theta}\theta^2\right)\phi + (K_{\phi\phi\phi})\,\phi^3 \tag{4.7}$$

4.3.3 Results and Analysis

The 2D+t approach is used to compute the roll moment, populate a matrix of responses obtained by systematically varying heave, roll and pitch from the equilibrium position reported in Judge (2014a), and fit a multivariate polynomial regression surface of fifth order to it. The roll angle is assumed to vary in the range ($-20^\circ \leq \phi \leq 20^\circ$), and the heave and pitch perturbations (ζ_3, ζ_5) to be in the ranges ($-0.5\,T_D \leq \zeta_3 \leq 0.5\,T_D$) and ($-0.45\,\theta_E \leq \zeta_5 \leq 0.45\,\theta_E$) respectively, where T_D and θ_E correspond to the non-dimensional transom draft and trim angle at equilibrium for each configuration and speed as reported in Judge and Judge (2013).

The results of the fitting corresponding to the heavier configuration run at the lower speed are presented in Fig. 4.1 and Table 4.1. In the regression analysis and analysis of variance, the standard error, the lower and higher values of the estimates at the 95% confidence level and the ratio between the t-statistic and its critical value (t_{crit}) at the same confidence level, referred to as t-ratio, are presented.

Values of this ratio below one (t-ratio$= t/t_{\text{crit}} < 1$) signify that the regressor is not significant from the statistical point of view and could be removed from the model.

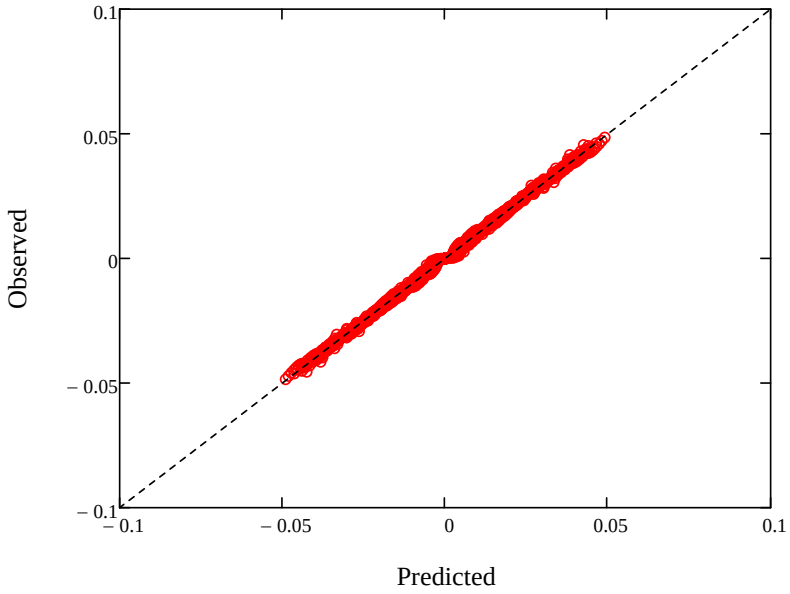

Figure 4.1: Observed versus predicted response plots: Least squares fit (LSF) to the numerical (2D+t) results for the stiffness component of the non-dimensional roll moment $K^S(z, \phi, \theta)$. Experimental condition: $C_\Delta = 0.29$, $C_v = 2.9$.

Term	Coefficient	Std. Error	95% CI Low	95% CI High	t-ratio
K_ϕ	-0.110	3.858E-3	-0.110	-0.109	144.78
$K_{z\phi}$	0.459	1.823E-3	0.455	0.462	128.304
$K_{\phi\theta}$	0.849	5.131E-3	0.839	0.859	84.326
$K_{z\phi\theta}$	5.451	0.083	5.289	5.613	33.660
$K_{zz\phi}$	-1.039	0.033	-1.104	-0.974	15.945
$K_{\phi\theta\theta}$	-1.886	0.263	-2.402	-1.370	3.653
$K_{\phi\phi\phi}$	0.145	4.969E-3	0.135	0.154	15.691

Table 4.1: Regression analysis and analysis of variance for $K^S(z, \phi, \theta)$; ${R_{\text{adj}}}^2 = 0.999$. Experimental condition: $C_\Delta = 0.29$, $C_v = 2.9$.

The results of the fitting corresponding to the lighter configuration run at the higher speed are presented in Fig. 4.2 and Table 4.2. Notice that in this case the coefficient $K_{z\phi\theta}$ does not contribute significantly to the fitting and could be removed from the model.

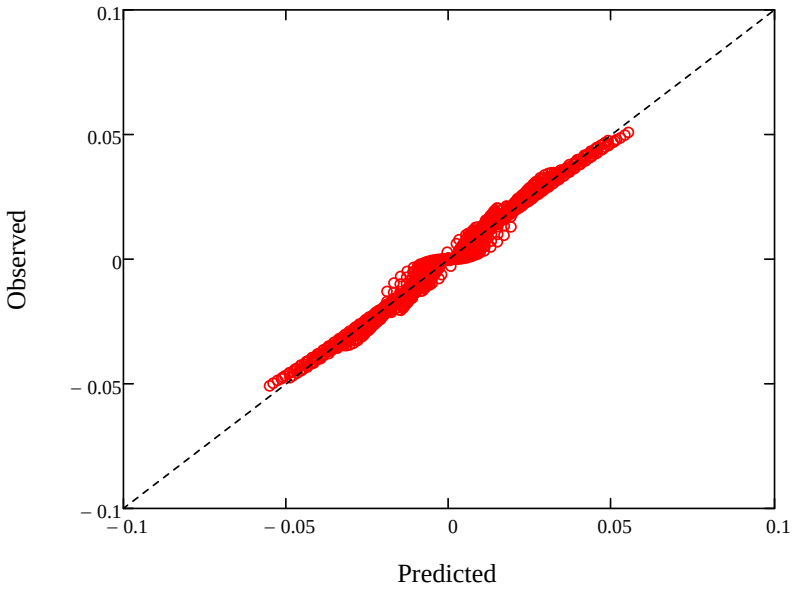

Figure 4.2: Observed versus predicted response plot: Least squares fit (LSF) to the numerical (2D+t) results for the stiffness component of the non-dimensional roll moment $K^S(z, \phi, \theta)$. Experimental condition: $C_\Delta = 0.15$, $C_v = 4.3$.

Term	Coefficient	Std. Error	95% CI Low	95% CI High	t-ratio
K_ϕ	-0.104	1.155E-3	-0.106	-0.102	45.946
$K_{z\phi}$	0.832	0.011	0.810	0.854	37.537
$K_{\phi\theta}$	2.144	0.021	2.102	2.185	51.551
$K_{z\phi\theta}$	-0.166	0.706	-1.551	1.219	0.120
$K_{zz\phi}$	5.292	0.426	4.455	6.128	6.328
$K_{\phi\theta\theta}$	-5.749	1.499	-8.691	-2.808	1.954
$K_{\phi\phi\phi}$	0.047	0.014	0.020	0.075	1.709

Table 4.2: Regression analysis and analysis of variance for $K^S(z, \phi, \theta)$; ${R_{\text{adj}}}^2 = 0.987$. Experimental condition: $C_\Delta = 0.15$, $C_v = 4.3$.

The fitting to the results corresponding to the heavier configuration run at the lower speed is better than the fitting corresponding to the lighter configuration run at the higher speed. Even though the adjusted correlation coefficient squared is high (${R_{\text{adj}}}^2 = 0.987$), observation of the residuals shows bias suggesting the need to include additional higher coefficients, possibly up to fifth order, to improve the fitting. A comparison between the pure roll stiffness coefficients obtained by a third order fitting to the experimental results presented in Judge and Judge (2013) and those reported in Tables 4.1 and 4.2 is presented in Tables 4.3 and 4.4.

	K_ϕ	$K_{\phi\phi\phi}$
Experimental	-0.127	0.042
Numerical	-0.110	0.145

Table 4.3: Pure roll stiffness coefficients. Comparison between experimental and numerical results. Experimental condition: $C_\Delta = 0.29$, $C_v = 2.9$.

	K_ϕ	$K_{\phi\phi\phi}$
Experimental	-0.124	0.321
Numerical	-0.104	0.047

Table 4.4: Pure roll stiffness coefficients. Comparison between experimental and numerical results. Experimental condition: $C_\Delta = 0.15$, $C_v = 4.3$.

In both cases the third order coefficient is of different sign than the first order coefficient, characteristic of a softening spring. However, the experimental results suggest a weaker non-linear behavior for the heavier configuration while the numerical results suggest the opposite. The numerical results for the lighter configuration run at the higher speed are validated further by comparing the fitting to the experimental results in heave-roll (Judge, 2014a). Contours of the response surface constructed with the same perturbation values used in the experiments are presented in Fig. 4.3. The two response surfaces resemble one another showing fair agreement.

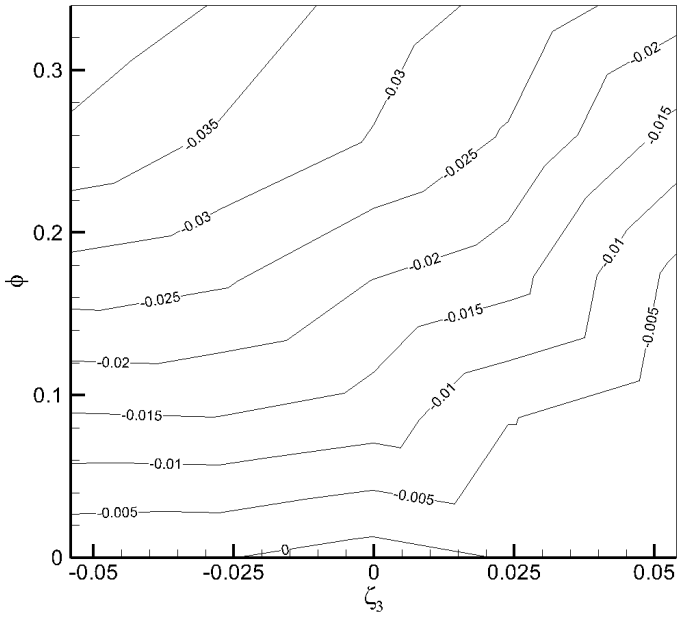

(a) Experimental (ϕ in radians)

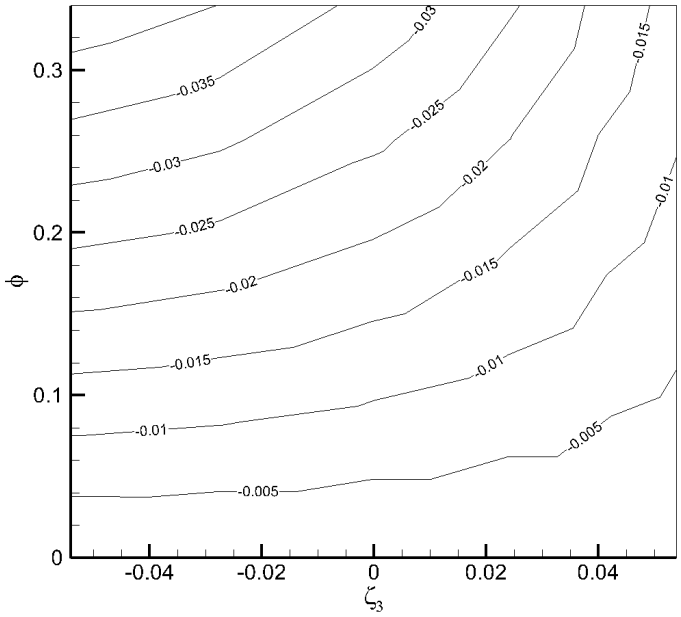

(b) LSF to numerical (ϕ in radians)

Figure 4.3: Response surface to the stiffness component of the non-dimensional roll moment $K^S(z, \phi, \theta)$ to the conditions tested by Judge (2014a). Comparison between experimental results (a) and the least squares fit (LSF) to the numerical (2D+t) results (b). Experimental condition: $C_\Delta = 0.15$, $C_v = 4.3$.

4.4 Time Dependent Coefficients

Gawthrop et al. (1988) described traditional methods to produce signals (time series) to identify the time dependent coefficients in the roll equation of motion. Those methods include roll decay tests, forced oscillations with prescribed monofrequency motion (roll amplitude) and forced oscillations with prescribed monofrequency excitation (roll moment). Examples of the application of these methods on planing hull's scale models, found in the open literature, are presented in Table 4.5.

	Method	Example
Roll decay		Arguin Jr. et al. (2001)
Forced rolling	Monofrequency motion	Judge (2010, 2012)
	Monofrequency excitation	Balsamo et al. (2001, 2002)

Table 4.5: Examples of the application of some traditional methods to obtain the roll time dependent coefficients on planing hull models

4.4.1 Experiments and Simulations

As mentioned above, two of the configurations (C_Δ,C_v) tested by Judge and Judge (2013) have been selected to investigate the dynamic behaviour of planing hulls, and therefore their experimental results are reduced, together with the simulations of the same experimental conditions by the 2D+t approach. The time dependent coefficients in Eq. (4.2) are identified from forced roll oscillations where the amplitude and the frequency of oscillation is kept constant for each run. A simple harmonic roll oscillation with amplitude ϕ_0 and circular frequency ω is assumed:

$$\phi(t) = \phi_0(t)\sin\omega t \qquad \phi_t(t) = \omega\phi_0(t)\cos\omega t \qquad \phi_{tt}(t) = -\omega^2\phi_0(t)\sin\omega t \tag{4.8}$$

Since the model was tested with only one degree of freedom, Judge and Judge (2013) assumed a non-linear model of the form:

$$(I_x)\phi_{tt} = (K_{\phi_{tt}})\phi_{tt} + (K_{\phi_t})\,\phi_t + (K_\phi)\,\phi + (K_{\phi\phi\phi})\,\phi^3 \tag{4.9}$$

Tascon and Algarin (2013) used Fourier analysis and made preliminary observations regarding the relative size of the higher-order harmonics in the roll moment time series. Those preliminary observations suggested the existence of inertial and dissipative non-linearities not included in the model assumed by Judge and Judge (2013). Here, the work in Tascon and Algarin (2013) is continued by using Fourier analysis and regression analysis to investigate non-linear models for the added mass and damping in roll. First, Fourier analysis is used to show the importance of the different harmonics and to make preliminary conclusions regarding inertial and dissipative non-linearities.

4.4.2 Functional Series Methods - Fourier Analysis

Fourier analysis is applied to the time series of the roll moment required to oscillate the planing hull scaled model in harmonic motion. The signals are separated into *in-phase* (IP) and *out-of-phase* (OP) components and the Fourier representation of the roll moment is written as follows:

$$K_{\text{Fou}}(t) = {K_{\text{Fou}}}^{IP}(t) + {K_{\text{Fou}}}^{OP}(t) \tag{4.10}$$

where ${K_{\text{Fou}}}^{IP}(t)$ and ${K_{\text{Fou}}}^{OP}(t)$ are given by:

$$K_{\text{Fou}}{}^{OP}(t) = a_1 \cos \omega t + a_3 \cos 3\omega t + a_5 \cos 5\omega t + \ldots \tag{4.11}$$

$$K_{\text{Fou}}{}^{IP}(t) = b_1 \sin \omega t + b_3 \sin 3\omega t + b_5 \sin 5\omega t + \ldots \tag{4.12}$$

Two experimental conditions are expected to be extremes with regards to linear and non-linear behavior, the heavier configuration oscillated at small amplitude of oscillation and the lighter configuration at large amplitude of oscillation.

First, a comparison of the results for the out-of-phase component of the non-dimensional roll moment time series for these two extreme conditions is presented. The results in Fig. 4.4 clearly indicate an almost linear behavior for the heavier configuration at the lower speed when oscillated at small amplitude and low frequency of oscillation. In contrast, the results presented in Fig. 4.5 show that in the case of the lighter configuration at the higher speed oscillated at large amplitude, there is an important third order harmonic present. Also, at both frequencies this third order harmonic is of different sign than the first order harmonic. This behavior is present in both the experimental and the numerical results; however, at the higher frequency of oscillation the experimental results appear more non-linear than the numerical results.

A side by side comparison between these two configurations for the out-of-phase component of the non-dimensional roll moment time series is presented in Fig. 4.6. These results suggest the existence of non-linear dissipative terms in the roll equation of motion, specially important in the lighter configuration run at the higher speed tested.

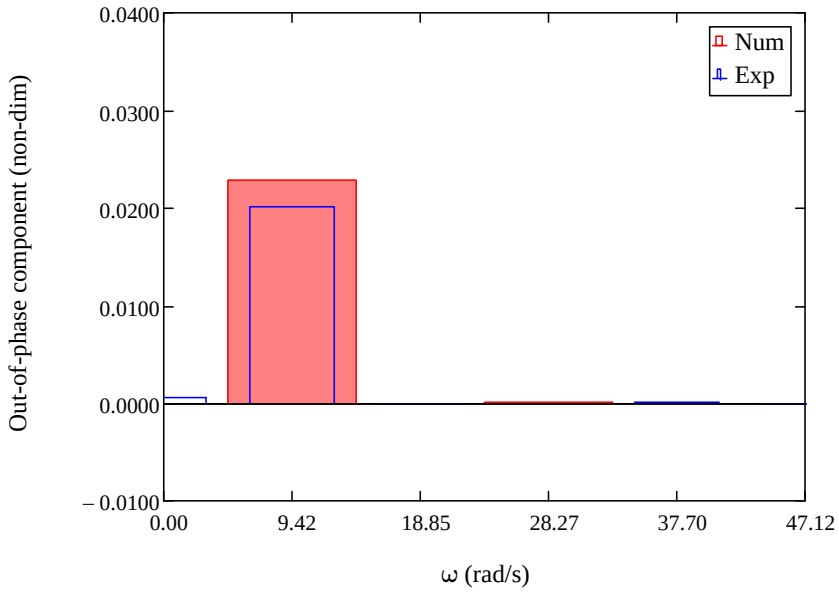

(a) $f = 1.5$ Hz

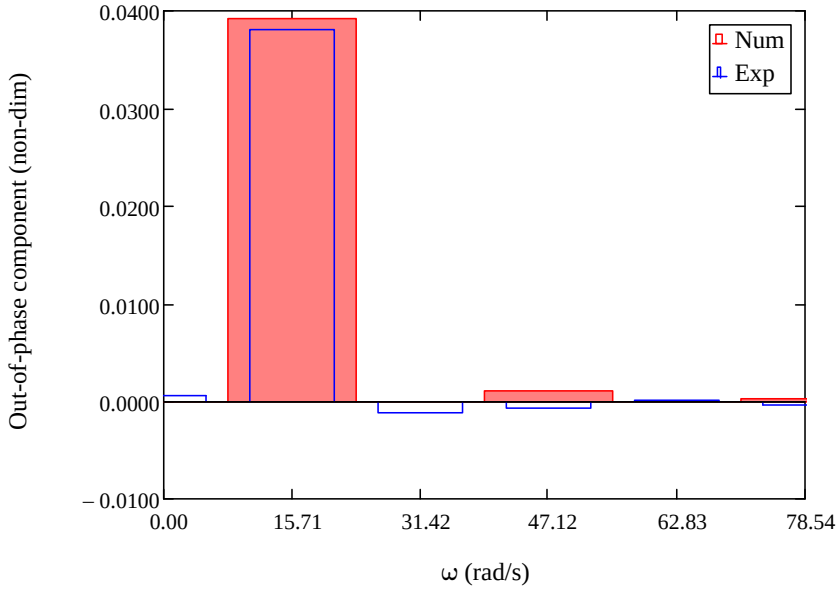

(b) $f = 2.5$ Hz

Figure 4.4: Harmonic analysis: Out-of-phase component of the non-dimensional roll moment. Comparison between experimental (bar) and numerical (solid bar) results. Experimental condition: $C_\Delta = 0.29$, $C_v = 2.9$, $\phi_0 = 10°$

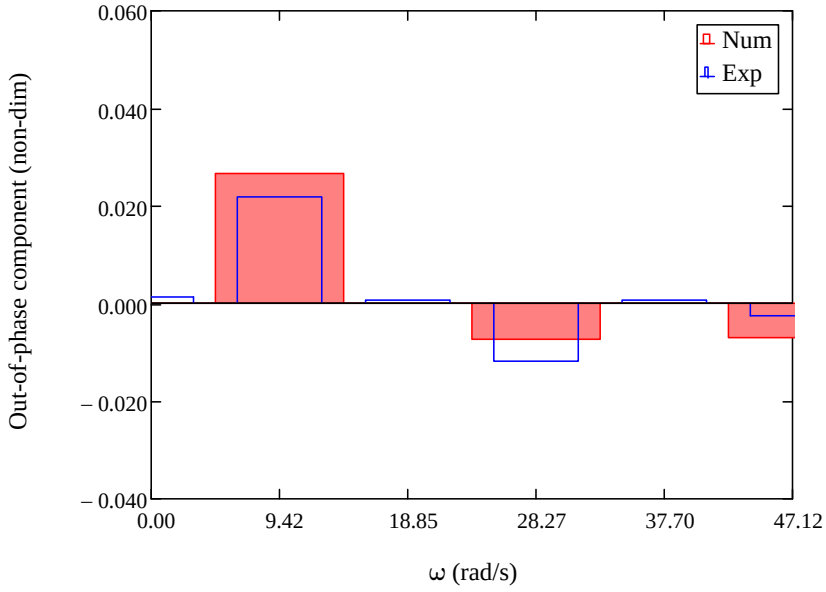

(a) $f = 1.5$ Hz

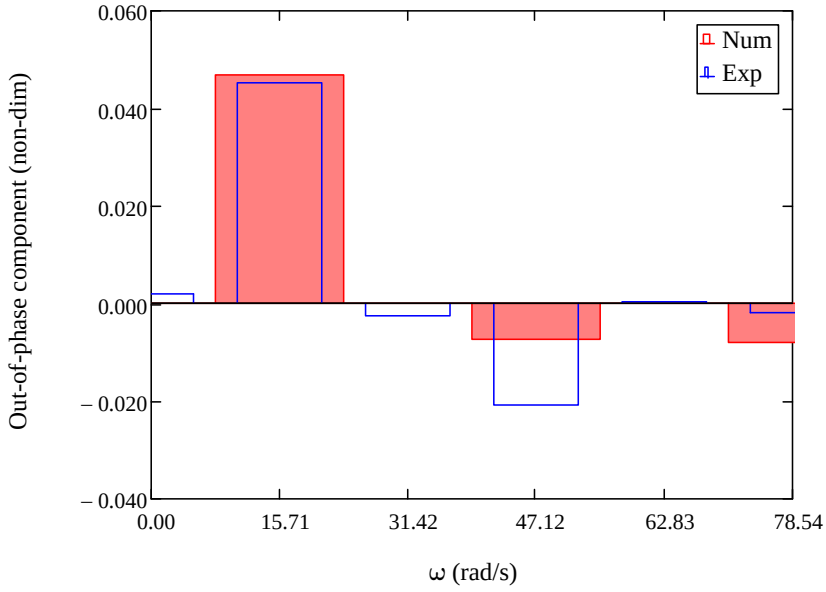

(b) $f = 2.5$ Hz

Figure 4.5: Harmonic analysis: Out-of-phase component of the non-dimensional roll moment. Comparison between experimental (bar) and numerical (solid bar) results. Experimental condition: $C_\Delta = 0.15$, $C_v = 4.3$, $\phi_0 = 20°$

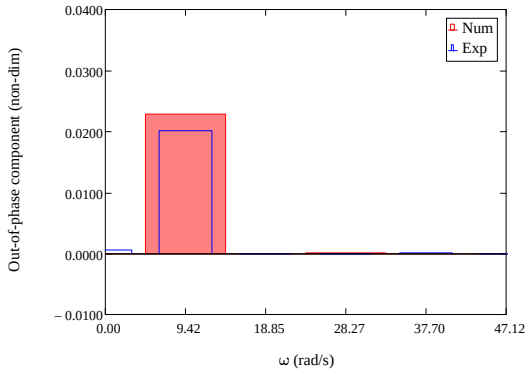

(a) $C_\Delta = 0.29$, $C_v = 2.9$, $\phi_0 = 10°$, $f = 1.5$ Hz

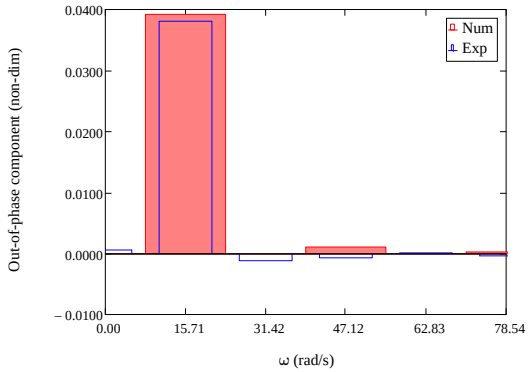

(b) $C_\Delta = 0.29$, $C_v = 2.9$, $\phi_0 = 10°$, $f = 2.5$ Hz

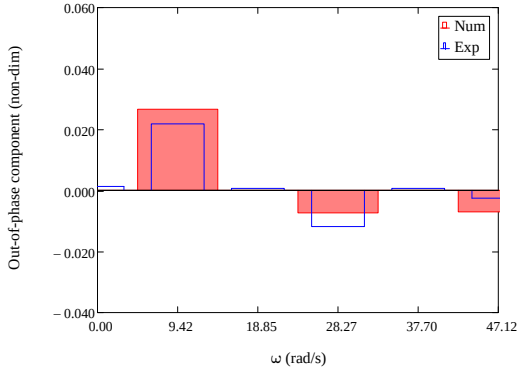

(c) $C_\Delta = 0.15$, $C_v = 4.3$, $\phi_0 = 20°$, $f = 1.5$ Hz

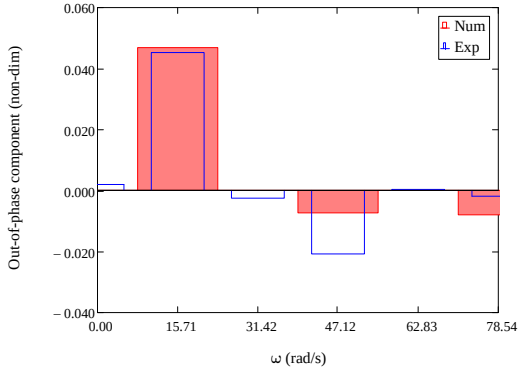

(d) $C_\Delta = 0.15$, $C_v = 4.3$, $\phi_0 = 20°$, $f = 2.5$ Hz

Figure 4.6: Harmonic analysis: Out-of-phase component of the non-dimensional roll moment. Comparison between experimental (bar) and numerical (solid bar) results.

A comparison of the results for the in-phase component of the non-dimensional roll moment time series for the same conditions shown in Fig. 4.4, Fig. 4.5 and Fig. 4.6 is presented in Fig. 4.7, Fig. 4.8 and Fig. 4.9 repectively.

As before, the results show an almost linear behavior for the heavier configuration run at the lower speed when oscillated at small amplitude and low frequency of oscillation (Fig. 4.7a). At the higher frequency of oscillation (Fig. 4.7b) there are important non-linearities in both the experimental and the numerical results; however, the magnitude of the in-phase component is small in comparison with the out-of phase component indicating that this frequency is close to the (fluid) natural frequency.

In the case of the lighter configuration run at the higher speed and oscillated at large amplitude (Fig. 4.8), there are important third order harmonics present at both frequencies. The same behavior is found in both the experimental and the numerical results; however, at the higher frequency of oscillation the numerical results appear more non-linear than the experimental results with the third order harmonic having almost the same size of the first order harmonic.

A side by side comparison between these two configurations for the in-phase component of the non-dimensional roll moment time series is presented in Fig. 4.9. Again, these results suggest the presence of important higher order inertial and/or stiffness terms in the roll equation of motion, specially in the case of the lighter configuration run at the higher speed tested.

In the case of the roll moment, the dissipative coefficients can be obtained from the out-of-phase component while the inertial and the stiffness coefficients are confounded in the in-phase component. Therefore, the stiffness coefficients are usually found first from static tests and their values used to solve for the inertial coefficients from the different harmonics of the Fourier representation. This suggests that in this case the in-phase component can be written as composed by inertial $\left({K_{\text{Fou}}}^{IP-A}\right)$ and stiffness $\left({K_{\text{Fou}}}^{IP-S}\right)$ sub-components as follows:

$$ {K_{\text{Fou}}}^{IP}(t) = {K_{\text{Fou}}}^{IP-A}(t) + {K_{\text{Fou}}}^{IP-S}(t) \tag{4.13} $$

where ${K_{\text{Fou}}}^{IP-S}(t)$ and ${K_{\text{Fou}}}^{IP-A}(t)$ are given by:

$$ {K_{\text{Fou}}}^{IP-S}(t) = b_1^S \sin\omega t + b_3^S \sin 3\omega t + b_5^S \sin 5\omega t + \ldots \tag{4.14} $$

$$ {K_{\text{Fou}}}^{IP-A}(t) = (b_1 - b_1^S)\sin\omega t + (b_3 - b_3^S)\sin 3\omega t + (b_5 - b_5^S)\sin 5\omega t + \ldots \tag{4.15} $$

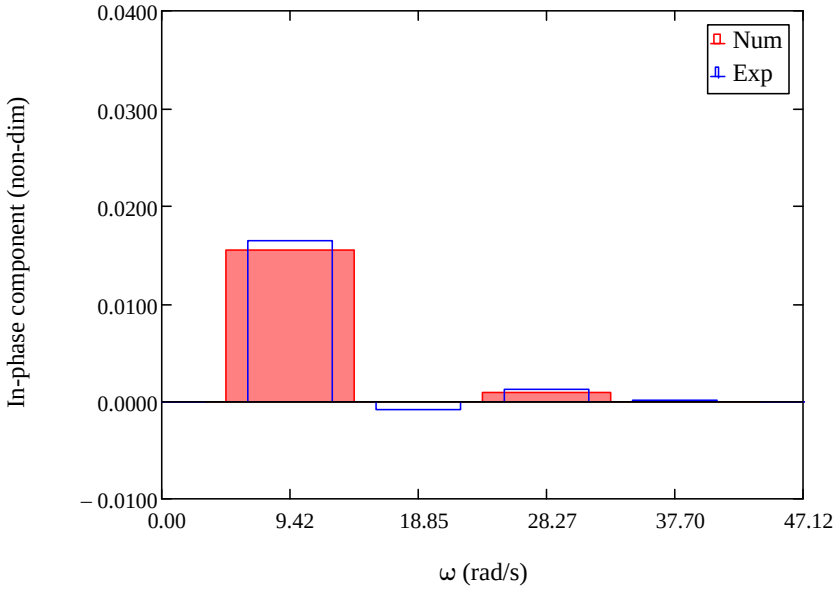

(a) $f = 1.5$ Hz

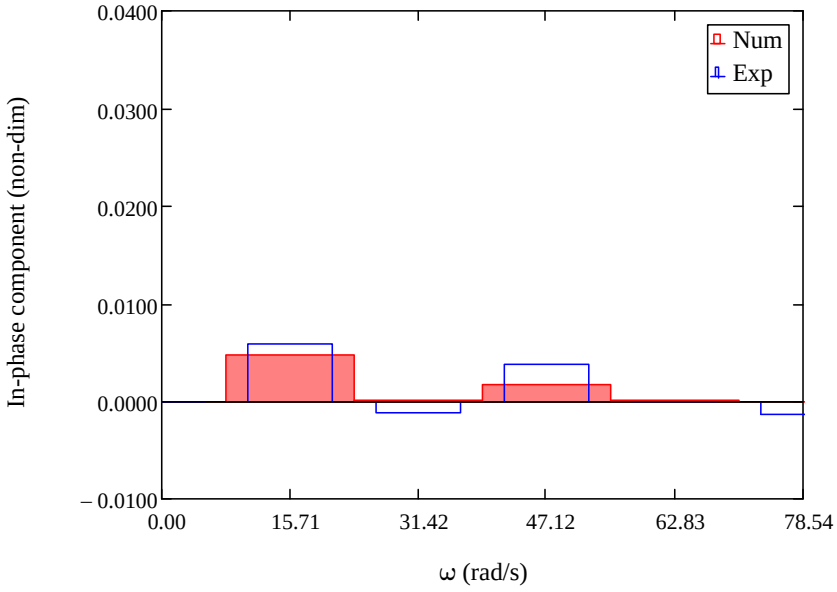

(b) $f = 2.5$ Hz

Figure 4.7: Harmonic analysis: In-phase component of the non-dimensional roll moment. Comparison between experimental (bar) and numerical (solid bar) results. Experimental condition: $C_\Delta = 0.29$, $C_v = 2.9$, $\phi_0 = 10°$

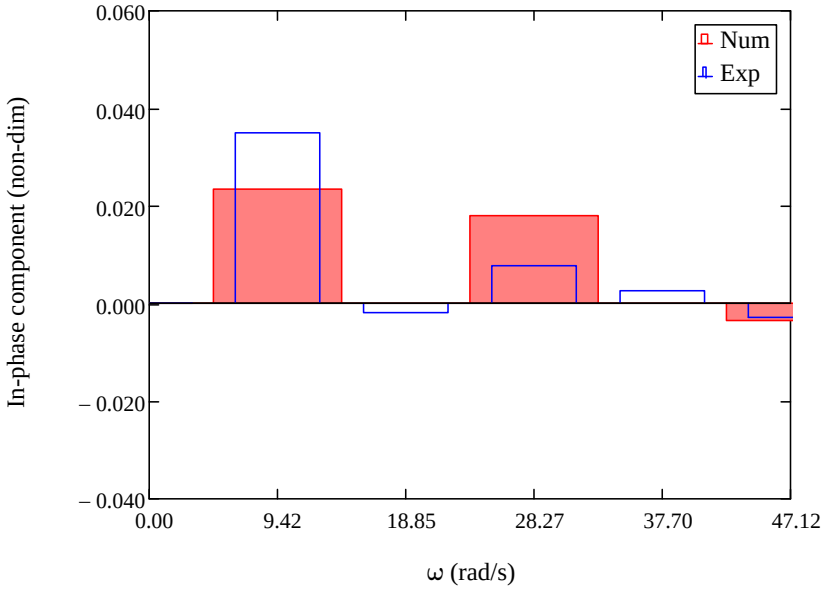

(a) $f = 1.5$ Hz

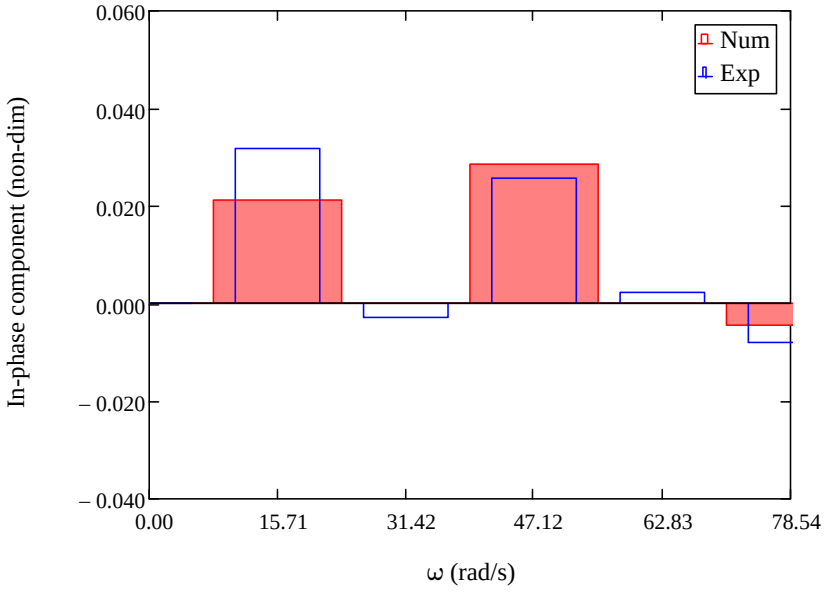

(b) $f = 2.5$ Hz

Figure 4.8: Harmonic analysis: In-phase component of the non-dimensional roll moment. Comparison between experimental (bar) and numerical (solid bar) results. Experimental condition: $C_\Delta = 0.15$, $C_v = 4.3$, $\phi_0 = 20°$

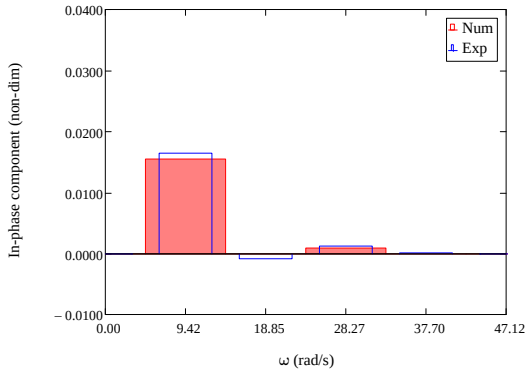

(a) $C_\Delta = 0.29$, $C_v = 2.9$, $\phi_0 = 10°$, $f = 1.5$ Hz

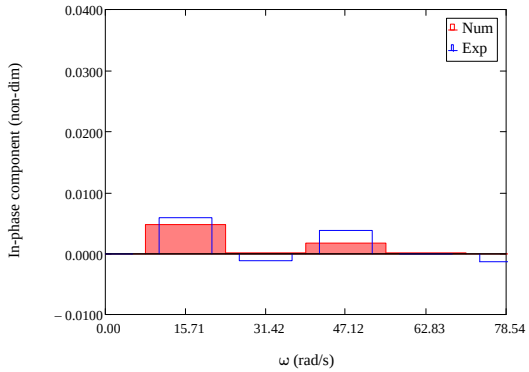

(b) $C_\Delta = 0.29$, $C_v = 2.9$, $\phi_0 = 10°$, $f = 2.5$ Hz

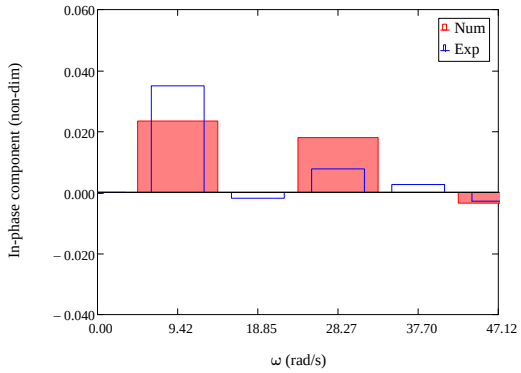

(c) $C_\Delta = 0.15$, $C_v = 4.3$, $\phi_0 = 20°$, $f = 1.5$ Hz

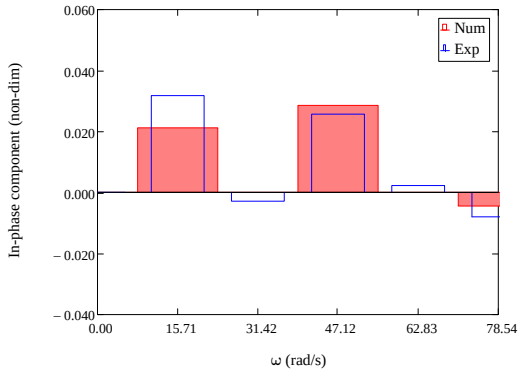

(d) $C_\Delta = 0.15$, $C_v = 4.3$, $\phi_0 = 20°$, $f = 2.5$ Hz

Figure 4.9: Harmonic analysis: In-phase component of the non-dimensional roll moment. Comparison between experimental (bar) and numerical (solid bar) results.

Assuming a stiffness model for the pure roll motion of the form:

$$K^S(\phi_{tt}, \phi_t, \phi) = C_1\phi + C_3\phi^3 + C_5\phi^5 \tag{4.16}$$

Making use of Eq. (4.8) and identities for powers of trigonometric functions, the arguments of the coefficients in Eq. (4.16) can be written as follows:

$$\phi^3 = \frac{3}{4}\phi_0^3 \sin\omega t - \frac{1}{4}\phi_0^3 \sin 3\omega t \tag{4.17}$$

$$\phi^5 = \frac{5}{8}\phi_0^5 \sin\omega t - \frac{5}{16}\phi_0^5 \sin 3\omega t + \frac{1}{16}\phi_0^5 \sin 5\omega t \tag{4.18}$$

Equating the coefficients of $\sin\omega t$, $\sin 3\omega t$ and $\sin 5\omega t$ between Eq. (4.16) and Eq. (4.14) yields the following matrix representation for the harmonics corresponding to the stiffness coefficients:

$$\begin{pmatrix} b_1^S \\ b_3^S \\ b_5^S \end{pmatrix} = \begin{bmatrix} \phi_0 & \frac{3}{4}\phi_0^3 & \frac{5}{8}\phi_0^5 \\ 0 & -\frac{1}{4}\phi_0^3 & -\frac{5}{16}\phi_0^5 \\ 0 & 0 & \frac{1}{16}\phi_0^5 \end{bmatrix} \begin{pmatrix} C_1 \\ C_3 \\ C_5 \end{pmatrix} \tag{4.19}$$

These values can be used to remove the stiffness contribution from the harmonics of the in-phase component. Another possibility is to remove directly the stiffness contribution from the time series by subtracting the function $K^S(\phi_{tt}, \phi_t, \phi)$ (Eq. (4.16)) from the time record knowing the roll angle at each time step. These two approaches yield exactly the same result when the prescribed motion is perfectly sinusoidal as represented by Eq. (4.8).

For the results presented in this chapter a third order model is assumed for the stiffness and therefore $C_5 = 0$. In this sense b_1^S is equivalent to the model used in Judge and Judge (2013) to obtain the linear added mass coefficient from the first harmonic of the in-phase component of the roll moment by considering the contribution of up to third order stiffness non-linearities.

The results presented in Fig. 4.6 and Fig. 4.9 clearly suggest the existence of important non-linear inertial, dissipative and restoring terms in the roll equation of motion. Therefore, in the following sections different models to represent the inertial and dissipative non-linearities are investigated.

4.4.3 Added Mass Model

Based on Eq. (4.4) a model for the inertial coefficients is assumed:

$$K^A(\phi_{tt}, \phi_t, \phi) = A_1\phi_{tt} + A_2\phi_{tt}\phi^2 + A_3\phi\phi_t^2 \tag{4.20}$$

where the objective is to identify the coefficients on the left hand side of the roll equation of motion and the notation A_j has been adopted for simplicity. Making use of Eq. (4.8) and identities for powers of trigonometric functions, the arguments of the coefficients in Eq. (4.20) can be written as follows:

$$\phi_{tt}\,\phi^2 = \frac{-3}{4}\omega^2\phi_0^3\sin\omega t + \frac{1}{4}\omega^2\phi_0^3\sin 3\omega t \tag{4.21}$$

$$\phi\,\phi_{tt}^2 = \frac{1}{4}\omega^2\phi_0^3\sin\omega t + \frac{1}{4}\omega^2\phi_0^3\sin 3\omega t \tag{4.22}$$

Equating the coefficients of $\sin\omega t$ and $\sin 3\omega t$ between Eq. (4.20) and Eq. (4.15) yields the following matrix representation for the harmonics corresponding to the inertial coefficients up to third order:

$$\begin{bmatrix} -\omega^2\phi_0 & \frac{-3}{4}\omega^2\phi_0^3 & \frac{1}{4}\omega^2\phi_0^3 \\ 0 & \frac{1}{4}\omega^2\phi_0^3 & \frac{1}{4}\omega^2\phi_0^3 \end{bmatrix} \begin{pmatrix} A_1 \\ A_2 \\ A_3 \end{pmatrix} = \begin{pmatrix} b_1 - b_1^S \\ \\ b_3 - b_3^S \end{pmatrix} \tag{4.23}$$

Notice that in order to identify the coefficients in Eq. (4.20) the results from at least two tests are required (assuming that the coefficients are frequency and/or amplitude independent) since the system represented by Eq. (4.23) is under-determined (i.e., there are fewer equations than unknowns). However, the arguments of the coefficients A_2 and A_3 even though different are multiplied by the same $\omega^2\phi_0^3$ term. Therefore, in trying to solve an over-determined system of equations by the least squares method

it will be impossible to distinguish between A_2 and A_3 unless a relationship between them is known or assumed. Since the argument of A_2 in Eq. (4.20) might cause problems for numerical integration, and since the effect of keeping A_2 or A_3 for the non-linear stability analysis will be the same, it was decided to keep only A_3. With these considerations Eq. (4.20) reduces to:

$$K^A(\phi_{tt}, \phi_t, \phi) = A_1\phi_{tt} + A_3\phi\phi_t^2 \tag{4.24}$$

which in matrix form is written as:

$$\begin{bmatrix} -\omega^2\phi_0 & \frac{1}{4}\omega^2\phi_0^3 \\ 0 & \frac{1}{4}\omega^2\phi_0^3 \end{bmatrix} \begin{pmatrix} A_1 \\ \\ A_3 \end{pmatrix} = \begin{pmatrix} b_1 - b_1^S \\ \\ b_3 - b_3^S \end{pmatrix} \tag{4.25}$$

and solving for A_1 and A_3 yields:

$$A_1 = \frac{(b_3 - b_3^S) - (b_1 - b_1^S)}{\omega^2\phi_0} \qquad A_3 = \frac{4(b_3 - b_3^S)}{\omega^2\phi_0^3} \tag{4.26}$$

This result is used to obtain in subsection 4.4.7.1 the inertial coefficients in Eq. (4.20) and make conclusions regarding their relative importance and their dependence on amplitude (ϕ_0) and frequency (ω). The results of the linear added mass are compared with those obtained following the model suggested in Judge and Judge (2013). Their results are labelled as A_{1eq} since they were obtained solely from the information contained in the first harmonic of the in-phase component of the Fourier representation of the roll moment time series; this corresponds to:

$$A_{1eq} = \frac{-(b_1 - b_1^S)}{\omega^2\phi_0} \tag{4.27}$$

4.4.4 Damping Models

The correct model to describe the damping on ships is still nowadays a subject of research given the interest on understanding the effect of large amplitude roll motions on new hull forms (e.g., tumblehome) and their capsizing limits (Bassler et al., 2010). Therefore, there is no total agreement in what the best model is, with different models having different advocates and adepts. Regarding traditional hull forms, the International Towing Tank Conference (ITTC) suggests the use of what is known as the "mixed quadratic-cubic model" (Eq. (4.28)) for the numerical estimation of roll damping (ITTC, 2011), in the cases in which non-linearities are expected to be important.

$$K^D_{ITTC}(\phi_t) = B_1\phi_t + B_2\phi_t|\phi_t| + B_3\phi_t^3 \tag{4.28}$$

However, this model has the mathematical disadvantage of not being infinitely differentiable, posing difficulties to the study of non-linear dynamics by some analytical methods (e.g., the functional series expansion). In fact, this model is a mixture of the linear-quadratic model proposed by Froude (1955) and the linear-cubic alternative proposed by Dalzell (1978) to avoid the non-analytical quadratic term ($\phi_t|\phi_t|$) in the linear-quadratic model. There appears to be consensus in the non-linear dependence of the roll damping on roll amplitude, with Haddara and Bennett (1989) one of the first and main advocates for the inclusion of a roll angle dependent term (e.g., $|\phi|\phi_t$ or $\phi^2\phi_t$) in the model for damping.

Due to the fact that the model derived in Chapter 2 was obtained from a Taylor series expansion, all its elements are continuously differentiable. In the case of pure roll,

Eq. (4.5) reduces to the following model for the dissipative coefficients (B_j):

$$K^D(\phi_t, \phi) = B_1\phi_t + B_2\phi_t\phi^2 + B_3\phi_t^3 \tag{4.29}$$

where, as in the added mass case, the coefficients on the left hand side of the roll equation of motion need to be identified and the notation B_j is used for simplicity.

ITTC (2011) recognizes the difficulties associated to analyze Eq. (4.28) and suggests the use of the concept of *equivalent linear damping* (B_{1eq}):

$$B(\phi_t) = \left(\frac{a_1}{\omega\phi_0}\right)\omega\phi_0\cos\omega t + \cdots = (B_{1eq})\,\phi_t + \ldots \tag{4.30}$$

For the case when the motion is simple harmonic, as in Eq. (4.8), the equivalent linear damping can be obtained directly from the first harmonic of the out-of-phase component of the Fourier representation of the roll moment (i.e., Eq. (4.11)). Taking the mixed quadratic-cubic model, Eq. (4.28), suggested in ITTC (2011), equating to the out-of-phase component of the Fourier representation of the roll moment and discarding harmonics higher than third order yields:

$$B_1\phi_t + B_2\phi_t|\phi_t| + B_3\phi_t^3 = a_1\cos\omega t + a_3\cos 3\omega t \tag{4.31}$$

using Eq. (4.8) and trigonometric identities for powers of sines and cosines the following correspondence can be shown:

$$\phi_t|\phi_t| = \frac{8}{3\pi}\omega^2\phi_0^2\cos\omega t + \frac{8}{15\pi}\omega^2\phi_0^2\cos 3\omega t \tag{4.32}$$

$$\phi_t^3 = \frac{3}{4}\omega^3\phi_0^3\cos\omega t + \frac{1}{4}\omega^3\phi_0^3\cos 3\omega t \tag{4.33}$$

where the following Fourier approximation of the products of absolute values has been

used:

$$\cos\omega t \ |\cos\omega t| = \frac{8}{3\pi}\cos\omega t + \frac{8}{15\pi}\cos 3\omega t + \ldots \tag{4.34}$$

Equating the coefficients of $\cos\omega t$ and $\cos 3\omega t$ in Eq. (4.31) yields the following matrix representation for the harmonics corresponding to the damping coefficients in Eq. (4.28):

$$\begin{bmatrix} \omega\phi_0 & \frac{8}{3\pi}\omega^2\phi_0^2 & \frac{3}{4}\omega^3\phi_0^3 \\ 0 & \frac{8}{15\pi}\omega^2\phi_0^2 & \frac{1}{4}\omega^3\phi_0^3 \end{bmatrix} \begin{pmatrix} B_1 \\ B_2 \\ B_3 \end{pmatrix} = \begin{pmatrix} a_1 \\ \\ a_3 \end{pmatrix} \tag{4.35}$$

where the equivalent linear damping can be obtained from the first row of Eq. (4.35):

$$B_{1eq}(\phi_0, \omega) = \frac{a_1}{\omega\phi_0} = B_1 + B_2\frac{8}{3\pi}\omega\phi_0 + B_3\frac{3}{4}\omega^2\phi_0^2 \tag{4.36}$$

This procedure can be applied to any given damping model in order to produce a *design matrix* and a *vector of responses*. The results of this analysis to three of damping models presented in Haddara and Bennett (1989), including two models with angle dependent terms, is presented next:

1. Mixed quadratic with respect to ϕ and linear-cubic with respect to ϕ_t damping model:

$$K^D(\phi_t, \phi) = B_1\phi_t + B_2\phi_t\phi^2 + B_3\phi_t^3 \tag{4.37}$$

$$\begin{bmatrix} \omega\phi_0 & \frac{1}{4}\omega\phi_0^3 & \frac{3}{4}\omega^3\phi_0^3 \\ 0 & \frac{-1}{4}\omega\phi_0^3 & \frac{1}{4}\omega^3\phi_0^3 \end{bmatrix} \begin{pmatrix} B_1 \\ B_2 \\ B_3 \end{pmatrix} = \begin{pmatrix} a_1 \\ \\ a_3 \end{pmatrix} \tag{4.38}$$

$$B_{1eq}(\phi_0,\omega)=\frac{a_1}{\omega\phi_0}=B_1+B_2\frac{1}{4}\phi_0^2+B_3\frac{3}{4}\omega^2\phi_0^2 \tag{4.39}$$

2. Mixed linear with respect to ϕ and linear-quadratic with respect to ϕ_t damping model:

$$K^D(\phi_t,\phi)=B_1\phi_t+B_2\phi_t|\phi|+B_3\phi_t|\phi_t| \tag{4.40}$$

$$\begin{bmatrix}\omega\phi_0 & \frac{4}{3\pi}\omega\phi_0^2 & \frac{8}{3\pi}\omega^2\phi_0^2\\ 0 & \frac{-4}{5\pi}\omega\phi_0^2 & \frac{8}{15\pi}\omega^2\phi_0^2\end{bmatrix}\begin{pmatrix}B_1\\B_2\\B_3\end{pmatrix}=\begin{pmatrix}a_1\\\\a_3\end{pmatrix} \tag{4.41}$$

$$B_{1eq}(\phi_0,\omega)=\frac{a_1}{\omega\phi_0}=B_1+B_2\frac{4}{3\pi}\phi_0+B_3\frac{8}{3\pi}\omega\phi_0 \tag{4.42}$$

3. Quadratic-cubic with respect to ϕ_t damping model:

$$K^D(\phi_t)=B_1\phi_t+B_2\phi_t|\phi_t|+B_3\phi_t^3 \tag{4.43}$$

$$\begin{bmatrix}\omega\phi_0 & \frac{8}{3\pi}\omega^2\phi_0^2 & \frac{3}{4}\omega^3\phi_0^3\\ 0 & \frac{8}{15\pi}\omega^2\phi_0^2 & \frac{1}{4}\omega^3\phi_0^3\end{bmatrix}\begin{pmatrix}B_1\\B_2\\B_3\end{pmatrix}=\begin{pmatrix}a_1\\\\a_3\end{pmatrix} \tag{4.44}$$

$$B_{1eq}(\phi_0,\omega)=\frac{a_1}{\omega\phi_0}=B_1+B_2\frac{8}{3\pi}\omega\phi_0+B_3\frac{3}{4}\omega^2\phi_0^2 \tag{4.45}$$

4.4.5 Third Order Models Fitted

In this section, two of the most used non-linear models to describe the pure rolling of ships are fitted, the mixed quadratic with respect to ϕ and linear-cubic with respect to ϕ_t model, given by Eq. (4.46), and the mixed quadratic-cubic model suggested by the International Towing Tank Conference (ITTC) for the numerical estimation of roll damping (ITTC, 2011), given by Eq. (4.49). Also, the mixed quadratic with respect to ϕ and cubic with respect to ϕ_t (Eq. (4.47)) and the linear-cubic with respect to ϕ_t (Eq. (4.48)) models are investigated, both of them understood as sub-models of the more general mixed quadratic with respect to ϕ and linear-cubic with respect to ϕ_t model (Eq. (4.46)).

$$K^D(\phi_t, \phi)_{3\_1} = B_1\phi_t + B_2\phi_t\phi^2 + B_3\phi_t^3 \tag{4.46}$$

$$K^D(\phi_t, \phi)_{3\_2} = B_1\phi_t + B_2\phi_t\phi^2 \tag{4.47}$$

$$K^D(\phi_t)_{3\_3} = B_1\phi_t + B_3\phi_t^3 \tag{4.48}$$

$$K^D(\phi_t)_{3\_4} = B_1\phi_t + B_{2A}\phi_t|\phi_t| + B_3\phi_t^3 \tag{4.49}$$

4.4.6 Least Squares Fit (LSF) on Harmonics

In order to obtain the coefficients in Eq. (4.46) and Eq. (4.49) a combination of least squares fit and functional series (Fourier series) is applied. First, the value of the harmonics in the out-of-phase component of the roll moment is obtained. Next, an over-determined system of equations is construted by changing systematically amplitude and frequency. The results for the different amplitudes and frequencies tested are stacked in a *design matrix* and the values of the corresponding harmonics of the out-of-phase component of the roll moment in a *vector of responses* (with

elements a_{j_k}; $j = 1, 3$; $k = 1 \ldots n$). Lastly, the *vector of regression coefficients* (with elements B_j; $j = 1 \ldots 3$) is solved by the least squares method. An example of the construction of the design matrix and the vector of responses for identification of the coefficients in the mixed quadratic with respect to ϕ and linear-cubic with respect to ϕ_t damping model follows:

$$K^D(\phi_t, \phi)_{3\_1} = B_1\phi_t + B_2\phi_t\phi^2 + B_3\phi_t^3 \tag{4.50}$$

$$\begin{bmatrix} \omega_1\phi_{0_1} & \frac{1}{4}\omega_1\phi_{0_1}^3 & \frac{3}{4}\omega_1^3\phi_{0_1}^3 \\ 0 & \frac{-1}{4}\omega_1\phi_{0_1}^3 & \frac{1}{4}\omega_1^3\phi_{0_1}^3 \\ \omega_2\phi_{0_2} & \frac{1}{4}\omega_2\phi_{0_2}^3 & \frac{3}{4}\omega_2^3\phi_{0_2}^3 \\ 0 & \frac{-1}{4}\omega_2\phi_{0_2}^3 & \frac{1}{4}\omega_2^3\phi_{0_2}^3 \\ \vdots & & \\ \omega_n\phi_{0_n} & \frac{1}{4}\omega_n\phi_{0_n}^3 & \frac{3}{4}\omega_n^3\phi_{0_n}^3 \\ 0 & \frac{-1}{4}\omega_n\phi_{0_n}^3 & \frac{1}{4}\omega_n^3\phi_{0_n}^3 \end{bmatrix} \begin{pmatrix} B_1 \\ B_2 \\ B_3 \end{pmatrix} = \begin{pmatrix} a_{1_1} \\ a_{3_1} \\ a_{1_2} \\ a_{3_2} \\ \vdots \\ a_{1_n} \\ a_{3_n} \end{pmatrix} \tag{4.51}$$

Himeno (1981) suggests that the non-linear roll coefficients can be obtained by solving the equivalent linear damping for different values of amplitude and frequency. This is in fact equivalent to neglecting the third harmonic a_{3_k} and solving an over-determined system of equations. For the mixed quadratic with respect to ϕ and linear-cubic with respect to ϕ_t damping model this approach implies the following system of equations:

$$\begin{bmatrix} \omega_1\phi_{0_1} & \frac{1}{4}\omega_1\phi_{0_1}^3 & \frac{3}{4}\omega_1^3\phi_{0_1}^3 \\ \omega_2\phi_{0_2} & \frac{1}{4}\omega_2\phi_{0_2}^3 & \frac{3}{4}\omega_2^3\phi_{0_2}^3 \\ \vdots & & \\ \omega_n\phi_{0_n} & \frac{1}{4}\omega_n\phi_{0_n}^3 & \frac{3}{4}\omega_n^3\phi_{0_n}^3 \end{bmatrix} \begin{pmatrix} B_1 \\ B_2 \\ B_3 \end{pmatrix} = \begin{pmatrix} a_{1_1} \\ a_{1_2} \\ \vdots \\ a_{1_n} \end{pmatrix} \tag{4.52}$$

Interestingly, this coincides with the observation of Sutulo and Guedes Soares (2007), in their work on estimation of the maneuvering derivatives from (sway-yaw) oscillatory tests, that higher-order (in their case second order) harmonics do not affect significantly the estimates of the regression coefficients and in the majority of the cases do not improve the uncertainty and accuracy of the model. In agreement with Sutulo and Guedes Soares (2007), the higher-order harmonics in this context can be interpreted as additional test points (replicates) since they are obtained from the same test (same experimental conditions). However, as will be shown with an example, in the presence of important non-linearities, neglecting the higher-order harmonics in the construction of the design matrix does affect the uncertainty and accuracy of the model.

4.4.7 Results and Analysis

The theory developed in the previous sections is applied to the experimental and numerical time series of the roll moment obtained for the configurations of interest, as it was done in section 4.3.3 for the stiffness coefficients.

4.4.7.1 Added Mass Coefficients

First, the added mass coefficients given by Eq. (4.26) are obtained from the in-phase component of the Fourier representation of the roll moment time series. The pure roll stiffness coefficients obtained in section 4.3.3 for the numerical results, and the results given in Judge and Judge (2013) for the experimental results, are used to solve for b_1^S and b_3^S. The results of the added mass coefficients corresponding to the lighter configuration run at the higher speed are presented in Tables 4.6 and 4.7. The results corresponding to the heavier configuration run at the lower speed are presented in Tables 4.8 and 4.9. In both cases, the value of A_{1eq} is smaller than the value of A_1 and therefore the effect of the third order harmonic is to increase the linear added mass. In the case of the heavier configuration run at the lower speed, A_3 appears to be both frequency and amplitude independent and A_1 weakly amplitude dependent. In the case of the lighter configuration run at the higher speed, the experimental and numerical results are inconclusive. A_1 appears to be both frequency and amplitude dependent; however, the values are very small. Analysis of other amplitudes and frequencies of oscillation would be required in order to make better conclusions. Also, the Fourier analysis of the numerical results suggest important fifth order harmonics. However, it is worth mentioning that for the reduction of the experimental results for the cases with high speed and low frequency of oscillation only a couple of cycles are available. Also, in the large amplitude cases there are small super harmonics in the roll amplitude that introduce "noise" in the higher order harmonics of the roll moment. A visual fitting of averages of the added mass coefficients (i.e., assuming amplitude and frequency independence) to the in-phase component of Fourier representation of the roll moment experimental time series for the two configurations of interest is presented in Fig. 4.10 and Fig. 4.11. The results show fair agreement for both configurations, amplitudes and frequencies of oscillation.

ϕ	f(Hz)	A_{1eq}	A_1	A_3
10	1.5	-4.213E-4	1.061E-3	0.196
10	2.5	1.203E-3	2.455E-3	0.163
20	1.5	-6.371E-4	4.177E-3	0.156
20	2.5	3.386E-4	6.085E-3	0.183

Table 4.6: Added-mass coefficients for $K^A(\phi_{tt}, \phi_t, \phi)$ corresponding to the experimental results. Experimental conditions: $C_\Delta = 0.15$, $C_v = 4.3$.

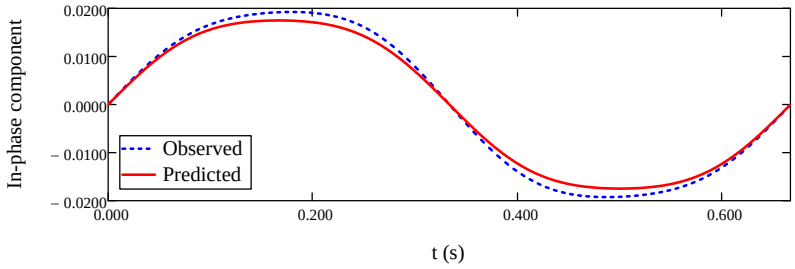

(a) $\phi_0 = 10°$, $f = 1.5$ Hz

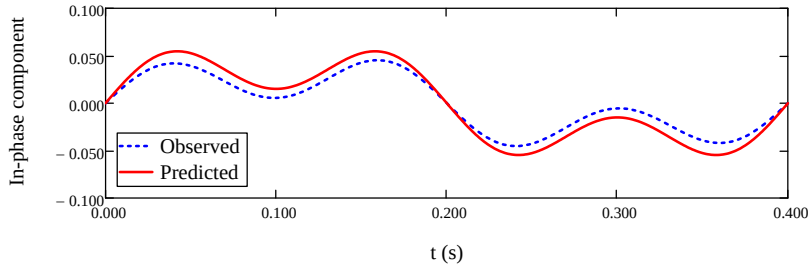

(b) $\phi_0 = 20°$, $f = 2.5$ Hz

Figure 4.10: In-phase component of the non-dimensional roll moment corresponding to the experimental results. Fitting of the sum of $K^A(\phi_{tt}, \phi_t, \phi)$ with $A_1 = 0.009$ and $A_3 = 0.211$ plus $K^S(\phi)$ with $C_1 = 0.144$ and $C_3 = -0.186$. Experimental condition: $C_\Delta = 0.15$, $C_v = 4.3$.

ϕ	f(Hz)	A_{1eq}	A_1	A_3
10	1.5	-5.183E-3	-4.768E-3	0.055
10	2.5	-1.143E-3	-1.270E-4	0.133
20	1.5	3.196E-3	0.013	0.308
20	2.5	2.211E-3	8.580E-3	0.209

Table 4.7: Added-mass coefficients for $K^A(\phi_{tt}, \phi_t, \phi)$ corresponding to the numerical (2D+t) results. Experimental conditions: $C_\Delta = 0.15$, $C_v = 4.3$.

ϕ	f(Hz)	A_{1eq}	A_1	A_3
10	1.5	0.011	0.013	0.247
10	2.5	0.010	0.012	0.248
20	1.5	0.012	0.019	0.247
20	2.5	8.434E-3	0.016	0.246

Table 4.8: Added-mass coefficients for $K^A(\phi_{tt}, \phi_t, \phi)$ corresponding to the experimental results. Experimental conditions: $C_\Delta = 0.29$, $C_v = 2.9$.

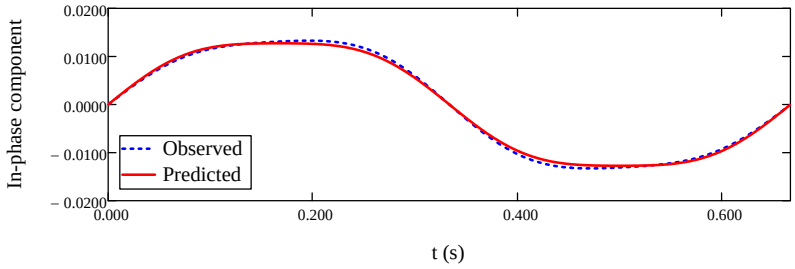

(a) $\phi_0 = 10°$, $f = 1.5$ Hz

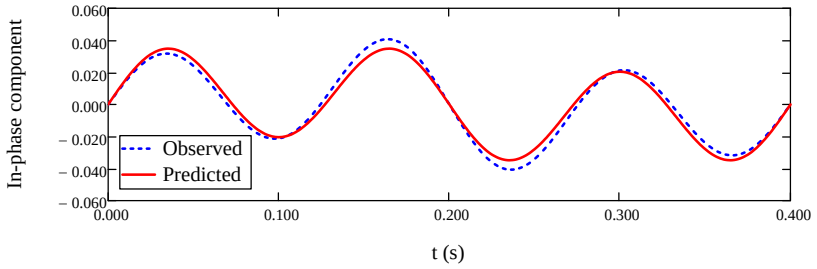

(b) $\phi_0 = 20°$, $f = 2.5$ Hz

Figure 4.11: In-phase component of the non-dimensional roll moment corresponding to the experimental results. Fitting of the sum of $K^A(\phi_{tt}, \phi_t, \phi)$ with $A_1 = 0.016$ and $A_3 = 0.247$ plus $K^S(\phi)$ with $C_1 = 0.127$ and $C_3 = -0.042$. Experimental condition: $C_\Delta = 0.29$, $C_v = 2.9$.

ϕ	f(Hz)	A_{1eq}	A_1	A_3
10	1.5	3.970E-3	4.923E-3	0.125
10	2.5	7.027E-3	7.797E-3	0.101
20	1.5	9.203E-3	0.018	0.273
20	2.5	6.694E-3	0.011	0.151

Table 4.9: Added-mass coefficients for $K^A(\phi_{tt}, \phi_t, \phi)$ corresponding to the numerical (2D+t) results. Experimental conditions: $C_\Delta = 0.29$, $C_v = 2.9$.

4.4.7.2 Damping Coefficients

Two groups of coefficients can be distinguished from the model for dissipative coefficients given by Eq. (4.5). The first group is composed by coefficients that are only function of roll velocity and displacement, $K^D(\phi_t, \phi)$. The second group is composed by coefficients that are function of roll velocity and heave and pitch displacements, $K^D(\phi_t, z, \theta)$:

$$K^D(\phi_t, \phi) = (K_{\phi_t})\,\phi_t + (K_{\phi\phi\phi_t})\,\phi^2\phi_t + (K_{\phi_t\phi_t\phi_t})\,\phi_t^3 \tag{4.53}$$

$$K^D(\phi_t, z, \theta) = \left(K_{z\phi_t} z + K_{\theta\phi_t}\theta + K_{zz\phi_t} z^2 + K_{z\theta\phi_t} z\theta + K_{\theta\theta\phi_t}\theta^2\right)\phi_t \tag{4.54}$$

The first group of coefficients can be identified from the experiments described in section 4.3.1. The models described in section 4.4.5, which include the one given by Eq. (4.53), are fitted in this section.

The results of the fitting of the models given by Eq. (4.46) and Eq. (4.49) to the lighter configuration run at the higher speed are presented in Tables 4.10 and 4.12. For comparison, the results of the fitting of the same models but using the approach suggested by Himeno (1981) are presented in Tables 4.11 and 4.13. In the latter case, these models are labelled as $K^D(\phi_t, \phi)_{3\_1eq}$ and $K^D(\phi_t)_{3\_4eq}$ respectively.

Notice that for the model $K^D(\phi_t, \phi)_{3\_4}$, given by Eq. (4.49), none of the coefficients is statistically significant. Also, notice that when following the approach suggested by Himeno (1981) the adjusted correlation coefficient squared increases for the two models. However, this result alone might be misleading since the comparison between observed and predicted in this case is done over the first harmonic alone and not over the time series record. Also, notice that the third order coefficient B_3 in model $K^D(\phi_t, \phi)_{3\_1}$, given by Eq. (4.46), is not significant and could be eliminated from the model.

Term	Coefficient	Std. Error	95% CI Low	95% CI High	t-ratio
B_1	0.023	2.180E-3	0.018	0.028	4.744
B_2	0.563	0.038	0.479	0.647	6.610
B_3	2.670E-3	2.260E-3	-2.299E-3	7.639E-3	0.531

Table 4.10: Regression analysis and analysis of variance for $K^D(\phi_t, \phi)_{3\_1}$, fitting to the experimental results; ${R_{\text{adj}}}^2 = 0.991$. Experimental condition: $C_\Delta = 0.15$, $C_v = 4.3$.

Term	Coefficient	Std. Error	95% CI Low	95% CI High	t-ratio
B_1	0.024	8.093E-4	0.021	0.026	9.176
B_2	0.430	0.050	0.291	0.569	2.697
B_3	6.258E-3	1.319E-3	2.596E-3	9.921E-3	1.491

Table 4.11: Regression analysis and analysis of variance for $K^D(\phi_t, \phi)_{3\_1eq}$, fitting to the experimental results; ${R_{\text{adj}}}^2 = 0.999$. Experimental condition: $C_\Delta = 0.15$, $C_v = 4.3$.

Term	Coefficient	Std. Error	95% CI Low	95% CI High	t-ratio
B_1	0.022	0.031	-0.045	0.090	0.330
B_{2A}	0.060	0.095	-0.149	0.269	0.284
B_3	-0.045	0.064	-0.185	0.096	0.315

Table 4.12: Regression analysis and analysis of variance for $K^D(\phi_t)_{3\_4}$, fitting to the experimental results; ${R_{\text{adj}}}^2 = 0.795$. Experimental condition: $C_\Delta = 0.15$, $C_v = 4.3$.

Term	Coefficient	Std. Error	95% CI Low	95% CI High	t-ratio
B_1	0.016	0.012	-0.016	0.048	0.427
B_{2A}	0.042	0.038	-0.064	0.147	0.347
B_3	-0.014	0.026	-0.087	0.059	0.163

Table 4.13: Regression analysis and analysis of variance for $K^D(\phi_t)_{3\_4eq}$, fitting to the experimental results; ${R_{\text{adj}}}^2 = 0.980$. Experimental condition: $C_\Delta = 0.15$, $C_v = 4.3$

In the following figures combinations of the two extremes of the amplitudes and frequencies of oscillation are used to present visually the fitting of these two models to the out-of-phase component of the Fourier representation of the experimental roll moment time series for the lighter configuration run at the higher speed.

Fig. 4.12 shows the fitting to the two models when the coefficients are predicted using the information from the first and the third harmonics. Fig. 4.13 presents the fitting when only the first harmonics is used to predict the same coefficients. In Fig. 4.14 a side by side comparison between the fitting obtained by using the two different approaches is presented. Two conclusions can be drawn from these three figures; first, the fitting when using both the first and the third harmonics to predict the coefficients is better than when using the first harmonic alone; second, the model suggested by ITTC (2011) fails to fit the out-of-phase component of the time series for the roll moment at both combinations of amplitudes and frequencies.

A comparison of the fitting of the four models represented by Eqs. (4.46) to (4.49) to the out-of-phase component of the Fourier representation of the experimental roll moment time series for the lighter configuration run at the higher speed and oscillated at small amplitude and low frequency is presented in Fig. 4.15. An equivalent comparison for the large amplitude and high frequency runs for the same configuration is presented in Fig. 4.16. A side by side comparison of the fitting to the small amplitude and low frequency runs versus the large amplitude and high frequency runs is presented in Fig. 4.17.

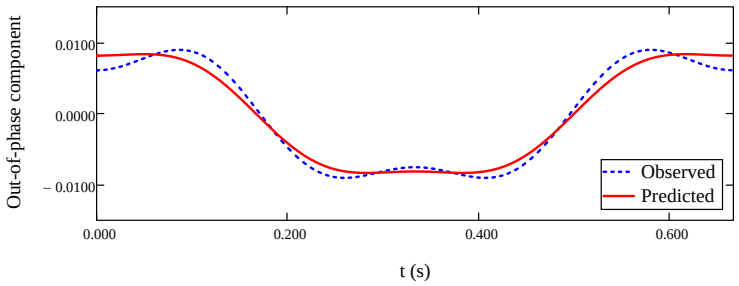

(a) $K^D(\phi_t, \phi)_{3\_1}$, $\phi_0 = 10°$, $f = 1.5$ Hz

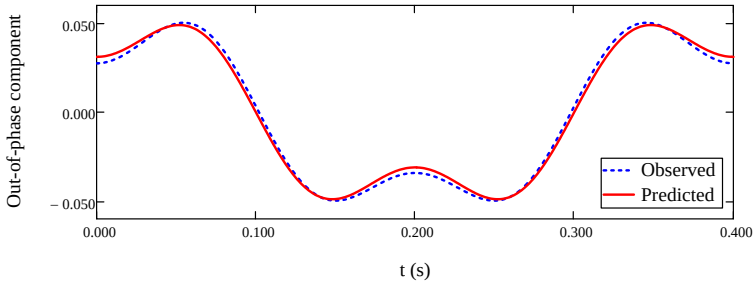

(b) $K^D(\phi_t, \phi)_{3\_1}$, $\phi_0 = 20°$, $f = 2.5$ Hz

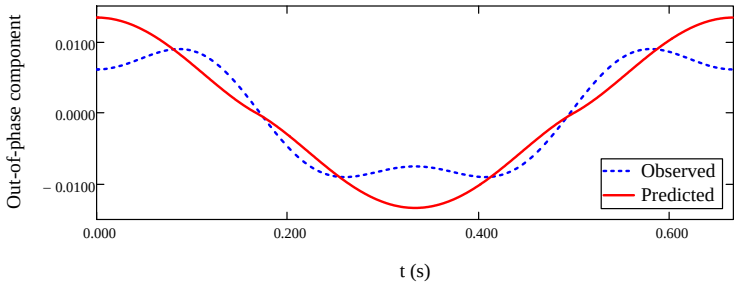

(c) $K^D(\phi_t)_{3\_4}$, $\phi_0 = 10°$, $f = 1.5$ Hz

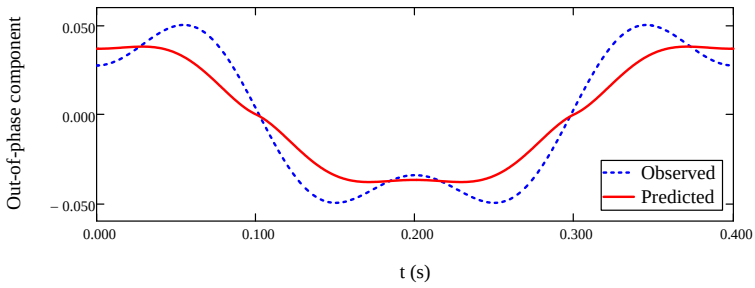

(d) $K^D(\phi_t)_{3\_4}$, $\phi_0 = 20°$, $f = 2.5$ Hz

Figure 4.12: Out-of-phase component of the non-dimensional roll moment. Comparison between the fitting of the third order damping models with contribution from the third harmonic. Experimental condition: $C_\Delta = 0.15$, $C_v = 4.3$.

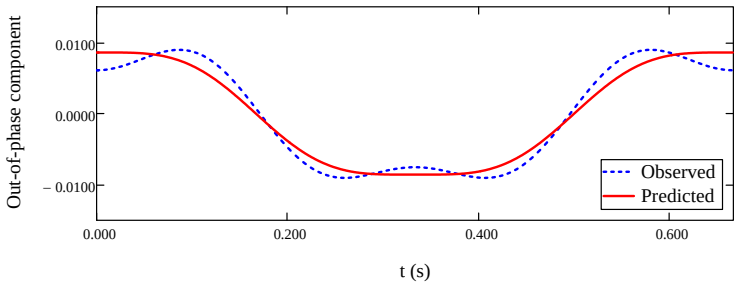

(a) $K^D(\phi_t, \phi)_{3\_1eq}$, $\phi_0 = 10°$, $f = 1.5$ Hz

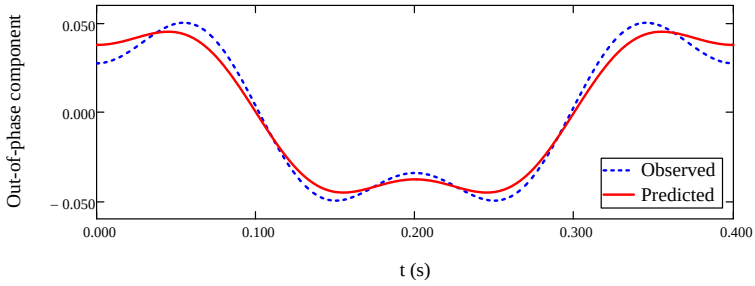

(b) $K^D(\phi_t, \phi)_{3\_1eq}$, $\phi_0 = 20°$, $f = 2.5$ Hz

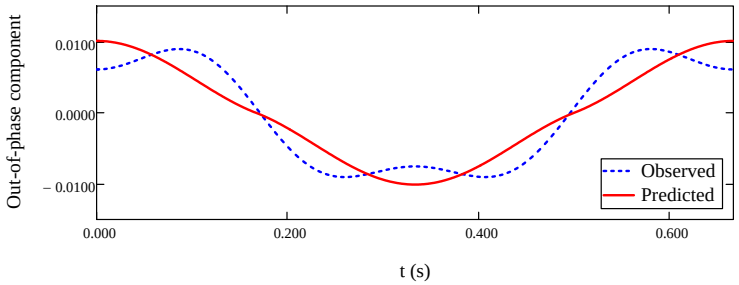

(c) $K^D(\phi_t)_{3\_4eq}$, $\phi_0 = 10°$, $f = 1.5$ Hz

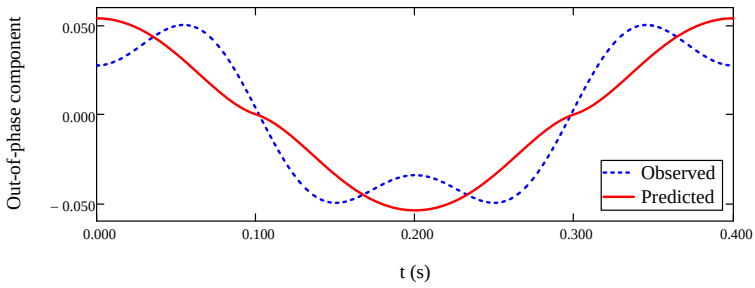

(d) $K^D(\phi_t)_{3\_4eq}$, $\phi_0 = 20°$, $f = 2.5$ Hz

Figure 4.13: Out-of-phase component of the non-dimensional roll moment. Comparison between the fitting of the third order damping models without contribution from the third harmonic. Experimental condition: $C_\Delta = 0.15$, $C_v = 4.3$.

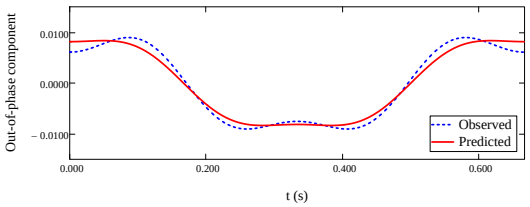

(a) $K^D(\phi_t, \phi)_{3\_1}$, $\phi_0 = 10°$, $f = 1.5$ Hz

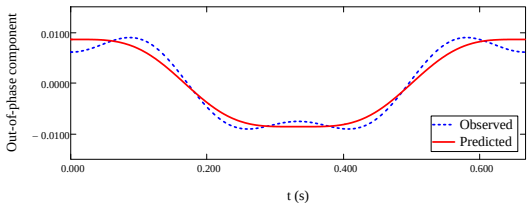

(b) $K^D(\phi_t, \phi)_{3\_1eq}$, $\phi_0 = 10°$, $f = 1.5$ Hz

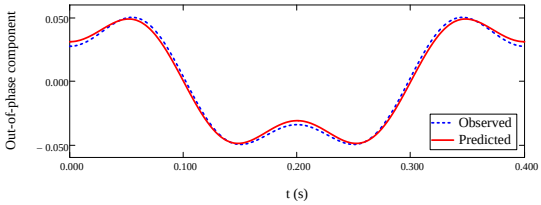

(c) $K^D(\phi_t, \phi)_{3\_1}$, $\phi_0 = 20°$, $f = 2.5$ Hz

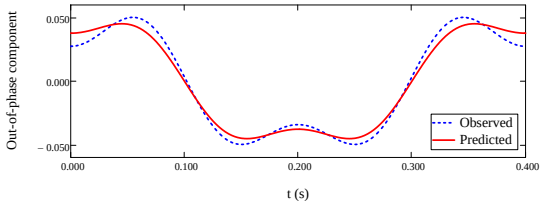

(d) $K^D(\phi_t, \phi)_{3\_1eq}$, $\phi_0 = 20°$, $f = 2.5$ Hz

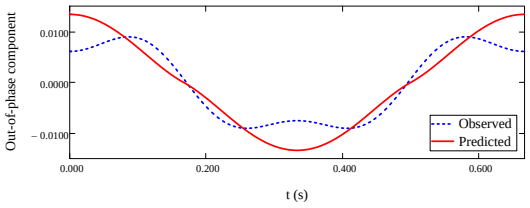

(e) $K^D(\phi_t)_{3\_4}$, $\phi_0 = 10°$, $f = 1.5$ Hz

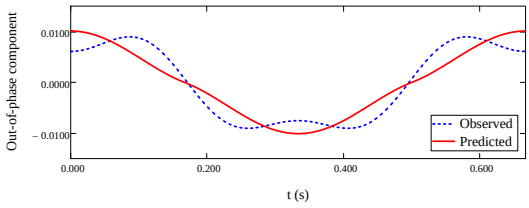

(f) $K^D(\phi_t)_{3\_4eq}$, $\phi_0 = 10°$, $f = 1.5$ Hz

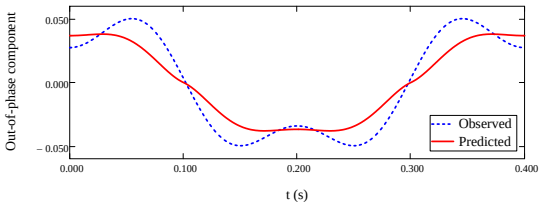

(g) $K^D(\phi_t)_{3\_4}$, $\phi_0 = 20°$, $f = 2.5$ Hz

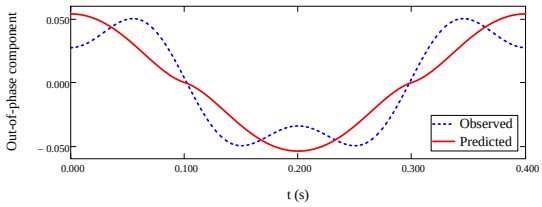

(h) $K^D(\phi_t)_{3\_4eq}$, $\phi_0 = 20°$, $f = 2.5$ Hz

Figure 4.14: Out-of-phase component of the non-dimensional roll moment. Comparison between the fitting of the third order damping models with (left) and without (right) contribution from the third harmonic. Experimental condition: $C_\Delta = 0.15$, $C_v = 4.3$.

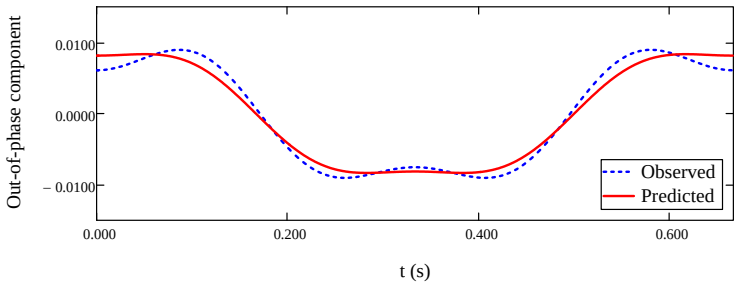

(a) $K^D(\phi_t, \phi)_{3\_1}$

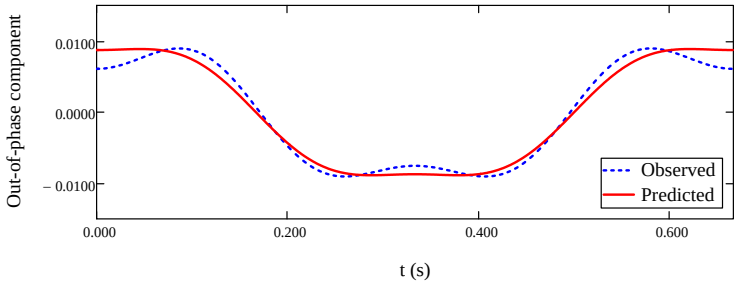

(b) $K^D(\phi_t, \phi)_{3\_2}$

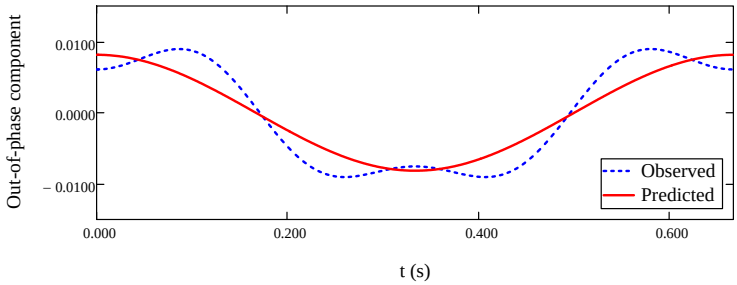

(c) $K^D(\phi_t)_{3\_3}$

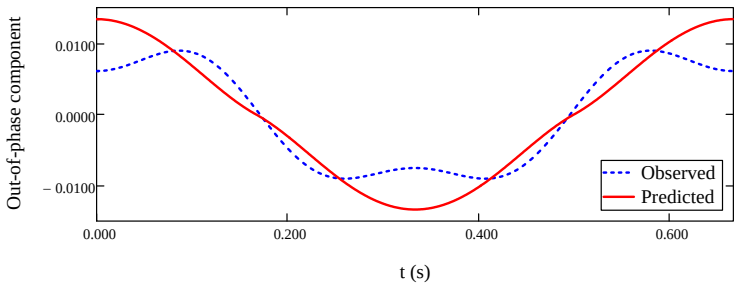

(d) $K^D(\phi_t)_{3\_4}$

Figure 4.15: Out-of-phase component of the non-dimensional roll moment. Comparison between the fitting of the different third order damping models. Experimental condition: $C_\Delta = 0.15$, $C_v = 4.3$, $\phi_0 = 10°$, $f = 1.5$ Hz.

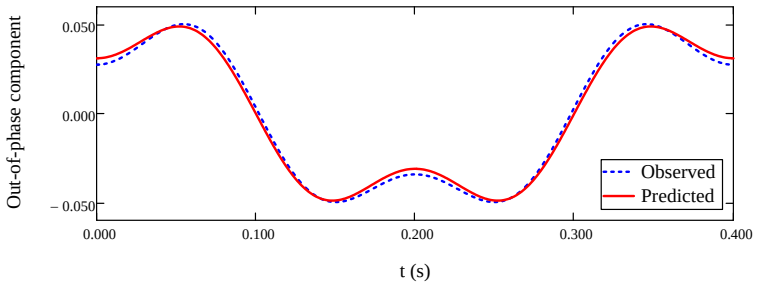

(a) $K^D(\phi_t, \phi)_{3\_1}$

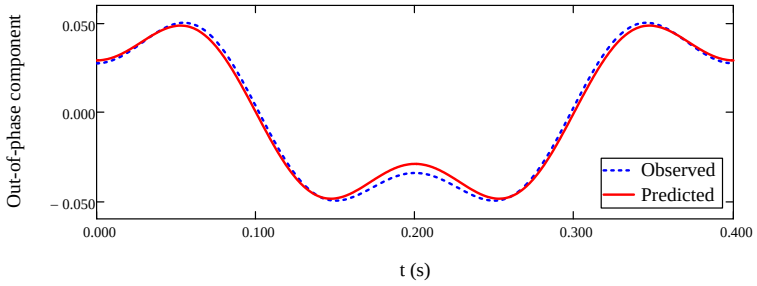

(b) $K^D(\phi_t, \phi)_{3\_2}$

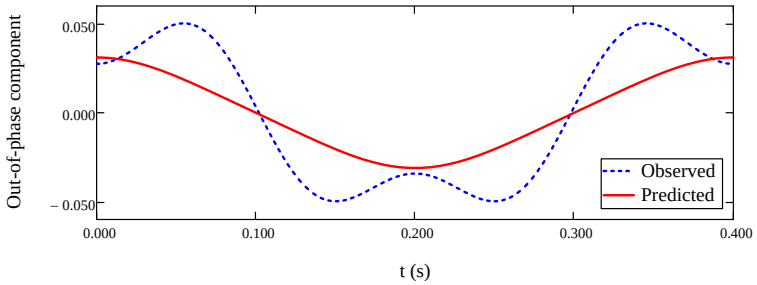

(c) $K^D(\phi_t)_{3\_3}$

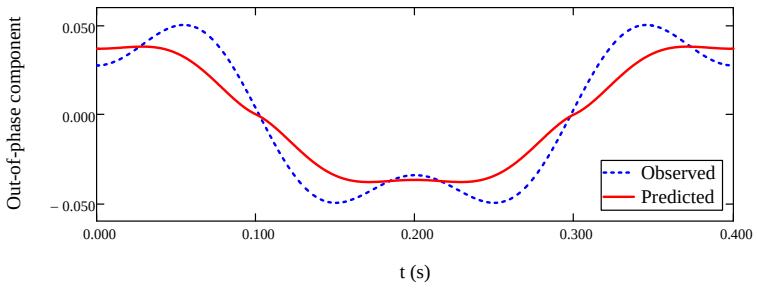

(d) $K^D(\phi_t)_{3\_4}$

Figure 4.16: Out-of-phase component of the non-dimensional roll moment. Comparison between the fitting of the different third order damping models. Experimental condition: $C_\Delta = 0.15$, $C_v = 4.3$, $\phi_0 = 20°$, $f = 2.5$ Hz.

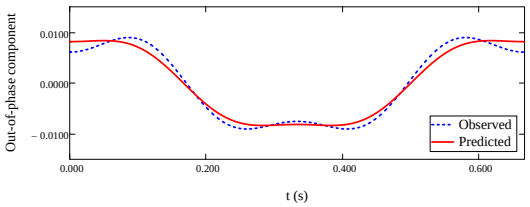

(a) $K^D(\phi_t, \phi)_{3\_1}$, $\phi_0 = 10°$, $f = 1.5$ Hz

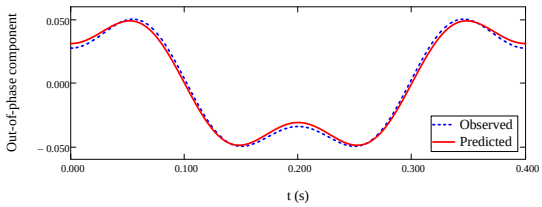

(b) $K^D(\phi_t, \phi)_{3\_1}$, $\phi_0 = 20°$, $f = 2.5$ Hz

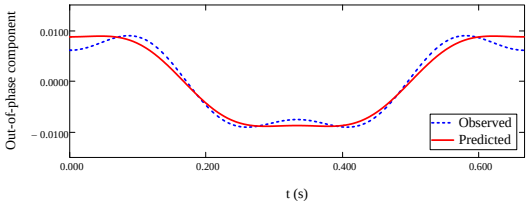

(c) $K^D(\phi_t, \phi)_{3\_2}$, $\phi_0 = 10°$, $f = 1.5$ Hz

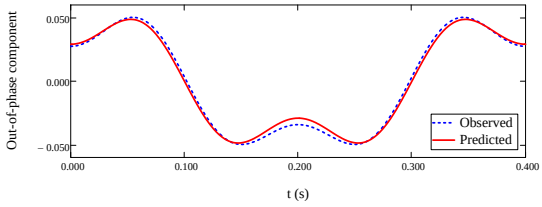

(d) $K^D(\phi_t, \phi)_{3\_2}$, $\phi_0 = 20°$, $f = 2.5$ Hz

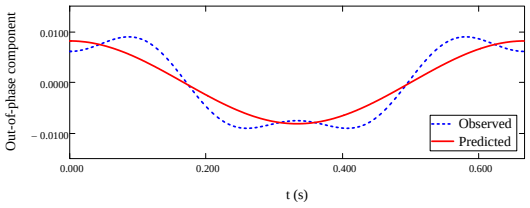

(e) $K^D(\phi_t)_{3\_3}$, $\phi_0 = 10°$, $f = 1.5$ Hz

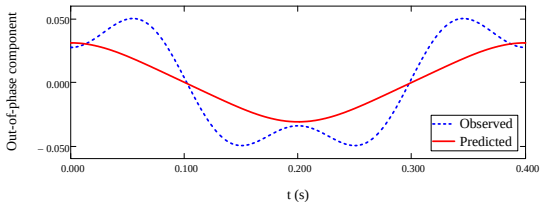

(f) $K^D(\phi_t)_{3\_3}$, $\phi_0 = 20°$, $f = 2.5$ Hz

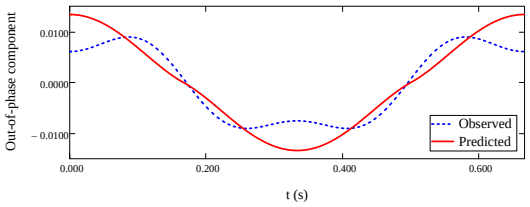

(g) $K^D(\phi_t)_{3\_4}$, $\phi_0 = 10°$, $f = 1.5$ Hz

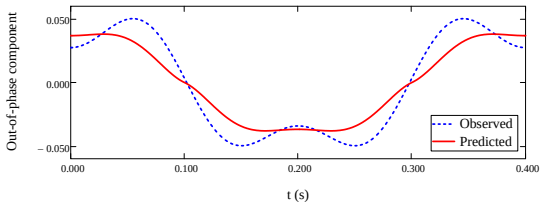

(h) $K^D(\phi_t)_{3\_4}$, $\phi_0 = 20°$, $f = 2.5$ Hz

Figure 4.17: Out-of-phase component of the non-dimensional roll moment. Comparison between the fitting of the different third order damping models. Experimental condition: $C_\Delta = 0.15$, $C_v = 4.3$

For this particular configuration, the model $K^D(\phi_t, \phi)_{3\_2}$ shows the best fitting as expected, given the results presented in Table 4.10, highlighting the importance of B_2 and therefore the dependence of the damping moment on roll amplitude. If the damping coefficient B_3 is omitted, taking into consideration that is not significant (t-ratio< 1), then the linear damping coefficient B_1 can be solved for from Eq. (4.38) yielding:

$$B_1 = \frac{a_1 + a_3}{\omega \phi_0} \tag{4.55}$$

Eq. (4.55) shows that for the lighter configuration run at the higher speed tested the effect of the third order harmonic in the out-of-phase component of the roll moment is to reduce the value of the linear damping coefficient B_1, since the first and the third harmonics are of different sign as shown in Fig. 4.5.

Judge and Judge (2013) observed the amplitude dependence of the equivalent linear damping coefficient (B_{1eq}) for the lighter configuration run at the higher speed. A comparison between the linear damping coefficient (B_1) obtained from the model $K^D(\phi_t, \phi)_{3\_1}$ and their results is presented in Fig. 4.18. Two conclusions can be derived from this comparison; first, the dependence in roll amplitude is adequately accounted for in the model $K^D(\phi_t, \phi)_{3\_1}$ and therefore the coefficients appear both frequency and amplitude independent; and second, from the small amplitude experiments it is possible to obtain an approximate value for the linear damping coefficient B_1.

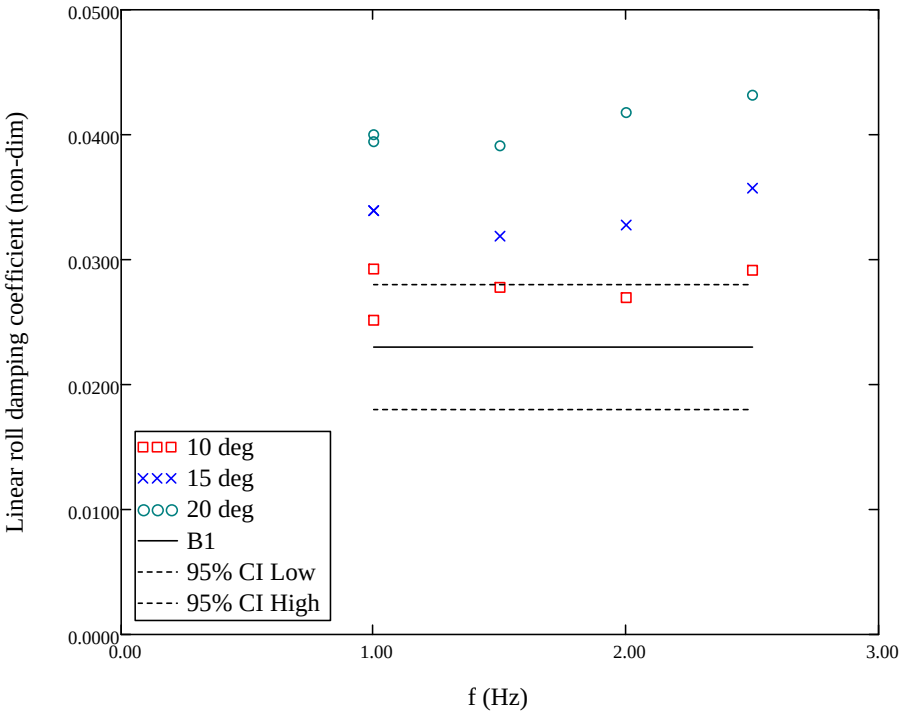

Figure 4.18: Linear roll damping coefficient as a function of amplitude (ϕ_0) and frequency (f) of oscillation. Comparison between B_{1eq} obtained from the first harmonic (a_1) and B_1 obtained from model $K^D(\phi_t, \phi)_{3\_1}$. Experimental condition: $C_\Delta = 0.15$, $C_v = 4.3$.

Taking this result into consideration, the out-of-phase component of the Fourier representation of the numerical roll moment time series for the lighter configuration run at the higher speed is fitted to the model $K^D(\phi_t, \phi)_{3\_1}$; the statistics of this fitting are presented in Table 4.14. The results are consistent with those obtained from the experimental results, the values of the three coefficients overlap in the confidence intervals and the coefficient B_3 is not significant at this confidence level.

Term	Coefficient	Std. Error	95% CI Low	95% CI High	t-ratio
B_1	0.021	4.007E-3	0.011	0.032	1.910
B_2	0.371	0.061	0.216	0.527	2.208
B_3	2.608E-3	3.839E-3	-7.260E-3	0.012	0.245

Table 4.14: Regression analysis and analysis of variance for $K^D(\phi_t, \phi)_{3\_1}$, fitting to the numerical results; ${R_{\text{adj}}}^2 = 0.981$. Experimental conditions: $C_\Delta = 0.15$, $C_v = 4.3$.

The analysis is repeated for the heavier configuration at the lower speed and the results of the regression analysis are presented in Table 4.15 for the $K^D(\phi_t, \phi)_{3\_1}$ model given by Eq. (4.46) and those corresponding to the $K^D(\phi_t)_{3\_4}$ model given by Eq. (4.49) are presented in Table 4.16. As before, the visual results of the fitting are presented in Fig. 4.19 and Fig. 4.20 respectively. Equivalent results for the analysis of the numerical time series are presented in Table 4.17. Also in this case the coefficients overlap in the confidence intervals; however, in contrast with the lighter configuration, B_3 is significant. Here it is interesting to notice that no constraint has been imposed in the sign of the damping coefficients and a negative value of the damping coefficient B_2 has been obtained in the fitting. In Haddara and Bennett (1989) it is suggested that all the damping coefficients must be positive for the system to be dissipative. In this work, the linear damping coefficient is expected to be positive since the system is asymptotically stable in the absence of parametric excitation; however, no reason was found to impose constraints on the sign of the non-linear damping coefficients.

Term	Coefficient	Std. Error	95% CI Low	95% CI High	t-ratio
B_1	0.062	1.042E-3	0.059	0.065	22.208
B_2	-0.097	0.016	-0.137	-0.057	2.631
B_3	7.313E-3	9.984E-4	4.747E-3	9.879E-3	2.114

Table 4.15: Regression analysis and analysis of variance for $K^D(\phi_t, \phi)_{3\_1}$, fitting to the experimental results; ${R_{\text{adj}}}^2 = 0.999$. Experimental condition: $C_\Delta = 0.29$, $C_v = 2.9$.

Term	Coefficient	Std. Error	95% CI Low	95% CI High	t-ratio
B_1	0.064	0.014	0.028	0.099	1.657
B_{2A}	-0.013	0.040	-0.116	0.090	0.115
B_3	0.017	0.026	-0.049	0.083	0.233

Table 4.16: Regression analysis and analysis of variance for $K^D(\phi_t)_{3\_4}$, fitting to the experimental results; ${R_{\text{adj}}}^2 = 0.992$. Experimental condition: $C_\Delta = 0.29$, $C_v = 2.9$.

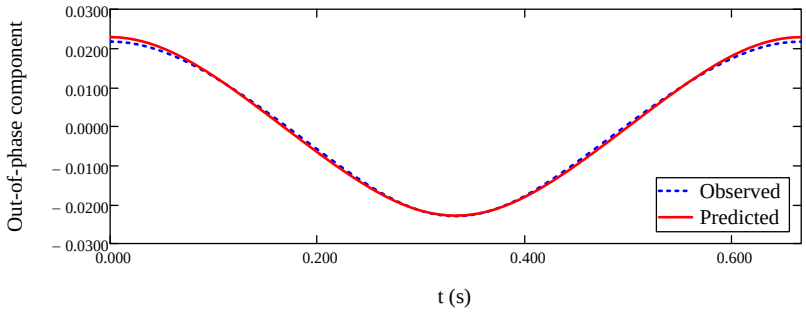

(a) $K^D(\phi_t, \phi)_{3\_1}$, $\phi_0 = 10°$, $f = 1.5$ Hz

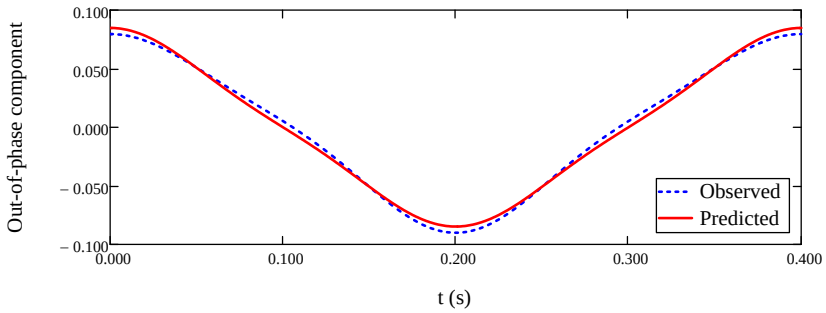

(b) $K^D(\phi_t, \phi)_{3\_1}$, $\phi_0 = 20°$, $f = 2.5$ Hz

Figure 4.19: Out-of-phase component of the non-dimensional roll moment. Comparison between the fitting of the third order damping models $K^D(\phi_t, \phi)_{3\_1}$ and $K^D(\phi_t)_{3\_4}$. Experimental condition: $C_\Delta = 0.29$, $C_v = 2.9$.

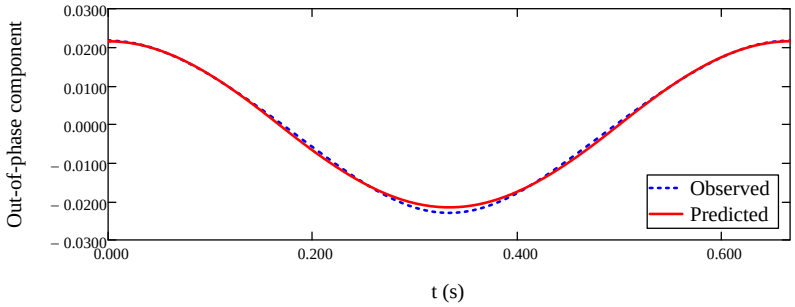

(a) $K^D(\phi_t)_{3\_4}$, $\phi_0 = 10°$, $f = 1.5$ Hz

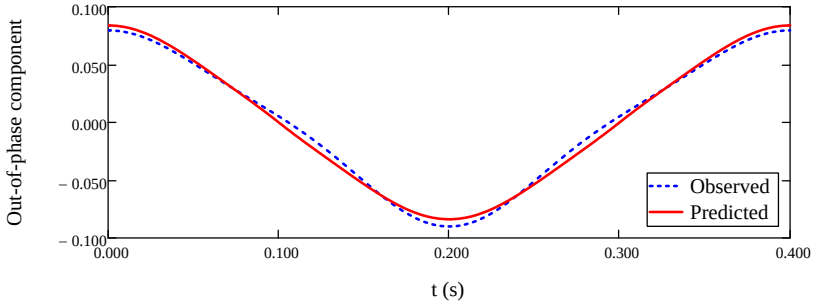

(b) $K^D(\phi_t)_{3\_4}$, $\phi_0 = 20°$, $f = 2.5$ Hz

Figure 4.20: Out-of-phase component of the non-dimensional roll moment. Comparison between the fitting of the third order damping models $K^D(\phi_t, \phi)_{3\_1}$ and $K^D(\phi_t)_{3\_4}$. Experimental condition: $C_\Delta = 0.29$, $C_v = 2.9$.

Term	Coefficient	Std. Error	95% CI Low	95% CI High	t-ratio
B_1	0.067	1.489E-3	0.063	0.071	16.278
B_2	-0.174	0.023	-0.232	-0.116	2.780
B_3	4.340E-3	1.427E-3	6.726E-4	8.008E-3	1.096

Table 4.17: Regression analysis and analysis of variance for $K^D(\phi_t, \phi)_{3\_1}$, fitting to the numerical results; ${R_{\text{adj}}}^2 = 0.999$. Experimental condition: $C_\Delta = 0.29$, $C_v = 2.9$.

A comparison of the equivalent linear damping (B_{1eq}) obtained from the experimental and numerical results with results found by the application of semi-empirical formulae available in the open literature is presented in Table 4.18. Specifically, the comparison is carried out with the formulae presented in Ikeda et al. (1998) for the vertical component of lift damping and in Brown and Klosinski (1995b) (B&K) for the linear roll damping coefficient.

Ikeda's formula has been re-derived in order to obtain the value of the coefficient with respect to a given vertical position of the center of gravity. Ikeda's formula for the vertical component of lift damping is given by:

$$B_{44_{VL}} = \frac{1}{2} C_v \left(\frac{\partial C_{L\beta}}{\partial \theta_E} \right) \frac{B_{wl}}{12 \cos^2 \beta_G} \left(B_{wl} - \frac{3}{2} V_{cg} \sin 2\beta_G \right) \tag{4.56}$$

where B_{wl} corresponds to the non-dimensional wetted beam at the transom (i.e. $B_{wl} = 1$ when the non-dimensional chine wetted length is greater than zero ($\lambda_c > 0$)). With this notation $B_{44_{VL}} \sim B_{1eq}$.

Both, Ikeda's and Brown and Klosinski's formulae are frequency and amplitude independent. Since the numerical and experimental results show dependence on roll amplitude, the maximum and minimum values obtained for each of the two configurations of interest are presented as ranges.

C_Δ	C_v	λ	θ_E	Ikeda	B&K	Experimental	Numerical
0.29	2.9	2.009	4°	0.116	0.083	0.061 – 0.066	0.063 – 0.068
0.15	4.3	0.938	2.9°	0.051	0.096	0.028 – 0.041	0.023 – 0.036

Table 4.18: Equivalent linear damping (B_{1eq}). Comparison with formulae available in the open literature.

Notice that both formulae over-predict the equivalent linear damping. However, Ikeda's formula presents the same trend as the experimental and numerical results. This is in contrast with Brown and Klosinski's formula where the trend is the opposite.

Taking into consideration this consistent trend, Ikeda's formula is used to produce values of the linear damping coefficients for the same heave and pitch perturbations used to find the stiffness coefficients in section 4.3.3.

Fitting a multivariate polynomial regression to these values yields the following results for the damping coefficients of the form $K^D(z, \theta, \phi_t)$. In Table 4.19 the results for the damping coefficients dependent on heave and pitch displacements for the lighter configuration at the higher speed are presented:

Term	Coefficient	Std. Error	95% CI Low	95% CI High	t-ratio
$K_{z\phi_t}$	0.369	4.169E-3	0.360	0.377	44.396
$K_{\theta\phi_t}$	2.537	7.819E-3	2.521	2.553	162.886
$K_{z\theta\phi_t}$	-16.369	0.510	-17.413	-15.379	16.128
$K_{zz\phi_t}$	-1.105	0.310	-1.723	-0.488	1.790
$K_{\theta\theta\phi_t}$	-30.569	1.091	-32.742	-28.396	14.067

Table 4.19: Regression analysis and analysis of variance for $K^D(z, \theta, \phi_t)$; ${R_{\text{adj}}}^2 = 0.999$. Experimental condition: $C_\Delta = 0.15$, $C_v = 4.3$.

The results for the damping coefficients dependent on heave and pitch displacements for the heavier configuration at the lower speed are presented in Table 4.20:

Term	Coefficient	Std. Error	95% CI Low	95% CI High	t-ratio
$K_{z\phi_t}$	0.815	3.806E-3	0.807	0.822	107.46
$K_{\theta\phi_t}$	-0.320	0.011	-0.342	-0.299	14.657
$K_{z\theta\phi_t}$	13.002	0.338	12.329	13.675	19.320
$K_{zz\phi_t}$	-1.821	0.134	-2.087	-1.555	6.846
$K_{\theta\theta\phi_t}$	-7.229	1.110	-9.440	-5.017	3.268

Table 4.20: Regression analysis and analysis of variance for $K^D(z, \theta, \phi_t)$; ${R_{\text{adj}}}^2 = 0.998$. Experimental condition: $C_\Delta = 0.29$, $C_v = 2.9$.

4.5 Conclusions

The time independent (restoring) and time dependent (inertial and dissipative) coefficients for the roll equation of motion derived in Chapter 2, have been obtained for two of the experimental conditions reported in Judge and Judge (2013), by using a combination of Fourier analysis and regression analysis.

The results of the analysis have highlighted the importance of the dissipative non-linearities, particularly in the case of the lighter configuration run at the higher speed. For this configuration, it has been demonstrated that the mixed quadratic with respect to roll amplitude (ϕ) and linear-cubic with respect to roll velocity (ϕ_t) damping model is capable to adequately represent the dependence of the linear damping coefficient on roll amplitude. Also, it has been shown that in this regard this model is superior than the mixed quadratic-cubic damping model suggested in ITTC (2011).

It is important to mention that if an equivalent linear damping coefficient to be used in the roll equation of motion is derived from the large amplitude runs, this value would be about two times the value of the linear damping coefficient in the case of the lighter configuration run at the higher speed. In Chapter 6, the consequences of using one value or the other in the construction of the stability boundaries for the prediction of unstable roll oscillatory motions will be addressed.

With regards to the contribution of the higher order harmonics, it has been shown that even though the statistics of the fitting with the first harmonic alone might be better than those obtained when fitting both the first and the third harmonic, the fitting of the time series is not. Therefore, it is suggested to include the higher order harmonics in the computation of the damping coefficients in the cases with important dissipative non-linearities.

Regarding the inertial coefficients, further analysis of the in-phase component of the Fourier representation of the roll moment time series is required. The results of both the stiffness and the inertial coefficients has suggested the need to include up to fifth order non-linearities in order to improve the fitting and obtain coefficients independent of amplitude and frequency, specially in the case of the lighter configuration run at the higher speed.

CHAPTER 5

Stability Analysis: A Hill's Equation with Cubic Non-linearities

5.1 Chapter Overview

In this chapter the dynamics of a non-linear form of Hill's equation in the neighborhood of a 2:1 resonance are investigated. The analysis is restricted to positive values of linear stiffness and linear damping since the system that gives rise to the equation is asymptotically stable in the absence of parametric excitation. Stability boundaries resulting from a first order solution obtained by the Two Variable Expansion Method are presented in order to show the effect of the periodic damping term in the stability boundaries of the damped Mathieu's equation with cubic non-linearities.

5.2 Introduction

In Chapter 2 the non-dimensional heave-roll-pitch system to a single degree of freedom was reduced by assuming an ordering in the different coefficients of the equation of motion obtaining an effective one-way coupling between heave-pitch and roll.

Also, by assuming the response of the autonomous heave-pitch system to be a stable harmonic motion (limit cycle) and by rescaling the non-dimensional time with the exciting frequency, the non-dimensional roll equation of motion was written in the form:

$$\begin{aligned}
&\phi_{\tau\tau} + \frac{1}{\omega}\left(K_1^D + f_0^{\phi_t}\right)\phi_\tau + \frac{1}{\omega}\left(f_1^{\phi_t}\cos\left(\tau - \psi_1^{\phi_t}\right)\right)\phi_\tau \\
&\quad + \frac{1}{\omega^2}\left(K_1^S + f_0^{\phi}\right)\phi + \frac{1}{\omega^2}\left(f_1^{\phi}\cos\left(\tau - \psi_1^{\phi}\right)\right)\phi \\
&\quad + \frac{1}{\omega}\left(f_2^{\phi_t}\cos\left(2\,\tau - \psi_2^{\phi_t}\right)\right)\phi_\tau + \frac{1}{\omega^2}\left(f_2^{\phi}\cos\left(2\,\tau - \psi_2^{\phi}\right)\right)\phi \\
&\quad + \left(K_{11}^A\right)\phi^2\phi_{\tau\tau} + \left(K_{23}^A\right)\phi\,\phi_\tau^2 + \frac{1}{\omega}\left(K_{12}^D\right)\phi^2\phi_\tau + \omega\left(K_{17}^D\right)\phi_\tau^3 + \frac{1}{\omega^2}\left(K_7^S\right)\phi^3 = 0
\end{aligned} \tag{5.1}$$

It has been suggested in Katayama (2002) that what is known in the small craft community as *chine-walking* could be roll parametrically excited by periodic motions in heave and/or pitch when their frequency is nearly twice the roll natural frequency (i.e., *parametric rolling*). Therefore, it is of interest to investigate the existence of bounded periodic motions (stable limit cycles) in roll (i.e., Eq. (5.1)) parametrically excited by heave and pitch, when the frequency of the heave and pitch motion (ω) is nearly twice the roll natural frequency (a 2:1 resonance). A first order approximate solution to Eq. (5.1) will be sought by the Two Variable Expansion Method (or Method of Multiple Scales) in the vicinity of the principal parametric resonance. With this in mind, Eq. (5.1) is written in the form of a nonlinear Hill's equation:

$$\begin{aligned}
&x_{tt} + \left(\delta + \epsilon\cos(t - \psi_1)\right)x + \left(B_1 + f_{\phi_t}\cos(t - \psi_2)\right)x_t + \\
&\qquad C_3x^3 + A_2x^2\,x_{tt} + A_3x\,x_t^2 + B_2x^2x_t + B_3x_t^3 = 0
\end{aligned} \tag{5.2}$$

where the correspondence between Eq. (5.1) and Eq. (5.2) is as follows:

$$\delta = \frac{1}{\omega^2}\left(K_1^S + f_0^\phi\right) \qquad \epsilon = \frac{1}{\omega^2}\left(f_1^\phi\right) \qquad \psi_1 = \psi_1^\phi$$

$$B_1 = \frac{1}{\omega}\left(K_1^D + f_0^{\phi_t}\right) \qquad f_{\phi_t} = f_1^{\phi_t} \qquad \psi_2 = \psi_1^{\phi_t} \qquad C_3 = \frac{1}{\omega^2}\left(K_7^S\right)$$

$$A_2 = K_{11}^A \qquad A_3 = K_{23}^A \qquad B_2 = \frac{1}{\omega}\left(K_{12}^D\right) \qquad B_3 = \omega\left(K_{17}^D\right)$$

In Eq. (5.2) the parametric excitations with higher harmonics in Eq. (5.1) has been omitted since in the vicinity of the principal parametric resonance, when $\delta \approx 0.25$, they will not appear in the approximate solution.

In Eq. (5.2) x represents roll amplitude, f_{ϕ_t} is the amplitude of the linear periodic damping term, the A_3 term represents non-linear added mass, the $B_{2,3}$ terms represent non-linear damping and the C_3 term represents non-linear stiffness. Here $\epsilon > 0$ and $f_{\phi_t} > 0$ are assumed without loss of generality. Moreover, the analysis is restricted to positive values of linear stiffness and linear damping ($\delta > 0\,, B_1 > 0$) since the system Eq. (5.1) is assumed to be asymptotically stable in the absence of parametric excitation and non-linearities.

Eq. (5.2) has been previously studied by Ng and Rand (2002) for the case without linear damping, by Rand et al. (2005) for the case without time dependent damping and by Oh et al. (2000) for the case without A_3 and B_2. Here, the results of the first order approximation to Eq. (5.2) are generalized by using the (δ, ϵ) parameter space (or the Ince-Strutt diagram). The results are presented in the (δ, ϵ) parameter space taking into consideration that the naval architecture community is familiar with the stability boundaries (transition curves) in the Ince-Strutt diagram (e.g. Neves (2007)).

5.3 First Order Approximation

The amplitude of the periodic damping and the non-linear terms are scaled with the forcing amplitude ϵ in order to perturb the linear harmonic oscillator; therefore $B_1 = \epsilon\mu, A_{2,3} = \epsilon\alpha_{2,3}, B_{2,3} = \epsilon\beta_{2,3}, C_3 = \epsilon\chi_3, f_{\phi_t} = \epsilon F$. Substitution of these into Eq. (5.2) yields:

$$\begin{aligned} x_{tt} + (\delta + \epsilon\cos(t-\psi_1))\, x + \epsilon\left(\mu + F\cos(t-\psi_2)\right) x_t + \\ \epsilon\left(\chi_3 x^3 + \alpha_2 x^2\, x_{tt} + \alpha_3 x\, x_t^2 + \beta_2 x^2 x_t + \beta_3 x_t^3\right) = 0 \end{aligned} \tag{5.3}$$

Following Rand (2012) the Two Variable Expansion Method (or Method of Multiple Scales) is applied with $\xi = t$ and $\eta = \epsilon t$ in order to investigate the dynamics of Eq. (5.2) for small forcing amplitude ϵ:

$$x_t = x_\xi + \epsilon x_\eta \qquad x_{tt} = x_{\xi\xi} + 2\epsilon x_{\xi\eta} + \epsilon^2 x_{\eta\eta} \tag{5.4}$$

To investigate the principal subharmonic resonance in which the forcing frequency is twice the natural frequency, the detuning parameter δ_1 is introduced by expanding δ in a power series around the 2:1 subharmonic resonance:

$$\delta = \frac{1}{4} + \epsilon\,\delta_1 \tag{5.5}$$

Next, x is expanded in a power series:

$$x = x_0 + \epsilon\, x_1 \tag{5.6}$$

Replacing Eq. (5.4), Eq. (5.5) and Eq. (5.6) in Eq. (5.3) and collecting terms of equal

order in ϵ yields:

$$x_{0_{\xi\xi}} + \frac{1}{4}x_0 = 0 \tag{5.7}$$

$$x_{1_{\xi\xi}} + \frac{1}{4}x_1 = -2x_{0_{\xi\eta}} - \delta_1 x_0 - x_0\cos(\xi - \psi_1) - \mu x_{0_\xi} - F\cos(\xi - \psi_2)\, x_{0_\xi} + \tag{5.8}$$

$$- \chi_3 x_0^3 - \alpha_2 x_0^2 x_{0_{\xi\xi}} - \alpha_3 x_0 x_{0_\xi}^2 - \beta_2 x_0^2 x_{0_\xi} - \beta_3 x_{0_\xi}^3$$

The general solution of Eq. (5.7) is given by:

$$x_0 = u(\eta)\cos\frac{\xi}{2} + v(\eta)\sin\frac{\xi}{2} \tag{5.9}$$

After replacing Eq. (5.9) in Eq. (5.8), removal of secular terms yields the following slow-flow that describes the dynamics of Eq. (5.3) for small ϵ:

$$\begin{aligned} u_\eta = &\left(\frac{3}{4}\chi_3 + \frac{1}{16}\alpha_3 - \frac{3}{16}\alpha_2\right) v\left(u^2+v^2\right) - \left(\frac{1}{8}\beta_2 + \frac{3}{32}\beta_3\right) u\left(u^2+v^2\right) + \\ &\left(\delta_1 - \frac{1}{2}\cos\psi_1 + \frac{1}{4}F\sin\psi_2\right) v + \left(-\frac{1}{2}\mu + \frac{1}{2}\sin\psi_1 + \frac{1}{4}F\cos\psi_2\right) u \equiv f_1(u,v) \\ v_\eta = &-\left(\frac{1}{8}\beta_2 + \frac{3}{32}\beta_3\right) v\left(u^2+v^2\right) - \left(\frac{3}{4}\chi_3 + \frac{1}{16}\alpha_3 - \frac{3}{16}\alpha_2\right) u\left(u^2+v^2\right) - \\ &\left(\frac{1}{2}\mu + \frac{1}{2}\sin\psi_1 + \frac{1}{4}F\cos\psi_2\right) v + \left(-\delta_1 - \frac{1}{2}\cos\psi_1 + \frac{1}{4}F\sin\psi_2\right) u \equiv f_2(u,v) \end{aligned} \tag{5.10}$$

In order to investigate periodic motions in Eq. (5.3), the slow-flow is transformed to polar coordinates with:

$$u(\eta) = R(\eta)\cos\theta(\eta) \qquad v(\eta) = R(\eta)\sin\theta(\eta) \tag{5.11}$$

where Eq. (5.9) takes the alternative form:

$$x_0 = R(\eta)\cos\left(\frac{\xi}{2} - \theta(\eta)\right) \tag{5.12}$$

Replacing Eq. (5.11) in Eq. (5.10) yields the slow-flow in polar form:

$$\begin{aligned} R_\eta &= -\frac{\beta}{32}R^3 - \frac{R}{4}\left(2\mu + 2\sin\left(2\theta - \psi_1\right) - F\cos\left(2\theta - \psi_2\right)\right) \equiv f_1(R,\theta) \\ \theta_\eta &= -\frac{\alpha}{16}R^2 - \frac{1}{4}\left(4\delta_1 + 2\cos\left(2\theta - \psi_1\right) + F\sin\left(2\theta - \psi_2\right)\right) \equiv f_2(R,\theta) \end{aligned} \tag{5.13}$$

where $\alpha = 12\chi_3 + \alpha_3 - 3\alpha_2$ represents the effect of the non-dissipative non-linearities and $\beta = 4\beta_2 + 3\beta_3$ represents the effect of the dissipative non-linearities. Additional third order non-dissipative and dissipative non-linearities can be added rationally to α and β affecting their values but not their general effect in the dynamics of the system, as predicted by the first order approximation.

5.4 Periodic Motions

As mentioned in the introduction, the interested of this research lies in the existence of periodic motions (stable limit cycles) in Eq. (5.2) since they will correspond to *parametric roll*. Eq. (5.10) represents the dynamics of Eq. (5.2) in the slow-time scale $\eta = \epsilon t$; so, the solution to Eq. (5.10) can be understood as the amplitude envelope of the solution in the fast-time scale $\xi = t$. Therefore, non-trivial real equilibria ($R \neq 0$) of the slow-flow Eq. (5.13) correspond to limit cycles in Eq. (5.3); they are found by setting $f_{1,2}(R,\theta) = 0$.

The two resulting equations can be manipulated to yield:

$$\sin 2\theta = -\frac{(2q\alpha + p\beta)\, R^2 + 32q\delta_1 + 16p\mu}{p^2 + q^2} \tag{5.14}$$
$$\cos 2\theta = -\frac{(q\beta - 2p\alpha)\, R^2 - 32p\delta_1 + 16q\mu}{p^2 + q^2}$$

where

$$p = 8\,(2\cos\psi_1 - F\sin\psi_2)$$
$$q = 8\,(2\sin\psi_1 + F\cos\psi_2)$$
$$p^2 + q^2 = 64\,(F_\psi + 4)$$
$$F_\psi = F(F - 4\sin\psi)$$
$$\psi = \psi_2 - \psi_1$$

Using the identity $\sin^2 2\theta + \cos^2 2\theta = 1$, yields a quadratic equation in R^2:

$$a_4 R^4 + a_2 R^2 + a_0 = 0 \tag{5.15}$$

with coefficients

$$a_4 = 4\alpha^2 + \beta^2 \tag{5.16}$$
$$a_2 = 32\,(4\alpha\delta_1 + \beta\mu)$$
$$a_0 = 64\left(4\left(\mu^2 + 4\delta_1^2 - 1\right) - F_\psi\right)$$

Changes in the number of real roots in Eq. (5.15) correspond to bifurcations in Eq. (5.13). Defining its discriminant as $\Delta = a_2^2 - 4a_4a_0$; the stability boundaries in the (δ_1, μ) parameter space correspond to changes in the number of real roots in

Eq. (5.15) and are given by $a_0 = 0$ and $\Delta = 0$, which yields:

$$\left(\mu^2 + 4\delta_1^2 - 1\right) - \frac{F_\psi}{4} = 0 \tag{5.17}$$

$$(4\alpha^2 + \beta^2)\left(\frac{F_\psi}{4} + 1\right) - 4(\alpha\mu - \beta\delta_1)^2 = 0 \tag{5.18}$$

Defining Λ as the ratio between dissipative and non-dissipative non-linearities and replacing $\beta = \Lambda\alpha$ in Eq. (5.18) above yields:

$$-(\mu - \Lambda\delta_1)^2 + \left(\frac{\Lambda^2}{4} + 1\right)\left(\frac{F_\psi}{4} + 1\right) = 0 \tag{5.19}$$

The number of real roots (limit cycles) in Eq. (5.15) as a function of Δ and a_0, given $a_4 > 0$, can be summarized as follows:

$$\begin{aligned}
&\Delta < 0 && \text{no real roots (no limit cycles)} \\
&\Delta > 0 && \\
&\quad a_0 < 0,\ a_2 > 0, && \text{two real roots (one limit cycle)} \\
&\quad\ \ a_2 < 0, && \text{two real roots (one limit cycle)} \\
&\quad a_0 > 0,\ a_2 > 0, && \text{no real roots (no limit cycles)} \\
&\quad\ \ a_2 < 0, && \text{four real roots (two limit cycles)}
\end{aligned} \tag{5.20}$$

Equations Eq. (5.17) and Eq. (5.19) correspond to conics in the (δ_1, μ) space; specifically, Eq. (5.17) draws an ellipse and Eq. (5.19) draws two parallel lines tangent to the ellipse. Figure 5.1 shows schematically Eq. (5.17) and Eq. (5.19) for $\Lambda = 1$, $\Lambda = -1$, and for the limiting cases $\Lambda = 0$ (only non-dissipative non-linearities, $\beta = 0$) and $\Lambda = \infty$ (only dissipative non-linearities, $\alpha = 0$). In the latter case, when there is no time dependent damping term ($F_\psi = 0$) the two parallel lines correspond to the stability boundaries $\delta_1 = \pm 1/2$ in the linear undamped Mathieu's equation.

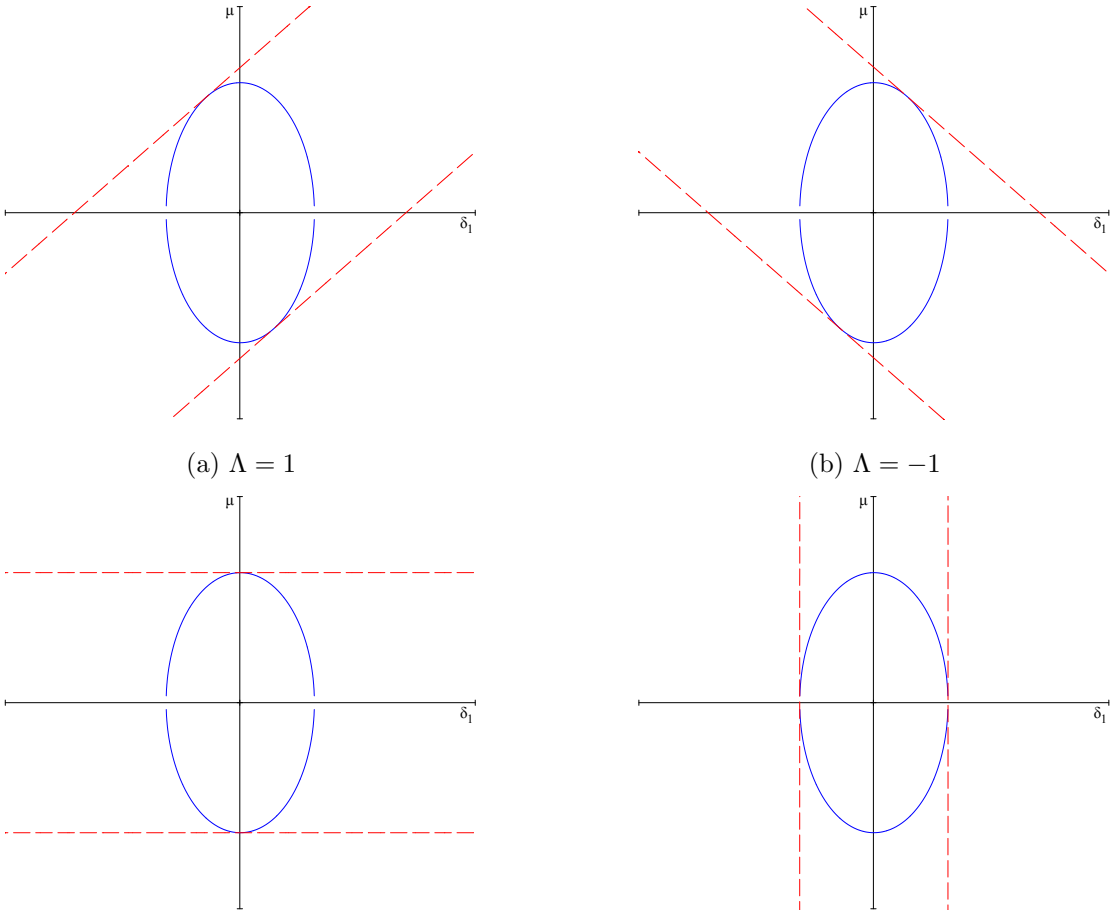

(a) $\Lambda = 1$ (b) $\Lambda = -1$

(c) $\Lambda = 0$ ($\beta = 0$) (d) $\Lambda = \infty$ ($\alpha = 0$)

Figure 5.1: Stability boundaries. $a_0 = 0$ and $\Delta = 0$ as a function of Λ in the (δ_1, μ) Parameter Space

In general, for $\Lambda > 0$ the points of tangency between the ellipse and the two parallel lines are in the second and the fourth quadrants, and for $\Lambda < 0$ they are in the first and the third quadrants. The effect of F_ψ is to scale what is depicted in Fig. 5.1; its largest size is obtained when $\psi = 3\pi/2$ and its smallest size when $\psi = \pi/2$. Also, in the special case when $F = 2$ and $\psi = \pi/2$ the ellipse collapses to the origin of the (δ_1, μ) parameter space and the two parallel lines collapse to a single line passing through this point.

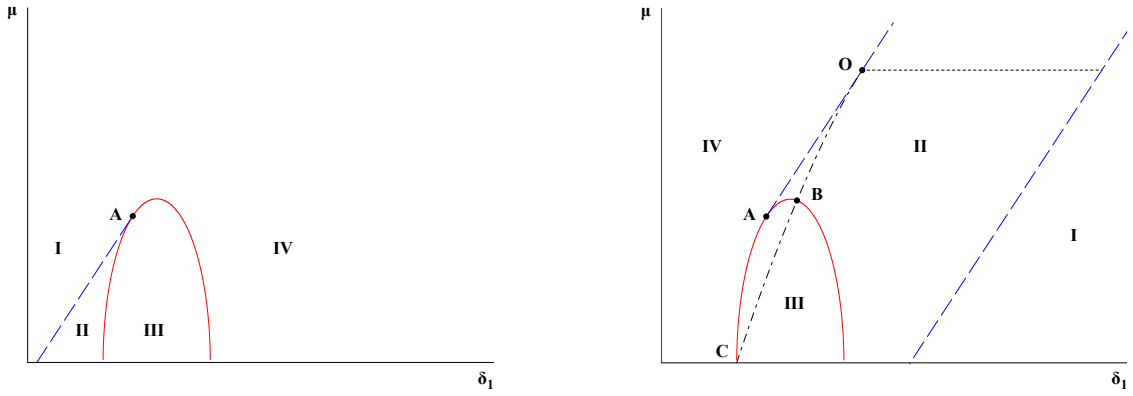

(a) $\beta > 0 \quad \Lambda > 0$ (b) $\beta < 0 \quad \Lambda > 0$

Figure 5.2: Stability Regions in the (δ_1, μ) Parameter Space

In Fig. 5.2, the plot on the left illustrates the case for $\beta > 0$ with $\Lambda > 0$ ($\Lambda = 1$) and the plot on the right the case for $\beta < 0$ with $\Lambda > 0$ ($\Lambda = 1$). In each case only the boundaries to the regions where the nature and the number of roots in Eq. (5.15) changes have been kept. It is of interest in the definition of the different regions the point of tangency A which depends on the value of Λ and F_ψ and is given in the first and second quadrant by Eq. (5.21). Also, in Fig. 5.2b the line segment $\overline{\text{CBO}}$ have been added corresponding to a Hopf bifurcation in the slow-flow solution which will be discussed later in the following Section 5.7, Eq. (5.38). Notice that in Fig. 5.2 the μ-axis has been shifted to the left (i.e., the μ-axis does not cross the δ_1-axis at $\delta_1 = 0$) in order to improve readability.

$$\delta_{1A} = \frac{\Lambda}{4}\sqrt{\frac{F_\psi + 4}{\Lambda^2 + 4}} \qquad \mu_A = \sqrt{\frac{F_\psi + 4}{\Lambda^2 + 4}} \tag{5.21}$$

The attention is restricted to the first two quadrants in the (δ_1, μ) parameter space since only cases with positive linear damping $\mu > 0$ are being considered. Notice that as Λ increases the point of tangency moves toward the δ_1-axis reducing the area bounded by the axis itself, the ellipse and the tangent to the ellipse (Region II when $\beta > 0$).

The maximum value of μ on the half ellipse when $\delta_1 = 0$ is given by Eq. (5.22).

$$\mu_{max} = \sqrt{\frac{F_\psi}{4} + 1} \tag{5.22}$$

The value of δ_1 at the intersection with the half ellipse, $\delta_{1_{a,b}}$, and at the intersection with the tangent line, $\delta_{1_{c,d}}$, for a given value of μ_* is given by:

$$\delta_{1_{a,b}} = \pm\frac{1}{2}\sqrt{1 - \mu_*^2 + \frac{F_\psi}{4}} \qquad \mu_* \leq \mu_{max} \tag{5.23}$$

$$\delta_{1_{c,d}} = \frac{1}{\Lambda}\left(\mu_* \mp \sqrt{\left(\frac{\Lambda^2}{4} + 1\right)\left(\frac{F_\psi}{4} + 1\right)}\right) \tag{5.24}$$

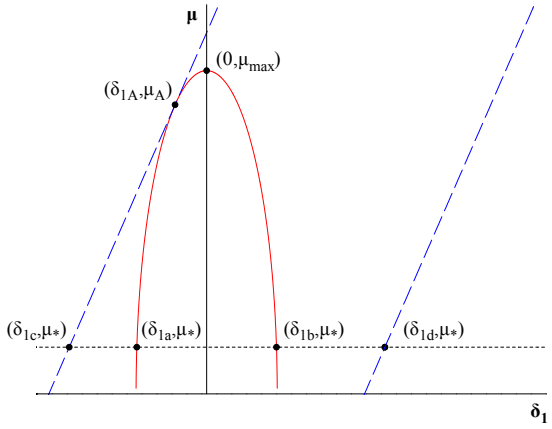

Figure 5.3: The (δ_1, μ) Parameter Space.

Important for the discussion on the number of real roots in Eq. (5.15), is the fact that inside the ellipse $a_0 < 0$ and outside the two parallel lines $\Delta < 0$. Contrasting with Eq. (5.20), the regions in Fig. 5.2 as a function of the discriminant Δ and the coefficients in Eq. (5.15) can be characterized as follows:

Region I	$\Delta < 0$	$a_0 > 0$	$a_2 < 0$	No limit cycles
Region II	$\Delta > 0$	$a_0 > 0$	$a_2 < 0$	Two limit cycles
Region III	$\Delta > 0$	$a_0 < 0$	$a_2 < 0$	One limit cycle
			$a_2 > 0$	One limit cycle
Region IV	$\Delta > 0$	$a_0 > 0$	$a_2 > 0$	No limit cycles

In summary, it is found that in regions I and IV there are no real solutions other than the trivial equilibrium ($R = 0$). In the following Section 5.5 it will be shown that the origin (the trivial equilibrium corresponding to the planing hull in its upright position) is asymptotically stable everywhere but in region III (where it is unstable). Therefore, referring to the physical system represented by Eq. (5.2), for a set of parameters (δ_1, μ) in regions I and IV every set of initial conditions will yield roll motions that will end with the planing hull in the upright position. In contrast, in region III the periodic motion (limit cycle) in roll is the only possible behavior since in this region the origin is unstable, so infinitesimally small perturbations from the upright position will grow into a periodic roll motion about the trivial equilibrium. In Region II there are two possible behaviors depending on initial conditions, either the planing hull will return to its upright position or it will roll about this equilibrium, so this region is characterized by bi-stability. The stability of the limit cycles found in regions II and III is discussed later in Section 5.6.

5.5 Stability of the Origin

Eq. (5.2) represents the roll motion of a planing hull parametrically excited by harmonic heave and pitch motions. Notice that the origin $(u, v) = (0, 0)$ is a fixed point of Eq. (5.10) ($R = 0$ is a fixed point of Eq. (5.13)). Referring to the physical system Eq. (5.1), as mentioned above, the origin corresponds to the upright position

of the planing hull ($\phi = 0$). The stability of the origin is investigated by looking at the eigenvalues in the Jacobian of the (u, v) system Eq. (5.10) linearized about $(0, 0)$.

$$\mathbf{J}(\mathbf{u}, \mathbf{v}) = \begin{bmatrix} f_{1_u} & f_{1_v} \\ f_{2_u} & f_{2_v} \end{bmatrix} \tag{5.25}$$

where

$$\begin{aligned}
f_{1_u} &= -\frac{3}{32}\beta\, u^2 + \frac{1}{8}\alpha\, uv - \frac{1}{32}\beta\, v^2 - \frac{1}{2}\mu + \frac{1}{4}F\cos\psi_2 + \frac{1}{2}\sin\psi_1 \\
f_{1_v} &= \frac{1}{16}\alpha\, u^2 - \frac{1}{16}\beta\, uv + \frac{3}{16}\alpha\, v^2 + \delta_1 + \frac{1}{4}F\sin\psi_2 - \frac{1}{2}\cos\psi_1 \\
f_{2_u} &= -\frac{3}{16}\alpha\, u^2 - \frac{1}{16}\beta\, uv - \frac{1}{16}\alpha\, v^2 - \delta_1 + \frac{1}{4}F\sin\psi_2 - \frac{1}{2}\cos\psi_1 \\
f_{2_v} &= -\frac{1}{32}\beta\, u^2 - \frac{1}{8}\alpha\, uv - \frac{3}{32}\beta\, v^2 - \frac{1}{2}\mu - \frac{1}{4}F\cos\psi_2 - \frac{1}{2}\sin\psi_1
\end{aligned}$$

Solving for the eigenvalues when $(u, v) = (0, 0)$ yields:

$$\lambda_{1,2} = -\frac{1}{2}\mu \pm \frac{1}{2}\sqrt{(1 - 4\delta_1^2) + \frac{1}{4}F_\psi} \tag{5.26}$$

For a stable origin $\Re(\lambda_{1,2}) < 0$ is required, which due to the fact that $\mu > 0$ is assumed allows re-writting it in terms of Eq. (5.26) as follows:

$$\mu^2 > \left(1 - 4\delta_1^2\right) + \frac{1}{4}F_\psi \tag{5.27}$$

In terms of the coefficients of the quartic Eq. (5.17), the condition above corresponds to $a_0 > 0$; therefore, inside the ellipse described by $a_0 = 0$ the origin is unstable and outside of it the origin is stable. For a given μ there is a change in the stability of the origin every time the boundary described by $a_0 = 0$ is crossed by changing, quasi-statically, δ_1. In other words, for $\mu > \mu_{max}$ the origin is always stable.

5.6 Stability of Periodic Motions

The stability of the limit cycles in Eq. (5.3) is investigated by looking at the eigenvalues in the Jacobian of the (R, θ) system Eq. (5.13) linearized about a non-trivial equilibrium ($R \neq 0$). The dependency on θ and ψ_1 can be eliminated by noticing that at fixed points the following two equations are satisfied:

$$\begin{aligned} 2\cos(2\theta - \psi_1) + F\sin(2\theta - \psi_2) &= -\frac{1}{4}\left(\alpha R^2 + 4\delta_1\right) \\ F\cos(2\theta - \psi_1) - 2\sin(2\theta - \psi_2) &= \frac{1}{8}\left(\beta R^2 + 2\mu\right) \end{aligned} \tag{5.28}$$

The Jacobian of the polar form of the slow-flow Eq. (5.13) can be written as:

$$\mathbf{J}(\mathbf{R}) = \begin{bmatrix} -\frac{\beta}{16}R^2 & \frac{\alpha}{8}R^3 + 2\delta_1 R \\ -\frac{\alpha}{8}R & -\frac{\beta}{16}R^2 - \mu \end{bmatrix} \tag{5.29}$$

with eigenvalues:

$$\lambda_{1,2} = -\frac{1}{2}\left(\mu + \frac{\beta}{8}R^2\right) \pm \frac{1}{4}\sqrt{4\left(\mu^2 + 4\delta_1^2\right) - \frac{1}{4}\left(\alpha R^2 + 8\delta_1\right)^2} \tag{5.30}$$

The condition for stability of the limit cycles is $\Re\left(\lambda_{1,2}\right) < 0$. Since $\mu > 0$ is assumed, then when $\beta > 0$ this condition can be re-write in terms of Eq. (5.30) as follows:

$$\left(\mu + \frac{1}{8}\beta R^2\right)^2 > \frac{1}{4}\left(4\left(\mu^2 + 4\delta_1^2\right) - \frac{1}{4}\left(\alpha R^2 + 8\delta_1\right)^2\right) \tag{5.31}$$

$$R^2\left(4\alpha^2 + \beta^2\right) + 16\left(4\alpha\delta_1 + \beta\mu\right) > 0 \tag{5.32}$$

which upon substitution of $\beta = \Lambda\alpha$, yields:

$$\alpha^2(\Lambda^2 + 4)R^2 + 16\alpha(4\delta_1 + \mu\Lambda) > 0 \tag{5.33}$$

In terms of the coefficients of the quartic Eq. (5.15), the inequality above can be written as:

$$a_4 R^2 + \frac{1}{2} a_2 > 0 \qquad \text{or} \qquad 2a_4 R^2 + a_2 > 0 \tag{5.34}$$

The solution to the quartic equation Eq. (5.15) is given by:

$$R^2 = \frac{1}{2a_4}\left(-a_2 \pm \sqrt{a_2^2 - 4a_4 a_0}\right) \quad \text{or} \quad 2a_4 R^2 + a_2 = \pm\sqrt{a_2^2 - 4a_4 a_0} \tag{5.35}$$

Therefore, looking at Fig. 5.2 it is observed that in region III ($a_0 < 0$) the limit cycle is stable and in region II ($a_0 > 0, a_2 < 0$) the larger limit cycle is stable and the smaller limit cycle is unstable.

When $\beta < 0$ the larger limit cycle is stable when the following condition is satisfied:

$$R < 2\sqrt{-2\frac{\mu}{\beta}} \tag{5.36}$$

5.7 Quasi-periodic Motions

Quasi-periodic motions in Eq. (5.3) correspond to periodic motions (limit cycles) in the slow-flow Eq. (5.10). As shown in Rand et al. (2005), one way to have limit cycles in this system is via Hopf bifurcations.

The condition for Hopf bifurcations to occur in the slow-flow is $tr(J) = 0$ and $det(J) > 0$, where J is the Jacobian of the slow-flow Eq. (5.25) about an equilibrium point. Setting $tr(J) = 0$ yields:

$$\mathbf{tr}(\mathbf{J}(\mathbf{0},\mathbf{0})) = -\mu - \frac{1}{8}\beta\left(u^2+v^2\right) = -\left(\mu + \frac{1}{8}\beta R^2\right) = 0 \tag{5.37}$$

Therefore the condition for the Hopf is to have μ and β of opposite signs. Under the assumption of positive linear damping ($\mu > 0$) the first order analysis predicts that there are periodic orbits (limit cycles) in the slow-flow Eq. (5.10), and therefore there are quasi-periodic motions in Eq. (5.3), only when the averaged nonlinear damping is negative ($\beta < 0$). Replacing Eq. (5.37) in Eq. (5.15) with $\beta = \Lambda\alpha$ yields the following equation for the Hopf bifurcation:

$$\left(\frac{\Lambda^2}{4}+1\right)\mu^2 - 4\Lambda\delta_1\mu + \Lambda^2\left[4\delta_1^2 - \left(\frac{F_\psi}{4}+1\right)\right] = 0 \tag{5.38}$$

Eq. (5.38) draws a rotated ellipse in the (δ_1, μ) parameter space with points of tangency on the two parallel lines described by Eq. (5.19). The coordinates of the point of tangency O in the first and second quadrants are given by:

$$\delta_{1O} = \left(\frac{4-\Lambda^2}{4\Lambda}\right)\sqrt{\frac{F_\psi+4}{\Lambda^2+4}} \qquad \mu_O = 2\sqrt{\frac{F_\psi+4}{\Lambda^2+4}} \tag{5.39}$$

The value of δ_1 at the intersection with the rotated ellipse, $\delta_{1H_{a,b}}$, for a given value of μ_* is given by:

$$\delta_{1H_{a,b}} = \frac{1}{2}\left(\frac{\mu_*}{\Lambda}\right) \mp \frac{1}{2}\sqrt{\left(\frac{F_\psi}{4}+1\right) - \left(\frac{\mu_*}{2}\right)^2} \qquad \mu_* \leq \mu_O \tag{5.40}$$

It turns out that only δ_{1H_a} is relevant since it is on this curve where the stability of the equilibrium corresponding to the largest R changes from stable to unstable and

a stable limit cycle in the slow-flow is born around this equilibrium. For this reason, only segment $\overline{\text{CBO}}$ of the rotated ellipse is plotted in Fig. 5.2b.

The coordinates of the point of intersection B between Eq. (5.17) and Eq. (5.38) in the first and second quadrants depend on the sign of Λ and are given by:

$$\delta_{1B} = \text{sgn}(\Lambda)\left(\frac{4-3\Lambda^2}{4}\right)\sqrt{\frac{F_\psi+4}{(\Lambda^2+4)(9\Lambda^2+4)}} \tag{5.41}$$

$$\mu_B = \text{sgn}(\Lambda)(4\Lambda)\sqrt{\frac{F_\psi+4}{(\Lambda^2+4)(9\Lambda^2+4)}}$$

5.8 Bifurcations

The information presented in the previous sections is summarized by discussing the bifurcations involved in the (δ_1, μ) parameter space.

When $\beta > 0$ three different scenarios are observed and discussed below assuming $\Lambda > 0$ ($\alpha > 0$):

1. $\mu_* \geq \mu_{max}$: The origin is stable and its stability does not change as δ_1 is changed.

2. $\mu_* \in [\mu_A, \mu_{max})$: The origin becomes unstable as δ_1 is decreased from right to left across the right side of the half ellipse ($\delta_1 = \delta_{1_b}$) and at the same time a stable subharmonic 2:1 motion is born. This motion grows in amplitude and near the left side of the half ellipse decreases sharply until it disappears when this boundary is crossed ($\delta_1 = \delta_{1_a}$), at the same time the stability of the origin changes becoming stable again. This scenario is depicted in Fig. 5.4a.

3. $\mu_* \in [0, \mu_A)$: The origin becomes unstable as δ_1 is decreased from right to left across the right side of the half ellipse ($\delta_1 = \delta_{1_b}$) and at the same time a

stable subharmonic 2:1 motion is born. This motion grows in amplitude as δ_1 continues to decrease. When the left side of the half ellipse is crossed ($\delta_1 = \delta_{1_a}$), the origin becomes stable and an unstable 2:1 subharmonic motion is born. As δ_1 continues to decrease, the unstable motion continues to grow. When the boundary given by the tangent line is crossed ($\delta_1 = \delta_{1_c}$), the stable and the unstable motions collapse and disappear. This scenario is depicted in Fig. 5.4b.

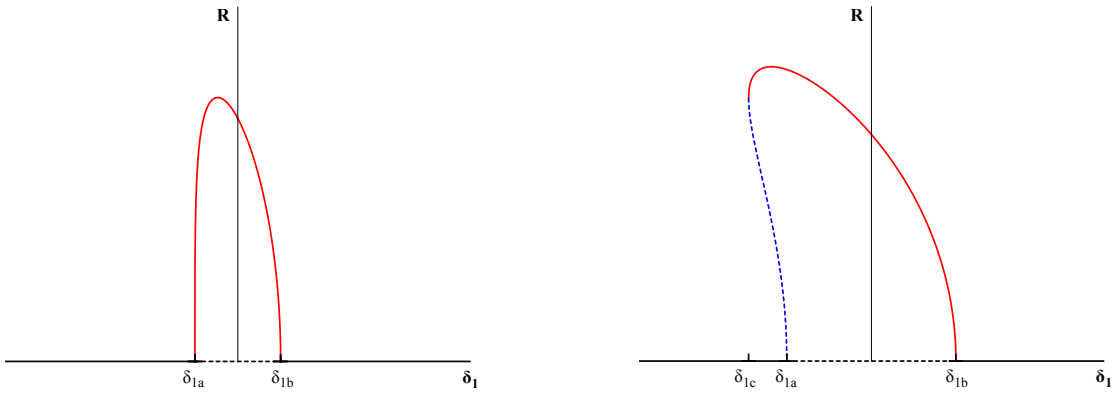

(a) $\mu_* \in [\mu_A, \mu_{max})$ (b) $\mu_* \in [0, \mu_A)$

Figure 5.4: Sequence of Bifurcations in (R, δ_1) for $\beta > 0$ when $\Lambda > 0$ ($\alpha > 0$)

In terms of bifurcations, these changes in the stability of the origin (the trivial solution) and the creation and destruction of periodic motions (limit cycles) correspond in the second scenario to a sequence of Hopf bifurcations (pitchfork bifurcations in the cartesian form of the slow-flow), and in the third scenario to a sequence of Hopf bifurcations (supercritical and subcritical) followed by a bifurcation of cycles (saddle-node bifurcation in the cartesian form of the slow-flow). If $\Lambda < 0$ ($\alpha < 0$) is assumed, then a similar sequence of bifurcations is observed if the stability boundaries are crossed from left to right by increasing δ_1.

When $\beta < 0$, four different scenarios are observed and discussed below assuming $\Lambda > 0$ ($\alpha < 0$):

1. $\mu_* \geq \mu_O$: The origin is stable and its stability does not change as δ_1 is changed.

However, as δ_1 is increased across the left side of the parallel lines ($\delta_1 = \delta_{1_c}$) two unstable subharmonic 2:1 motions are born simultaneously away from the origin. These motions change in amplitude at different rates, but collapse and disappear when the parallel line on the right side is crossed ($\delta_1 = \delta_{1_d}$). This scenario is depicted in Fig. 5.5a.

2. $\mu_* \in [\mu_{max}, \mu_O)$: The origin is stable and its stability does not change as δ_1 is changed. However, as δ_1 is increased across the left side of the parallel lines ($\delta_1 = \delta_{1_c}$) two subharmonic 2:1 motions are born simultaneously away from the origin, one stable and the other one unstable. As δ_1 is increased and the boundary of the Hopf bifurcation is crossed ($\delta_1 = \delta_{1H_a}$) the stable subharmonic 2:1 motion becomes unstable and a periodic motion in the slow-flow is born around this equilibrium. These motions change in amplitude at different rates, but collapse and disappear when the parallel line on the right side is crossed ($\delta_1 = \delta_{1_d}$). This scenario is depicted in Fig. 5.5b.

3. $\mu_* \in [\mu_A, \mu_{max})$: As δ_1 is increased across the left side of the parallel lines ($\delta_1 = \delta_{1_c}$) two subharmonic 2:1 motions are born simultaneously, one stable and the other one unstable. The stable motion grows in size and the unstable motion shrinks until it collapses with the origin as δ_1 is increased across the left side of the half ellipse ($\delta_1 = \delta_{1_a}$); at the same time the origin becomes unstable. As δ_1 is increased and the boundary of the Hopf bifurcation is crossed ($\delta_1 = \delta_{1H_a}$) the stability of the subharmonic 2:1 motion changes and a periodic motion in the slow-flow is born. As δ_1 is increased across the right side of the half ellipse ($\delta_1 = \delta_{1_b}$) the origin changes its stability and a second unstable subharmonic 2:1 motion is born. As δ_1 is increased across the right side of the parallel lines ($\delta_1 = \delta_{1_d}$) the two unstable subharmonic 2:1 motions collapse and disappear. This scenario is depicted in Fig. 5.5c.

4. $\mu_* \in [0, \mu_A)$: The origin becomes unstable as δ_1 is increased across the left side of the half ellipse ($\delta_1 = \delta_{1_a}$) and a stable subharmonic 2:1 motion is born. As δ_1 is increased and the boundary of the Hopf bifurcation is crossed ($\delta_1 = \delta_{1H_a}$) the stability of the subharmonic 2:1 motion changes and a periodic motion in the slow-flow is born. As δ_1 is increased across the right side of the half ellipse ($\delta_1 = \delta_{1_b}$) the origin changes its stability and a second unstable subharmonic 2:1 motion is born. As δ_1 is increased across the right side of the parallel lines ($\delta_1 = \delta_{1_d}$) the two unstable subharmonic 2:1 motions collapse and disappear. This scenario is depicted in Fig. 5.5d.

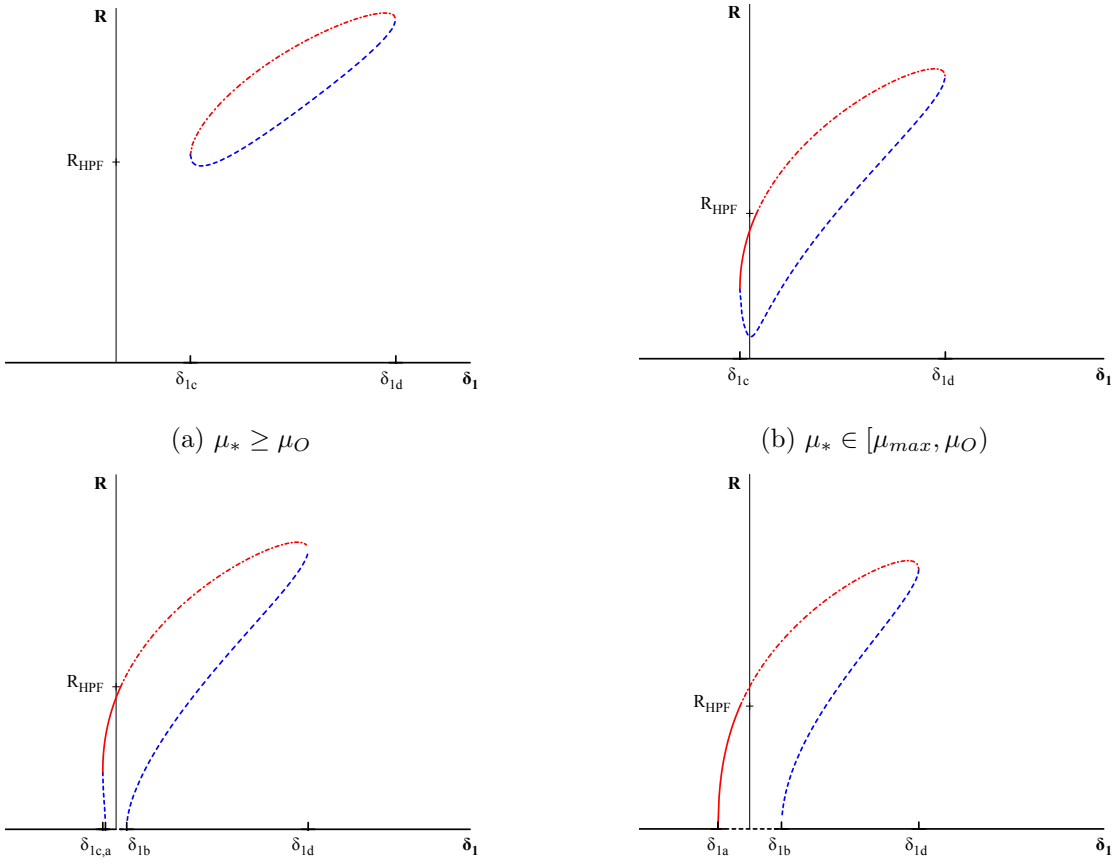

(a) $\mu_* \geq \mu_O$

(b) $\mu_* \in [\mu_{max}, \mu_O)$

(c) $\mu_* \in [\mu_A, \mu_{max})$

(d) $\mu_* \in [0, \mu_A)$

Figure 5.5: Sequence of Bifurcations in (R, δ_1) for $\beta < 0$ when $\Lambda > 0$ ($\alpha < 0$)

In the last three scenarios the Hopf bifurcations in the slow-flow are accompanied by bifurcations of the same type reported in Ng and Rand (2002). In the cartesian form of the slow-flow they correspond to homoclinic and heteroclinic bifurcations as well as limit cycles at infinity. In general terms, the limit cycles in the slow-flow born at the Hopf bifurcation are destroyed when the unstable manifold of the saddle point feeding the limit cycle turns into a homoclinic orbit as δ_1 is varied. In the cases when there are two real roots (Region III) this saddle point corresponds to the origin and therefore the homoclinic orbit has two loops. In this scenario, a limit cycle that encircles the origin is born from the homoclinic bifurcation and is destroyed at infinity as δ_1 is further increased. This sequence of bifurcations is shown in Fig. 5.6. In the cases when there are four real roots (Region II) the saddle point feeding the limit cycle corresponds to the equilibrium closer to the origin. In this case, the limit cycle encircling the origin is not born from the homoclinic bifurcation but from a heteroclinic bifurcation. This sequence of bifurcations is shown in Fig. 5.7, where the nomenclature in Ng and Rand (2002) has been kept and limit cycles as those that encircle non-origin equilibria are referred to as type 1 and those that encircle the origin are referred to as type 2. Numerical integration of Eq. (5.10) indicates that the curves where these bifurcations are born run nearly parallel to the right of the Hopf bifurcation curve Eq. (5.38) starting at point C and ending at point O. A dashed line has been drawn in Fig. 5.2b running parallel to the δ_1 axis at $\mu = \mu_O$ to indicate that above that value these bifurcations have not been found in this part of region II.

The information above is summarized in relation to the physical system represented by Eq. (5.2), for a set of parameters (δ_1, μ) in regions II and III where periodic motions are found. It is noticed that the characteristics of these periodic motions depend on the sign of the averaged dissipative non-linearities β. If $\beta > 0$, for values of (δ_1, μ) in regions II and III, it is possible to observe the planing hull oscillating in a limit cycle

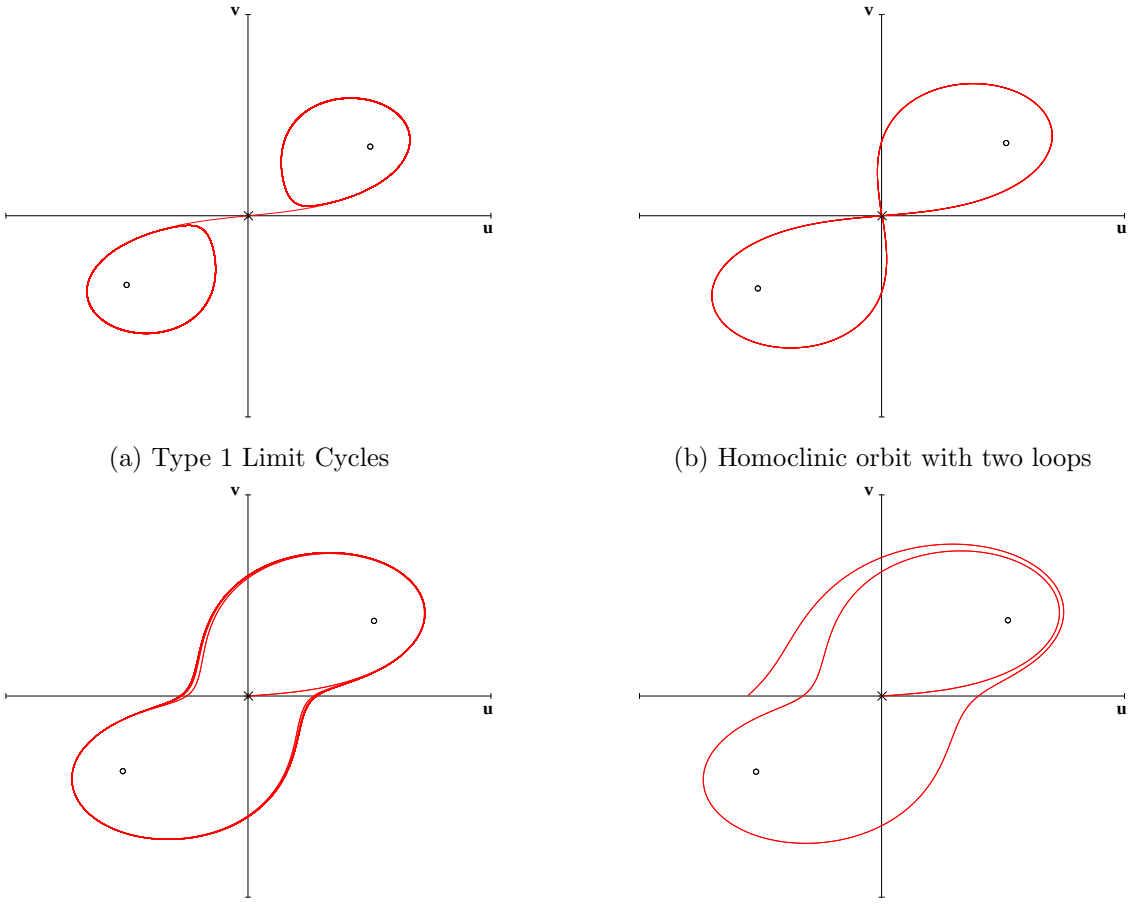

(a) Type 1 Limit Cycles

(b) Homoclinic orbit with two loops

(c) Type 2 Limit Cycle

(d) Type 2 Limit Cycle destroyed at ∞

Figure 5.6: Sequence of Bifurcations in (u, v) for $\beta < 0$; $(\delta_1, \mu) \in$ Region III

about the upright position. If $\beta < 0$, then for values of (δ_1, μ) in regions II and III it is possible to observe the planing hull oscillating with unbounded periodic motions until it capsizes. The exception to this behaviour is found in the region bounded by the segments $\overline{\text{CAO}}$ and $\overline{\text{CBO}}$ and a very narrow region to the right of the segment $\overline{\text{CBO}}$ (when $\Lambda > 0$) where stable periodic and quasi-periodic motions exist respectively. For values of (δ_1, μ) in this region it is possible to observe the planing hull oscillating in a limit cycle about the upright position. However, independent of the sign of β, in region II these behaviors depend on initial conditions so for a set of them it is possible that the planing hull returns to the upright position since region II is characterized by bi-stability and the upright position is stable.

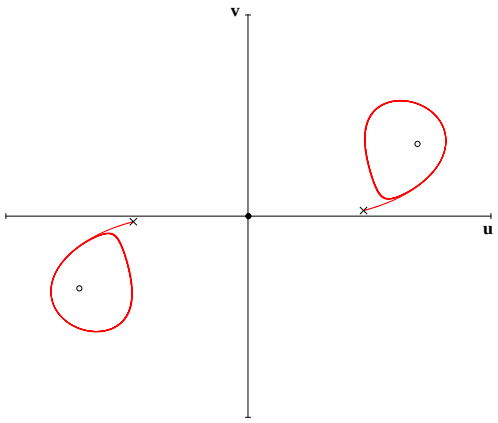

(a) Type 1 Limit Cycles

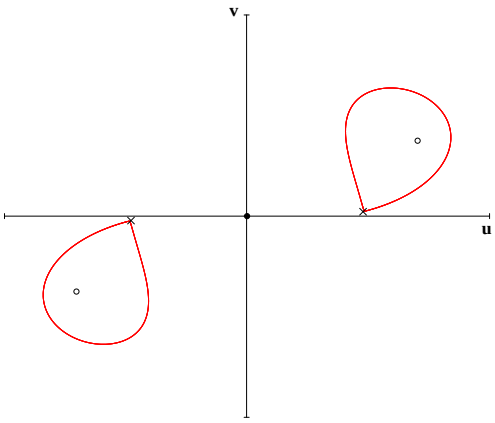

(b) Homoclinic orbits

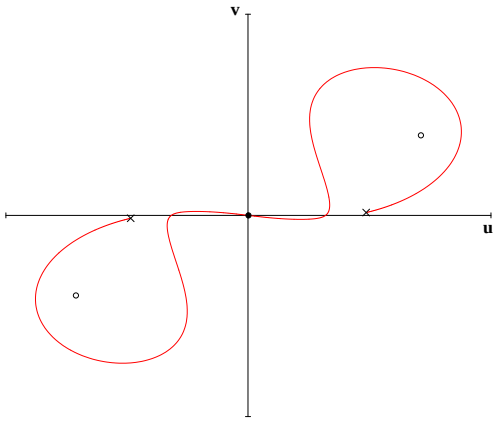

(c) Homoclinic orbits destroyed

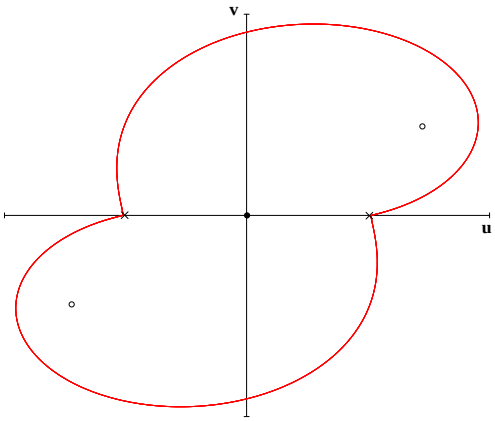

(d) Heteroclinic orbit

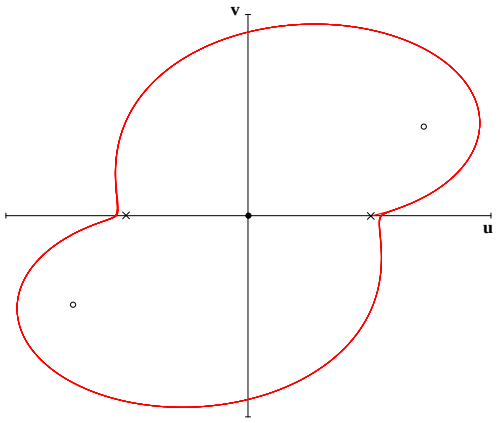

(e) Type 2 Limit Cycle

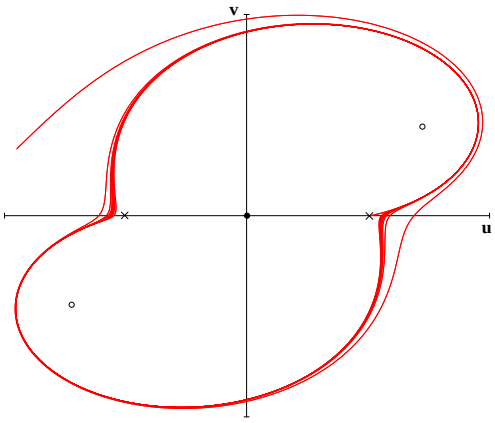

(f) Type 2 Limit Cycle destroyed at ∞

Figure 5.7: Sequence of Bifurcations in (u, v) for $\beta < 0$; $(\delta_1, \mu) \in$ Region II

5.9 Numerical Integration

In this section, Eq. (5.2) is numerically integrated to compare the behaviors observed with those predicted by the first order analysis, including the stability and the amplitude of periodic and quasi-periodic motions. As an example, the following values of the parameters are chosen: $\Lambda = 1$, $\alpha = \beta$, $F = 5$, $\psi = \pi/5$. With this information the coordinates of the degenerate points A, B, and O in the (δ_1, μ) parameter space are computed with Eq. (5.21), Eq. (5.41) and Eq. (5.39) respectively. These results are summarized in Table 5.1. Also, $\mu_{max} = 2.076$ is computed with Eq. (5.22).

	δ_1	μ
A	-0.464	1.857
B	0.129	2.060
O	1.393	3.714

Table 5.1: Degenerate points in the (δ_1, μ) parameter space

To exemplify some behaviours in region III $\mu = 1$ is chosen and to exemplify them in region II $\mu = 2.1$ is chosen. Next the values of the detuning parameter δ_1 corresponding to crossing of the stability boundaries are computed using Eq. (5.23), Eq. (5.24) and Eq. (5.40). These results are summarized in Table 5.2, where the values corresponding to the creation/destruction of homoclinic orbits (HO), heteroclinic orbits (HE) and limit cycles at infinity (LC) have been added. These values have been obtained by iterating the value of the detuning δ_1 and numerically integrating Eq. (5.10) since no analytical expressions have been derived for these bifurcations.

μ	δ_{1_c}	δ_{1_a}	δ_{1H_a}	δ_{1HO}	δ_{1HE}	δ_{1LC}	δ_{1_b}	δ_{1_d}
1.0	-1.321	-0.910	-0.508	-0.391		-0.361	0.910	3.321
2.1	-0.221		0.154	0.337	0.416	0.425		4.421

Table 5.2: Stability boundaries in the (δ_1, μ) parameter space

In order to illustrate the behavior in region III when $\beta > 0$, $(\delta_1, \mu) = (-0.5, 1)$ is chosen and Eq. (5.10) is numerically integrated perturbing slightly the trivial equilibrium and obtaining a limit cycle as predicted. In Fig. 5.8 the results of the numerical integration of Eq. (5.2) is presented together with the amplitude envelope predicted by Eq. (5.10) for $\epsilon = 0.01$. In Fig. 5.9 these results are repeated showing the final two cycles in the time series and comparing them, and the corresponding state space representation, with the results of the first order approximation for three different values of ϵ. As expected, the approximation deteriorates as ϵ is increased; however, the amplitude of the motion and its period are well predicted.

Next quasi-periodic orbits are illustrated, in particular at the sequence of bifurcations presented in Fig. 5.6 and Fig. 5.7. Since $\mu > 0$ ($B_1 > 0$) has been assumed then $\beta < 0$ is required in order to satisfy Eq. (5.37), so $\beta = -1$ is chosen. Eq. (5.2) is numerically integrated with $(\delta_1, \mu) = (-0.45, 1)$ and perturbing slightly the larger fixed point predicted by Eq. (5.15). The result is presented in Fig. 5.10a and corresponds to a type 1 slow-flow limit cycle as shown in Fig. 5.6a. An example of type 2 slow-flow limit cycles is found by choosing $(\delta_1, \mu) = (-0.38, 1)$; the result is presented in Fig. 5.10b and corresponds to the behavior shown in Fig. 5.6c. These results correspond to bifurcations of slow-flow limit cycles found in region III. For readability, in Fig. 5.10 the results of the numerical integration of Eq. (5.2) are compared with the amplitude envelope predicted by the first order approximation Eq. (5.9). Even though there is phase shift difference between the two solutions, the behavior is as predicted and the amplitudes are again well predicted for engineering purposes.

To illustrate the same sequence of bifurcation in region II, the same procedure as above is followed by choosing in this case $(\delta_1, \mu) = (0.25, 2.1)$ to illustrate a type 1 slow-flow limit cycle and $(\delta_1, \mu) = (0.42, 2.1)$ to illustrate a type 2 limit cycle. The results are presented in Fig. 5.11 together with comparisons with the amplitude envelope predicted by the first order approximation. The two behaviors correspond to those presented in Fig. 5.7a and Fig. 5.7e for type 1 and type 2 limit cycles respectively. In the case with detuning $\delta_1 = 0.42$ it is found that starting with equivalent initial conditions (approximated to order ϵ) the solution of the numerical integration is attracted to the trivial equilibrium failing to reproduce the result predicted by the first order approximation but demonstrating the existence of bi-stability in this region.

It is worth mentioning that the values of the parameters in Eq (5.2) have been chosen in order to demonstrate the existence of the different stability regions and the capability of the first order approximation to predict them. Also, the results have been related to what they will physically represent in the case of a planing hull parametrically excited in roll by heave and pitch motions. However, the amplitudes of the motions obtained ($\sim$ 4 rad) would be unrealistic in the case of a planing hull or a ship in general.

5.10 Stability Boundaries - The (δ, ϵ) Parameter Space

The (δ, ϵ) parameter space is typically used in naval architecture to present regions of stability in the study of *parametric roll*; one recent example can be found in Neves (2007). Therefore, it is of interest to relate the discussion of the stability boundaries in the first order (δ_1, μ) parameter space to the (δ, ϵ) parameter space, where any order of approximation of the solution to Eq. (5.2) can be represented.

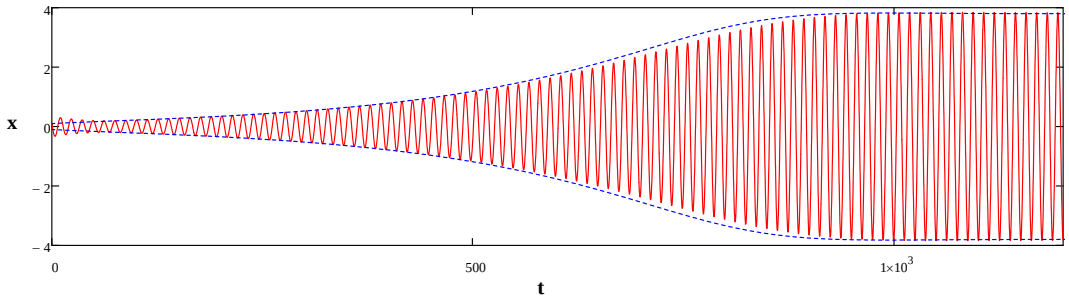

(a) $\epsilon = 0.01$

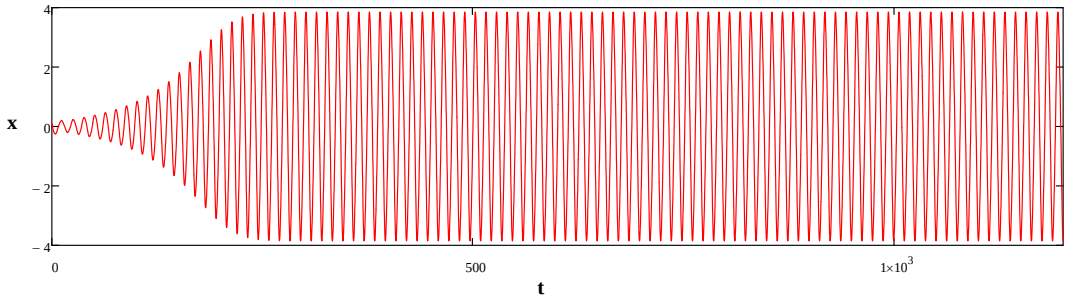

(b) $\epsilon = 0.05$

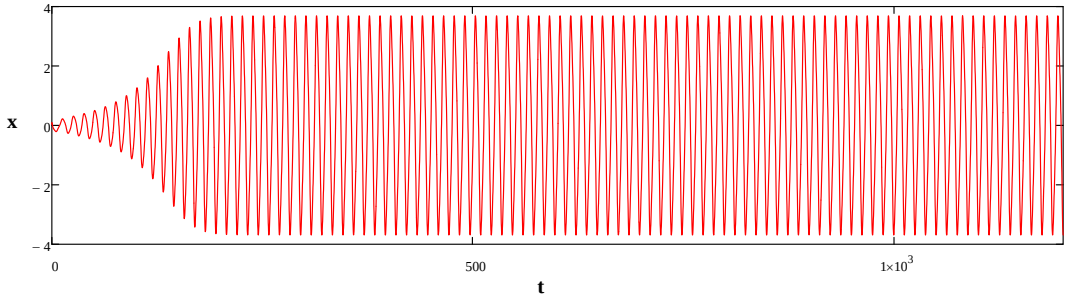

(c) $\epsilon = 0.1$

Figure 5.8: Roll time series for different values of ϵ obtained by numerical integration of Eq. (5.2). Parameters: $(\delta_1, \mu) = (-0.5, 1)$, $\Lambda = 1$ $(\beta = 1, \alpha = 1)$, $F = 5$, $\psi = \pi/5$. Solid lines correspond to numerical integration of Eq. (5.2). Dotted lines in (a) correspond to the amplitude envelope predicted by the slow-flow Eq. (5.10).

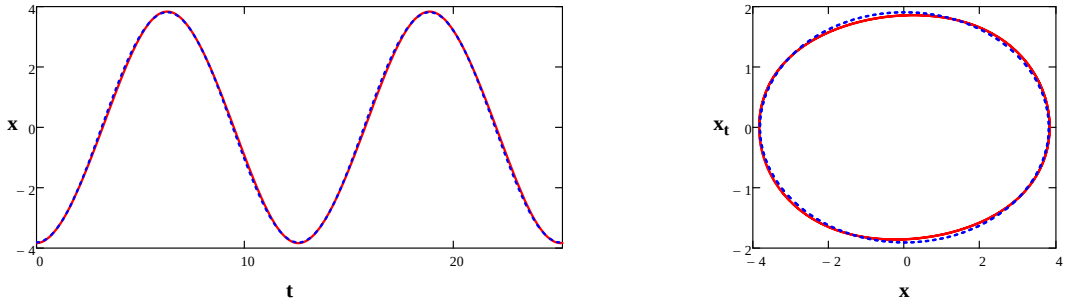

(a) $\epsilon = 0.01$

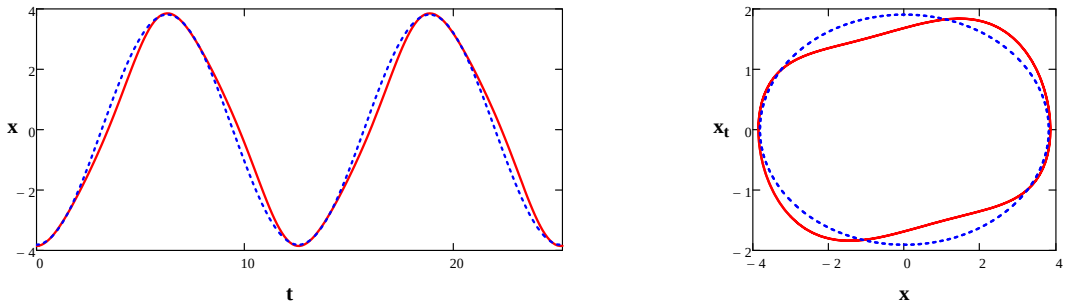

(b) $\epsilon = 0.05$

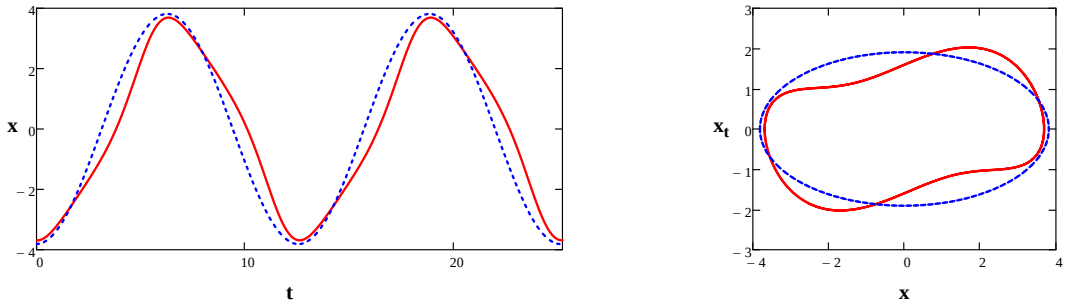

(c) $\epsilon = 0.1$

Figure 5.9: Roll time series and corresponding state space representation for different values of ϵ. Parameters: $(\delta_1, \mu) = (-0.5, 1)$, $\Lambda = 1$ $(\beta = 1, \alpha = 1)$, $F = 5$, $\psi = \pi/5$. Solid lines correspond to numerical integration of Eq. (5.2). Dotted lines correspond to the first order approximation given by Eq. (5.9).

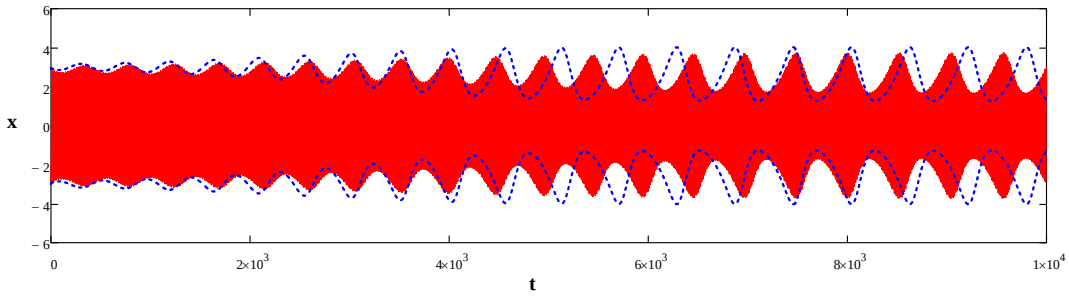

(a) $\delta_1 = -0.45$ - Type 1 slow-flow limit cycle

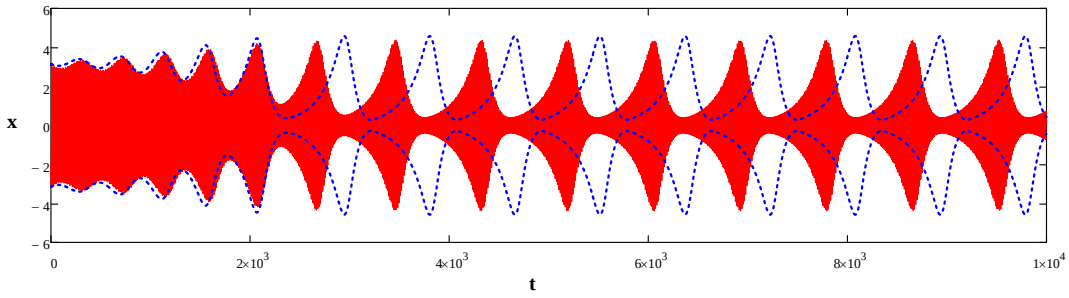

(b) $\delta_1 = -0.38$ - Type 2 slow-flow limit cycle

Figure 5.10: Roll time series for two different values of δ_1 in Region III where quasi-periodic motions are predicted. Parameters: $\epsilon = 0.01$, $\mu = 1$, $\Lambda = 1$ ($\beta = -1, \alpha = -1$), $F = 5$, $\psi = \pi/5$. Solid lines correspond to numerical integration of Eq. (5.2). Dotted lines correspond to the amplitude envelope of the first order approximation given by Eq. (5.9).

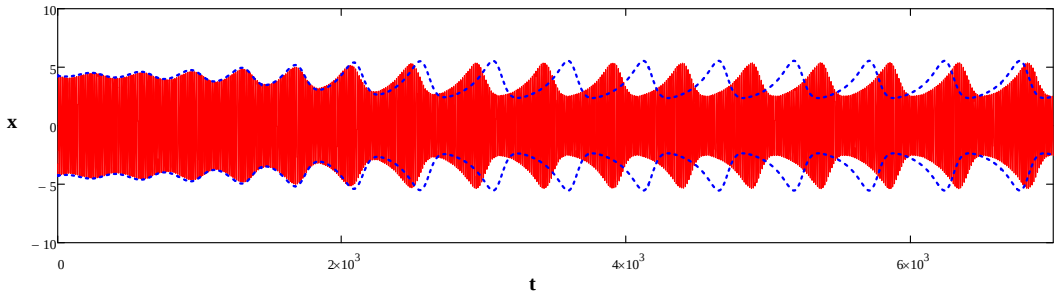

(a) $\delta_1 = 0.25$ - Type 1 slow-flow limit cycle

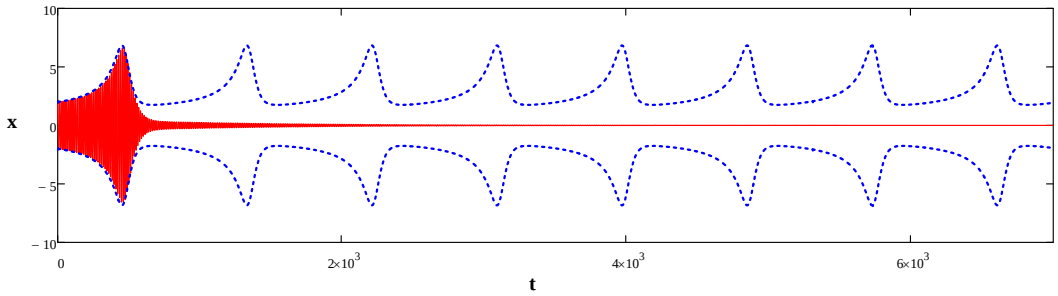

(b) $\delta_1 = 0.42$ - Type 2 slow-flow limit cycle

Figure 5.11: Roll time series for two different values of δ_1 in Region II where quasi-periodic motions are predicted. Parameters: $\epsilon = 0.01$, $\mu = 2.1$, $\Lambda = 1$ ($\beta = -1, \alpha = -1$), $F = 5$, $\psi = \pi/5$. Solid lines correspond to numerical integration of Eq. (5.2). Dotted lines correspond to the amplitude envelope of the first order approximation given by Eq. (5.9).

The stability boundaries in the (δ, ϵ) parameter space are constructed by recalling:

$$\delta_1 = \frac{1}{\epsilon}\left(\delta - \frac{1}{4}\right) \qquad \mu = \frac{B_1}{\epsilon} \qquad F = \frac{f_{\phi_t}}{\epsilon} \tag{5.42}$$

Replacing Eq. (5.42) in Eq. (5.17) and Eq. (5.19) yields respectively:

$$4\left(\delta - \frac{1}{4}\right)^2 - \left(\epsilon - \frac{f_{\phi_t}}{2}\sin\psi\right)^2 + B_1^2 - \left(\frac{f_{\phi_t}}{2}\cos\psi\right)^2 = 0 \tag{5.43}$$

$$\left(\frac{\Lambda^2}{4} + 1\right)\left(\epsilon - \frac{f_{\phi_t}}{2}\sin\psi\right)^2 - \left[B_1 - \Lambda\left(\delta - \frac{1}{4}\right)\right]^2 + \left(\frac{\Lambda^2}{4} + 1\right)\left(\frac{f_{\phi_t}}{2}\cos\psi\right)^2 = 0 \tag{5.44}$$

$$\left(\epsilon - \frac{f_{\phi_t}}{2}\sin\psi\right)^2 - \left[2\left(\delta - \frac{1}{4}\right) - \frac{B_1}{\Lambda}\right]^2 - \frac{1}{4}\left[B_1^2 - (f_{\phi_t}\cos\psi)^2\right] = 0 \tag{5.45}$$

Equations Eq. (5.43), Eq. (5.44) and Eq. (5.45) correspond to conics in the (δ, ϵ) parameter space. Notice that the last two terms in Eq. (5.43) decide the type of conic. Defining P as:

$$P = \frac{B_1}{f_{\phi_t}} - \frac{1}{2}\left|\cos\psi\right|$$

Eq. (5.43) draws the following:

$P = 0$	two intersecting lines
$P < 0$	hyperbola with horizontal transverse axis
$P > 0$	hyperbola with vertical transverse axis

Eq. (5.44) is a hyperbola with horizontal transverse axis except in two specific cases:

$\psi = \frac{\pi}{2}$	two intersecting lines
$P > 0$	($\Lambda = 0$) two lines parallel to the δ-axis

Eq. (5.45) draws the following:

$P = \frac{1}{2}\lvert\cos\psi\rvert$	two intersecting lines
$P < \frac{1}{2}\lvert\cos\psi\rvert$	hyperbola with vertical transverse axis
$P > \frac{1}{2}\lvert\cos\psi\rvert$	hyperbola with horizontal transverse axis

The correspondence in the stability regions where periodic motions are present (Regions II and III) between the (δ_1, μ) and the (δ, ϵ) parameter spaces for four different values of the phase difference ψ between the periodic stiffness and the periodic damping is presented in Fig. 5.12 and Fig. 5.13. For illustration purposes B_1 has been chosen such that it satisfies $P = 0$ for $\psi = 2\pi/5$ (or $\psi = 7\pi/5$). In Fig. 5.13 the curves corresponding to the Hopf bifurcation in the slow-flow, Eq. (5.45), have been omitted for readability.

The discussion of the (δ, ϵ) parameter space is limited to the first quadrant. Notice that in the absence of the periodic damping term the stability boundary Eq. (5.43) corresponds to a hyperbola with vertical transverse axis through $\delta_1 = 0.25$ and horizontal conjugate axis through $\epsilon = 0$, where this boundary is represented, to first order, as a parabola in the first quadrant of the (δ, ϵ) parameter space. The ratio of the averaged third order nonlinearities (Λ), represented by α and β, add a stability boundary that would appear as a tangent line on either side of the parabola depending on the sign of Λ (right side for $\Lambda < 0$ or left side for $\Lambda > 0$).

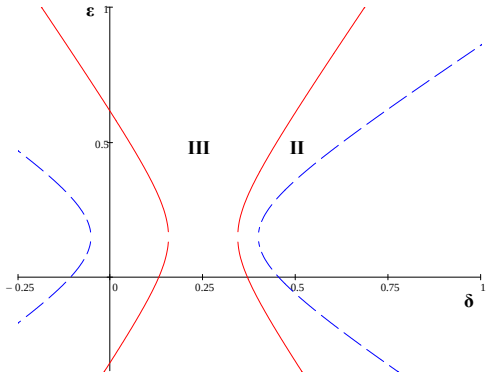

(a) $\psi = \frac{\pi}{5} \quad P = -0.251$

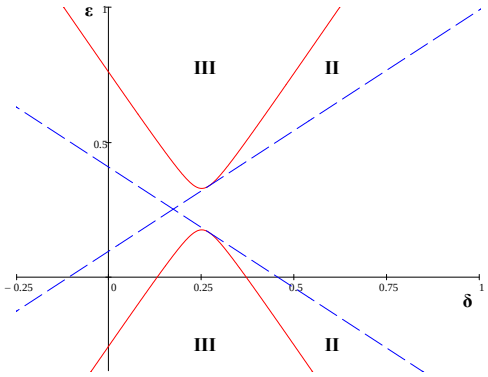

(b) $\psi = \frac{\pi}{2} \quad P = 0.154$

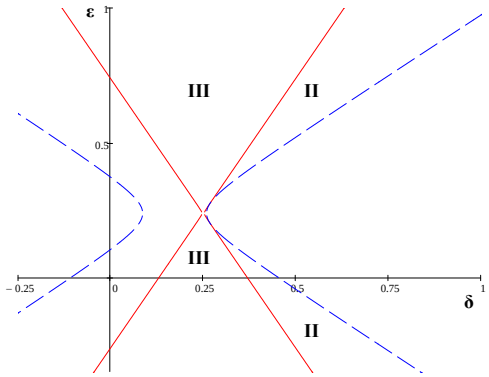

(c) $\psi = \frac{2\pi}{5} \quad P = 0$

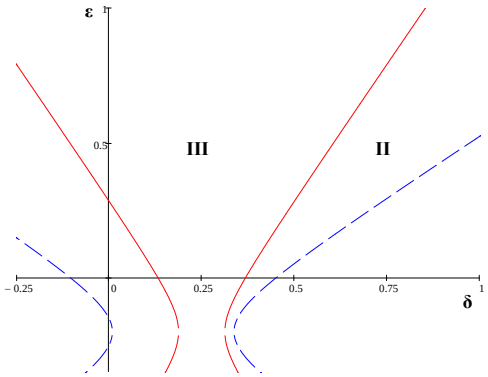

(d) $\psi = \frac{17\pi}{10} \quad P = -0.140$

Figure 5.12: Stability Regions in the (δ, ϵ) Parameter Space. $B_1 = 0.077$, $\Lambda = -1$ $(\beta = 1, \alpha = -1)$, $f_{\phi_t} = 0.5$

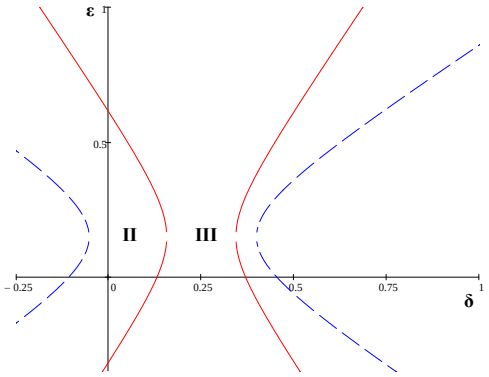

(a) $\psi = \frac{\pi}{5} \quad P = -0.251$

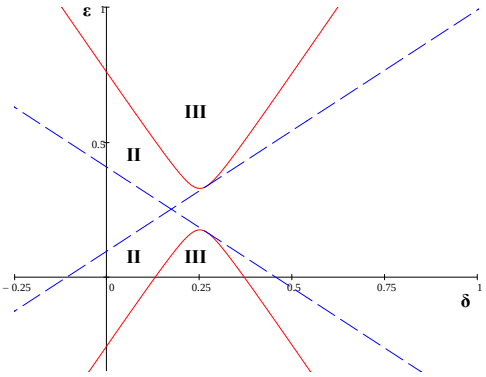

(b) $\psi = \frac{\pi}{2} \quad P = 0.154$

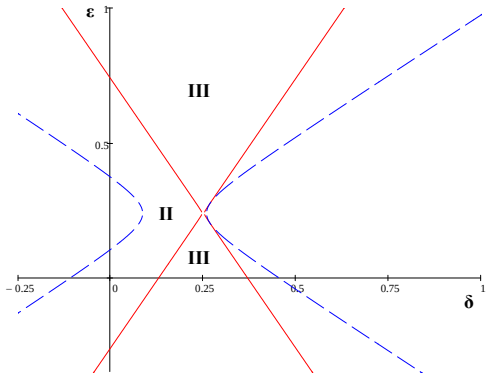

(c) $\psi = \frac{2\pi}{5} \quad P = 0$

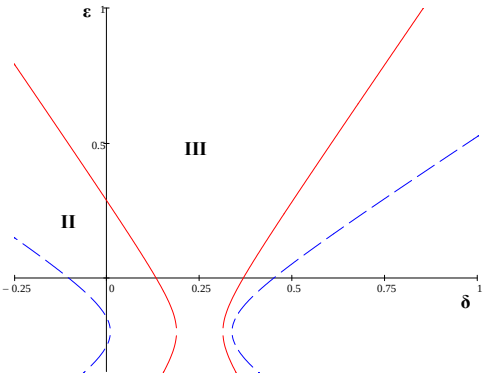

(d) $\psi = \frac{17\pi}{10} \quad P = -0.140$

Figure 5.13: Stability Regions in the (δ, ϵ) Parameter Space. $B_1 = 0.077$, $\Lambda = -1$ $(\beta = -1, \alpha = 1)$, $f_{\phi_t} = 0.5$

This picture corresponds to a Mathieu's equation with third order non-linearities as treated in Rand et al. (2005). The addition of periodic damping changes this picture by either moving this hyperbola with vertical transverse axis up or down ($P > 0$) or by transforming it into a hyperbola with horizontal transverse axis ($P < 0$), creating regions where periodic motions would not have been expected.

5.11 Conclusions

The stability boundaries for a Hill's equation with third order non-linearities, in the vicinity of the 2:1 resonance, have been presented. It has been shown to first order that the effect of the time dependent damping term in the bifurcation set of the linear and nonlinear damped Mathieu's equation is to produce a scaling in that set without changing the nature of the solutions. The interest has been centered in the prediction of periodic orbits, their amplitude and stability, since they represent *parametric rolling*. Formulae for predicting the amplitude and stability of limit cycles for a case of the non-linear Hill's equation has been presented. It has been found that the case with negative averaged dissipative non-linearities ($\beta < 0$) is more interesting from the mathematical point of view than the case with positive averaged dissipative non-linearities ($\beta > 0$) due to the richness in bifurcations present in the former case. It has been shown via an example that the amplitude and stability of periodic and quasi-periodic motions can be predicted within engineering accuracy as required for the purposes of this research. However, it is worth mentioning that the values for the parameters in the example have been selected in order to highlight specific behaviors, particularly those related to quasi-periodic motions. In the next chapter the theory developed in this chapter will be applied to specific configurations of a planing hull model tested at the United States Naval Academy (USNA).

The results presented here correspond to the case with $B_1 > 0$ in Eq. (5.2). However, notice that F_ψ does not appear in Eq. (5.37) and the condition is the same found via equation (26) in Rand et al. (2005); therefore, introducing the time dependent damping in equation (1) in Rand et al. (2005) will only cause a scaling in the bifurcation set presented in their Figure 3, so if negative values for the linear damping ($B_1 < 0$) were admitted, not only Hopf bifurcations would be observed but also limit cycle folds, symmetry-breaking bifurcations and saddle-connection bifurcations as found by continuation methods in Rand et al. (2005).

Lastly, even though the interest in Eq. (5.2) was born in the study of the transverse stability of planing hulls, the theory developed in this chapter is generic. It can be applied in the naval architecture field to study *parametric roll* in any type of vessel satisfying the assumptions made in this and in previous chapters. In fact, in Neves (2007) the bi-stability observed in some regions of what would be equivalent to the (δ, ϵ) parameter space, via numerical integration of their mathematical model, could be explained by the theory developed in this chapter.

CHAPTER 6

Case Studies

6.1 Chapter Overview

In this chapter, the first order approximation to the non-linear Hill's equation, derived in Chapter 5, is used to investigate conditions that could lead to stable periodic roll motions parametrically excited by harmonic pitch and heave motions using a 20 degrees constant deadrise planing hull as case study. The investigation is carried out in two stages; first, a region of interest in the design parameter space is identified by using stiffness coefficients obtained by the 2D+t approach, together with linear added mass and damping coefficients derived from semi-empirical formulae available in the open literature; and second, two particular configurations inside the region of interest, for which experimental results are available, are investigated using linear and nonlinear added mass, damping and stiffness coefficients obtained from reduction of experimental and numerical time series.

6.2 Introduction

In Chapter 2 the non-dimensional heave-roll-pitch system was reduced to a single degree of freedom by assuming an ordering in the different coefficients of the equation of motion, obtaining an effective one-way coupling between heave-pitch and roll. Also, by assuming the response of the autonomous heave-pitch system to be a stable harmonic motion (limit cycle) and by rescaling the non-dimensional time with the exciting frequency the non-dimensional roll equation of motion was written in the form:

$$\begin{aligned}
&\phi_{\tau\tau} + \frac{1}{\omega}\left(K_1^D + f_0^{\phi_t}\right)\phi_\tau + \frac{1}{\omega}\left(f_1^{\phi_t}\cos\left(\tau - \psi_1^{\phi_t}\right)\right)\phi_\tau \\
&\quad + \frac{1}{\omega^2}\left(K_1^S + f_0^{\phi}\right)\phi + \frac{1}{\omega^2}\left(f_1^{\phi}\cos\left(\tau - \psi_1^{\phi}\right)\right)\phi \\
&\quad + \frac{1}{\omega}\left(f_2^{\phi_t}\cos\left(2\,\tau - \psi_2^{\phi_t}\right)\right)\phi_\tau + \frac{1}{\omega^2}\left(f_2^{\phi}\cos\left(2\,\tau - \psi_2^{\phi}\right)\right)\phi \\
&\quad + \left(K_{23}^A\right)\phi\,\phi_\tau^2 + \frac{1}{\omega}\left(K_{12}^D\right)\phi^2\phi_\tau + \omega\left(K_{17}^D\right)\phi_\tau^3 + \frac{1}{\omega^2}\left(K_7^S\right)\phi^3 = 0
\end{aligned} \tag{6.1}$$

Since the behavior of the system in the vicinity of the principal parametric resonance, i.e., when the excitation frequency is nearly twice the roll natural frequency, is the one of interest, in Chapter 5 Eq. (6.1) was written in the form of a nonlinear Hill's equation:

$$\begin{aligned}
x_{tt} + \left(\delta + \epsilon\cos(t - \psi_1)\right)x + \left(B_1 + f_{\phi_t}\cos(t - \psi_2)\right)x_t + \\
C_3x^3 + A_3x\,x_t^2 + B_2x^2x_t + B_3x_t^3 = 0
\end{aligned} \tag{6.2}$$

where the correspondence between Eq. (6.1) and Eq. (6.2) is as follows:

$$\delta = \frac{1}{\omega^2}\left(K_1^S + f_0^\phi\right) \qquad \epsilon = \frac{1}{\omega^2}\left(f_1^\phi\right) \qquad \psi_1 = \psi_1^\phi$$
$$B_1 = \frac{1}{\omega}\left(K_1^D + f_0^{\phi_t}\right) \qquad f_{\phi_t} = f_1^{\phi_t} \qquad \psi_2 = \psi_1^{\phi_t}$$
$$C_3 = \frac{1}{\omega^2}\left(K_7^S\right) \qquad A_3 = K_{23}^A \qquad B_2 = \frac{1}{\omega}\left(K_{12}^D\right) \qquad B_3 = \omega\left(K_{17}^D\right)$$

The solution to Eq. (6.2) was approximated in the vicinity of the principal parametric resonance, when $\delta \approx 0.25$, by using a perturbation method. It was shown comprehensively the effect of the different terms in Eq. (6.2) in the stability boundaries in both the (δ_1, μ) and the (δ, ϵ) parameter spaces; where δ_1 is a detuning parameter from the 2:1 resonance, μ is the scaled linear damping and ϵ is the forcing amplitude.

It was shown that in order to observe stable periodic motions (limit cycles) in roll, parametrically excited by small heave and pitch, it is necessary for the forcing (ϵ) to overcome a critical value of the linear damping (B_1). This critical value is a function of the ratio of the exciting frequency to the roll natural frequency, and a function of the averaged ratio of the third order dissipative to non-dissipative nonlinearities (Λ).

Recall that in order to get Eq. (6.1) the solution of heave-pitch system was assumed to be of the form:

$$z = \zeta_3 \cos \omega t \qquad \theta = \zeta_5 \cos\left(\omega t + \alpha_5\right) \tag{6.3}$$

where ζ_3 and ζ_5 are the non-dimensional heave and pitch amplitudes of the perturbations from equilibrium respectively, ω is the non-dimensional frequency of oscillation and α_5 represents the phase difference between the pitch and heave motions.

The coefficients in Eq. (6.2) can be written in terms of the the heave-pitch motion described by Eq. (6.3) and the hydrodynamic derivatives in the roll equation of motion (in classical maneuvering notation) as follows:

$$\delta = \left(\frac{\omega_4}{\omega}\right)^2 - \left(\frac{\zeta_3^2 K_{zz\phi} + \zeta_3\zeta_5 \cos\alpha_5 K_{z\phi\theta} + \zeta_5^2 K_{\phi\theta\theta}}{2\,\omega^2\,(I_x - K_{\phi_{tt}})}\right)$$

$$\epsilon = \frac{1}{\omega^2\,(I_x - K_{\phi_{tt}})}\sqrt{\zeta_3^2 K_{z\phi}^2 + 2\zeta_3\zeta_5 \cos\alpha_5 K_{z\phi} K_{\phi\theta} + \zeta_5^2 K_{\phi\theta}^2}$$

$$\psi_1 = \tan^{-1}\left(\frac{-\zeta_5 \sin\alpha_5 K_{\phi\theta}}{\zeta_3 K_{z\phi} + \zeta_5 \cos\alpha_5 K_{\phi\theta}}\right)$$

$$B_1 = \frac{1}{\omega}\left(\frac{-K_{\phi_t}}{I_x - K_{\phi_{tt}}}\right) - \left(\frac{\zeta_3^2 K_{zz\phi_t} + \zeta_3\zeta_5 \cos\alpha_5 K_{z\theta\phi_t} + \zeta_5^2 K_{\theta\theta\phi_t}}{2\,\omega\,(I_x - K_{\phi_{tt}})}\right)$$

$$f_{\phi_t} = \frac{1}{(I_x - K_{\phi_{tt}})}\sqrt{\zeta_3^2 K_{z\phi_t}^2 + 2\zeta_3\zeta_5 \cos\alpha_5 K_{z\phi_t} K_{\theta\phi_t} + \zeta_5^2 K_{\theta\phi_t}^2}$$

$$\psi_2 = \tan^{-1}\left(\frac{-\zeta_5 \sin\alpha_5 K_{\theta\phi_t}}{\zeta_3 K_{z\phi_t} + \zeta_5 \cos\alpha_5 K_{\theta\phi_t}}\right)$$

$$C_3 = \frac{1}{\omega^2}\left(\frac{-K_{\phi\phi\phi}}{I_x - K_{\phi_{tt}}}\right) \qquad A_3 = \left(\frac{-K_{\phi\phi_t\phi_t}}{I_x - K_{\phi_{tt}}}\right)$$

$$B_2 = \frac{1}{\omega}\left(\frac{-K_{\phi\phi\phi_t}}{I_x - K_{\phi_{tt}}}\right) \qquad B_3 = \omega\left(\frac{-K_{\phi_t\phi_t\phi_t}}{I_x - K_{\phi_{tt}}}\right)$$

In this chapter the theory developed in Chapter 5 is applied to selected configurations of the model tested at the United States Naval Academy (USNA) as reported in Judge (2010, 2012); Judge and Judge (2013). Before doing that, and in order to gain an insight into the expected behavior, some of the coefficients in the roll equation of motion are studied as a function of the *mean wetted length* (λ) and the *speed coefficient* (C_v).

6.3 Design (λ, C_v) Parameter Space

In general, the hydrodynamic forces acting on a prismatic planing hull are functions of the *deadrise angle* (β_G), the *trim angle* (θ_E), the *mean wetted length* (λ) and the *speed coefficient* (C_v). Also, the generalized forces and moments are written with respect to a reference frame, in this case with origin at the center of gravity.

Since the interest lies in the study of some configurations of the model tested at the USNA, the deadrise angle ($\beta_G = 20°$) and the non-dimensional vertical position of the center of gravity ($V_{cg} = 0.321$) are given. The information of interest is computed in the design parameter space (λ, C_v) bounded by $1 \leq \lambda \leq 2.5$ and $1 \leq C_v \leq 5$.

The longitudinal position of the center of gravity is assumed to coincide with the longitudinal center of pressure (λ_p) so each point in the (λ, C_v) space satisfies static equilibrium, Eq. (6.4) (Savitsky, 1964):

$$\begin{aligned} C_\Delta &= \frac{1}{2} C_v^2 \, C_{L\beta} \\ L_{cg} = \lambda_p &= \left(0.75 - \frac{\lambda^2}{5.21 C_v^2 + 2.39\lambda^2}\right) \lambda \end{aligned} \tag{6.4}$$

where

$$\begin{aligned} C_{L\beta} &= C_{L0} - 0.0065 \left(\frac{180}{\pi}\beta_G\right) C_{L0}^{0.6} \\ C_{L0} &= \left(\frac{180}{\pi}\theta_E\right)^{1.1} \left(0.012\lambda^{0.5} + 0.0055\frac{\lambda^{2.5}}{C_v^2}\right) \end{aligned}$$

Fig. 6.1 shows the behavior of the non-dimensional longitudinal center of pressure (λ_p) as a function of λ and C_v. Notice that according to Eq. (6.4) λ_p is a function of λ and C_v only.

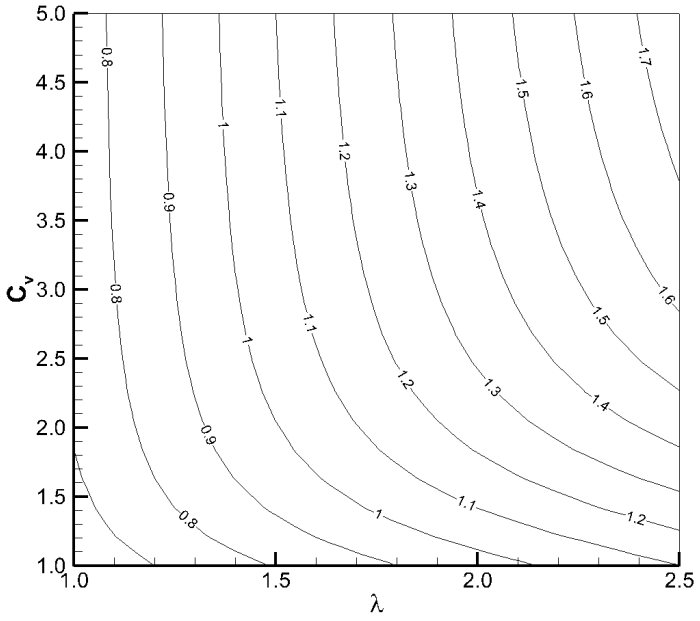

Figure 6.1: Non-dimensional longitudinal center of pressure (λ_p) as a function of Mean Wetted Length (λ) and Speed Coefficient (C_v)

Fig. 6.2 shows the behavior of the Displacement Coefficient C_Δ for two different trim angles ($\theta_E = 2^\circ$ and $\theta_E = 4^\circ$).

Following Pauling and Rosenberg (1959) and keeping only stiffness non-linearities up to second order in the heave-roll-pitch system, the roll equation of motion represented by Eq. (6.2) reduces to the linear damped Mathieu's equation, Eq. (6.5).

$$x_{tt} + (\delta + \epsilon \cos(t - \psi_1))\, x + B_1 x_t = 0 \tag{6.5}$$

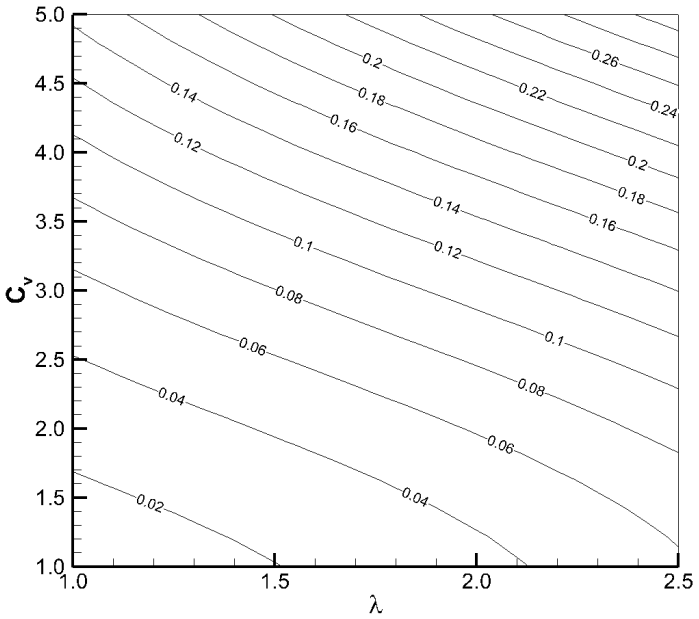

(a) $\theta_E = 2^o$

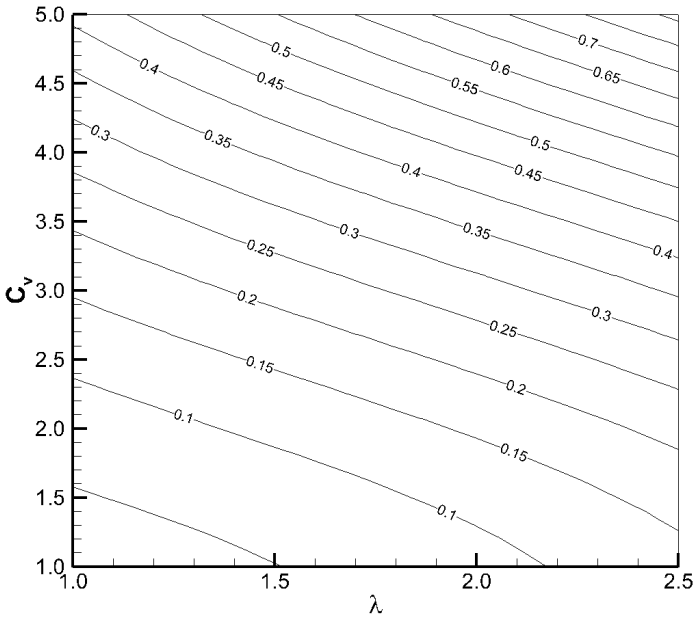

(b) $\theta_E = 4^o$

Figure 6.2: Displacement Coefficient (C_Δ) as a function of Mean Wetted Length (λ) and Speed Coefficient (C_v)

where

$$\delta = \frac{1}{\omega^2}\left(\frac{-K_\phi}{I_x - K_{\phi_{tt}}}\right) = \left(\frac{\omega_4}{\omega}\right)^2$$

$$\epsilon = \frac{1}{\omega^2\left(I_x - K_{\phi_{tt}}\right)}\sqrt{\zeta_3^2 K_{z\phi}^2 + 2\zeta_3\zeta_5\cos\alpha_5 K_{z\phi}K_{\phi\theta} + \zeta_5^2 K_{\phi\theta}^2}$$

$$B_1 = \frac{1}{\omega}\left(\frac{-K_{\phi_t}}{I_x - K_{\phi_{tt}}}\right) \qquad \psi_1 = \tan^{-1}\left(\frac{-\zeta_5\sin\alpha_5 K_{\phi\theta}}{\zeta_3 K_{z\phi} + \zeta_5\cos\alpha_5 K_{\phi\theta}}\right)$$

In Eq. (6.5) the forcing (ϵ) is a function of the non-dimensional coupling restoring coefficients ($K_{z\phi}, K_{\phi\theta}$) and the non-dimensional heave and pitch perturbations from equilibrium (ζ_3, ζ_5), and B_1 is directly related to the non-dimensional linear damping coefficient (K_{ϕ_t}). Therefore, assuming a nearly 2:1 tuning between the excitation frequency and the roll natural frequency, a vessel prone to develop parametric roll would be characterized by small damping and large coupling restoring coefficients.

First, the behavior of the roll coupling restoring coefficients $K_{z\phi}$ and $K_{\phi\theta}$ is investigated. These coefficients are computed by the 2D+t theory by perturbing the vessel from equilibrium and fitting a second order polynomial to the response surface of the roll moment computed at the center of gravity. For consistency, the heave and pitch perturbations are assumed to be in the same ranges used in in Chapter 4 for the computation of the stiffness and damping coefficients coupling heave-roll-pitch (i.e., $-0.5\,T_D \leq \zeta_3 \leq 0.5\,T_D$ and $-0.45\,\theta_E \leq \zeta_5 \leq 0.45\,\theta_E$).

The behavior of the coupling restoring coefficient between roll and heave ($K_{z\phi}$) for two different trim angles ($\theta_E = 2^o$ and $\theta_E = 4^o$) is presented in Fig. 6.3. It is observed that in both cases the largest values of the coefficients correspond to the lowest λ and the largest C_v, with the largest values obtained for the lowest trim angle.

The same information is presented for the restoring coefficient coupling roll and pitch ($K_{\phi\theta}$) in Fig. 6.4. In this case notice that for a given value of C_v the value of the coefficient is weakly dependent on λ. As in the case of $K_{z\phi}$, the highest value of the coefficient is observed for the lowest λ and the largest C_v, with the largest values obtained for the lowest trim angle even though the difference is not as significant as in the case of $K_{z\phi}$. Therefore, looking at Eq. (6.2) the largest value of the forcing (ϵ) would be obtained for vessels running at small trim angle, small transom draft and high speed.

In Chapter 4 it was shown that the equivalent roll linear damping coefficient ($K_{\phi_t eq}$) can be reasonably approximated by Ikeda's formula for the vertical lift component of roll damping ($-B_{44_{VL}}$). It was found that for the heavier configuration the third order harmonic of the out of phase component is very small in comparison with the first order harmonic and therefore the difference between the equivalent linear damping ($K_{\phi_t eq}$) and the linear damping (K_{ϕ_t}) is negligible; however, this was not the case for the lighter configuration. For the exploration of the design parameter space it is assumed that $K_{\phi_t} = K_{\phi_t eq} \approx -B_{44_{VL}}$ keeping in mind that for the lighter configuration the values obtained will be reduced by the effect of the third order harmonic in the out of phase component of the roll moment. Ikeda's formulation, as presented in Ikeda et al. (1998), written in non-dimensional form, Eq. (6.6), is repeated here for convenience.

$$B_{44_{VL}} = \frac{1}{2} C_v \left(\frac{\partial C_{L\beta}}{\partial \theta_E} \right) \frac{B_{wl}}{12 \cos^2 \beta_G} \left(B_{wl} - \frac{3}{2} V_{cg} \sin 2\beta_G \right) \tag{6.6}$$

where B_{wl} corresponds to the non-dimensional wetted beam at the transom (i.e. $B_{wl} = 1$ when the non-dimensional chine wetted length is greater than zero ($\lambda_c > 0$)).

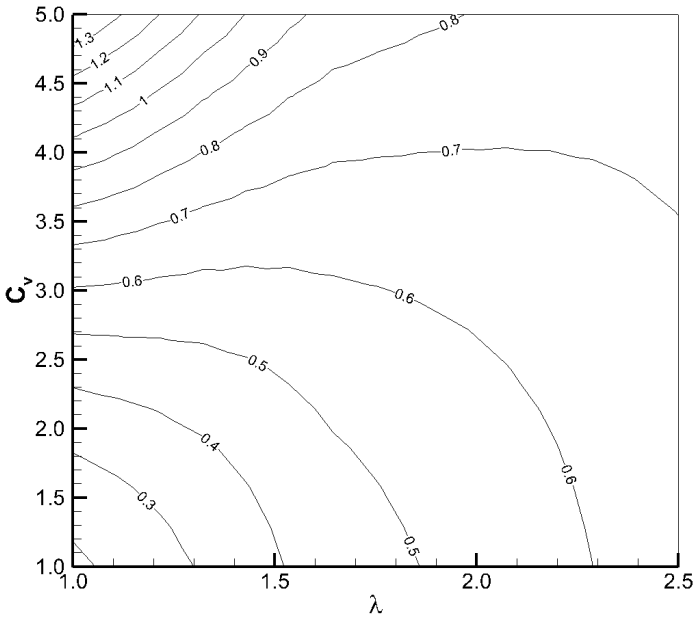

(a) $\theta_E = 2^o$

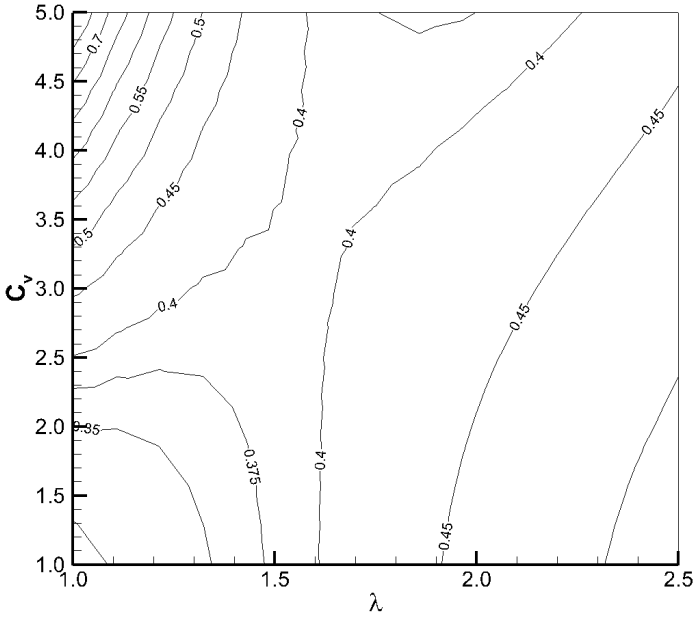

(b) $\theta_E = 4^o$

Figure 6.3: $K_{z\phi}$ as a function of Mean Wetted Length (λ) and Speed Coefficient (C_v)

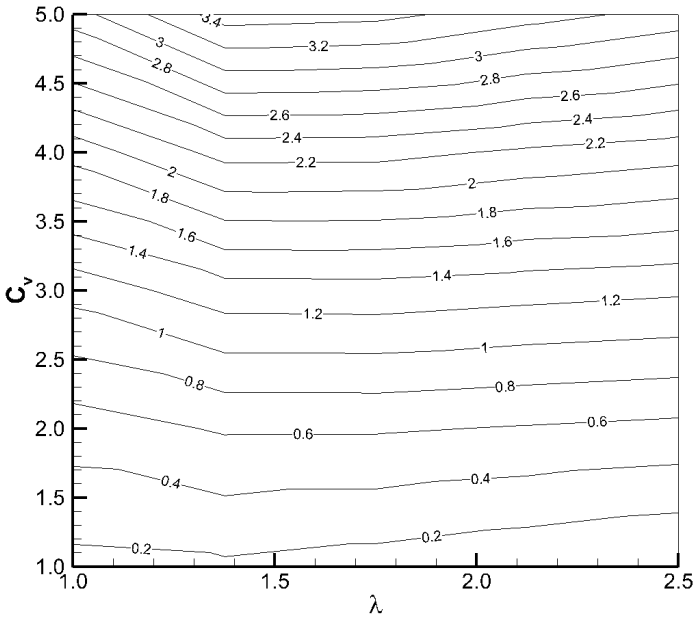

(a) $\theta_E = 2^o$

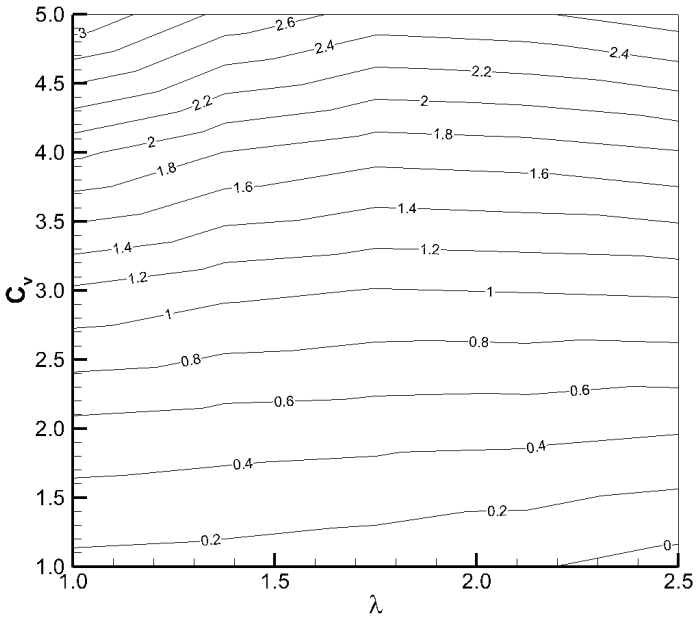

(b) $\theta_E = 4^o$

Figure 6.4: $K_{\phi\theta}$ as a function of Mean Wetted Length (λ) and Speed Coefficient (C_v)

In Fig. 6.5 contours of $-K_{\phi_t}$ are presented as a function of λ and C_v for two different trim angles $\theta_E = 2^o$ and $\theta_E = 4^o$. Observe that $-K_{\phi_t}$ increases with λ, C_v and θ_E; however, for the lowest trim angle ($\theta_E = 2^o$) the roll damping coefficient appears to be less sensitive to variations in the lower range of the mean wetted length ($1 \leq \lambda \leq 1.5$).

The results suggest that for this particular geometry the lighter configuration run at high speed would be more prone to develop parametric rolling than the heavier configuration run at low speed, since large values of coupling restoring coefficients and small values of damping are predicted for high values of speed coefficient and low values of mean wetted length and trim.

6.4 Case Studies - USNA Model Configurations

Based on the results of the (λ, C_v) parameter space exploration, in this section two of the configurations tested at the USNA are investigated, the heavier configuration run at the minimum testing speed and the lighter configuration run at the maximum speed tested. The heavier configuration at the minimum speed tested is referred to as 20H and the lighter configuration at the maximum speed tested as 30L, where the number corresponds to the testing speed in feet per second (ft/s) and H and L stand for *Heavy* and *Light* respectively. In Table 6.1 the non-dimensional characteristics of these two configurations are summarized.

	C_Δ	λ	C_v	$\theta_E(^\circ)$	L_{cg}	V_{cg}	T_D
20H	0.295	2.009	2.908	4.0	1.327	0.321	0.197
30L	0.157	0.938	4.362	2.9	0.680	0.321	0.095

Table 6.1: Configurations Investigated

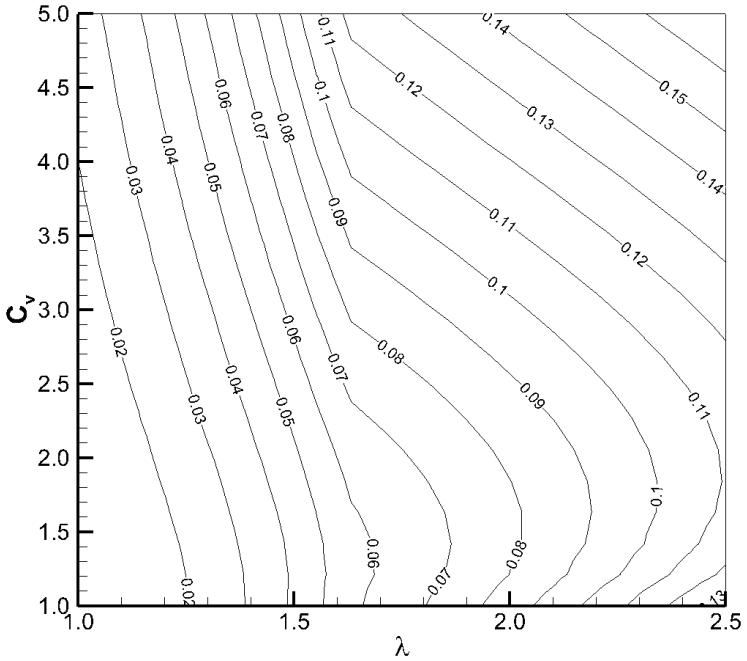

(a) $\theta_E = 2^o$

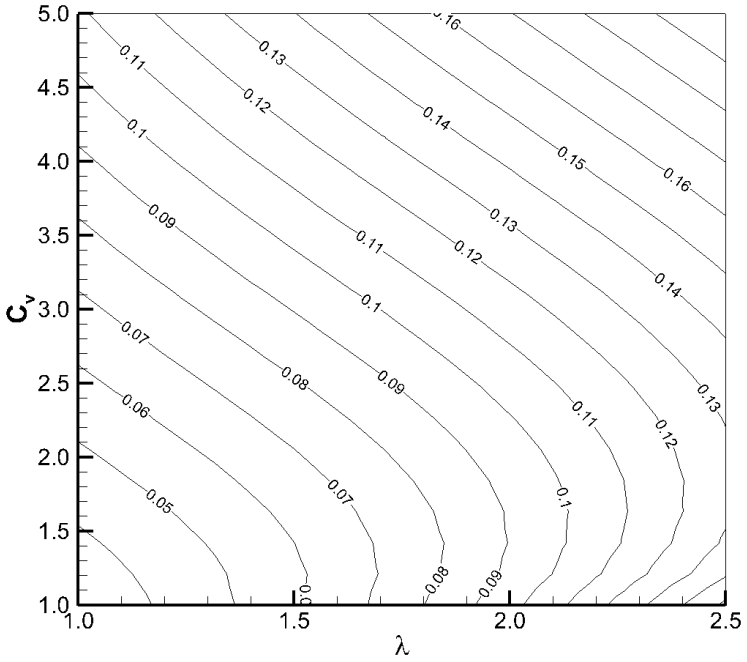

(b) $\theta_E = 4^o$

Figure 6.5: Linear roll damping coefficient ($-K_{\phi_t}$) as a function of Mean Wetted Length (λ) and Speed Coefficient (C_v) - Ikeda's formulation for vertical lift component

The coefficients for the nonlinear Hill's equation, Eq. (6.2), are obtained by different methods. The inertial and dissipative coefficients are obtained from the reduction of the experimental time series by regression analysis, as presented in Chapter 4. In Tables 6.2 and 6.3 the expected values for the inertial and damping coefficients obtained from large amplitude runs for these two configurations are summarized.

	C_Δ	I_x	$K_{\phi_{tt}}$	$K_{\phi\phi_t\phi_t}$
20H	0.295	0.038	-0.016	-0.271
30L	0.157	0.020	-0.009	-0.211

Table 6.2: Inertial Coefficients (non-dimensional)

	$K_{\phi_t eq}$	K_{ϕ_t}	$K_{\phi\phi\phi_t}$	$K_{\phi_t\phi_t\phi_t}$	$K_{z\phi_t}$	$K_{\theta\phi_t}$	$K_{z\theta\phi_t}$	$K_{zz\phi_t}$	$K_{\theta\theta\phi_t}$
20H	-0.067	-0.062	0.097	-0.007	0.815	-0.320	13.002	-1.821	-7.229
30L	-0.043	-0.023	-0.563	-0.002	0.369	2.537	-16.396	-1.105	-30.569

Table 6.3: Damping Coefficients (non-dimensional)

Since no experimental results for coupling between roll and pitch have been reported, and since the agreement between the 2D+t results and the experimental results for coupling between heave and roll has been shown to be very good, for consistency all the stiffness coefficients are computed numerically, following the approach presented in Chapter 4, assuming that the geometry is fully prismatic. It is acknowledged that this assumption introduces the largest error in the computation of the time independent roll moment for the heavier configuration since the actual geometry of the boat tested is prismatic over most of the wetted surface except at the bow. In Table 6.4 the expected values obtained for the non-dimensional stiffness coefficients are summarized.

	K_ϕ	$K_{z\phi}$	$K_{\phi\theta}$	$K_{z\phi\theta}$	$K_{zz\phi}$	$K_{\phi\theta\theta}$	$K_{\phi\phi\phi}$
20H	-0.110	0.459	0.849	5.451	-1.039	-1.886	0.145
30L	-0.104	0.832	2.144	-0.166	5.292	-5.749	0.047

Table 6.4: Stiffness Coefficients (non-dimensional)

In order to compute the forcing (ϵ) the heave and pitch perturbations are assumed to be in the same ranges assumed for the computation of the stiffness coefficients, i.e., $-0.5\,T_D \leq \zeta_3 \leq 0.5\,T_D$ and $-0.45\,\theta_E \leq \zeta_5 \leq 0.45\,\theta_E$. Also, the forcing frequency (ω) is assumed to be such that there is perfect 2:1 tuning ($\delta = 0.25$). Notice that due to the effect of the high order coupling non-linearities this does not correspond exactly to a 2:1 ratio between the excitation frequency and the roll natural frequency. Lastly, based on numerical results obtained by running the commercial code Powersea® as part of a different research effort (Castro-Feliciano, 2016), the phase difference between pitch and heave in porpoising is assumed to be in the range $0.8 \leq \alpha_5 \leq 1.2$. Table 6.5 summarizes the values for the heave and pitch motions used in the computations; the values are non-dimensional and therefore for consistency the angles are in radians.

	ζ_3	ζ_5	ω	α_5
20H	0.049	0.017	2.86	1.0
30L	0.024	0.023	3.79	0.9

Table 6.5: Heave and Pitch Periodic Motions

Fig. 6.6 presents the stability boundaries for the heavier configuration (20H) in both the (δ_1, μ) and the (δ, ϵ) parameter spaces. This configuration is far removed from the regions where periodic motions (III) and bi-stability (II) would be observed. Notice that in order to be inside any of these two regions it would be necessary to either reduce the roll damping by more than three times or to increase the heave and pitch motions by almost the same amount. However, if the later is done the results would be out of the range of validity of the model since these motions would exceed the values of the perturbations (ζ_3, ζ_5) used for the computation of the coupling restoring and dissipative coefficients. Also, the boat would be out of the water at some instants in time.

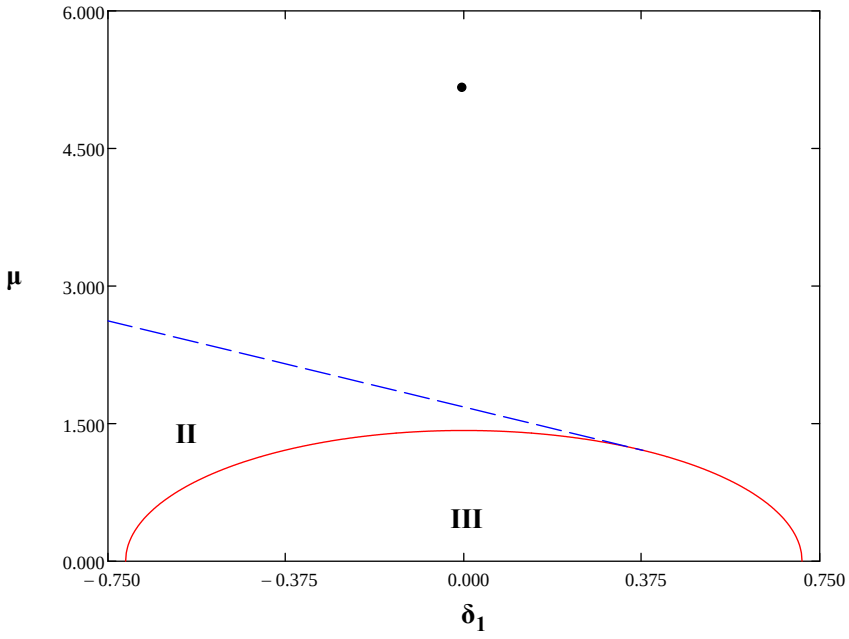

(a) (δ_1, μ) Parameter Space

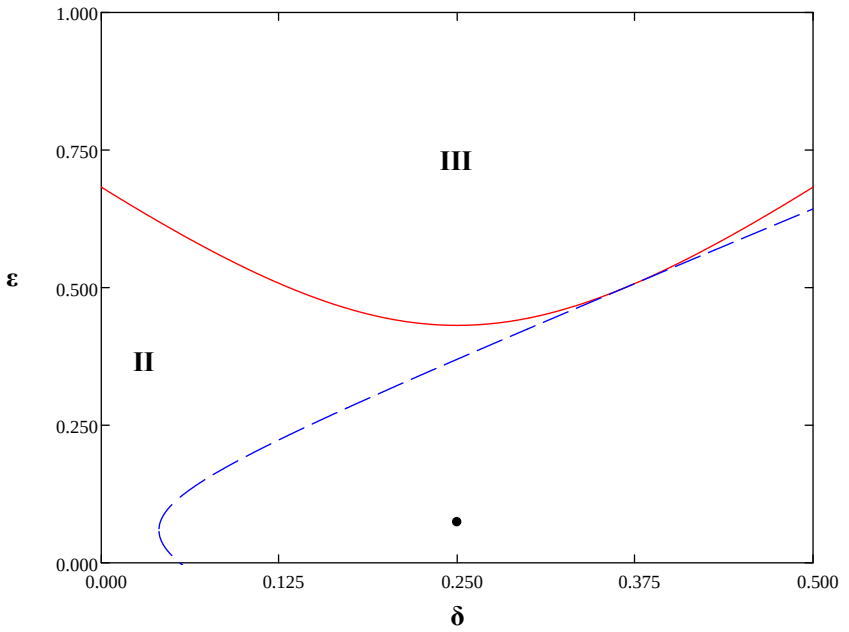

(b) (δ, ϵ) Parameter Space

Figure 6.6: Judge's heavier configuration $C_\Delta = 0.295$ $C_v = 2.908$ $B_1 = 0.387$ $\Lambda = -1.251$ $(\beta = -18.045)$ $f_{\phi_t} = 0.242$ $\psi = -5.77$

Fig. 6.7 presents the stability boundaries for the lighter configuration (30L) in both the (δ_1, μ) and the (δ, ϵ) parameter spaces. In this case the results are presented assuming two different scenarios related to the use in the construction of the stability boundaries of the equivalent linear damping B_{1eq} (obtained from $K_{\phi_t eq}$) and the linear damping B_1 (obtained from K_{ϕ_t}). This is done taking into consideration that for this configuration B_1 is almost half of B_{1eq} so the effect of using one or the other in the computation is important. In fact, notice that the difference between using B_1 or B_{1eq} is the difference between being inside or outside of the region where stable periodic motions would be observed (III). In Table 6.6 the non-dimensional coefficients in Eq. (6.2) are summarized including the effect of the position damping coupling coefficients $(K_{z\phi_t}, K_{\theta\phi_t}, K_{zz\phi_t}, K_{z\theta\phi_t}, K_{\theta\theta\phi_t})$ in B_1 and f_{ϕ_t}.

	δ	ϵ	ψ_1	B_1	f_{ϕ_t}	ψ_2	A_3	C_3	B_2	B_3
20H	0.25	0.075	2.755	0.387	0.242	-3.016	5.019	-0.328	-0.628	0.387
30L	0.25	0.151	2.490	0.325	0.579	2.350	7.276	-0.113	5.122	0.349

Table 6.6: Coefficients in Eq. (6.2) including position damping coupling coefficients

Regarding the effect of the third order dissipative and non-dissipative non-linearities, it is worth highlighting that there is a clear difference between the heavier and the lighter configurations. In the case of the lighter configuration the averaged dissipative non-linearities dominate resulting in a very narrow region of bi-stability (II). In the case of the heavier configuration there is a balance between the two resulting in a large region of bi-stability. However, in this configuration the averaged dissipative non-linearity (β) is negative and the steady states other than the trivial equilibrium could be far removed from the range of applicability of the problem, so for realistic initial conditions the result in the region II would be the trivial equilibrium.

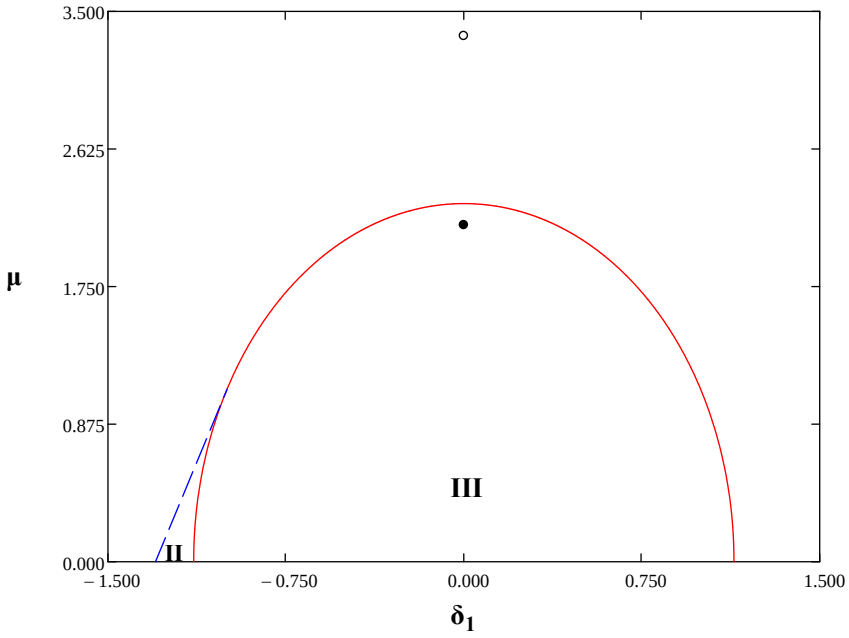

(a) (δ_1, μ) Parameter Space: $\bullet B_1$ $\circ B_{1eq}$

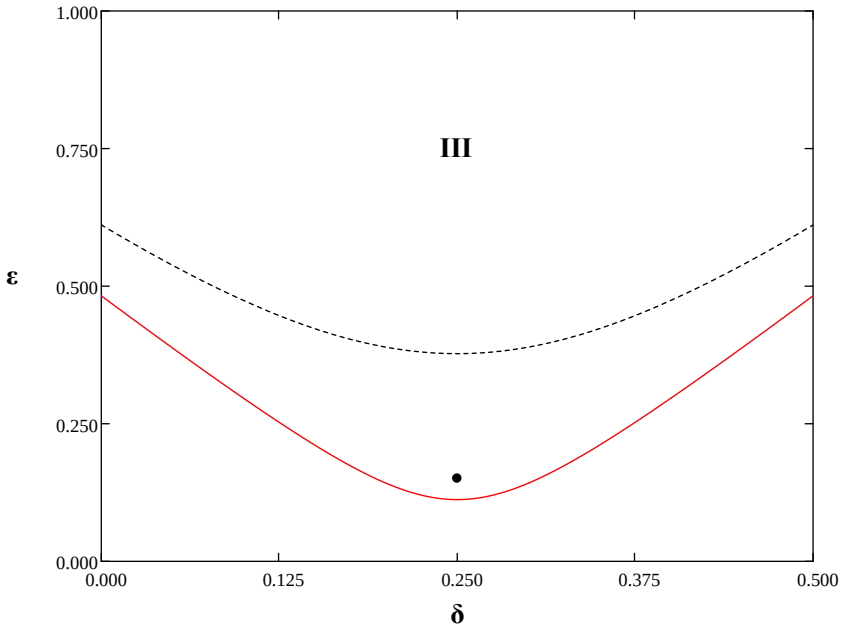

(b) (δ, ϵ) Parameter Space: —B_1 - - -B_{1eq}

Figure 6.7: Judge's lighter configuration $C_\Delta = 0.157$ $C_v = 4.362$ $B_{1eq} = 0.507$ $B_1 = 0.325$ $\Lambda = 3.637$ $f_{\phi_t} = 0.579$ $\psi = -0.14$

The difference of ratios of dissipative to non-dissipative non-linearities between 20H and 30L is partly the result of the third order stiffness non-linearity ($K_{\phi\phi\phi}$) being very small in the lighter configuration in comparison with the heavier configuration, a behavior that was already noticed in Chapter 4, combined with the fact that for 30L the position damping B_2 is of the same order as the nonlinear added mass A_3. In Eq. (6.7) the effect of the non-dimensional coefficients in the roll equation of motion in the ratio Λ is shown explicitly.

$$\Lambda = \frac{\beta}{\alpha} = \frac{4\beta_2 + 3\beta_3}{12\chi_3 + \alpha_3} = \frac{4B_2 + 3B_3}{12C_3 + A_3} = \omega \left(\frac{4K_{\phi\phi\phi_t} + 3\omega^2 K_{\phi_t\phi_t\phi_t}}{12K_{\phi\phi\phi} + \omega^2 K_{\phi\phi_t\phi_t}} \right) \tag{6.7}$$

Notice that due to the dependence of Λ on ω, in 20H it is possible to observe a change in the sign of Λ (caused by the change of sign in α) as shown in Fig. 6.8.

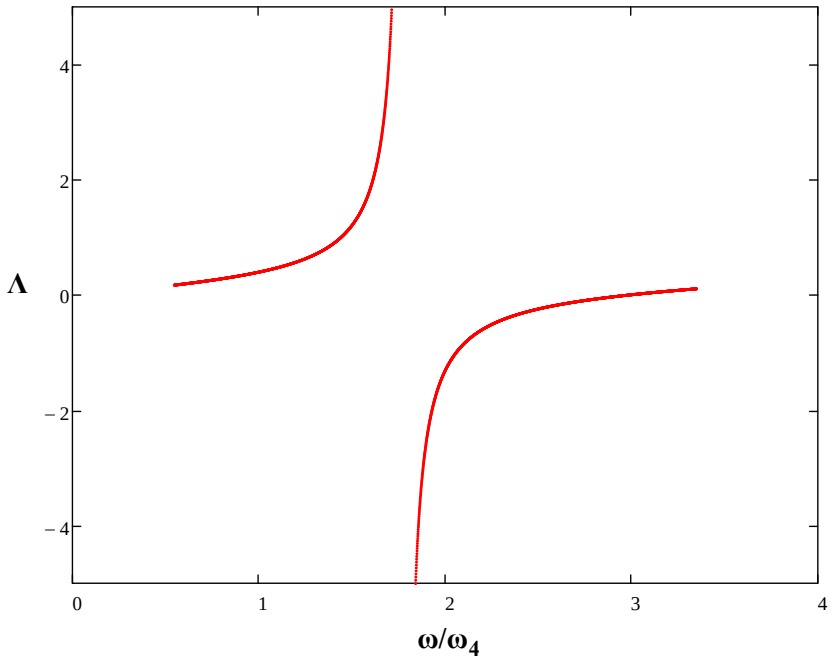

Figure 6.8: Averaged ratio (Λ) of dissipative to non-dissipative third order non-linearities as a function of the excitation frequency (ω) for configuration 20H

Fig. 6.9 and Fig. 6.10 present the stability boundaries for the same configurations but neglecting the coupling position damping coefficients ($K_{z\phi_t}, K_{\theta\phi_t}, K_{zz\phi_t}, K_{z\theta\phi_t}, K_{\theta\theta\phi_t}$) that will produce coefficients of the form $f_1^{\phi_t}$ and $f_0^{\phi_t}$ in the non-linear roll equation of motion. Notice that in both cases the inclusion of these terms increases the area where periodic motions (III) and bi-stability (II) are observed (by effect of $f_1^{\phi_t}$); however, for the heavier configuration the effect of $f_0^{\phi_t}$ is to decrease the linear damping coefficient while the opposite is true for the lighter configuration. In Table 6.7 the non-dimensional coefficients in Eq. (6.2) are summarized neglecting position damping coupling coefficients.

	δ	ϵ	ψ_1	B_1	f_{ϕ_t}	ψ_2	A_3	C_3	B_2	B_3
20H	0.25	0.075	2.755	0.401	0	0	5.019	-0.328	-0.628	0.387
30L	0.25	0.151	2.490	0.209	0	0	7.276	-0.113	5.122	0.349

Table 6.7: Coefficients in Eq. (6.2) neglecting position damping coupling coefficients

It is worth mentioning that the values of the different coefficients in the roll equation of motion used to construct the stability boundaries and the points (δ_1, μ) and (δ, ϵ) in Figs. 6.6 to 6.10 correspond to expected values; therefore, there is uncertainty associated to both of them. However, the individual uncertainty of the most influential coefficients is very small, as suggested by the t-ratios presented in Tables 4.2 and 4.10 in Chapter 4, and hence the uncertainty regions associated to the stability boundaries and the points are expected to be narrow. If the problem is treated as one of "error propagation", then a rapid computation by the Delta method (e.g., Casella and Berger (2002)) indicates that in the case of the configuration 30L the standard deviation of the forcing (ϵ) is approximately one percent (1%) of its mean value. In general, the formulae for the stability boundaries includes coefficients estimated from different sets of experiments and consequently a sensitivity analysis needs to be performed on the covariances that are not available from the statistics of the regressions. This is out of the scope of this work and it is suggested as future work.

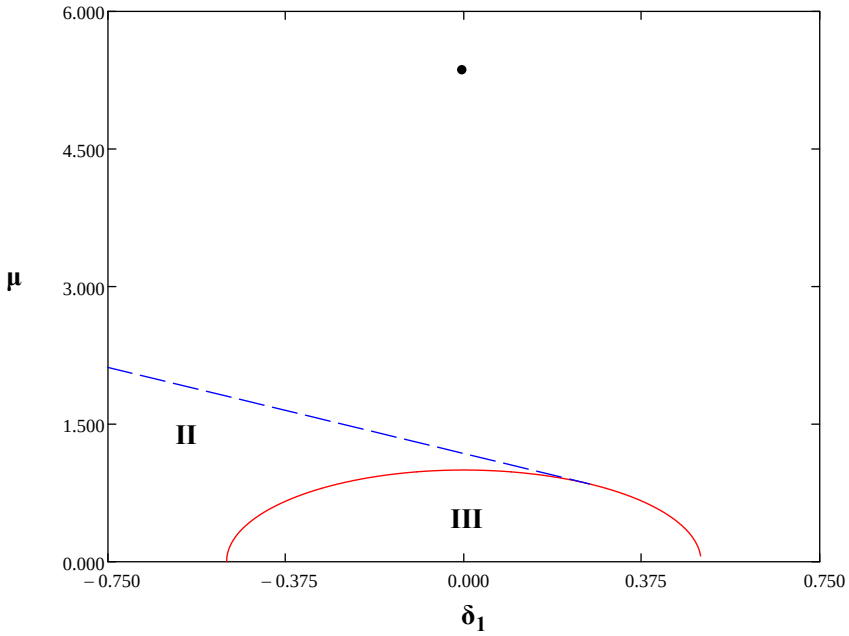

(a) (δ_1, μ) Parameter Space

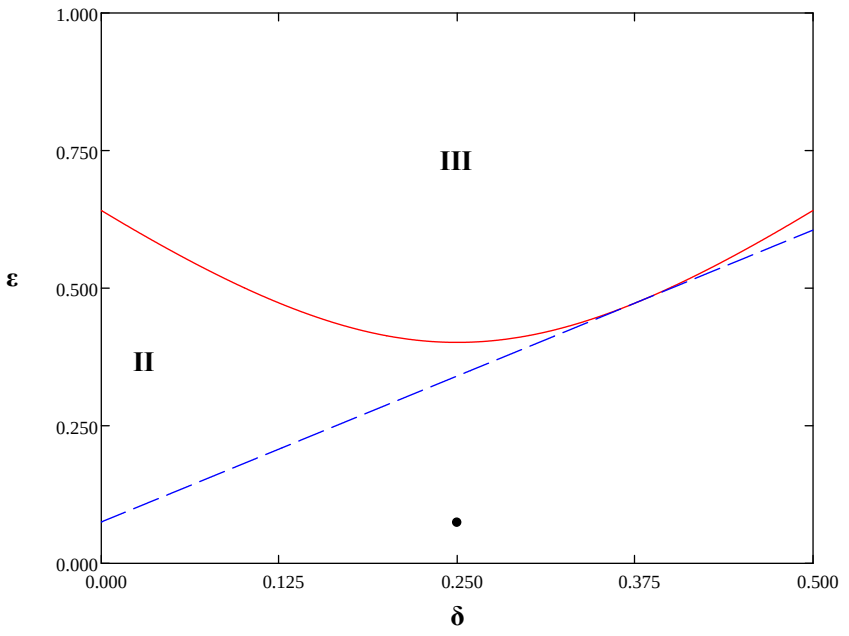

(b) (δ, ϵ) Parameter Space

Figure 6.9: Judge's heavier configuration $C_\Delta = 0.295$ $C_v = 2.908$ $B_1 = 0.401$ $\Lambda = -1.251$ $(\beta = -18.045)$ $f_{\phi_t} = 0$ $\psi = -2.755$

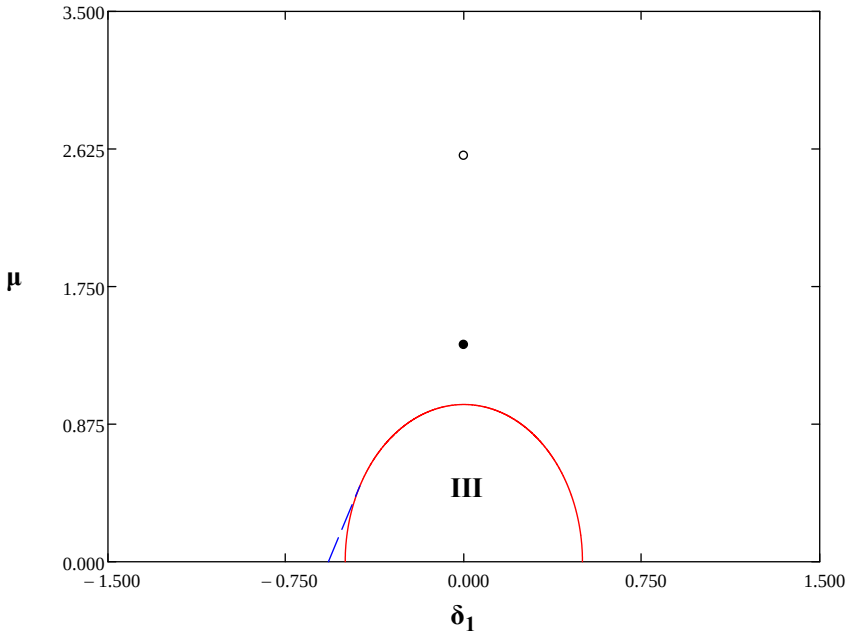

(a) (δ_1, μ) Parameter Space: $\bullet B_1$ $\circ B_{1eq}$

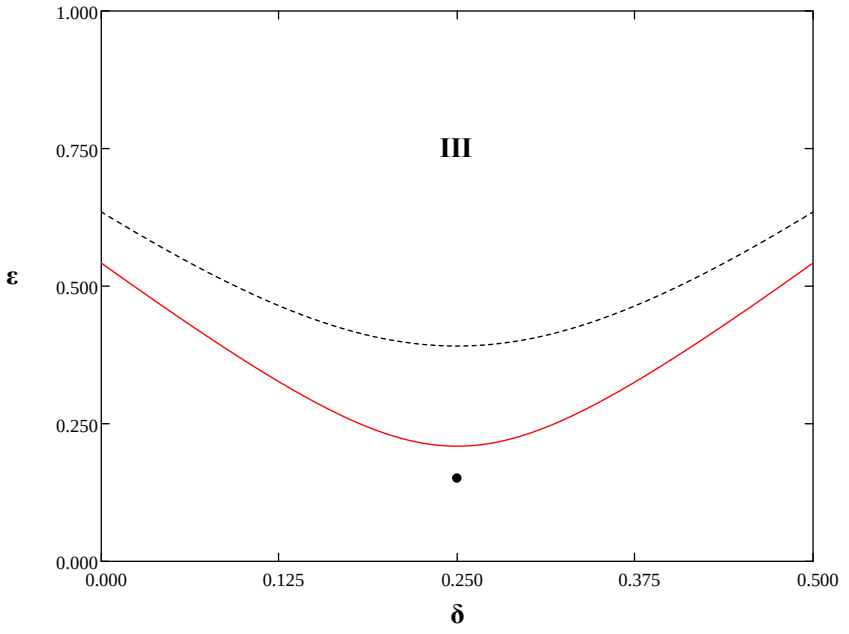

(b) (δ, ϵ) Parameter Space: $—B_1$ $- - -B_{1eq}$

Figure 6.10: Judge's lighter configuration $C_\Delta = 0.157$ $C_v = 4.362$ $B_{1eq} = 0.391$ $B_1 = 0.209$ $\Lambda = 3.637$ $f_{\phi_t} = 0$ $\psi = -2.49$

6.5 Conclusions

In this chapter, the first order approximation to the solution of the non-linear Hill's equation, derived in Chapter 5, has been used to investigate conditions that could lead to stable periodic roll motions parametrically excited by harmonic pitch and heave motions. Two configurations of a 20 degrees constant deadrise planing hull run at the United States Naval Academy (USNA) have been used as case studies. The exploration of the design parameter space (λ, C_v) has suggested that for the geometry investigated the lighter configuration run at high speed would be more prone to develop parametric rolling than the heavier configuration run at low speed, since large values of coupling restoring coefficients and small values of damping are predicted for high values of speed coefficient and low values of mean wetted length and trim. These observations have been confirmed by looking at two specific points in the testing matrix carried out at the USNA, these are the heavier configuration run at the minimum testing speed and the lighter configuration run at the maximum testing speed. For both configurations, the effect of the position damping coefficients coupling roll with heave and roll with pitch is to increase the region where periodic motions (III) and bi-stability (II) would be observed. However, the effect of the third order position damping coupling coefficients is to decrease the linear damping coefficient in the heavier configuration and to increase the linear damping coefficient in the lighter configuration. The results have also highlighted the importance of the difference between using B_1 or B_{1eq} (obtained from large amplitude runs) for the lighter configuration run at high speed since this will determine whether the planing hull is inside or outside of the region where periodic motions would be observed.

CHAPTER 7

Contributions and Recommendations

7.1 Contributions

This thesis proposes a method for investigating the conditions under which high-speed planing hulls can exhibit large oscillatory roll motions which are parametrically excited by small heave and pitch motions. The main contributions from this research can be summarized as follows:

A reduced order model for the investigation of parametric roll. Assuming a one-way coupling between heave-pitch and roll, the roll equation of motion has been written as a non-linear equation with time dependent added-mass, damping and stiffness coefficients. Based on a limited set of experimental results available in the open literature, an ordering in the coefficients is postulated such that the general form of the roll equation further reduces to a Hill's equation with third order non-linearities. Stability boundaries in the Ince-Strutt diagram in the vicinity of the principal parametric resonance have been obtained to first order by the Method of Multiple Scales. The effect of the different terms in the stability boundaries has been discussed and conditions to be satisfied in order to avoid large amplitude periodic roll motions have been derived.

Computation of forces and moments acting on planing hulls in asymmetric conditions by the 2D+t approach. The generalized forces and moments acting on a planing hull in asymmetric conditions have been obtained numerically by the 2D+t approach (also known as Slender Body Theory or High-Speed-Strip-Theory). The 2-D unsteady problem of a constant deadrise wedge impacting the water with heel and horizontal and roll velocities (oblique water entry of an asymmetrical wedge with roll) has been solved by the Volume of Fluid (VOF) method using the commercial RANSE program Star-CCM+. The VOF method has been chosen since it allows for the possibility of reattached flow after separation from the keel and the chines. The computational results of the forces and moments have been validated by comparison with the experimental results available in the open literature. For the steady state runs, the numerical results show good agreement with the experimental results, with the largest difference present in the cases with the largest degree of asymmetry (e.g., combinations of positive drift angle with negative heel angle). In these cases, separation of the flow at the keel without re-attachment and side wetting are obtained in the 2-D impact problem and consequently the forces and moments are over-predicted. For the unsteady cases, with prescribed harmonic roll motions, the computational results of the roll moment time series show good to excellent agreement for all amplitudes and frequencies of oscillation.

Contribution of the higher-order harmonics to the linear added-mass, damping and stiffness coefficients in roll. The linear roll added mass and damping coefficients have been obtained via Fourier analysis of the roll moment determined from both experimental and numerical time series. The lack of fit of the linear equation of motion when used to predict the large amplitude runs suggested the need for a non-linear roll equation of motion to model large amplitude roll motions. Therefore, non-linear models for roll added mass and roll damping have been proposed based on a formal statistical analysis of the results of forced roll oscillations. The results

highlight the importance of the non-linear components of roll added mass and roll damping for low values of mean wetted length and static trim corresponding to lighter configurations running at high speed. The analysis has shown that the inclusion of non-linear terms alters the value of the linear coefficients obtained by taking into consideration only the first order harmonic (e.g., the equivalent linear damping). Of particular interest in the context of parametric roll is the effect of the third order harmonic in the out-of-phase component of the roll moment. For some of the cases investigated, this third order harmonic is of different sign of the first order harmonic causing a dramatic reduction of the linear roll damping and therefore reducing the magnitude of heave and/or pitch motions needed to parametrically excite roll.

An empirical correction for the separation of the flow at the transom to be applied to results obtained by the 2D+t approach. The 2D+t solution cannot capture some 3-D effects such as the transition from chines-dry to chines-wet condition and flow separation from the transom. The latter being the one with the greatest influences in the computation of forces and moments. The solutions obtained for forces and moments in the horizontal plane appear to be less affected by this due to a "cancellation" effect between the pressure distributions on the two opposite sides. However, when there is separation at the keel this cancellation effect breaks and the correction for flow separation at the transom plays an important role in preventing the forces and moments to be over-predicted. Taking this into consideration, an empirical correction for separation at the transom has been proposed. This correction, obtained from re-analysis of 3-D high fidelity inviscid RANSE simulations of prismatic geometries with 10° and 20° constant deadrise angles, is independent of deadrise angle and dependent on aspect ratio as suggested by researchers at NACA on their early work on seaplanes back in the thirties (Pabst, 1931) and fifties (Shuford, 1958).

Two of the conditions tested by Professor Judge have been used as case studies for this research: the lightly loaded configuration at the maximum speed tested and the heavy loaded configuration at the minimum speed tested. Looking at the values of the coefficients for each configuration, in the context of the reduced order model, it has been shown that high-speed planing hulls running at low mean wetted length and low trim are more prone to develop parametric roll than planing hulls running at high mean wetted length and high trim. This result is consistent with what is observed in the field where lightly loaded high-speed planing hulls sometimes develop what is known in the small-craft community as *chine-walking*.

7.2 Recommendations for Future Work

Future work specifically related to this research effort would be to carry out a combination of high fidelity 3-D RANSE simulations, model and full scale tests in order to:

1. Explore the stability boundaries in order to validate the predictions obtained by the reduced order model. In this case, the simulations/tests correspond to models forced in heave and/or pitch and free in roll (first stage) and free in heave-roll-pitch (second stage).

2. Validate the assumptions made with regards to the ordering of the coefficients in the heave-roll-pitch equations of motion for a larger set of experimental conditions. In this case, the simulations/tests correspond to models forced first in each of the three degrees of freedom (heave-roll-pitch) and then systematically combined in order to generate the information required to obtain the coefficients coupling these three degrees of freedom via inertial, dissipative and stiffness terms.

3. Validate the assumptions made with regards to the characteristics of the limit cycles (amplitude, frequency and phase difference) in the heave-pitch autonomous system (porpoising). In this case, the simulations/tests correspond to models free in heave and pitch.

Besides, comparisons between high fidelity 3-D RANSE solutions and 2D+t solutions are required in order to assess the limits of applicability of the asymmetric 2D+t theory by looking at the relative orders of magnitude of the perturbation flow velocities in the longitudinal and transverse directions and by comparing pressure distributions and free surface profiles.

The uncertainty in the stability boundaries was treated briefly at the end of Chapter 6 by assuming the problem as one of "error propagation" due to the uncertainty associated to each of the coefficients used to construct them. Continuing in this direction, it is recommended to carry out a sensitivity analysis on the covariances of the coefficients, assuming that they are not independent, and to formally construct the uncertainty regions. Another possibility would be to construct probability basins in order to compute the probability of being inside or outside of the regions where periodic motions would be observed.

Also, it appears to be a common practice to model the heave-pitch motions on planing hulls by assuming a coupled system of equations with linear added mass, linear damping and non-linear stiffness coefficients (e.g., Sun and Faltinsen (2010)), as suggested in Troesch (1992) for the cases with high values of mean wetted length. However, a preliminary investigation into the heave-pitch system by the 2D+t approach showed that there are important dissipative non-linearities, specially in the cases with low mean wetted length. Therefore, an investigation into the best non-linear model to describe the heave-pitch system seems to be granted.

APPENDICES

APPENDIX A

Non-dimensional Coefficients in the Roll Equation of Motion

First order

$$\bar{K}_{\phi_{\bar{t}\bar{t}}} = \frac{K_{\phi_{tt}}}{\rho B^5} \qquad \bar{K}_{\phi_{\bar{t}}} = \frac{K_{\phi_t}}{\rho B^5 \sqrt{\frac{g}{B}}} \qquad \bar{K}_{\phi} = \frac{K_{\phi}}{\rho g B^4}$$

Second order

$$\bar{K}_{\bar{z}\phi_{\bar{t}\bar{t}}} = \frac{K_{z\phi_{tt}}}{\rho B^4} \qquad \bar{K}_{\theta\phi_{\bar{t}\bar{t}}} = \frac{K_{\theta\phi_{tt}}}{\rho B^5}$$

$$\bar{K}_{\bar{z}_{\bar{t}}\phi_{\bar{t}}} = \frac{K_{z_t\phi_t}}{\rho B^4} \qquad \bar{K}_{\theta_{\bar{t}}\phi_{\bar{t}}} = \frac{K_{\theta_t\phi_t}}{\rho B^5} \qquad \bar{K}_{\phi\bar{z}_{\bar{t}\bar{t}}} = \frac{K_{\phi z_{tt}}}{\rho B^4} \qquad \bar{K}_{\phi\theta_{\bar{t}\bar{t}}} = \frac{K_{\phi\theta_{tt}}}{\rho B^5}$$

$$\bar{K}_{\bar{z}\phi_{\bar{t}}} = \frac{K_{z\phi_t}}{\rho B^4 \sqrt{\frac{g}{B}}} \qquad \bar{K}_{\theta\phi_{\bar{t}}} = \frac{K_{\theta\phi_t}}{\rho B^5 \sqrt{\frac{g}{B}}} \qquad \bar{K}_{\phi\bar{z}_{\bar{t}}} = \frac{K_{\phi z_t}}{\rho B^4 \sqrt{\frac{g}{B}}} \qquad \bar{K}_{\phi\theta\bar{t}} = \frac{K_{\phi\theta_t}}{\rho B^5 \sqrt{\frac{g}{B}}}$$

$$\bar{K}_{\bar{z}\phi} = \frac{K_{z\phi}}{\rho g B^3} \qquad \bar{K}_{\phi\theta} = \frac{K_{\phi\theta}}{\rho g B^4}$$

Third order

$$\bar{K}_{\bar{z}\bar{z}\phi_{\bar{t}\bar{t}}} = \frac{K_{zz\phi_{tt}}}{\rho B^3} \qquad \bar{K}_{\bar{z}\theta\phi_{\bar{t}\bar{t}}} = \frac{K_{z\theta\phi_{tt}}}{\rho B^4} \qquad \bar{K}_{\theta\theta\phi_{\bar{t}\bar{t}}} = \frac{K_{\theta\theta\phi_{tt}}}{\rho B^5} \qquad \bar{K}_{\phi\phi\phi_{\bar{t}\bar{t}}} = \frac{K_{\phi\phi\phi_{tt}}}{\rho B^5}$$

$$\bar{K}_{\bar{z}\bar{z}_{\bar{t}}\phi_{\bar{t}}} = \frac{K_{zz_t\phi_t}}{\rho B^3} \qquad \bar{K}_{\theta\bar{z}_{\bar{t}}\phi_{\bar{t}}} = \frac{K_{\theta z_t\phi_t}}{\rho B^4} \qquad \bar{K}_{\bar{z}\phi_{\bar{t}}\theta_{\bar{t}}} = \frac{K_{z\phi_t\theta_t}}{\rho B^4} \qquad \bar{K}_{\theta\phi_{\bar{t}}\theta_{\bar{t}}} = \frac{K_{\theta\phi_t\theta_t}}{\rho B^5}$$

$$\bar{K}_{\bar{z}\phi\bar{z}_{\bar{t}\bar{t}}} = \frac{K_{z\phi z_{tt}}}{\rho B^3} \qquad \bar{K}_{\phi\theta\bar{z}_{\bar{t}\bar{t}}} = \frac{K_{\phi\theta z_{tt}}}{\rho B^4} \qquad \bar{K}_{\bar{z}\phi\theta_{\bar{t}\bar{t}}} = \frac{K_{z\phi\theta_{tt}}}{\rho B^4} \qquad \bar{K}_{\phi\theta\theta_{\bar{t}\bar{t}}} = \frac{K_{\phi\theta\theta_{tt}}}{\rho B^5}$$

$$\bar{K}_{\phi\bar{z}_{\bar{t}}\bar{z}_{\bar{t}}} = \frac{K_{\phi z_t z_t}}{\rho B^3} \qquad \bar{K}_{\phi\bar{z}_{\bar{t}}\theta_{\bar{t}}} = \frac{K_{\phi z_t\theta_t}}{\rho B^4} \qquad \bar{K}_{\phi\theta_{\bar{t}}\theta_{\bar{t}}} = \frac{K_{\phi\theta_t\theta_t}}{\rho B^5} \qquad \bar{K}_{\phi\phi_{\bar{t}}\phi_{\bar{t}}} = \frac{K_{\phi\phi_t\phi_t}}{\rho B^5}$$

$$\bar{K}_{\bar{z}\bar{z}\phi_{\bar{t}}} = \frac{K_{zz\phi_t}}{\rho B^3\sqrt{\frac{g}{B}}} \qquad \bar{K}_{\bar{z}\theta\phi_{\bar{t}}} = \frac{K_{z\theta\phi_t}}{\rho B^4\sqrt{\frac{g}{B}}} \qquad \bar{K}_{\theta\theta\phi_{\bar{t}}} = \frac{K_{\theta\theta\phi_t}}{\rho B^5\sqrt{\frac{g}{B}}} \qquad \bar{K}_{\phi_{\bar{t}}\phi_{\bar{t}}\phi_{\bar{t}}} = \frac{K_{\phi_t\phi_t\phi_t}}{\rho B^5\sqrt{\frac{B}{g}}}$$

$$\bar{K}_{\bar{z}_{\bar{t}}\bar{z}_{\bar{t}}\phi_{\bar{t}}} = \frac{K_{z_tz_t\phi_t}}{\rho B^3\sqrt{\frac{B}{g}}} \qquad \bar{K}_{\bar{z}_{\bar{t}}\phi_{\bar{t}}\theta_{\bar{t}}} = \frac{K_{z_t\phi_t\theta_t}}{\rho B^4\sqrt{\frac{B}{g}}} \qquad \bar{K}_{\phi_{\bar{t}}\theta_{\bar{t}}\theta_{\bar{t}}} = \frac{K_{\phi_t\theta_t\theta_t}}{\rho B^5\sqrt{\frac{B}{g}}} \qquad \bar{K}_{\phi\phi\phi_{\bar{t}}} = \frac{K_{\phi\phi\phi_t}}{\rho B^5\sqrt{\frac{g}{B}}}$$

$$\bar{K}_{\bar{z}\phi\bar{z}_{\bar{t}}} = \frac{K_{z\phi z_t}}{\rho B^3\sqrt{\frac{g}{B}}} \qquad \bar{K}_{\phi\theta\bar{z}_{\bar{t}}} = \frac{K_{\phi\theta z_t}}{\rho B^4\sqrt{\frac{g}{B}}} \qquad \bar{K}_{\bar{z}\phi\theta_{\bar{t}}} = \frac{K_{z\phi\theta_t}}{\rho B^4\sqrt{\frac{g}{B}}} \qquad \bar{K}_{\phi\theta\theta_{\bar{t}}} = \frac{K_{\phi\theta\theta_t}}{\rho B^5\sqrt{\frac{g}{B}}}$$

$$\bar{K}_{\bar{z}\bar{z}\phi} = \frac{K_{zz\phi}}{\rho g B^2} \qquad \bar{K}_{\bar{z}\phi\theta} = \frac{K_{z\phi\theta}}{\rho g B^3} \qquad \bar{K}_{\phi\theta\theta} = \frac{K_{\phi\theta\theta}}{\rho g B^4} \qquad \bar{K}_{\phi\phi\phi} = \frac{K_{\phi\phi\phi}}{\rho g B^4}$$

Fourth order

$$\bar{K}_{\bar{z}\bar{z}\bar{z}\phi} = \frac{K_{zzz\phi}}{\rho g B} \qquad \bar{K}_{\bar{z}\bar{z}\phi\theta} = \frac{K_{zz\phi\theta}}{\rho g B^2} \qquad \bar{K}_{\bar{z}\phi\theta\theta} = \frac{K_{z\phi\theta\theta}}{\rho g B^3} \qquad \bar{K}_{\phi\theta\theta\theta} = \frac{K_{\phi\theta\theta\theta}}{\rho g B^4}$$

$$\bar{K}_{\bar{z}\phi\phi\phi} = \frac{K_{z\phi\phi\phi}}{\rho g B^3} \qquad \bar{K}_{\phi\phi\phi\theta} = \frac{K_{\phi\phi\phi\theta}}{\rho g B^4}$$

Fifth order

$$\bar{K}_{\bar{z}\bar{z}\bar{z}\bar{z}\phi} = \frac{K_{zzzz\phi}}{\rho g} \qquad \bar{K}_{\bar{z}\bar{z}\bar{z}\phi\theta} = \frac{K_{zzz\phi\theta}}{\rho g B} \qquad \bar{K}_{\bar{z}\bar{z}\phi\theta\theta} = \frac{K_{zz\phi\theta\theta}}{\rho g B^2} \qquad \bar{K}_{\bar{z}\phi\theta\theta\theta} = \frac{K_{z\phi\theta\theta\theta}}{\rho g B^3}$$

$$\bar{K}_{\phi\theta\theta\theta\theta} = \frac{K_{\phi\theta\theta\theta\theta}}{\rho g B^4} \qquad \bar{K}_{\bar{z}\bar{z}\phi\phi\phi} = \frac{K_{zz\phi\phi\phi}}{\rho g B^2} \qquad \bar{K}_{\bar{z}\phi\phi\phi\theta} = \frac{K_{z\phi\phi\phi\theta}}{\rho g B^3} \qquad \bar{K}_{\phi\phi\phi\theta\theta} = \frac{K_{\phi\phi\phi\theta\theta}}{\rho g B^4}$$

$$\bar{K}_{\phi\phi\phi\phi\phi} = \frac{K_{\phi\phi\phi\phi\phi}}{\rho g B^4}$$

APPENDIX B

Periodic Coefficients in the Roll Equation of Motion

$$f_0^{\phi_{tt}} = \frac{1}{2}\left(K_8^A\zeta_3^2 + K_9^A\zeta_3\zeta_5\cos\alpha_5 + K_{10}^A\zeta_5^2\right)$$

$$f_{1s}^{\phi_{tt}} = -K_3^A\zeta_5\sin\alpha_5$$

$$f_{1c}^{\phi_{tt}} = K_2^A\zeta_3 + K_3^A\zeta_5\cos\alpha_5$$

$$f_{2s}^{\phi_{tt}} = -\frac{1}{2}\left(K_9^A\zeta_3\zeta_5\sin\alpha_5 + K_{10}^A\zeta_5^2\sin 2\alpha_5\right)$$

$$f_{2c}^{\phi_{tt}} = \frac{1}{2}\left(K_8^A\zeta_3^2 + K_9^A\zeta_3\zeta_5\cos\alpha_5 + K_{10}^A\zeta_5^2\cos 2\alpha_5\right)$$

$$
\begin{aligned}
f_0^{\phi_t} =& + \frac{1}{2}\omega \left(K_{13}^A - K_{14}^A\right) \zeta_3\zeta_5 \sin\alpha_5 \\
&+ \frac{1}{2}\left(K_6^D\zeta_3^2 + K_7^D\zeta_3\zeta_5\cos\alpha_5 + K_8^D\zeta_5^2\right) \\
&+ \frac{1}{2}\omega^2\left(K_9^D\zeta_3^2 + K_{10}^D\zeta_3\zeta_5\cos\alpha_5 + K_{11}^D\zeta_5^2\right)
\end{aligned}
$$

$$
\begin{aligned}
f_{1s}^{\phi_t} =& - \omega\left(K_4^A\zeta_3 + K_5^A\zeta_5\cos\alpha_5\right) - K_3^D\zeta_5\sin\alpha_5 \\
f_{1c}^{\phi_t} =& - \omega K_5^A\zeta_5\sin\alpha_5 + \left(K_2^D\zeta_3 + K_3^D\zeta_5\cos\alpha_5\right)
\end{aligned}
$$

$$
\begin{aligned}
f_{2s}^{\phi_t} =& - \frac{1}{2}\omega\left[K_{12}^A\zeta_3^2 + \left(K_{13}^A + K_{14}^A\right)\zeta_3\zeta_5\cos\alpha_5 + K_{15}^A\zeta_5^2\cos 2\alpha_5\right] \\
&- \frac{1}{2}\left(K_7^D\zeta_3\zeta_5\sin\alpha_5 + K_8^D\zeta_5^2\sin 2\alpha_5\right) + \frac{1}{2}\omega^2\left(K_{10}^D\zeta_3\zeta_5\sin\alpha_5 + K_{11}^D\zeta_5^2\sin 2\alpha_5\right) \\
f_{2c}^{\phi_t} =& - \frac{1}{2}\omega\left[\left(K_{13}^A + K_{14}^A\right)\zeta_3\zeta_5\sin\alpha_5 + K_{15}^A\zeta_5^2\sin 2\alpha_5\right] \\
&+ \frac{1}{2}\left(K_6^D\zeta_3^2 + K_7^D\zeta_3\zeta_5\cos\alpha_5 + K_8^D\zeta_5^2\cos 2\alpha_5\right) \\
&- \frac{1}{2}\omega^2\left(K_9^D\zeta_3^2 + K_{10}^D\zeta_3\zeta_5\cos\alpha_5 + K_{11}^D\zeta_5^2\cos 2\alpha_5\right)
\end{aligned}
$$

$$
\begin{aligned}
f_0^{\phi} =& - \frac{1}{2}\omega^2\left[\left(K_{16}^A - K_{20}^A\right)\zeta_3^2 + \left(K_{17}^A + K_{18}^A - K_{21}^A\right)\zeta_3\zeta_5\cos\alpha_5 + \left(K_{19}^A - K_{22}^A\right)\zeta_5^2\right] \\
&+ \frac{1}{2}\omega\left(K_{14}^D - K_{15}^D\right)\zeta_3\zeta_5\sin\alpha_5 \\
&+ \frac{1}{2}\left(K_4^S\zeta_3^2 + K_5^S\zeta_3\zeta_5\cos\alpha_5 + K_6^S\zeta_5^2\right) \\
&+ \frac{1}{8}\left[3K_{14}^S\zeta_3^4 + 3K_{15}^S\zeta_3^3\zeta_5\cos\alpha_5 + K_{16}^S\zeta_3^2\zeta_5^2\left(2 + \cos 2\alpha_5\right) + 3K_{17}^S\zeta_3\zeta_5^3\cos\alpha_5 + 3K_{18}^S\zeta_5^4\right]
\end{aligned}
$$

$$
\begin{aligned}
f_{1s}^{\phi} =& + \omega^2 K_7^A \zeta_5 \sin\alpha_5 - \omega \left(K_4^D \zeta_3 + K_5^D \zeta_5 \cos\alpha_5 \right) - K_3^S \zeta_5 \sin\alpha_5 \\
& - \frac{1}{4} \left(K_9^S \zeta_3^2 \zeta_5 \sin\alpha_5 + K_{10}^S \zeta_3 \zeta_5^2 \sin 2\alpha_5 + 3 K_{11}^S \zeta_5^3 \sin\alpha_5 \right) \\
f_{1c}^{\phi} =& - \omega^2 \left(K_6^A \zeta_3 + K_7^A \zeta_5 \cos\alpha_5 \right) - \omega K_5^D \zeta_5 \sin\alpha_5 + \left(K_2^S \zeta_3 + K_3^S \zeta_5 \cos\alpha_5 \right) \\
& + \frac{1}{4} \left(3 K_8^S \zeta_3^3 + 3 K_9^S \zeta_3^2 \zeta_5 \cos\alpha_5 + K_{10}^S \zeta_3 \zeta_5^2 \left(2 + \cos 2\alpha_5 \right) + 3 K_{11}^S \zeta_5^3 \cos\alpha_5 \right)
\end{aligned}
$$

$$
\begin{aligned}
f_{2s}^{\phi} =& + \frac{1}{2} \omega^2 \left[\left(K_{17}^A + K_{18}^A + K_{21}^A \right) \zeta_3 \zeta_5 \sin\alpha_5 + \left(K_{19}^A + K_{22}^A \right) \zeta_5^2 \sin 2\alpha_5 \right] \\
& - \frac{1}{2} \omega \left[K_{13}^D \zeta_3^2 + \left(K_{14}^D + K_{15}^D \right) \zeta_3 \zeta_5 \cos\alpha_5 + K_{16}^D \zeta_5^2 \cos 2\alpha_5 \right] \\
& - \frac{1}{2} \left(K_5^S \zeta_3 \zeta_5 \sin\alpha_5 + K_6^S \zeta_5^2 \sin 2\alpha_5 \right) \\
& - \frac{1}{8} \big[2 K_{15}^S \zeta_3^3 \zeta_5 \sin\alpha_5 + 2 K_{16}^S \zeta_3^2 \zeta_5^2 \sin 2\alpha_5 \\
& \qquad + K_{17}^S \zeta_3 \zeta_5^3 \left(3 \sin\alpha_5 + \sin 3\alpha_5 \right) + 4 K_{18}^S \zeta_5^4 \sin 2\alpha_5 \big] \\
f_{2c}^{\phi} =& - \frac{1}{2} \omega^2 \left[\left(K_{16}^A + K_{20}^A \right) \zeta_3^2 + \left(K_{17}^A + K_{18}^A + K_{21}^A \right) \zeta_3 \zeta_5 \cos\alpha_5 + \left(K_{19}^A + K_{22}^A \right) \zeta_5^2 \cos 2\alpha_5 \right] \\
& - \frac{1}{2} \omega \left[\left(K_{14}^D + K_{15}^D \right) \zeta_3 \zeta_5 \sin\alpha_5 + K_{16}^D \zeta_5^2 \sin 2\alpha_5 \right] \\
& + \frac{1}{2} \left(K_4^S \zeta_3^2 + K_5^S \zeta_3 \zeta_5 \cos\alpha_5 + K_6^S \zeta_5^2 \cos 2\alpha_5 \right) \\
& + \frac{1}{8} \big[4 K_{14}^S \zeta_3^4 + 4 K_{15}^S \zeta_3^3 \zeta_5 \cos\alpha_5 + 2 K_{16}^S \zeta_3^2 \zeta_5^2 \left(1 + \cos 2\alpha_5 \right) \\
& \qquad + K_{17}^S \zeta_3 \zeta_5^3 \left(3 \cos\alpha_5 + \cos 3\alpha_5 \right) + 4 K_{18}^S \zeta_5^4 \cos 2\alpha_5 \big]
\end{aligned}
$$

$$
\begin{aligned}
f_{3s}^{\phi} =& - \frac{1}{4} \left(K_9^S \zeta_3^2 \zeta_5 \sin\alpha_5 + K_{10}^S \zeta_3 \zeta_5^2 \sin 2\alpha_5 + K_{11}^S \zeta_5^3 \sin 3\alpha_5 \right) \\
f_{3c}^{\phi} =& \frac{1}{4} \left(K_8^S \zeta_3^3 + K_9^S \zeta_3^2 \zeta_5 \cos\alpha_5 + K_{10}^S \zeta_3 \zeta_5^2 \cos 2\alpha_5 + K_{11}^S \zeta_5^3 \cos 3\alpha_5 \right)
\end{aligned}
$$

$$
\begin{aligned}
f_{4s}^{\phi} =& - \frac{1}{8} \left(K_{15}^S \zeta_3^3 \zeta_5 \sin\alpha_5 + K_{16}^S \zeta_3^2 \zeta_5^2 \sin 2\alpha_5 + K_{17}^S \zeta_3 \zeta_5^3 \sin 3\alpha_5 + K_{18}^S \zeta_5^4 \sin 4\alpha_5 \right) \\
f_{4c}^{\phi} =& \frac{1}{8} \left(K_{14}^S \zeta_3^4 + K_{15}^S \zeta_3^3 \zeta_5 \cos\alpha_5 + K_{16}^S \zeta_3^2 \zeta_5^2 \cos 2\alpha_5 + K_{17}^S \zeta_3 \zeta_5^3 \cos 3\alpha_5 + K_{18}^S \zeta_5^4 \cos 4\alpha_5 \right)
\end{aligned}
$$

$$f_0^{\phi\phi\phi} = \frac{1}{2}\left(K_{19}^S\zeta_3^2 + K_{20}^S\zeta_3\zeta_5\cos\alpha_5 + K_{21}^S\zeta_5^2\right)$$

$$f_{1s}^{\phi\phi\phi} = -K_{13}^S\zeta_5\sin\alpha_5$$
$$f_{1c}^{\phi\phi\phi} = K_{12}^S\zeta_3 + K_{13}^S\zeta_5\cos\alpha_5$$

$$f_{2s}^{\phi\phi\phi} = -\frac{1}{2}\left(K_{20}^S\zeta_3\zeta_5\sin\alpha_5 + K_{21}^S\zeta_5^2\sin 2\alpha_5\right)$$
$$f_{2c}^{\phi\phi\phi} = \frac{1}{2}\left(K_{19}^S\zeta_3^2 + K_{20}^S\zeta_3\zeta_5\cos\alpha_5 + K_{21}^S\zeta_5^2\cos 2\alpha_5\right)$$

APPENDIX C

Time Series Comparison Between 2D+t Theory and Forced Roll Experiments

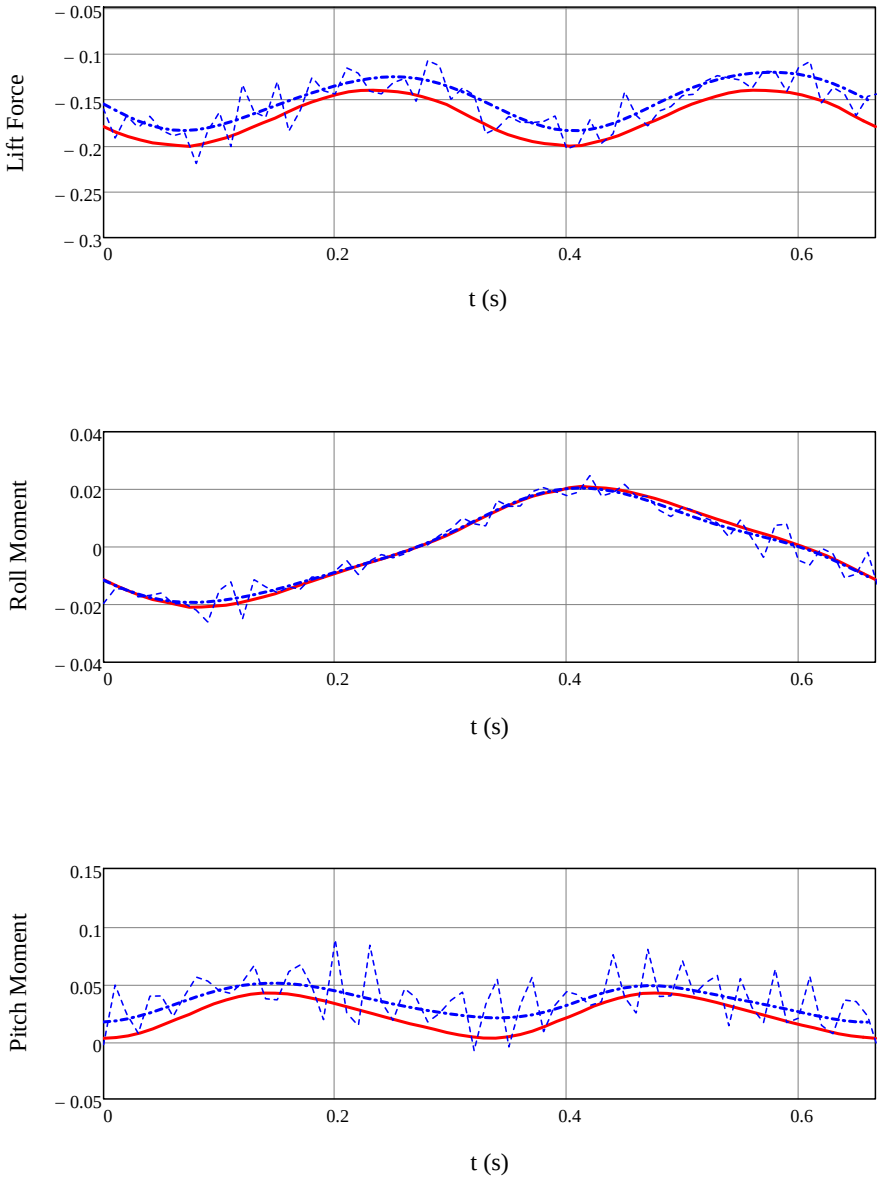

Figure C.1: Time series comparison of non-dimensional lift force and roll and pitch moments between 2D+t theory (solid line) and experiments (averaged: dash-dotted line; raw: dotted line) in forced roll. Experimental conditions: $C_\Delta = 0.15$, $C_v = 2.9$, $\phi_0 = 10°$, $f = 1.5$ Hz

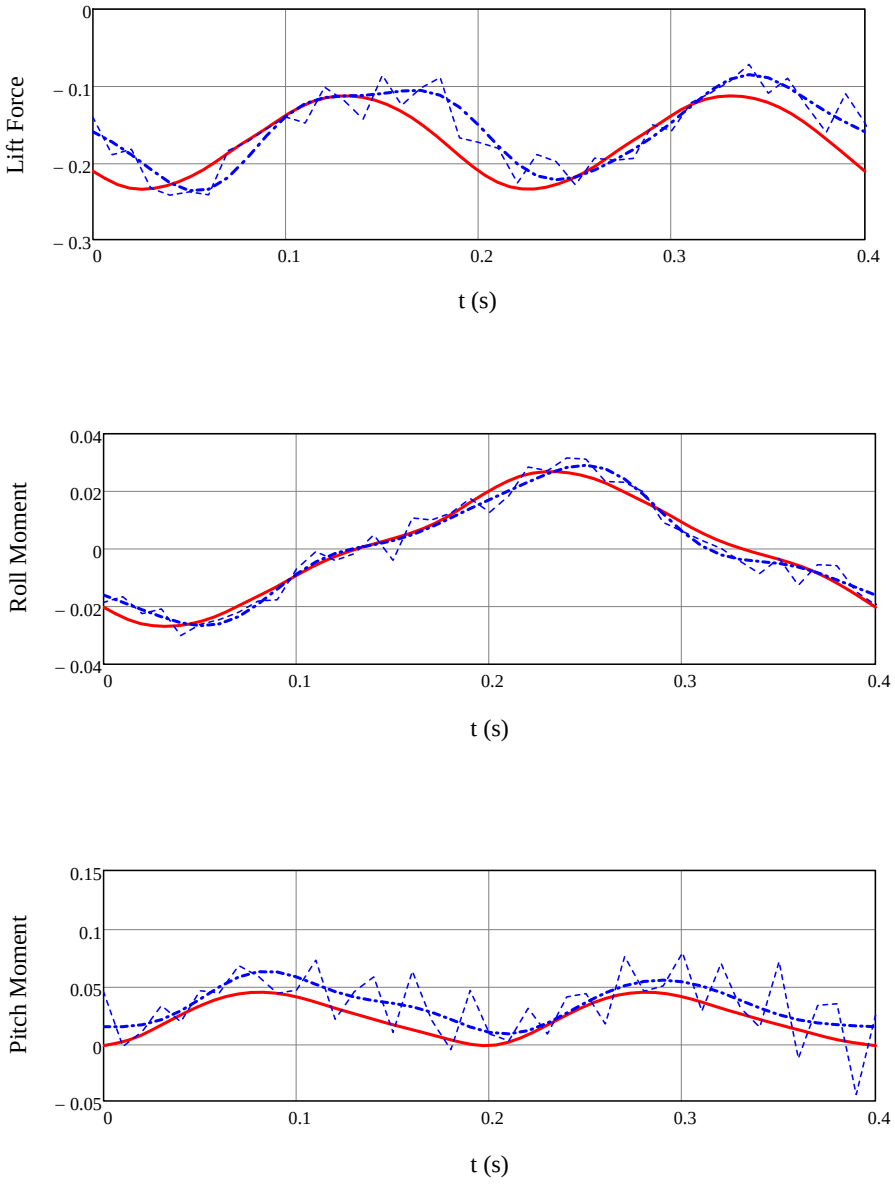

Figure C.2: Time series comparison of non-dimensional lift force and roll and pitch moments between 2D+t theory (solid line) and experiments (averaged: dash-dotted line; raw: dotted line) in forced roll. Experimental conditions: $C_\Delta = 0.15$, $C_v = 2.9$, $\phi_0 = 10°$, $f = 2.5$ Hz

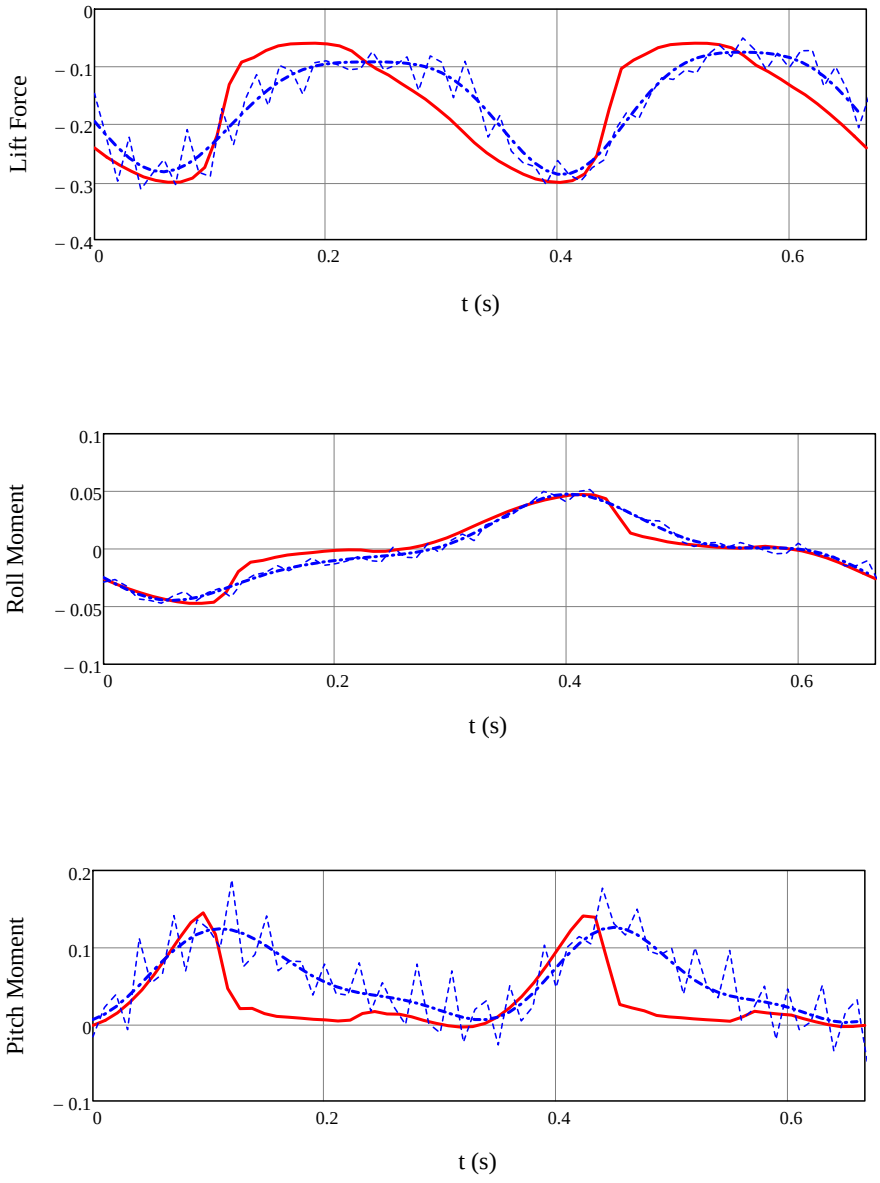

Figure C.3: Time series comparison of non-dimensional lift force and roll and pitch moments between 2D+t theory (solid line) and experiments (averaged: dash-dotted line; raw: dotted line) in forced roll. Experimental conditions: $C_\Delta = 0.15$, $C_v = 2.9$, $\phi_0 = 20°$, $f = 1.5$ Hz

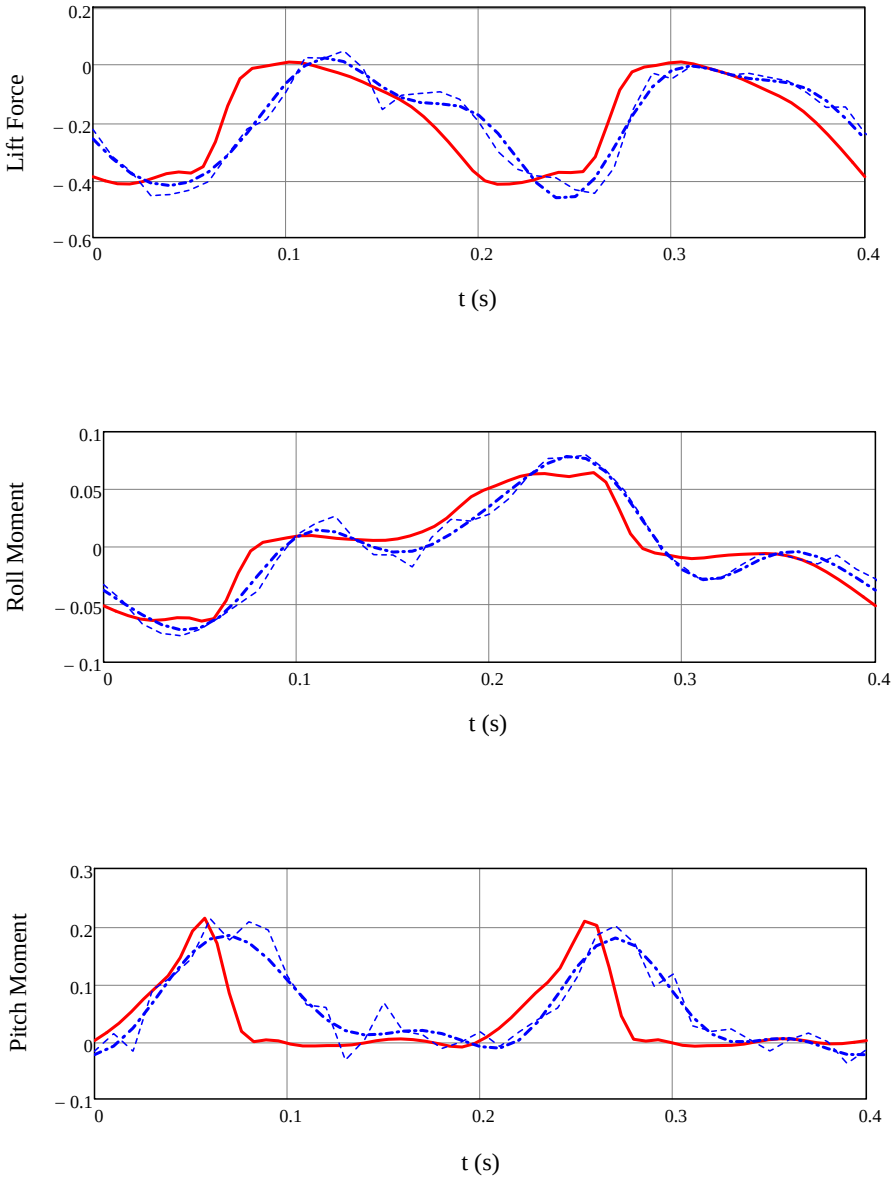

Figure C.4: Time series comparison of non-dimensional lift force and roll and pitch moments between 2D+t theory (solid line) and experiments (averaged: dash-dotted line; raw: dotted line) in forced roll. Experimental conditions: $C_\Delta = 0.15$, $C_v = 2.9$, $\phi_0 = 20°$, $f = 2.5$ Hz

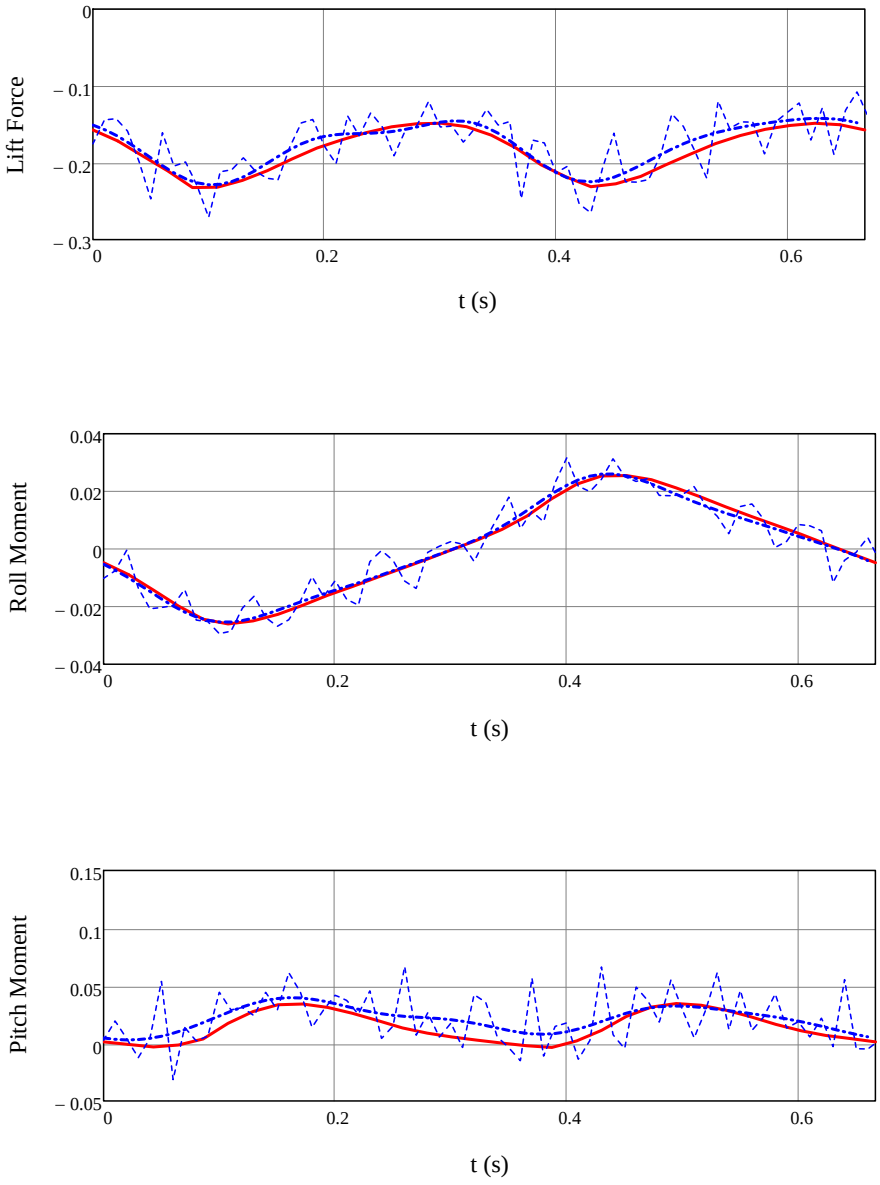

Figure C.5: Time series comparison of non-dimensional lift force and roll and pitch moments between 2D+t theory (solid line) and experiments (averaged: dash-dotted line; raw: dotted line) in forced roll. Experimental conditions: $C_\Delta = 0.15$, $C_v = 4.3$, $\phi_0 = 10°$, $f = 1.5$ Hz

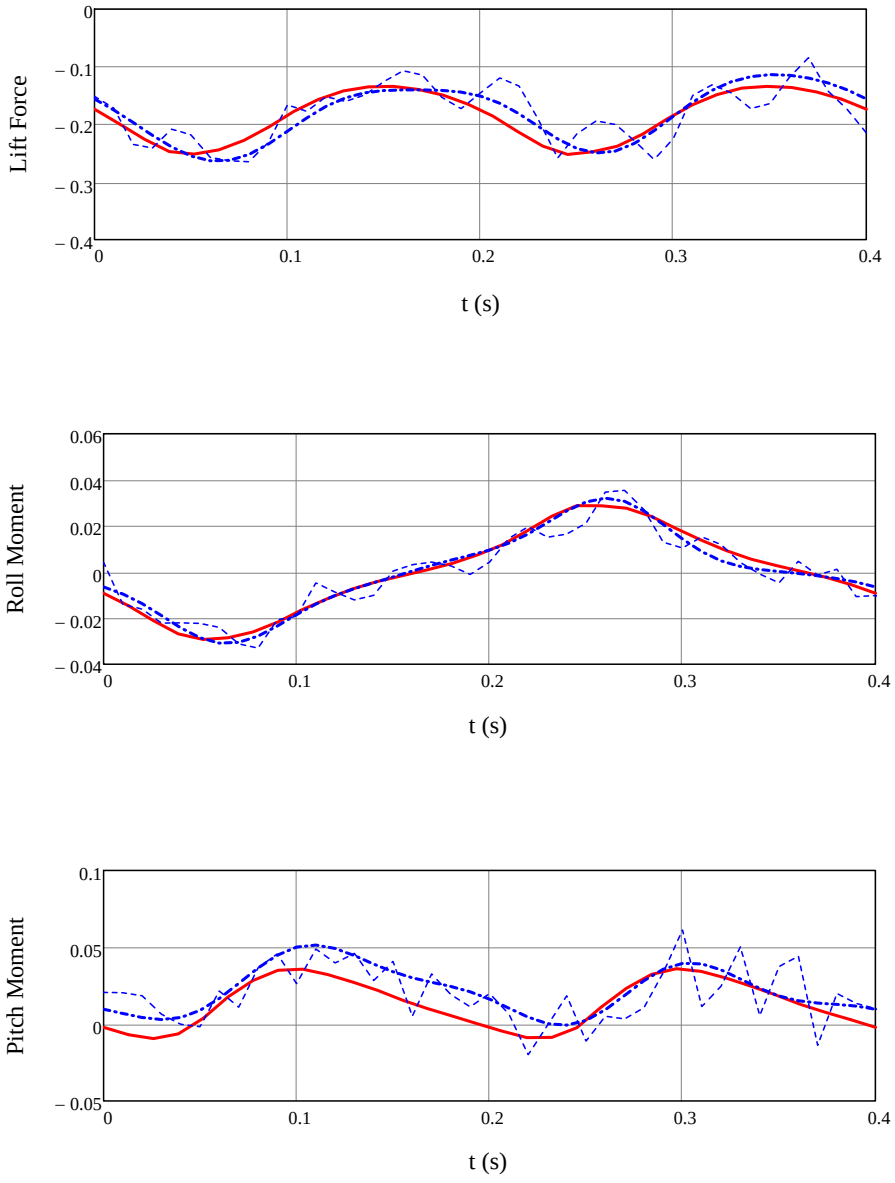

Figure C.6: Time series comparison of non-dimensional lift force and roll and pitch moments between 2D+t theory (solid line) and experiments (averaged: dash-dotted line; raw: dotted line) in forced roll. Experimental conditions: $C_\Delta = 0.15$, $C_v = 4.3$, $\phi_0 = 10°$, $f = 2.5$ Hz

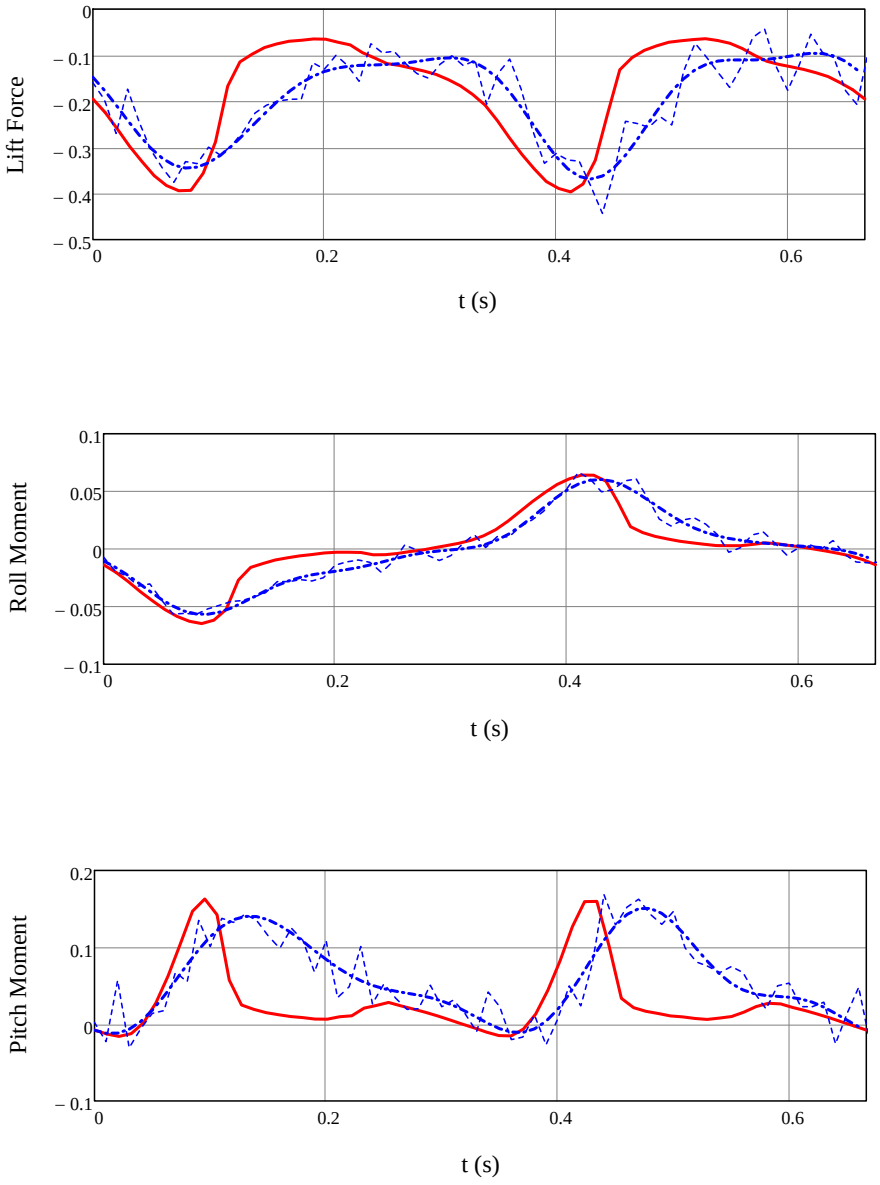

Figure C.7: Time series comparison of non-dimensional lift force and roll and pitch moments between 2D+t theory (solid line) and experiments (averaged: dash-dotted line; raw: dotted line) in forced roll. Experimental conditions: $C_\Delta = 0.15$, $C_v = 4.3$, $\phi_0 = 20°$, $f = 1.5$ Hz

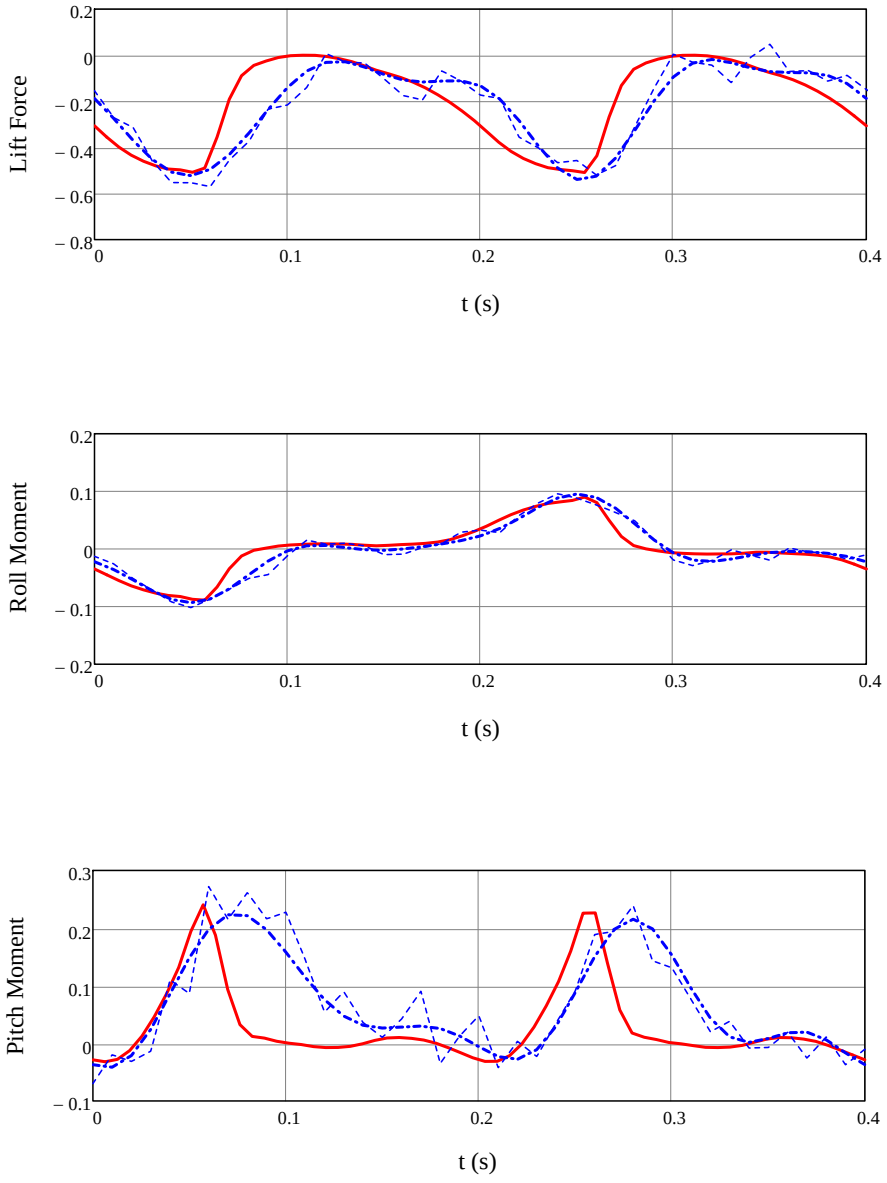

Figure C.8: Time series comparison of non-dimensional lift force and roll and pitch moments between 2D+t theory (solid line) and experiments (averaged: dash-dotted line; raw: dotted line) in forced roll. Experimental conditions: $C_\Delta = 0.15$, $C_v = 4.3$, $\phi_0 = 20°$, $f = 2.5$ Hz

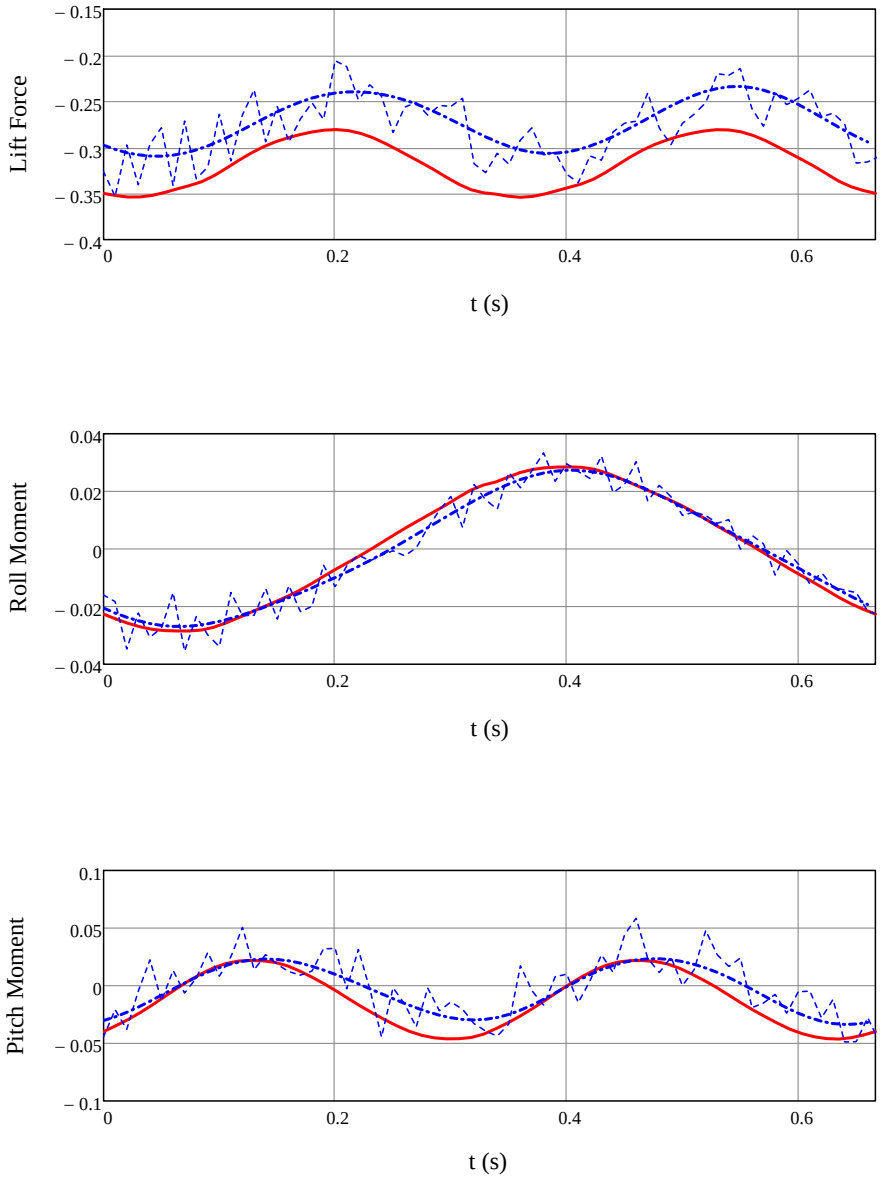

Figure C.9: Time series comparison of non-dimensional lift force and roll and pitch moments between 2D+t theory (solid line) and experiments (averaged: dash-dotted line; raw: dotted line) in forced roll. Experimental conditions: $C_\Delta = 0.29$, $C_v = 2.9$, $\phi_0 = 10°$, $f = 1.5$ Hz

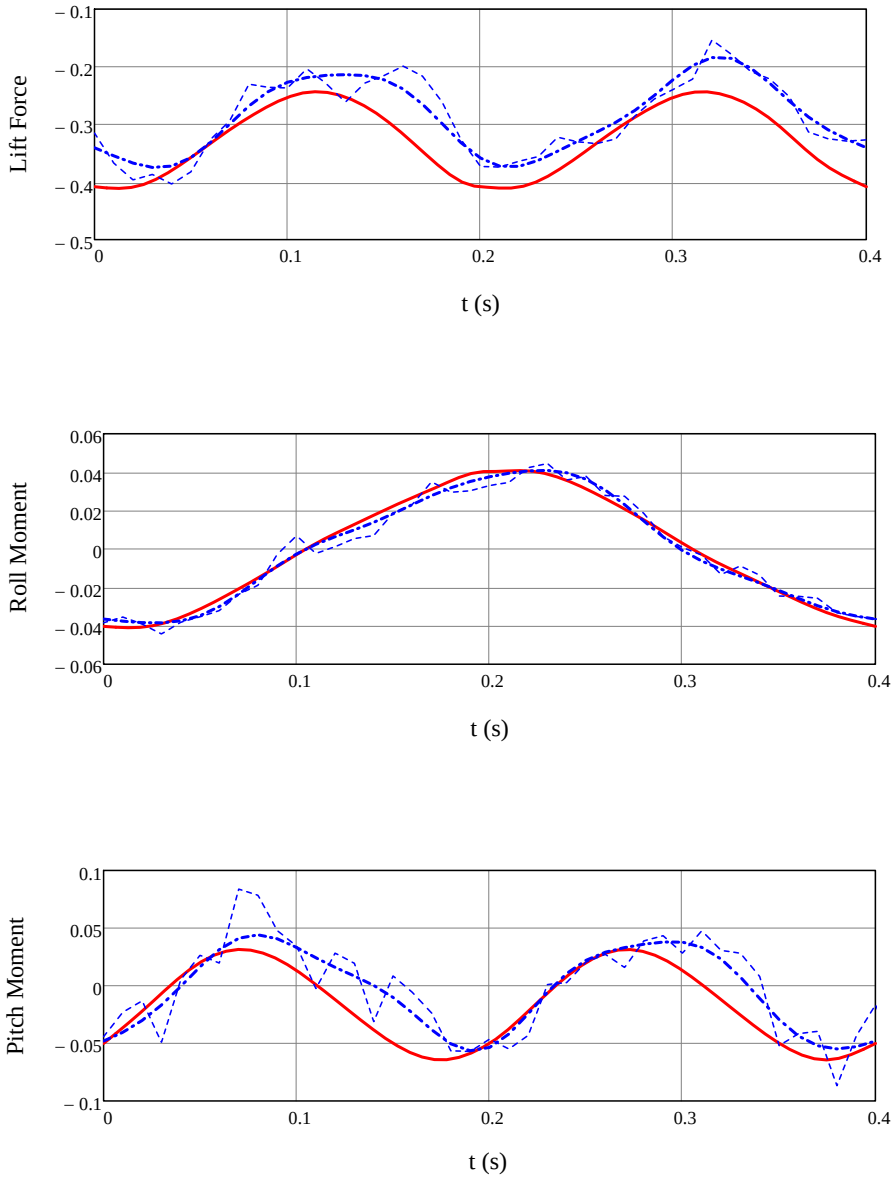

Figure C.10: Time series comparison of non-dimensional lift force and roll and pitch moments between 2D+t theory (solid line) and experiments (averaged: dash-dotted line; raw: dotted line) in forced roll. Experimental conditions: $C_\Delta = 0.29$, $C_v = 2.9$, $\phi_0 = 10°$, $f = 2.5$ Hz

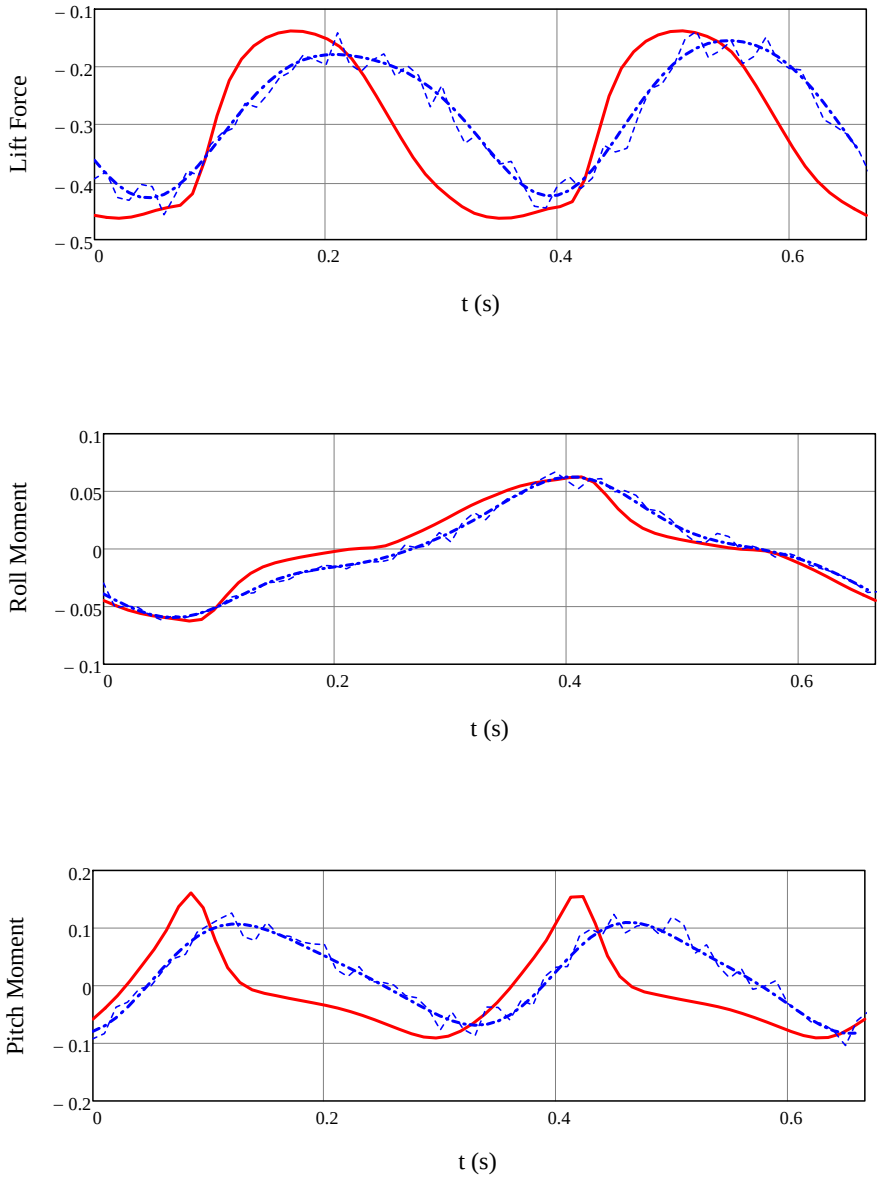

Figure C.11: Time series comparison of non-dimensional lift force and roll and pitch moments between 2D+t theory (solid line) and experiments (averaged: dash-dotted line; raw: dotted line) in forced roll. Experimental conditions: $C_\Delta = 0.29$, $C_v = 2.9$, $\phi_0 = 20°$, $f = 1.5$ Hz

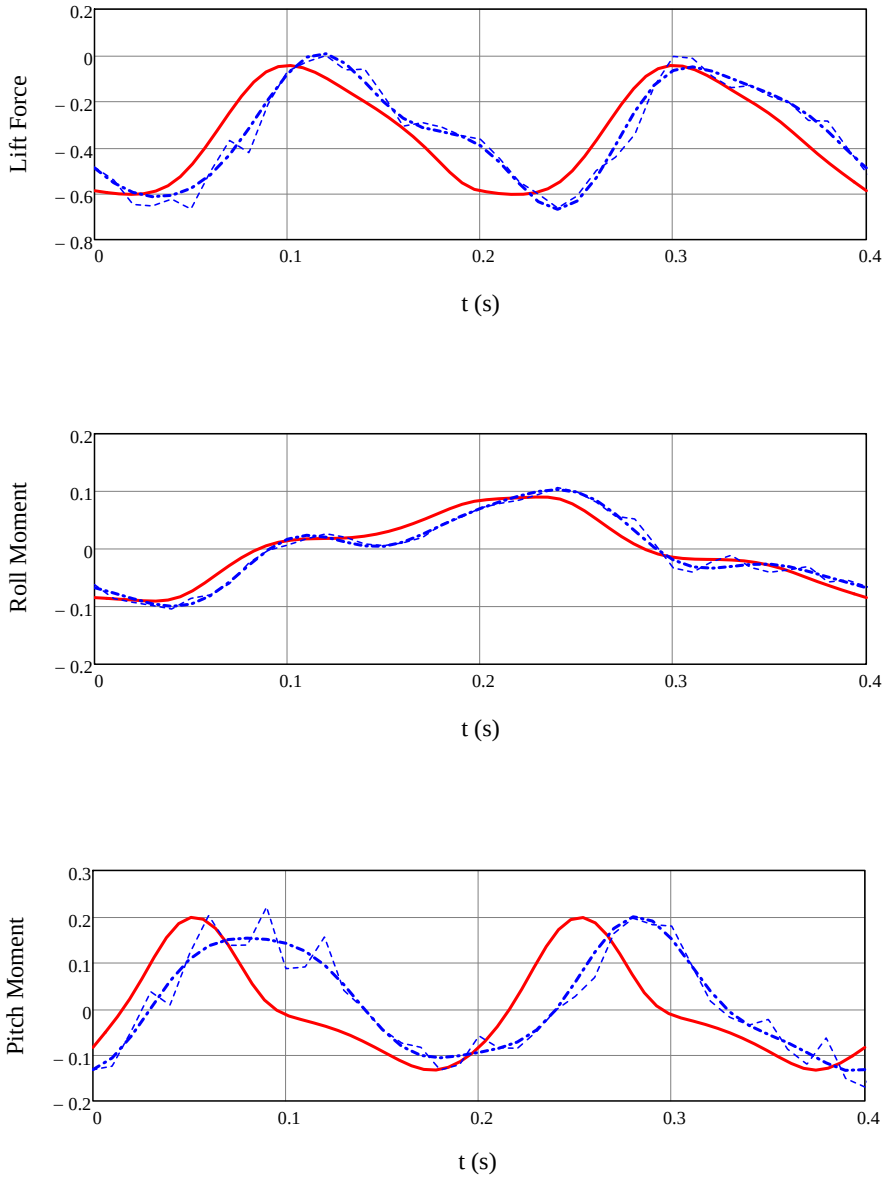

Figure C.12: Time series comparison of non-dimensional lift force and roll and pitch moments between 2D+t theory (solid line) and experiments (averaged: dash-dotted line; raw: dotted line) in forced roll. Experimental conditions: $C_\Delta = 0.29$, $C_v = 2.9$, $\phi_0 = 20°$, $f = 2.5$ Hz

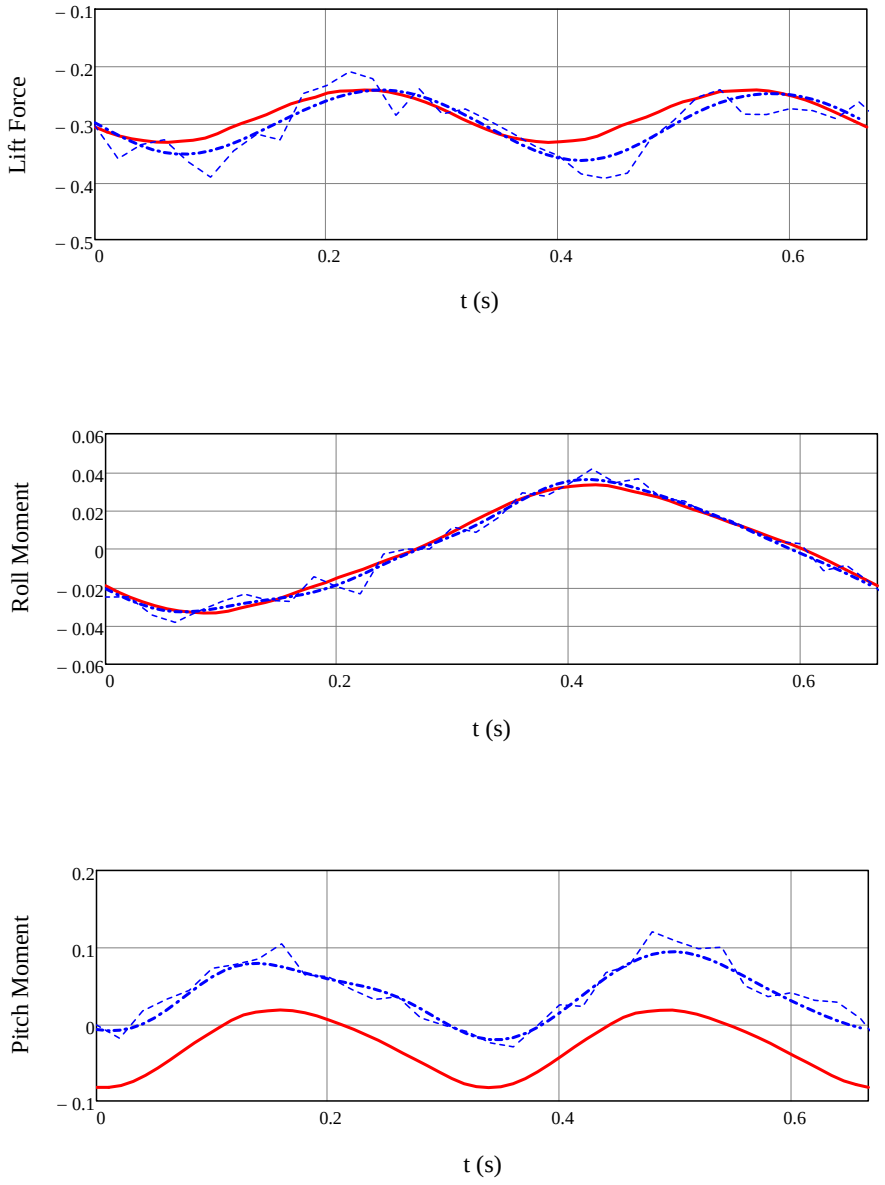

Figure C.13: Time series comparison of non-dimensional lift force and roll and pitch moments between 2D+t theory (solid line) and experiments (averaged: dash-dotted line; raw: dotted line) in forced roll. Experimental conditions: $C_\Delta = 0.29$, $C_v = 4.3$, $\phi_0 = 10°$, $f = 1.5$ Hz

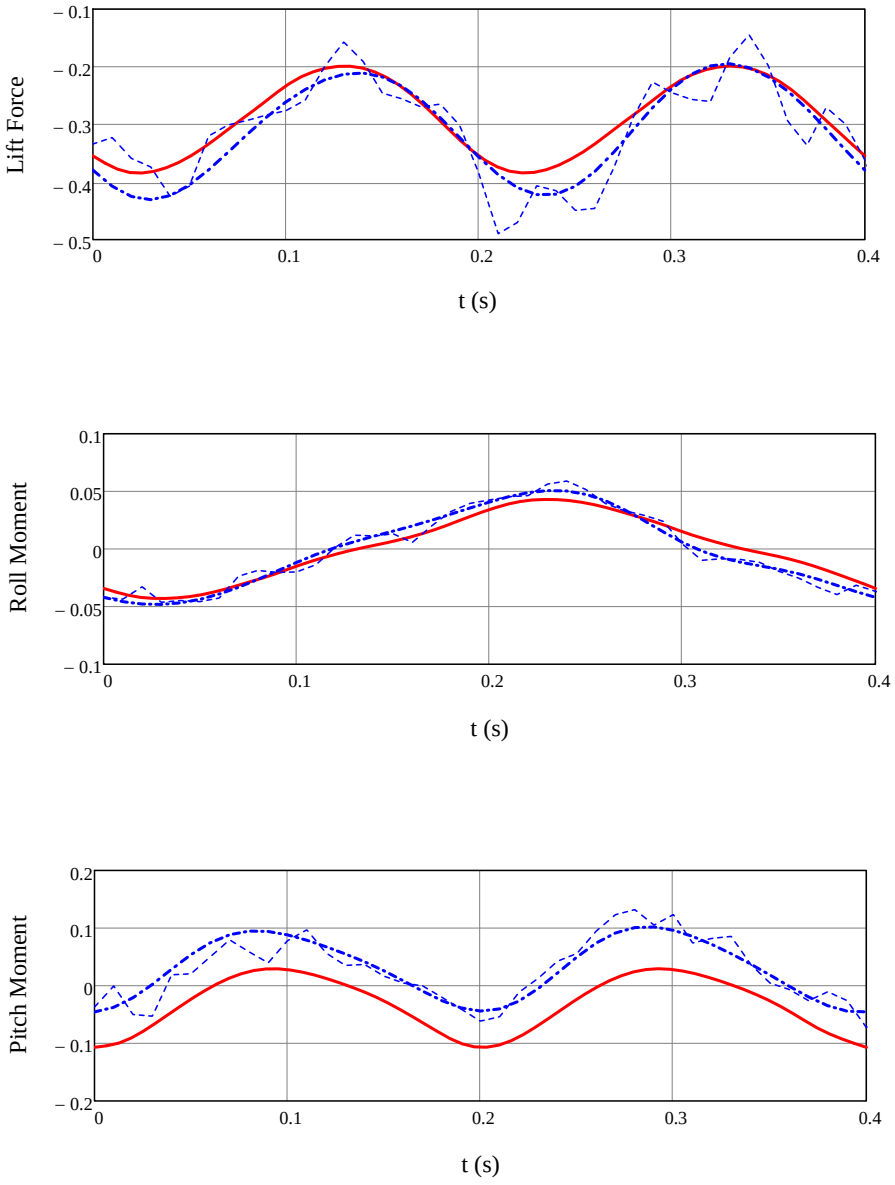

Figure C.14: Time series comparison of non-dimensional lift force and roll and pitch moments between 2D+t theory (solid line) and experiments (averaged: dash-dotted line; raw: dotted line) in forced roll. Experimental conditions: $C_\Delta = 0.29$, $C_v = 4.3$, $\phi_0 = 10°$, $f = 2.5$ Hz

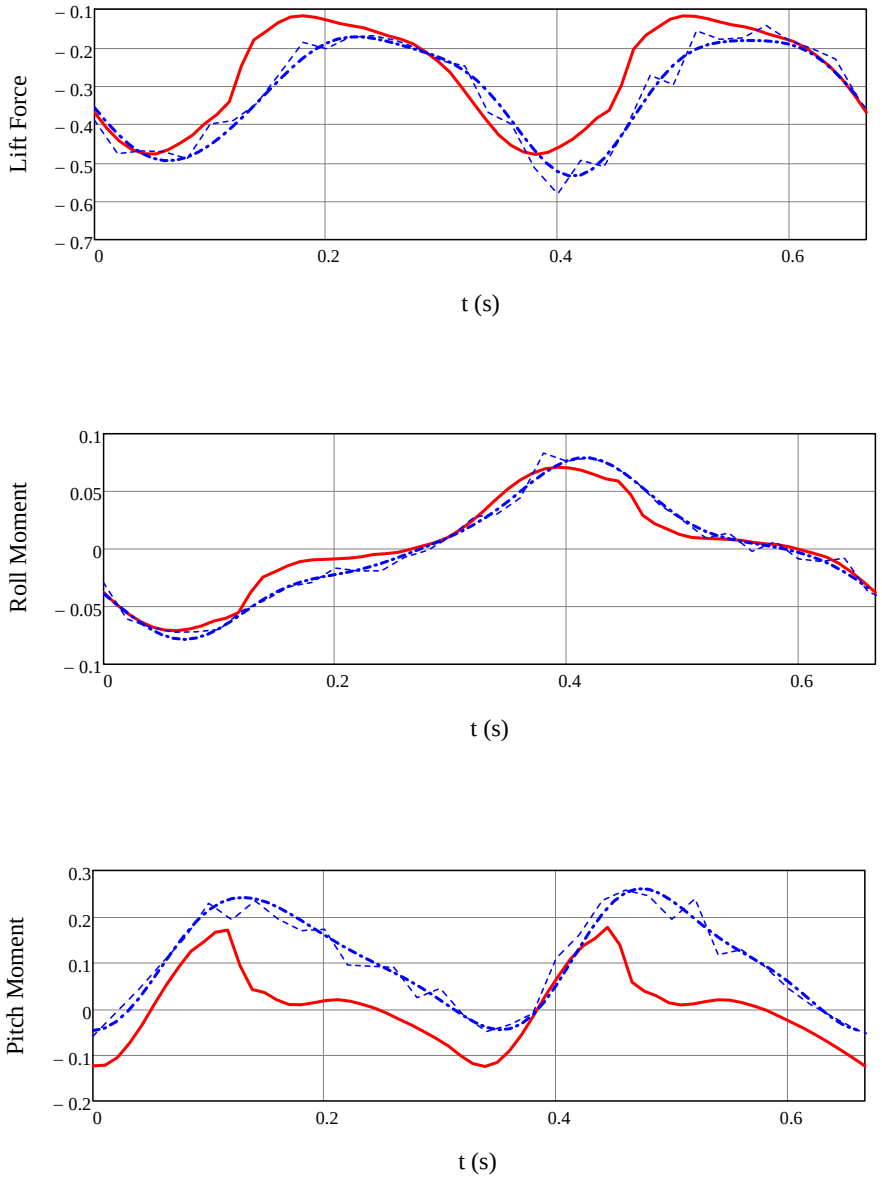

Figure C.15: Time series comparison of non-dimensional lift force and roll and pitch moments between 2D+t theory (solid line) and experiments (averaged: dash-dotted line; raw: dotted line) in forced roll. Experimental conditions: $C_\Delta = 0.29$, $C_v = 4.3$, $\phi_0 = 20°$, $f = 1.5$ Hz

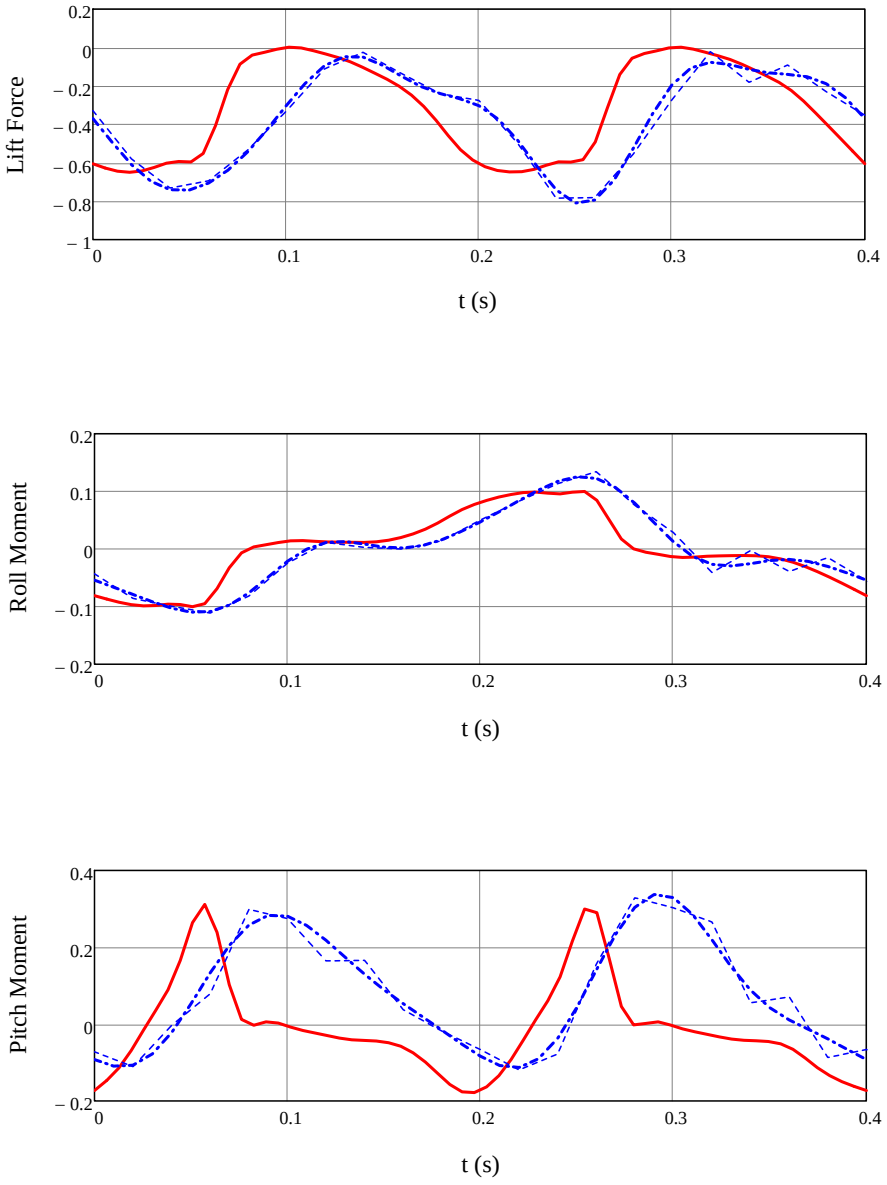

Figure C.16: Time series comparison of non-dimensional lift force and roll and pitch moments between 2D+t theory (solid line) and experiments (averaged: dash-dotted line; raw: dotted line) in forced roll. Experimental conditions: $C_\Delta = 0.29$, $C_v = 4.3$, $\phi_0 = 20°$, $f = 2.5$ Hz

BIBLIOGRAPHY

BIBLIOGRAPHY

Abkowitz, M. A. (1969). *Stability and Motion Control of Ocean Vehicles*. MIT Press, Cambridge, MA, USA. Chapter 2.

Algarin, R. and Tascon, O. D. (2014a). Estudio de la prueba de oscilación forzada en rolido de botes de planeo mediante herramientas CFD. Technical Report IT-3354-835-09, La Corporación de Ciencia y Tecnología para el Desarrollo de la Industria Naval Marítima y Fluvial COTECMAR, Cartagena, Colombia. In Spanish.

Algarin, R. and Tascon, O. D. (2014b). Estudio de la succión dinámica en popa en botes de planeo navegando en condición estable. Technical Report IT-3354-835-08, La Corporación de Ciencia y Tecnología para el Desarrollo de la Industria Naval Marítima y Fluvial COTECMAR, Cartagena, Colombia. In Spanish.

Arguin Jr., W. R., Connors, T. J., and Troesch, A. W. (2001). Experimental prediction of transverse planing hull dynamics for use in computer simulation. In *Proceedings of the 26th American Towing Tank Conference 26th ATTC*, Glen Cove, NY, USA.

Arguin Jr., W. R. and Troesch, A. W. (2001). Prediction of planing vessel hydrodynamic coefficients using least squares data fitting. In *Proceedings of the 26th American Towing Tank Conference 26th ATTC*, Glen Cove, NY, USA.

Balsamo, F., Milanesi, S., and Pensa, C. (2001). Rolling dynamic in planing and semi-planing range. In *Proceedings of the 6th International Conference on Fast Sea Transportation FAST 2001*, Southampton, UK.

Balsamo, F., Milanesi, S., and Pensa, C. (2002). Influence of deadrise angle on rolling dynamic. In *Proceedings of the 6th Symposium on High Speed Marine Vehicles: WEMT Conference 2002*, Castello di Baia, Italy.

Bassler, C. C., Reed, A. M., and Brown, A. J. (2010). Characterization of physical phenomena for large amplitude ship roll motion. In *Proceedings of the 29th American Towing Tank Conference 29th ATTC*, Annapolis, MD, USA.

Battistin, D. and Iafrati, A. (2002). Hydrodynamics of planing hulls through a 2D+t approach. In *Proceedings of International Summer Scientific School: High Speed Hydrodynamics*.

Blount, D. L. and Codega, L. T. (1992). Dynamic stability of planing boats. *Marine Technology*, 29(1):4–12.

Brown, P. W. (1971). An experimental and theoretical study of planing surfaces with trim flaps. Technical Report SIT-DL-71-1463, Davidson Laboratory, Stevens Institute of Technology, Hoboken, NJ, USA.

Brown, P. W. and Klosinski, W. E. (1994a). Directional stability tests of a 30 degree prismatic planing hull. Technical Report CG-D-27-94, Davidson Laboratory, Stevens Institute of Technology, Hoboken, NJ, USA.

Brown, P. W. and Klosinski, W. E. (1994b). Directional stability tests of two prismatic planing hulls. Technical Report USCG-D-11-94, Davidson Laboratory, Stevens Institute of Technology, Hoboken, NJ, USA.

Brown, P. W. and Klosinski, W. E. (1995a). Experimental determination of the added inertia and damping of a 30 degree deadrise planing boat in roll. Technical Report CG-D-04-95, Davidson Laboratory, Stevens Institute of Technology, Hoboken, NJ, USA.

Brown, P. W. and Klosinski, W. E. (1995b). Experimental determination of the added inertia and damping of planing boats in roll. Technical Report CG-D-03-95, Davidson Laboratory, Stevens Institute of Technology, Hoboken, NJ, USA.

Casella, G. and Berger, R. L. (2002). *Statistical Inference*. Duxbury, California, USA, second edition.

Castro-Feliciano, E. (2016). *Co-design of Planing Craft and Active Control Systems*. PhD dissertation, University of Michigan, Ann Arbor, MI, USA.

Chapman, R. B. (1976). Free-surface effects for yawed surface-piercing plates. *Journal of Ship Research*, 20(3):125–136.

Cohen, S. H. and Blount, D. L. (1986). Research plan for the investigation of dynamic instability of small high-speed craft. *SNAME Transactions*, 94(7):197–214.

Connors, T. J. (2001). Development of an experimental method to determine high-speed planing boat dynamic performance. Master's thesis, University of Michigan, Ann Arbor, MI, USA.

Dalzell, J. (1978). A note on the form of ship roll damping. *Journal of Ship Research*, 22(3):178–185.

Eça, L. and Hoekstra, M. (2014). A procedure for the estimation of the numerical uncertainty of CFD calculations based on grid refinement studies. *Journal of Computational Physics*, 262:104 – 130.

Fairlie-Clarke, A. and Tveitnes, T. (2008). Momentum and gravity effects during the constant velocity water entry of wedge-shaped sections. *Ocean Engineering*, 35(7):706 – 716.

Falstinsen, O. M. (2005). *Hydrodynamics of High-Speed Marine Vehicles*. Cambridge University Press, Cambridge, first edition.

Faltinsen, O. M., Landrini, M., and Greco, M. (2004). Slamming in marine applications. *Journal of Engineering Mathematics*, 48(3):187–217.

Ferrando, M., Gualeni, P., Viviani, M., Ruscelli, D., and Sapere, S. (2009). Static and dynamic stability of planning boats: Application cases for an harmonized rule perspective. In *Proceedings of the 10th International Conference on Fast Sea Transportation FAST 2009*, Athens, Greece.

Fontaine, E. and Tulin, M. (2001). On the prediction of nonlinear free surface flows past slender hulls using 2D+t theory: The evolution of an idea. *Ship Technology Research*, 48:56 – 67.

Fossen, T. I. (1994). *Guidance and Control of Ocean Vehicles*. John Wiley & Sons Ltd., Chichester, first edition.

Froude, W. (1955). *The Papers of William Froude*. The Institution of Naval Architects, London.

Garme, K. (2005). Improved time domain simulation of planing hulls in waves by correction of the near-transom lift. *International Shipbuilding Progress*, 52(3):201 – 230.

Gawthrop, P. J., Kountzeris, A., and Roberts, J. B. (1988). Parametric identification of nonlinear ship roll motion from forced roll data. *Journal of Ship Research*, 32(2):101–111.

Ghadimi, P., Tavakoli, S., and Dashtimanesh, A. (2015). An analytical procedure for time domain simulation of roll motion of the warped planing hulls. *Proceedings of the Institution of Mechanical Engineers, Part M: Journal of Engineering for the Maritime Environment*.

Ghadimi, P., Tavakoli, S., and Dashtimanesh, A. (2016a). Coupled heave and pitch motions of planing hulls at non-zero heel angle. *Applied Ocean Research*, 59:286 – 303.

Ghadimi, P., Tavakoli, S., Dashtimanesh, A., and Zamanian, R. (2016b). Steady performance prediction of a heeled planing boat in calm water using asymmetric 2D+t model. *Proceedings of the Institution of Mechanical Engineers, Part M: Journal of Engineering for the Maritime Environment*.

Godderidge, B., Phillips, A. B., Lewis, S., Turnock, S. R., Hudson, D. A., and Tan, M. (2008). The simulation of free surface flows with computational fluid dynamics. In *Proceedings of the 2008 ANSYS UK User Conference: Inspiring Engineering*. Oxford, UK.

Haddara, M. and Bennett, P. (1989). A study of the angle dependence of roll damping moment. *Ocean Engineering*, 16(4):411 – 427.

Himeno, Y. (1981). Prediction of ship roll damping – State of the Art. Report 239, University of Michigan, Department of Naval Architecture and Marine Engineering, Ann Arbor, MI, USA.

Holloway, D. S. and Davis, M. R. (2006). Ship motion computations using a high froude number time domain strip theory. *Journal of Ship Research*, 50(1):15–30.

Iafrati, A. and Broglia, R. (2008). Hydrodynamics of planing hulls: A comparison between RANS and 2D+t potential flow models. In *Proceedings of 27th Symposium on Naval Hydrodynamics*, Seoul, Korea.

Ikeda, Y. and Katayama, T. (2000). Roll damping prediction method for a high-speed planing craft. In Renilson, M., editor, *Proceedings of the 7th International Conference on Stability of Ship and Ocean Vehicles STAB2000*, volume B, pages 532–541, Launceston, Tasmania, Australia. Australian Maritime College.

Ikeda, Y., Katayama, T., and Okumura, H. (2000). Characteristics of hydrodynamic derivatives in maneuvering equations for super high-speed planing hulls. In Chung, J. S., Frederking, R. M., Saeki, H., and Koterayama, W., editors, *Proceedings of the Tenth (2000) International Offshore and Polar Engineering Conference*, volume 4, pages 434–444. International Society of Offshore and Polar Engineers.

Ikeda, Y., Katayama, T., and Tajima, S. (1998). A prediction method of vertical lift component in roll and heave damping. *Journal of Kansai Society of Naval Architects, Japan*, 229:127 – 134.

IMO (2008). *International Code of Safety for High Speed Craft, 2000 HSC Code*. International Maritime Organization (IMO), 2008 edition.

ISO (2015). *ISO 12217 Small Craft – Stability and Buoyancy Assessment and Categorization*. International Organization for Standardization (ISO), 2015 edition.

ITTC (2011). Numerical Estimation of Roll Damping. ITTC - Recommended Procedures and Guidelines No 7.5-02-07-04.5, International Towing Tank Conference.

Judge, C. (2010). Frequency dependence of hydrodynamic coefficients in roll. In *Proceedings of the 29th American Towing Tank Conference*, pages 285–290. Annapolis, MD, USA.

Judge, C. (2012). Static and dynamic forces and wetted lengths for a planing hull model forced in roll. In *Proceedings of the 3rd Chesapeake Power Boat Symposium*, St. John's College, Annapolis, MD, USA.

Judge, C. (2014a). Coupling of heave and roll for high-speed planing hulls. In *Proceedings of the ASME 2014 33rd International Conference on Ocean, Offshore and Artic Engineering OMAE2014*, San francisco, CA, USA.

Judge, C., Troesch, A. W., and Perlin, M. (1999). Water impact model with horizontal velocity. In *Proceedings of the 14th International Workshop on Water Waves and Floating Bodies IWWWFB14*, Port Huron, MI, USA.

Judge, C., Troesch, A. W., and Perlin, M. (2004). Initial water impact of a wedge at vertical and oblique angles. *Journal of Engineering Mathematics*, 48(3):279–303.

Judge, C. Q. (2013). Comparisons between prediction and experiment for lift force and heel moment for a planing hull. *Journal of Ship Production and Design*, 29(1):36–46.

Judge, C. Q. (2014b). Empirical methods for predicting lift and heel moment for a heeled planing hull. *Journal of Ship Production and Design*, 30(4):175–183.

Judge, C. Q. and Judge, J. A. (2013). Measurement of hydrodynamic coefficients on a planing hull using forced roll oscillations. *Journal of Ship Research*, 57(2):112–124.

Kashiwagi, M. (1997). Numerical seakeeping calculations based on the slender ship theory. *Ship Technology Research*, 44(4):167 – 192.

Katayama, T. (2002). Experimental techniques to assess dynamic instability of high-speed planing craft - non-zero heel, bow-diving, porpoising and transverse porpoising -. In Grochowalski, S., editor, *Proceedings of the Sixth International Ship Stability Workshop*, Glenn Cove, New York, USA. International Standing Stability Committee.

Katayama, T. and Ikeda, M. F. Y. (2007). A study on transverse stability loss of planing craft at super high forward speed. *International Shipbuilding Progress*, 54:365 – 377.

Katayama, T. and Ikeda, Y. (1996). A study on transverse instability of planing craft at high speeds in calm water. In *Proceedings of the Third Korea-Japan Joint Workshop on Ship and Marine Hydrodynamics*, pages 117 – 124.

Katayama, T. and Okumura, H. (2000). A study on unstable motions of a planing craft in maneuvering - large amplitude motion due to periodic maneuvering motion -. *Journal of the Society of Naval Architects of Japan*, 188:155 – 162.

Katayama, T., Taniguchi, T., and Habara, K. (2010). Tank tests to estimate onset of dynamic instabilities of high-speed planing craft. In *Proceedings of the Second Chesapeake Power Boat Symposium*.

Kihara, H., Naito, S., and Sueyoshi, M. (2005). Numerical analysis of the influence of above-water bow form on added resistance using nonlinear slender body theory. *Journal of Ship Research*, 49(3):191–206.

Kreuzer, E. J. and Sichermann, W. M. (2005). Slender body theory approach to nonlinear ship motions. In *Proceedings of the 20th International Workshop on Water Waves and Floating Bodies IWWWFB20*. Longyearbyen, Norway.

Lai, C. (1994). *Three-dimensional planing hydrodynamics based on a vortex lattice method*. PhD. dissertation, University of Michigan, Ann Arbor, MI, USA.

Lewandowski, E. M. (1994). Trajectory predictions for high speed planing craft. *International Shipbuilding Progress*, 41(426):137 – 148.

Lewandowski, E. M. (1996). Prediction of the dynamic roll stability of hard-chine planing craft. *Journal of Ship Research*, 40(2):144 – 148.

Lewandowski, E. M. (1997). Transverse dynamic stability of planing craft. *Marine Technology*, 34(2):109 – 118.

Lewandowski, E. M. (2004). *The Dynamics of Marine Craft: Maneuvering and Seakeeping*, volume 22 of *Advanced Series on Ocean Engineering*. World Scientific, Singapore, SG., first edition.

Martin, M. (1978). Theoretical determination of porpoising instability of high-speed planing boats. *Journal of Ship Research*, 22(1):32–53.

Maruo, H. (1967). High- and low-aspect ratio approximation of planing surfaces. *Shiffstechnik*, 72(14):57–64.

Maruo, H. (1982). New approach to the theory of slender ships with forward velocity. *Bulletin of the Faculty of Engineering, Yokohama National University*, 31:85–100.

Milanesi, S. (2002). *Studio Teorico e Sperimentale della Stabilta Dinamica Trasversale degli Scafi Veloci*. PhD thesis, University of Naples "Federico II", Naples, Italy. In Italian.

Morabito, M. G. (2014). Empirical equations for planing hull bottom pressures. *Journal of Ship Research*, 58(4):185–200.

Müller-Graf, B. (1997). Dynamic stability of high speed small craft. In *Proceedings of the 25th WEGEMT School on Small Craft Technology*, Athens, Greece.

Nayfeh, A. H., Mook, D. T., and Marshall, L. R. (1974). Perturbation-energy approach for the development of the nonlinear equations of ship motion. *Journal of Hydronautics*, 8(4):130–136.

Neves, M. A. S. (2007). An investigation on roll parametric resonance in regular waves. *International shipbuilding progress*, 54(4):207–225.

Ng, L. and Rand, R. (2002). Bifurcations in a Mathieu equation with cubic nonlinearities. *Chaos, Solitons & Fractals*, 14(2):173 – 181.

Oh, I. G., Nayfeh, A. H., and Mook, D. T. (2000). A theoretical and experimental investigation of indirectly excited roll motion in ships. *Philosophical Transactions of the Royal Society of London A: Mathematical, Physical and Engineering Sciences*, 358(1771):1853–1881.

Pabst, W. (1931). Landing impact of seaplanes. Technical Memorandum NACA TM 624, National Advisory Committee for Aeronautics, Washington, DC, USA.

Pauling, J. R. and Rosenberg, R. M. (1959). On unstable ship motions resulting from nonlinear coupling. *Journal of Ship Research*, 3(1):36–46.

Piro, D. J. and Maki, K. J. (2011). Hydroelastic wedge entry and exit. In *Proceedings of the 11th International Conference on Fast Sea Transportation FAST 2011*, Honolulu, HA, USA.

Piro, D. J. and Maki, K. J. (2012). Water exit of a wedge-shaped body. In *Proceedings of the 27th International Workshop on Water Waves and Floating Bodies IWWWFB12*, Copenhagen, Denmark.

Piro, D. J. and Maki, K. J. (2013). An adaptive interface compression method for water entry and exit. Report No 2013-350, University of Michigan, Department of Naval Architecture and Marine Engineering, Ann Arbor, MI, USA.

Plante, M. (1998). Mathematical model for the manoeuvring behaviour of planing ships. Master's thesis, TU Delft, Faculty of Mechanical Engineering and Marine Technology, The Netherlands. Ship Hydromechanics Laboratory, Report 1136-S.

Plante, M., Toxopeus, S., Blok, J., and Keuning, A. (1998). Hydrodynamic manoeuvring aspects of planing craft. In *Proceedings of the International Symposium and Workshop on Forces Acting on a Manoeuvring Vessel*, Val de Reuil, France.

Rand, R., Barcilon, A., and Morrison, T. (2005). Parametric resonance of Hopf bifurcation. *Nonlinear Dynamics*, 39(4):411–421.

Rand, R. H. (2012). *Lecture notes on nonlinear vibrations*. First University Press, Ithaca, NY, online by the Internet, http://ecommons.cornell.edu/handle/1813/79, v53 edition.

Roy, C. J. (2005). Review of code and solution verification procedures for computational simulation. *Journal of Computational Physics*, 205(1):131 – 156.

Ruscelli, D., Gualeni, P., and Viviane, M. (2012). An overview of planing monohulls transverse dynamic stability and possible implications with static stability rules. *RINA Transactions, International Journal of Small Craft Technology, Part B2*, 153:B–73–B–86.

Savander, B. R. (1997). *Planing Hull Steady Hydrodynamics*. PhD. dissertation, University of Michigan, Ann Arbor, MI, USA.

Savander, B. R., Scorpio, S. M., and Taylor, R. K. (2002). Steady hydrodynamic analysis of planing surfaces. *Journal of Ship Research*, 46(4):248–279.

Savitsky, D. (1964). Hydrodynamic design of planing hulls. *Marine Technology*, 1(1):71–96.

Savitsky, D., Prowse, R. E., and Lueders, D. H. (1958). High-speed hydrodynamic characteristics of a flat plate and 20 deadrise surface in unsymmetrical planing conditions. Technical Note NACA TN 4187, Stevens Institute of Technology, Hoboken, NJ, USA.

Seif, M. S., Mousaviraad, S. M., Saddathosseini, S. H., and Volker, B. (2005). Numerical analysis of the influence of above-water bow form on added resistance using nonlinear slender body theory. *Sintesis Tecnologica*, 2:79–84.

Semenov, Y. A. and Iafrati, A. (2006). On the nonlinear water entry problem of asymmetric wedges. *Journal of Fluid Mechanics*, 547:231–256.

Shuford, C. L. (1958). A theoretical and experimental study of planing surfaces including effects of cross section and plan form. Technical Report NACA TR 1355, National Advisory Committee for Aeronautics. Langley Aeronautical Lab., Langley Field, VA, USA.

Suleiman, B. M. (2000). *Identification of Finite-Degree-of-Freedom Models for Ship Motions*. PhD. dissertation, Virginia Polytechnic Institute and State University, Blacksburg, VA, USA.

Sun, H. and Faltinsen, O. M. (2007). The influence of gravity on the performance of planing vessels in calm water. *Journal of Engineering Mathematics*, 58:91–107.

Sun, H. and Faltinsen, O. M. (2010). Numerical study of planing vessels in waves. *Journal of Hydrodynamics, Ser. B*, 22(5):468 – 475.

Sun, H. and Faltinsen, O. M. (2012). Hydrodynamic forces on a semi-displacement ship at high speed. *Applied Ocean Research*, 34:68–77.

Sutulo, S. and Guedes Soares, C. (2007). Contribution of higher-order harmonics for estimating manoeuvring derivatives from oscillatory tests. *International Shipbuilding Progress*, 54:1 – 24.

Tascon, O. D. and Algarin, R. (2013). Numerical computation of the added mass and damping coefficients of planing hulls in roll via Slender Body Theory and 2-D impact theory. In *Proceedings of the 12th International Conference on Fast Sea Transportation FAST 2013*, Amsterdam, The Netherlands.

Tascon, O. D., Troesch, A. W., and Maki, K. J. (2009). Numerical computation of the hydrodynamic forces acting on a maneuvering planing hull via Slender Body Theory - SBT and 2-D impact theory. In *Proceedings of the 10th International Conference on Fast Sea Transportation FAST 2009*, Athens, Greece.

Tavakoli, S., Ghadimi, P., Dashtimanesh, A., and Sahoo, P. K. (2015). Determination of hydrodynamic coefficients related to roll motion of high-speed planing hulls. In *Proceedings of the 13th International Conference on Fast Sea Transportation FAST 2015*. Washington DC, USA.

Toxopeus, S., Keuning, J., and Hooft, J. P. (1997). Dynamic stability of planing ships. In *Proceedings of the RINA International Symposium and Seminar on the Safety of High Speed Craft*.

Toxopeus, S. L. (1996). A time domain simulation program for manoeuvring of planing ships. Master's thesis, TU Delft, Faculty of Mechanical Engineering and Marine Technology, The Netherlands. Ship Hydromechanics Laboratory, Report 1065-S.

Troesch, A. W. (1992). On the hydrodynamics of vertically oscillating planing hulls. *Journal of Ship Research*, 36(4):317 – 331.

Troesch, A. W. and Falzarano, J. M. (1993). Modern nonlinear dynamical analysis of vertical plane motion of planing hulls. *Journal of Ship Research*, 37(3):189 – 199.

Tuck, E. O. (1975). Low-aspect-ratio flat-ship theory. *Journal of Hydronautics*, 9(1):3–12.

Vorus, W. S. (1996). A flat cylinder theory for vessel impact and steady planing resistance. *Journal of Ship Research*, 40(2):89–106.

Wellicome, J. F. and Campbell, I. M. C. (1984). The transverse dynamic stability of planing craft. Ship Science Report No 12, University of Southampton, Southampton, UK.

Wu, G., Sun, H., and He, Y. (2004). Numerical simulation and experimental study of water entry of a wedge in free fall motion. *Journal of Fluids and Structures*, 19(3):277 – 289.

Xu, G., Duan, W., and Wu, G. (2008). Numerical simulation of oblique water entry of an asymmetrical wedge. *Ocean Engineering*, 35(16):1597 – 1603.

Xu, G. D., Duan, W. Y., and Wu, G. X. (2010). Simulation of water entry of a wedge through free fall in three degrees of freedom. *Proceedings of the Royal Society of London A: Mathematical, Physical and Engineering Sciences*, 466(2120):2219–2239.

Xu, L., Troesch, A. W., and Vorus, W. S. (1998). Asymmetric vessel impact and planing hydrodynamics surfaces. *Journal of Ship Research*, 42(3):187–198.

Yeung, R. W. and Kim, S. H. (1981). Radiation forces on ships with forward speed. In *Proceedings of the 3rd International Conference on Numerical Ship Hydrodynamics*, pages 499–515. Paris, France.

Yeung, R. W. and Kim, S. H. (1985). A new development in the theory of oscillating and translating slender ships. In *Proceedings of the 15th Symposium on Naval Hydrodynamics*, pages 195–218. National Academy Press.

Zarnick, E. E. (1978). A nonlinear mathematical model of motions of a planing boat in regular waves. Technical Report DTNSRDC-78/032, David W. Taylor Naval Ship Research and Development Center, Bethesda, MD, USA.

Zhao, R., Faltinsen, O. M., and Haslum, H. A. (1997). A simplified nonlinear analysis of a high-speed planing craft in calm water. In Baird, N. and Jeffs, A., editors, *Proceedings of the 4th International Conference on Fast Sea Transportation FAST 1997*, volume 1, pages 431–438. Baired Publications. Sidney, Australia.